Politecnico di Milano

SCHOOL OF INDUSTRIAL AND INFORMATION ENGINEERING

Master of Science in Green Power System – Energy Engineering

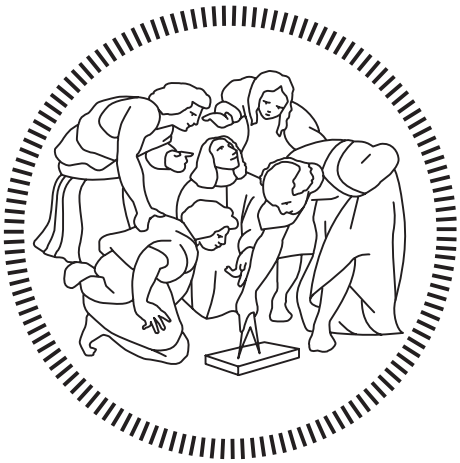

Ceramic and metal supported Solid Oxide Cells: low-temperature electrolysis performances and degradation assessment

Thesis Supervisor

Prof. Andrea CASALEGNO

Co-Supervisor

Prof. Anke HAGEN

Candidates

Riccardo CALDOGNO – 915007

Federico CAPOTONDO – 919261

Academic Year 2020 – 2021

Ringraziamenti

Arrivato alla fine del mio percorso di studi universitari, posso affermare quanto preziosi siano stati questi anni trascorsi al Politecnico. È stata un'esperienza che mi ha fatto crescere sia da un punto di vista formativo sia, specialmente, a livello umano, e che mi accompagnerà per sempre come un bellissimo ricordo. Svolgere la tesi magistrale al DTU di Copenhagen è stata senza dubbio la ciliegina sulla torta che mi ha permesso di concludere questa avventura nel migliore dei modi. Una cosa sicura è che da solo non ce l'avrei mai fatta ad arrivare fin qui, per questo vorrei ringraziare le persone che più mi sono state vicine durante questa importante fase della mia vita.

Mi sento di rivolgere il primissimo ringraziamento al mio collega e grande amico Federico, con cui ho condiviso questi ultimi indimenticabili mesi di lavoro e divertimento, e senza il quale probabilmente non sarei riuscito a iniziare questa esperienza all'estero.

Vorrei poi ringraziare il Professor Andrea Casalegno, in primis per aver accettato di essere nostro relatore nonostante le difficoltà date dalla distanza e, in particolare, per tutti i consigli utili offertici.

Un ringraziamento speciale va ad Anke e Xiufu, nostri supervisori al DTU, per la professionalità e pazienza dimostrataci, per la costante ed immancabile disponibilità, e per il prezioso aiuto datoci durante lo sviluppo di questo elaborato.

Un grande grazie anche a Jens e Henrik per la preziosa assistenza tecnica offertaci in laboratorio, a Elena e Nicola per averci accolto nel gruppo del DTU, a Jens Ole e Aiswarya per gli utili suggerimenti in fase di preparazione dei test.

Un grazie speciale a Kuba e Ola per tutte le serate di gioco, le chiacchiere, i piccoli viaggi, le cene, le avventure, e tutti gli altri splendidi momenti passati insieme a Copenhagen.

Importanti e memorabili sono stati tutti gli attimi trascorsi con gli amici incontrati al Poli, per questo vorrei ringraziare in particolar modo Michi, Simo, Tommi, Teo, Mati e, ancora una volta, Fede.

Indispensabili durante questi anni sono stati i miei amici storici, con i quali sono cresciuto e ho condiviso innumerevoli momenti che mi hanno sicuramente aiutato ad affrontare al meglio il mio percorso di studi. Un immenso grazie va quindi a Mirko, Leo e Zami, siete semplicemente i migliori.

È d'obbligo ringraziare anche tutti i membri, presenti e passati, della mia squadra di calcio, e tutto il mondo della Virtus Bisuschio, per aver reso ancora più speciali questi ultimi anni. Grazie anche a tutti i ragazzi del 2002 e, di nuovo, a Mirko. Porterò sempre con me gli innumerevoli viaggi in macchina e tutte le serate trascorse insieme a Pogliana, ospiti di Ettore ed Elena (grazie infinitamente anche a voi).

Il ringraziamento che mi sta più a cuore va alla mia ragazza, Lucía, che dopo essere entrata

inaspettatamente e improvvisamente nella mia vita, è riuscita a rivoluzionarla completamente. Grazie per la tua vicinanza, il supporto, la fiducia e l'immenso affetto che mi hai dimostrato sin dal primo giorno.
Grazie infine ai miei genitori e a mio fratello Lorenzo, ultimi della lista ma senza dubbio i più importanti, per avermi sempre sostenuto. Mamma e papà, grazie per tutti i sacrifici che avete sempre fatto per il mio bene, non sono mai passati inosservati. Non mi avete mai fatto mancare nulla, senza di voi non sarei mai arrivato dove sono oggi. Questa laurea è in parte anche vostra.

Riccardo

Non posso che iniziare ringraziando la mia famiglia che mi ha sempre sostenuto nelle mie scelte, particolarmente in quella di studiare. Durante la mia educazione ho avuto la possibilità di vivere a contatto con alcune delle realtà più stimolanti d'Europa e lavorare con delle persone che hanno reso i miei anni universitari indimenticabili. Ringrazio dunque i miei amici, a partire da Riccardo che ha condiviso con me questa nuova avventura, e continuando con tutte le persone con cui ho condiviso momenti che resteranno sempre impressi nella mia memoria, incontrate sia grazie al Politecnico, che al chaos che governa l'Universo. Un doveroso ringraziamento va al professor Andrea Casalegno, che ci ha appoggiato nella scelta della nostra tesi, ed alle persone che lavorano al DTU. In particolare ringrazio la professoressa Anke Hagen che ci ha dato la possibilità di lavorare ad un progetto riguardante uno dei settori più interessanti dell'industria energetica contemporanea, e tutte le persone conosciute al dipartimento di conversione dell' energia del DTU, sempre disponibili al confronto e che hanno contribuito a creare un' atmosfera serena in cui lavorare.

Federico

Sommario

La consapevolezza sulle cause e conseguenze del cambiamento climatico sta alimentando nuovi investimenti nel settore dell'energia rinnovabile. L'Unione Europea è leader mondiale nella ricerca e sviluppo di soluzioni che possano portare ad una società più sostenibile, e la produzione rinnovabile di idrogeno nei prossimi decenni giocherà un ruolo fondamentale per raggiungere gli obiettivi stabiliti. L'elettrolisi rappresenta la miglior alternativa per produrre idrogeno verde. In particolare gli elettrolizzatori basati su celle ad ossidi solidi (SOEC dall'inglese) offrono diversi vantaggi rispetto alle altre tecnologie, come l'alta efficienza di conversione, la possibilità di essere operati sia come celle a combustibile sia come elettrolizzatori, i bassi costi dei materiali, e la capacità di convertire idrocarburi, CO ed altri gas ad alta densità energetica. In questo progetto l'attenzione è rivolta a due diverse tipologie di SOEC: celle con supporto ceramico, rappresentanti lo stato dell'arte di tale tecnologia, e celle con supporto metallico, recentemente sviluppate per migliorare la resilienza agli stress termici e meccanici delle prime. Particolare importanza è data alla valutazione delle prestazioni e del degrado ottenuti operando a bassa temperatura. Con tutte le celle è stato eseguito un test di durabilità galvanostatico di 500 ore a 650 °C, operando in elettrolisi ed alimentando aria all'elettrodo positivo per aiutare la rimozione dei prodotti di reazione e una miscela 50% vapore – 50% idrogeno all'elettrodo negativo. La cella a supporto ceramico, testata applicando una densità di corrente di 0.25 A/cm^2, ha mostrato un peggioramento delle prestazioni, in termini di aumento di tensione, pari al 13.28% per 1000 h. Tale degrado è attribuito all'elettrodo negativo. Nonostante le celle a supporto ceramico siano state progettate per operare ad alte temperature, il tasso di degrado ottenuto a 650 °C si è dimostrato coerente con quello riportato in un test passato ad 800 °C. Due celle a supporto metallico sono state testate in questo studio, ed entrambe hanno mostrato un comportamento inaspettato durante i test galvanostatici, svolti a 0.25 A/cm^2 con la prima cella e a 0.5 A/cm^2 con la seconda. In entrambi i casi, la diminuzione della tensione misurata ha suggerito che fenomeni di attivazione hanno avuto luogo. Durante la caratterizzazione iniziale in entrambe le celle i supporti metallici si sono ossidati; invece, operando costantemente in elettrolisi per 500 ore l'atmosfera riducente mantenuta all'elettrodo negativo ha permesso il lento ripristino della struttura metallica ed il conseguente aumento della conducibilità elettrica. I risultati molto promettenti in termini di stabilità durante l'operazione in elettrolisi, insieme alle proiezioni ottimiste sui costi, suggeriscono che le celle a supporto metallico sono una tecnologia che ricoprirà un ruolo rilevante nel mercato energetico nel prossimo futuro. Ulteriori test sono necessari per comprendere a fondo il comportamento di tali celle, e la ricerca dovrebbe concentrarsi sul trovare soluzioni per i problemi relativi all'ossidazione del supporto metallico.

Parole chiave: accumulo di energia, idrogeno verde, elettrolisi, celle ad ossidi solidi, operazione a bassa temperatura, celle con supporto metallico.

Abstract

Nowadays the awareness of the causes and consequences of climate change is fuelling new investments in the renewable energy field. The European Union is a world leader in research and development (R&D) for solutions that could allow a more sustainable society, and hydrogen will play a very important role in the achievement of this goal in the next decades. Electrolysis represents the best alternative to produce green hydrogen. Solid Oxide Electrolysis Cells (SOECs) in particular offer different advantages when compared to the others electrolyzers, like the very high electrochemical conversion efficiency, the possibility to be operated in both electrolysis and fuel cell modes, the low materials costs, and the opportunity to directly convert hydrocarbons, CO and other high energy-density gases. The focus of this project is on two different SOEC technologies: a state-of-the-art ceramic-supported cell and a recently developed Metal-Supported Cell (MSC), designed to improve the thermal and mechanical stability of the first one. Particular importance is given to the electrolysis performances and degradation assessment at low temperature. All the tested cells went through a 500-hours durability test in SOEC mode, performed in galvanostatic conditions at 650 °C feeding air as sweep gas to the positive electrode and a mixture 50% steam – 50% hydrogen to the negative one. The ceramic-supported cell showed an average degradation rate in terms of voltage increase equal to 13.28% per 1000 h. The cell voltage increased linearly throughout the whole durability test duration, which in this case was performed at 0.25 A/cm^2. The loss of performances is attributed to degradation of the negative electrode. Ceramic-supported cells are designed to work at higher temperatures, anyway the degradation rate observed at 650 °C with the cell tested for this project was consistent with the one obtained at 800 °C in a past test. Two metal-supported cells were tested and both shown unexpected behaviour during durability tests, carried out at 0.25 A/cm^2 with the first MSC and at 0.5 A/cm^2 with the second one. Cells voltage did not increase, as would be a normal consequence of degradation, instead activation processes were observed as constant reduction of the measured voltage. Oxidation of the metallic supports occurred during the first characterization in both cells; instead, during durability test the reducing atmosphere held constantly at the negative electrode allowed to slowly restore the metallic structure and consequently increase its electric conductivity. The very promising results in terms of high stability in electrolysis operation, together with the optimistic cost projections, suggest that in the near future MSC technology will play a relevant role in energy market. Further tests are essential to achieve a better knowledge of such cell's behaviour and R&D should be aimed to overcome the problems related to metal support oxidation.

Keywords: energy storage, green hydrogen, electrolysis, solid oxide cells, low-temperature operation, metal-supported cell.

Extended Abstract

Nowadays the awareness of the consequences and causes of climate change is fuelling new investments in the renewable energy field. The boundaries for a greener future are imposed by economy as well as by challenges related to the energy infrastructure revolution. Focusing particularly on technical issues, the spread of intermittent renewable energy sources can be implemented only through highly efficient energy storage systems and cheap and effective energy vectors. The European Union is a world leader in research and development (R&D) for solutions that could allow a more sustainable society, and hydrogen will play a very important role in the achievement of this goal in the next decades. Hydrogen is a very important industrial commodity, being essential for fertilizers and refining industries. Nowadays more than 90% of hydrogen is produced from fossil fuels. The impact of a renewable production of H_2 would be very important to drastically reduce carbon emissions. In addition to that, it can also be used as a valid alternative to batteries (as high energy-density storage medium with no issues related to long term storage), as an efficient energy vector (requiring anyway the renewal of infrastructures for gas transport), and also to produce synthetic fuels through well-established chemical routes. Particularly, this last option would also help to contribute to the decarbonisation of the transport sector – the one that today mostly relies on fossil fuels and accounts for one-third of European primary energy consumption – without the need to change drastically the existing transport infrastructures and technologies, as well as people's lifestyle. Electrolysis represents the best alternative to produce green hydrogen. Different technologies have been developed in the last decades, some are already present in the market while others are still in research and development phase. For instance, Alkaline and PEM electrolyzers can be considered mature technologies (a small margin of improvement is expected in the future), while Solid Oxide Cells (SOCs) started to become commercial in these last years.

SOC technology offers different advantages when compared to the other electrolyzers, and the expected overcome of their issues thanks to future R&D will grant them an important role in the energy market. Among their advantages it is possible to highlight that the operation at high temperatures (between 600 °C and 1000 °C depending on the particular technology) allows high conversion efficiency thanks to the favoured thermodynamics and to the fast kinetics of the reactions. These systems also offer excellent flexibility in the integration with other synthesis processes, the possibility to be operated in both electrolysis (SOEC) and fuel cell (SOFC) modes – making SOCs very attractive also for grid balance applications – to directly convert hydrocarbons in SOFC mode with higher efficiency with respect to combustion, and CO_2 and H_2O to syngas in SOEC mode (syngas can be exploited for many industrial uses, synthetic fuels production above all). In addition to that, their production can be based on scalable processes that would drastically reduce their price, eventually making them even more competitive than established combustion-based systems.

Still, some issues are to be faced in order to increase the life of the cells and allow their spreading in the energy industry.

The focus of this project is on two different systems: a state-of-the-art ceramic-supported cell technology and a new developed Metal-Supported Cell (MSC). The first one is commercially available and, despite there is still margin of improvement that can be obtained studying different active layers materials, R&D is mostly focused on finding a solution that would allow to decrease operative temperatures and to reduce the issues related to mechanical and thermal stresses given by the adoption of ceramic materials. Metal-supported cells were thought particularly to achieve this desired resilience that would allow an easier coupling with intermittent renewable energy sources. The ceramic layers are very thin and the support structure is given by a metallic alloy instead of a thick ceramic lattice. This traduces in a lower thermal inertia allowing the cell to respond quicker to thermal cycles with respect to ceramic based technologies; in addition, the metallic support also contributes to the increase in electrical conductivity and provides high mechanical stability to the cell. This last feature particularly is crucial for the scale up of the production, allowing to manufacture mechanically-stable devices with a wider active area and hence to reduce stack costs. The lower temperature of operation, possible thanks to different materials adopted for the active layers, also contributes to the economic advantage by reducing the cost related to stack materials (cheaper stainless steel) and balance of system. The main problem of this new technology is related to the oxidation of the metallic support that is very likely to occur at high temperatures in the presence of steam, and hinders real cell performances. R&D is particularly focused on finding the best alloys to be used as a support structure that can limit this issue and to understand comprehensively the cell behaviour. Electrolysis performed with metal supported SOCs is only at the beginning of the testing phase, for this reason this project is also valuable for the scientific community. Both technologies were tested for this work: the main objective for the ceramic supported cell was to study its behaviour for low temperature operation, while the main goal for the metal supported cell was to give a first understanding of the cell behaviour in electrolysis mode.

Solid Oxide Cells are composed by different layers with different functions. Figure 1 shows the cross sections of the two SOCs technologies tested for this project. For the ceramic-supported cell, shown in the left image, the layers from left to right are: lanthanum strontium manganite (LSM) current collector, lanthanum strontium cobaltite and gadolinium doped ceria composite (LSC-CGO) positive electrode (the powder sintered to realize such electrode contained 40% LSC and 60% CGO in weight), CGO barrier layer, yttria stabilized zirconia (YSZ) electrolyte, nickel-yttria stabilized zirconia (Ni-YSZ) negative electrode and support structure. On the right, the metal-support cells layers can be observed, from left to right: LSC positive electrode, CGO barrier layer, scandium and yttrium co-doped stabilized zirconia (ScYSZ) electrolyte, negative electrode composed by 5% ScYSZ and 95% lanthanum strontium titanate (LSFNT) infiltrated with a nickel suspension in gadolinium-doped ceria (Ni-CGO), FeCr porous support structure.

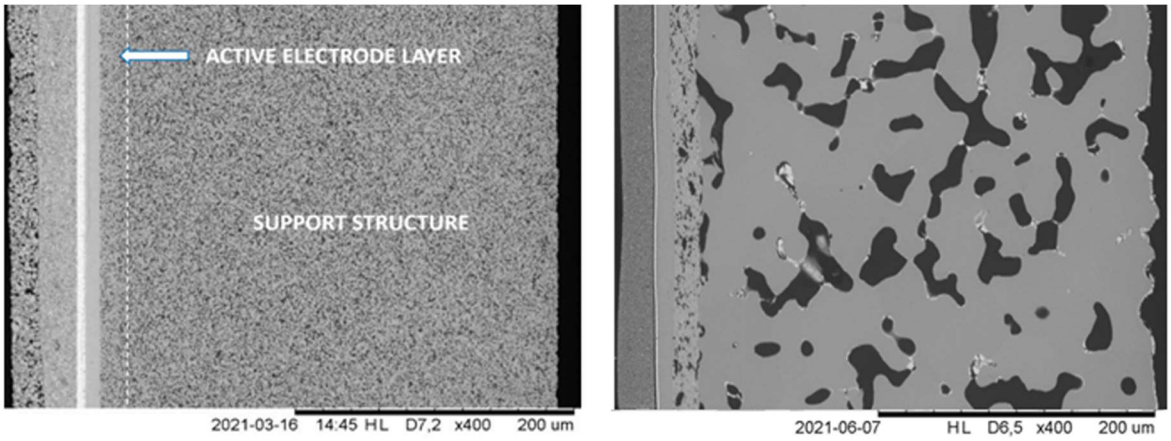

Figure 1 - Ceramic-supported (on the left) and metal-supported (on the right) cells cross sections images, taken with a scanning electron microscope using a magnification of x400.

The electrolyte separates the negative and positive sides of the cell and allows the transport of oxide ions from one side to the other, implying a flow of electrons accordingly. Zirconia (ZrO_2) is usually adopted since it is a very abundant material and presents the fluorite (cubic) structure at very high temperatures, which allows the conduction of oxide ions through point defects in the crystalline lattice. The addition of a dopant, with an ionic radius close to the one of Zr, can help to stabilize the fluorite structure at lower temperatures and affect the ionic conductivity. For instance, the addition of Y^{3+} produces a very stable cubic structure while Sc^{3+} increases the conductivity, and, as a consequence, gives the possibility to operate at even lower temperatures. For the tested ceramic supported cell, the electrolyte is composed by YSZ, while in the metal supported one also scandium is present as co-dopant (ScYSZ), trading off the advantages given by stability of the lattice and higher performances in ionic conductivity.

At the negative side, two functional layers can be found: the support and the fuel electrode. In the case of the ceramic supported cell, both these layers are composed by Ni-YSZ, where nickel catalyses hydrogen oxidation and evolution reactions. The difference between the two layers is in the concentration of yttrium and density of the porous structure. Close to the electrolyte the molar concentration of yttria in zirconia is 8% and 3% in the less dense support structure. The porosity allows the diffusion of gaseous species toward the active sites of the negative electrode where the electrochemical conversion takes place, the so-called triple phase boundary (TPB). In metal supported cells, the support function is given by a porous FeCr structure and the fuel electrode is composed by a LSFNT lattice infiltrated with Ni-CGO. The main catalytic function is always associated to nickel nanoparticles; the other elements combination is the result of optimizations aimed to enhance electronic and ionic conductivity, as well as electrochemical stability.

On the positive side, oxygen association in SOEC mode or dissociation in SOFC mode takes place. This reaction is responsible for the biggest energy conversion loss, and the materials that optimize it have been widely studied in the last years. An LSC perovskite structure is adopted for both the ceramic and metal supported technologies, providing the active sites for oxygen association/dissociation and allowing the transport of oxide ions from or toward the

electrolyte. In the case of the ceramic-supported cell, performances of the positive electrode are also enhanced by the presence of CGO as part of the structure and an additional LSM layer, with the function of current collector and gas diffusion layer. The acidic nature of the ceramic electrolyte is an issue for the stability of perovskites: lanthanum oxide present in LSC tends to react with zirconia, implying a degradation of both layers. In order to avoid that, a protective thin CGO layer is always present in between the electrolyte and positive electrode.

The main tools to characterize electrochemical devices used in this project are polarization curves, also referred to as i-V curves, and Electrochemical Impedance Spectroscopy (EIS). Polarization curves show the electric energy, in terms of potential difference between the two sides of the cell, associated with a specific current that can be produced or absorbed during fuel cell or electrolysis operation mode, respectively. Important information can be extracted from i-V curves: Open Circuit Voltage (OCV), Area Specific Resistance (ASR) of the cell, and the occurrence of reactant starvation. The OCV is the voltage measured at zero current and gives information about data reliability if compared to the theoretical value calculated from the Nernst equation. Such deviations indicate any unexpected operating temperature or feed gas composition change. The ASR represents the total cell's resistance (expressed in Ωcm^2) including all the different voltage loss contributions, and it is measured in the i-V plane as the slope of the polarization curve at a specific current density.

EIS is a tool used to measure the impedance of a system, which depends on the AC frequency. Frequency response analysis can be interpreted considering that ohmic phenomena are the fastest, occurring at very high frequencies, followed by kinetic ones spotted at medium frequencies, and by mass transport-related phenomena identified at the lowest frequencies. From EIS data, which can be visualized in Nyquist or Bode plots, it is possible to extract the several impedance contributions associated with processes of different nature occurring inside the cell. Anyway, for sake of simplicity, it was decided not to adopt any model to analyse the EIS curves and isolate the several impedance contributions, but only to distinguish ohmic and polarization resistances. The ASR corresponds to the real impedance recorded at very low frequencies. The ohmic resistance (modelling the conduction of ions in the electrolyte, conduction of electrons in the electrodes, and contact resistances), also referred to as serial resistance, corresponds to the real impedance recorded at very high frequency. The polarization resistance (modelling all the other phenomena) can be simply obtained as difference between ASR and ohmic resistance.

The solid oxide cells tested for this study were manufactured at DTU Risø National Laboratory. First, two nominally identical ceramic-supported cells were tested: one was used as a reference, so it was only exposed to activation process; the other one instead went through initial and final performance characterizations (also called fingerprints), before and after a long-term durability test. Then, two metal-supported cells were tested in the same way: initial characterization, durability test, final characterization.

Fingerprints consist in the recording of polarization curves and electrochemical impedance spectroscopies, both in electrolysis and fuel cell modes, changing the operating conditions (temperature, steam-to-hydrogen ratio in the feed to the negative electrode, oxygen partial pressure of the feed to the positive electrode) in order to understand how the cell reacts to such changes, in particular in terms of performances and limitations related to the single layers.

The durability tests are the most relevant parts of the experimental activity carried out. They were based on galvanostatic operation of the cell for 500 hours at 650 °C, feeding air as sweep gas to the positive side and a mixture 50% steam – 50% hydrogen to the negative electrode. During the galvanostatic operation electrochemical impedance spectroscopy was performed, to progressively follow the behaviour of the cells. The final characterizations performed afterwards were aimed to evaluate the change in cells performances across the 500 hours.

After these operations, samples were extracted from different sections of the cells to observe their structures through Scanning Electron Microscopy (SEM) and Energy-Dispersive X-ray Spectroscopy (EDS) and to check the assumptions made while investigating data recorded during the tests.

For this project's purpose particular importance is given to electrolysis performances and degradation assessment at low temperature, specifically 650 °C. The state-of-the-art ceramic-supported cell had never gone through a long-term test at such conditions before, being this technology designed to operate at higher temperatures. The specific metal-supported cell design adopted for this work, thought for low temperature operation, was never tested in electrolysis mode. These considerations highlight once again the importance of the experimental activity carried out during this work.

Figure 2 shows the cell voltage profile recorded during the durability test with the ceramic-supported cell. It showed a constant degradation rate throughout the whole test duration, which for this case was performed at 0.25 A/cm^2. The cell voltage increased quite linearly from 1280 mV to a final value of 1365 mV. The increase during the 500 hours was equal to 85 mV, resulting in an average degradation rate of 13.28% per 1000 hours.

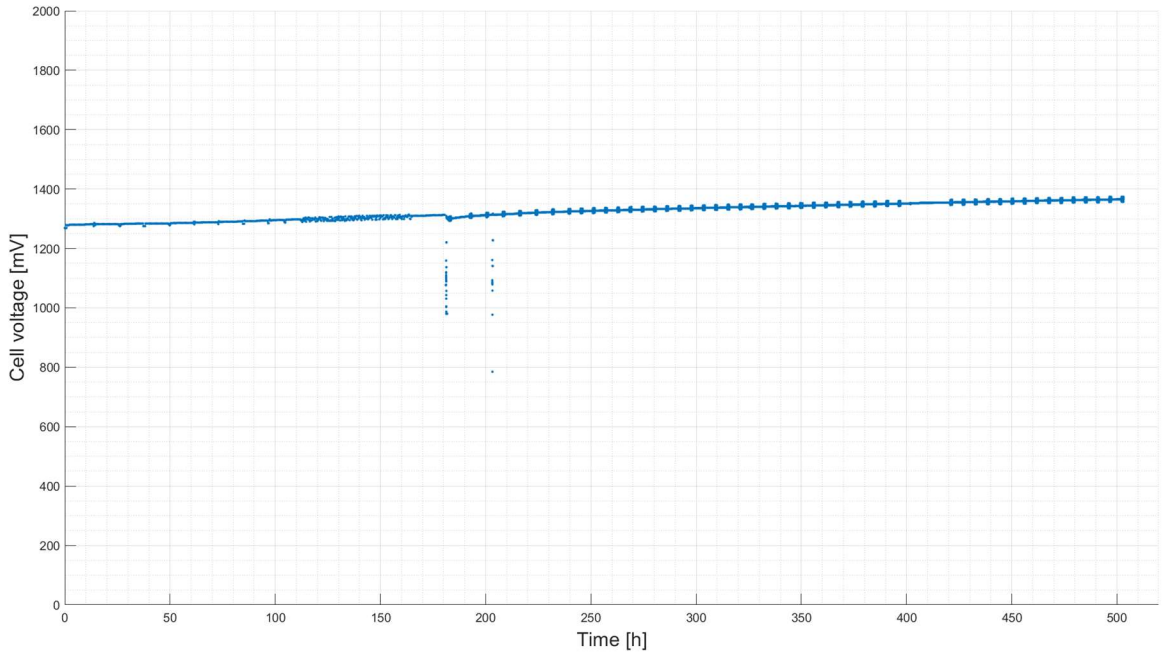

Figure 2 - Ceramic-supported cell voltage profile recorded during durability test.

EIS analysis indicated that the cell performance loss was mainly due to an increase in the polarisation resistance, equal to around 54%. The serial resistance remained more stable during the long-term test, with an increase lower that 5%. The analysis of the evolution of the cell impedance in time revealed that mainly medium-frequencies and slightly low frequencies were affected by changes. Both ranges were proven to be related to processes involving the negative electrode, therefore the conclusion is that the increase in polarization resistance is due to a degradation of such layer.

Unfortunately, SEM was not useful to confirm degradation phenomena occurred during durability test, because the observed structural changes are thought to be consequences of the formation of a crack during the final fingerprint, which broke the cell and led to an extreme oxidation of cell's centre and outlet. The crack formed because of the multiple changes of operating temperature that the cell went through during the characterization phases.

Figure 3 shows the cell voltage profiles recorded during the durability tests with the two metal-supported cells: the red curve is referred to the first one, tested with a current density of 0.25 A/cm^2, while the blue one refers to the second cell, tested at 0.5 A/cm^2.

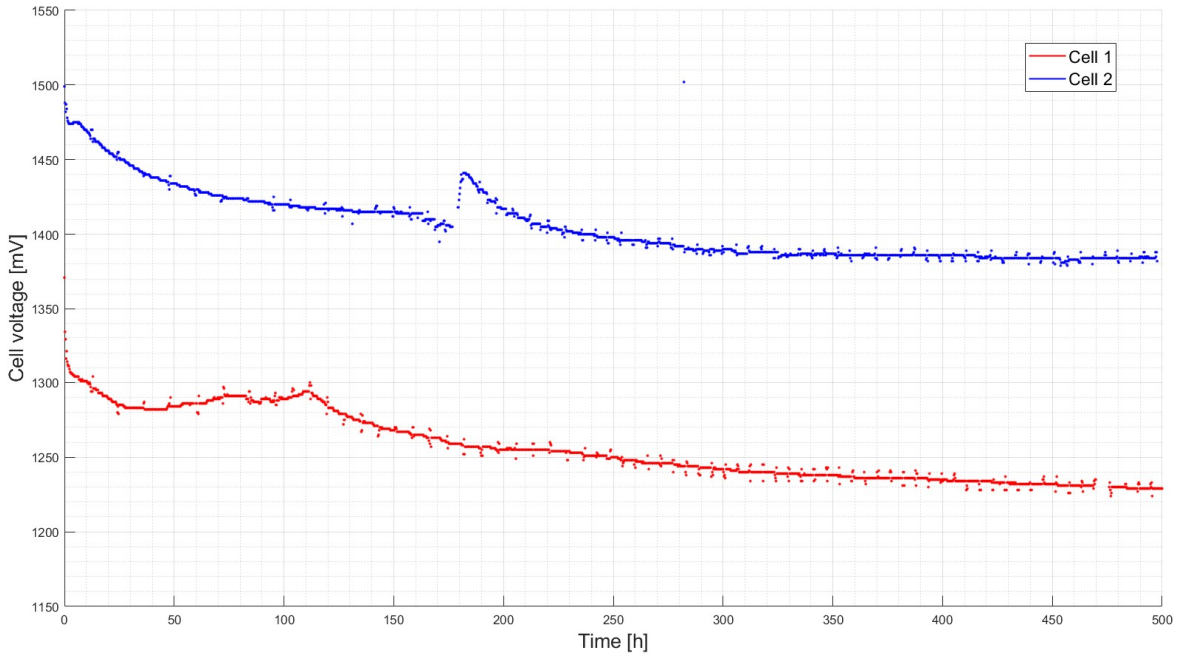

Figure 3 - Metal-supported cell voltage profiles recorded during durability tests. Red: first cell tested at 0.25 A/cm^2; blue: second cell tested at 0.5 A/cm^2.

During the first MSC galvanostatic test an unexpected behavior was observed: the cell voltage did not increase, as would be a normal consequence of degradation; instead, an activation process, detected as a constant reduction of cell voltage, was observed. The voltage changed from an initial value of 1371 mV to a final value of 1229 mV, resulting in a reduction of 142 mV in 500 hours. Most of this voltage reduction happened in the first 20 hours, while in the other 480 hours the decreasing trend resulted less steep. This decreasing trend is mainly attributed to oxidation of the metal support occurred along the first characterization. During the 500 hours, the voltage slowly decreased because in SOEC mode the reducing conditions at the negative electrode were held constantly, allowing to slowly restore the oxidized metal support and increase its electric conductivity. It was hence decided to test the second metal-supported cell following a different initial characterization procedure, aimed to limit support oxidation by avoiding operation above 700 °C and by reducing fuel cell mode as much as possible. During the second durability test the voltage changed from an initial value of 1499 mV to a final value of 1384 mV, resulting in a reduction of 115 mV in 500 hours. Also in this case the first hours were characterized by a fast voltage reduction, that became less important while approaching 350 hours, when the cell voltage became stable.

EIS analysis addressed in both cases that the ohmic resistance is the main responsible for the reduction of cell voltage, while the polarization resistance turned out to be very steady. In particular, the ohmic resistance decreased by around 46% in the first test and 33% in the second one, while the polarization resistance changes resulted equal to -3% with the first cell and +1% with the second one. The analysis of the evolution of cell impedances in time showed that the medium and especially low frequencies regions were the most affected by changes. These ranges were proven to be related to processes involving both positive and

negative electrodes. During the first test, an improvement of all processes has been spotted, since the imaginary impedance always decreased at all frequencies. This observation confirms that the initial cell conditions for the durability test, consequence of the first characterization, were so bad that all the processes improved thanks to reactivation processes. Instead, the second tested cell showed a continuous imaginary impedance decrease in the low-frequency region; while at medium frequencies, slight electrodes degradation was observed as impedance increase. The initial cell conditions for the durability test were less compromised with respect to the first one, therefore the benefits of the activation process hid less the always present degrading phenomena. The change of impedance in the low-frequency region could be related to better gas conversion at the negative side, thanks to the reduction of the metal support. While the change at medium frequencies could be attributed to electrodes degradation implying a worsening of reaction kinetics. In both cases, the module of impedance changes is much lower with respect to the ones registered with the ceramic-supported cell. This confirms that the magnitude of the capacitive-related degrading processes occurred during the galvanostatic test was limited, proving the high stability in electrolysis operation for this particular MSC.

SEM and EDS were useful to confirm the occurring of metallic support oxidation. Indeed, a high oxygen concentration was observed on the pores internal surface at the interface between FeCr and the flowing steam. Oxygen should be present just in the infiltrated CGO, hence close to cerium, instead it was also spotted in high concentration where Ce is not present. Unfortunately, it was not possible to have a mean of comparison with a reference cell that was only activated and did not go through a durability test, since the availability of MSC at DTU was very limited. Investigating the fuel electrode no differences were spotted between inlet and outlet for both the cells tested. It was not possible to observe the positive electrode since it detached during dismounting of the cell test-house in both cases.

Figure 4 shows polarization curves and Nyquist plots from EIS registered at 650 °C, feeding a mixture of 50% steam – 50% hydrogen to the negative electrode and air to the positive one, with both ceramic and metal-supported cells.

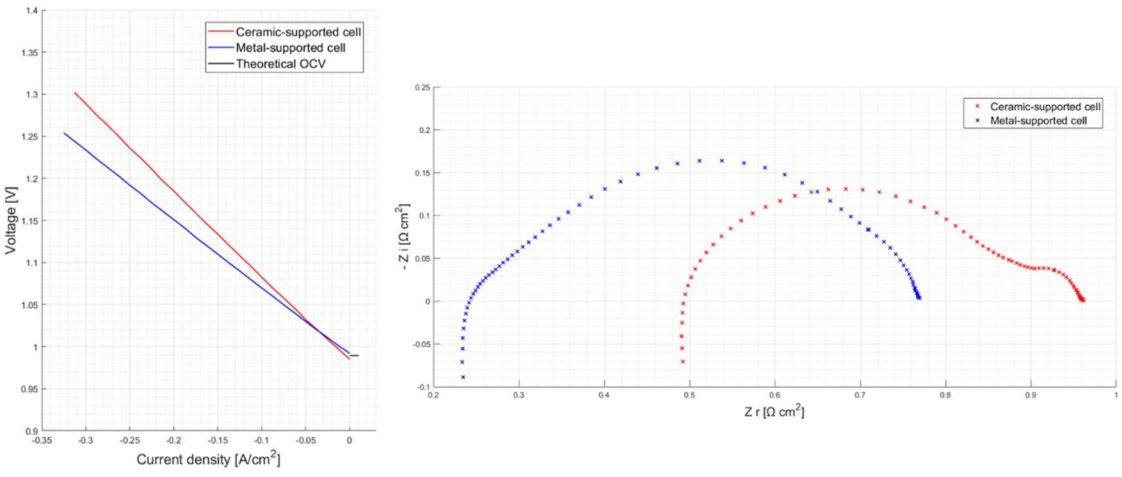

Figure 4 – Polarization curves and Nyquist plots of both technologies, obtained at 650°C, 50% H_2O – 50% H_2 to negative electrode, air to positive electrode.

Comparing the results obtained with the two different cell technologies, it is possible to conclude that the metal supported cell requires a lower voltage to electrolyze water at low temperatures with respect to the ceramic one. This is mainly due to the Sc-YSZ electrolyte, which ionic conductivity is higher than the one of the YSZ electrolyte present in the ceramic-supported cell. In addition, the metallic support structure contributes to decrease the electric resistivity, being more conductive than the nickel-infiltrated ceramic structure. On the other hand, the polarization resistance is slightly smaller in the case of the ceramic-supported cell. It cannot be clearly said if the ceramic-supported electrodes are better performing than the MSC ones. However, it is important to notice that nickel loading is three orders of magnitude higher in the negative electrode of the ceramic-supported cell with respect to the MSC (3.5 g/cm^2 vs 0.8-1 mg/cm^2 for the ceramic and metal supported negative electrodes, respectively). For this reason it its thought that the better performance, in terms of lower polarization resistance for the ceramic supported cell, can be mainly attributed to the negative electrode. What is certain is that the fuel electrode-related degradation phenomena are less severe in the case of the MSC.

In conclusion, the ceramic-supported cell gave very good results in term of durability even if operated at 650 °C. Ceramic-supported cells are indeed designed to work at higher temperatures, anyway the degradation rate observed with the cell tested for this project was consistent with the one observed using a similar cell operated at 800 °C for 4400 hours. In that particular case, testing the cell with a current density of 1 A/cm^2 (four times higher than the one adopted for this work), the degradation rate measured during the first 200 hours resulted equal to 52% per 1000 hours (four times higher than the one observed in this work). The formation of the crack during the final fingerprint, and the consequent break of the cell, demonstrate the sensitivity of this technology on thermal stresses and highlight the reason why metallic support structures were introduced. Regarding the metal-supported technology, it showed very promising results in terms of active layers electrochemical stability in electrolysis conditions. It is plausible that Ni catalytic particles are more stable in the LSFNT lattice with respect to the YSZ crystalline structure, hence migration and loss of catalytic surface is more limited. However, such cells demonstrated to be very sensitive to steam presence, especially if operated in SOFC mode: metallic support oxidation is thought to be the main phenomenon that hinders actual cell's potentiality, hence R&D should be focused on finding the best solution to overcome this issue. Further tests are required to achieve a more comprehensive cell behaviour knowledge; however, the tests performed during this work helped to develop a safer characterization protocol for metal-supported cells and proved how promising this technology is. Consolidated Alkaline and PEM technologies are not expected to reduce their specific costs as much as SOCs. In this scenario solid oxides cells, particularly metal-supported ones, could become very competitive. It is not easy to give a meaningful cost projection because of the early development of such technology; however, it can be speculated that the 500 €/kW target could be achieved in the next years, allowing a wide spread in the green energy market in the near future.

List of contents

List of Figures

List of Tables

Project's motivation

In order to achieve the climate goals of reducing CO_2 emissions, many installations for converting renewable energy, like wind and solar, into electricity are emerging rapidly throughout the world. The fluctuating nature of these sources makes it necessary to store this electricity efficiently for later use or for other applications, such as fuelling vehicles. Electrolysis provides the opportunity to convert electricity with high efficiency into a storage medium, hydrogen, which is transportable with minor losses through an infrastructure, even over large distances, and which can be source to produce other needed chemicals or fuels.

Among electrolysis technologies, Solid Oxide Electrolysis Cells (SOECs) are emerging as an important contributor, due to their very high conversion efficiency, flexibility towards input media and operating modes. For example, SOECs can follow wind profiles and the same device can produce electricity operating in fuel cell mode, if there is a period of lack of renewable energy.

The most mature versions of solid oxide cells are based on ceramic support layers, either fuel electrode-supported or electrolyte-supported cells. A number of projects have demonstrated the possibility for these cells to be adopted for practical applications, with scales up to few hundred kW. In order to allow their integration with wind turbines, a further upscaling toward several MW-GW is required, but the state-of-the-art configuration based on ceramic materials has issues related to mechanical stability, which limits the dimension of the cells (and stacks) and consequently makes the technology more expensive.

Danmarks Tekniske Universitet's Department of Energy Conversion and Storage has been one of the founders of the solid oxide cells research field and for this reason chosen to carry out this work. Recently DTU Energy has developed and started to test a solid oxide cell configuration based on metal supports. They have been designed to operate at lower temperatures, fundamental characteristic to reduce stack and balance-of-plant costs. In addition, another advantage is the cheaper metallic support, as well as the possibility to manufacture larger cells.

This project's purpose is to study low temperature electrolysis operation focusing on both ceramic and metal supported technologies that have never been studied in such conditions; particularly the metal supported, being more recently developed, has never been characterized in electrolysis mode.

It is important to understand how different operating conditions may affect the overall cell performance, this is possible through tests where different gas compositions are fed both to negative and positive electrodes, at different temperatures. In this way, it is possible to

understand how the single cell's components contribute to the overall cell behaviour, also identifying any limiting component or process.

Furthermore, degradation phenomena related to galvanostatic operation are assessed. This will help further R&D aimed to identify the best solutions that would maximise the lifetime and performances of these technologies, particularly metal supported cells.

Chapter 1
Introduction

Given the rising acknowledgement on climate change issues as well as on the need to pursuit sustainable development, renewable energy sources are becoming more and more attractive with a steady increase in share in all countries' energetic portfolios.

In this chapter, electrolysis technologies and their importance as mean to achieve the goals set by the international community toward climate change are introduced. After that, the focus is on solid oxide cells, starting with an introduction of the technology and concluding with a literature review about components, materials and relative processes occurring, to better assess the behaviour of the cells tested for this project purpose.

1.1 Background and overview of the technology

In this section the world energetic situation, goals on de-carbonization in Europe and why hydrogen production is attractive to achieve that, are discussed. Afterwards electrolysis is introduced, as well as solid oxide cells, discussing their advantages, disadvantages and research and development goals to overcome them. In conclusion, an economic overview dealing with production and use of green hydrogen in the future is presented.

1.1.1 Decarbonisation challenge, goals and possible solutions

After the first industrial revolution coal became the main source of power. Afterwards oil, which had higher potential in many sectors (in particular transport and the developing petrochemical sector), started spreading. The development of oil industry did not take place immediately because of the technical advancement required and, as a consequence, because of the boundaries imposed by economy. World scale events, especially wars (WWI, WWII and Cold War) in which technological supremacy is essential to prevail, pushed hard technological development in many fields in the last century. Just to make an example with the energetic one, during WWI scientists in Germany developed a process, the so-called Fischer-Tropsch synthesis, to obtain light fuels from coal in order to be energetically independent from other countries. This process was lately improved, allowing the scale up of plants that sustained most of the transport sector demand in South Africa.

Nowadays the rate of energetic transition toward renewable sources relies both on technological development - many are the challenges to integrate intermittent stationary power sources - and on economy. A too fast shift toward renewable sources of energy would slow down the world GDP growth if not well planned and this would imply a loss of welfare.

In an economy in which oil remains the most important commodity in the energetic sector, as shown in Figure 1.1 [1], its price is the main factor determining the competitiveness of renewable energy sources. The most industrialized countries are the ones leading the transition toward a sustainable world, thanks to the adoption of incentives which are allowing the spreading of such technologies; despite that, the current growth rate in renewable energy share worldwide is not sufficient to achieve goals to limit climate change damages. It is important to underline that, as Figure 1.2 [1] shows, the most developed countries are the ones with higher oil consumption pro-capita and, since the beginning of the first industrialization, they are the ones that contributed the most to anthropogenic greenhouse gases emissions. As consequence, they must lead the transition toward renewables, also helping developing countries that mostly or completely rely on fossil fuels, being cheaper energy sources.

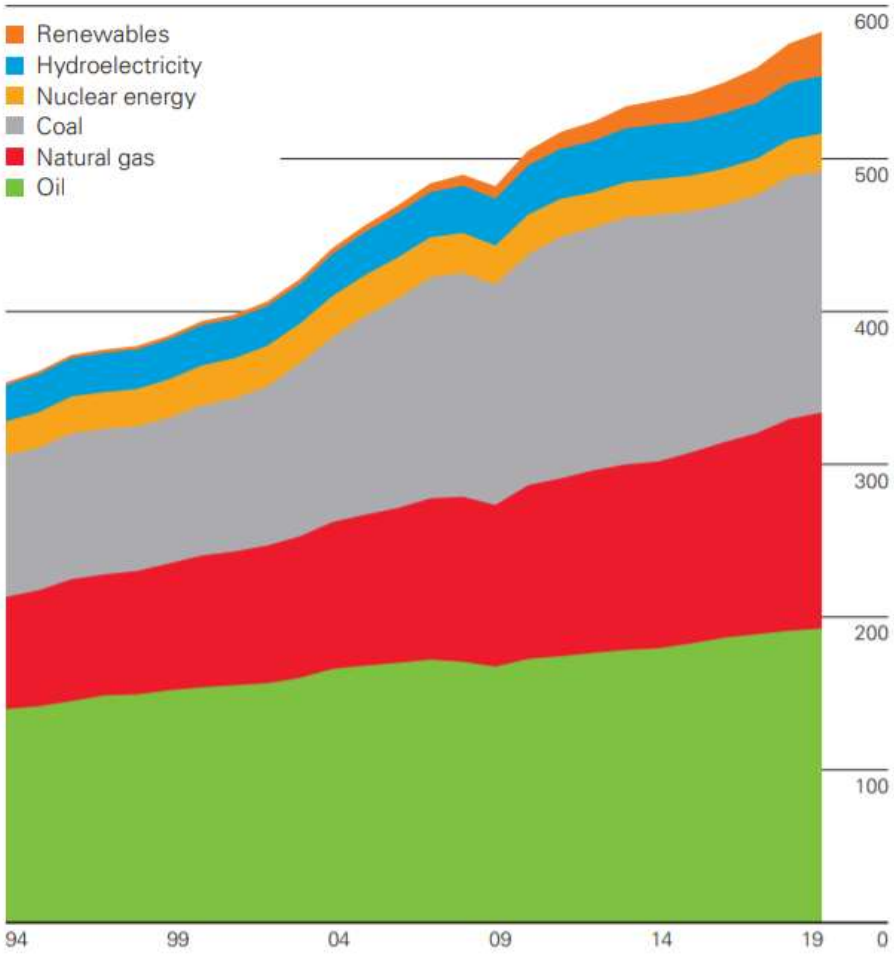

Figure 1.1 - World primary energy consumption in exajoules, until 2019.

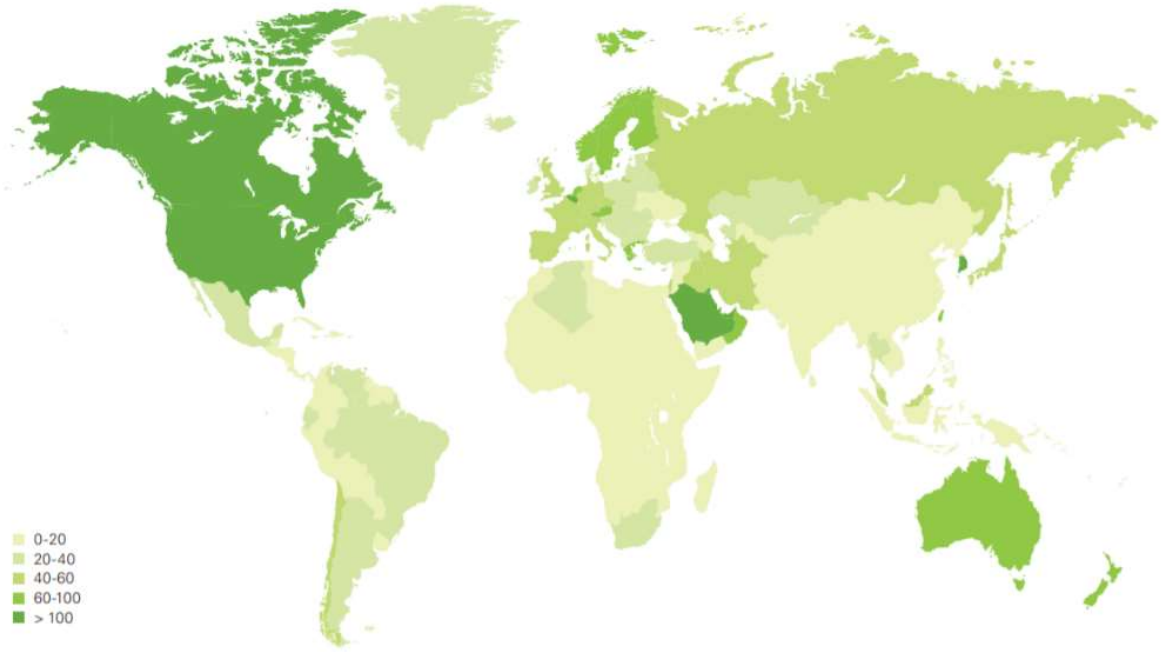

Figure 1.2 – Oil consumption in GJ per capita in 2019.

In 1988, the United Nations established a scientific body for the assessment of climate change, the IPCC (Intergovernmental Panel on Climate Change), and after four years world leaders met the first time at the Rio Earth Summit to discuss climate change challenges. The Paris Agreement, signed by 196 countries and adopted by consensus the 12th of December 2015, is the final achievement after almost two decades of attempts to promote cooperation among countries to face climate change. The main principle is the adoption of INDCs (Intended Nationally Determined Contributions) and transparency of communication among all the parties during revision processes, which are held every five years to correct the scenarios and the actions to take.

The long-term goal is to limit temperature anomaly well below 2 °C taking as reference the average temperature measured before any action was taken (end of the 80´s). Given the strong dependence of temperature rise on green-house gases (GHG) emissions increase (especially CO_2 and CH_4), these are to be limited and eventually their share in the atmosphere should be reduced through capture technologies. Mitigating climate change is one of the biggest challenges of our century to preserve a healthy ecosystem. In addition to that, if emissions would not be controlled at all, the rise in temperature would also lead to additional expenses related to health care, violent climatic events and energy demand for heating and cooling.

Comparing Figure 1.3 [2] and Figure 1.4 [3], it is appreciable that human activities in the last two centuries after the first industrialization gave rise to CO_2 concentration in the atmosphere (together with other GHG that for simplicity now are not considered) and, as a consequence, to the average temperature, which change could be appreciated only in the last

decades. The late response of temperature rise with respect to GHG concentration increase is due to the inertia of carbon cycle arrangements and other complex phenomena.

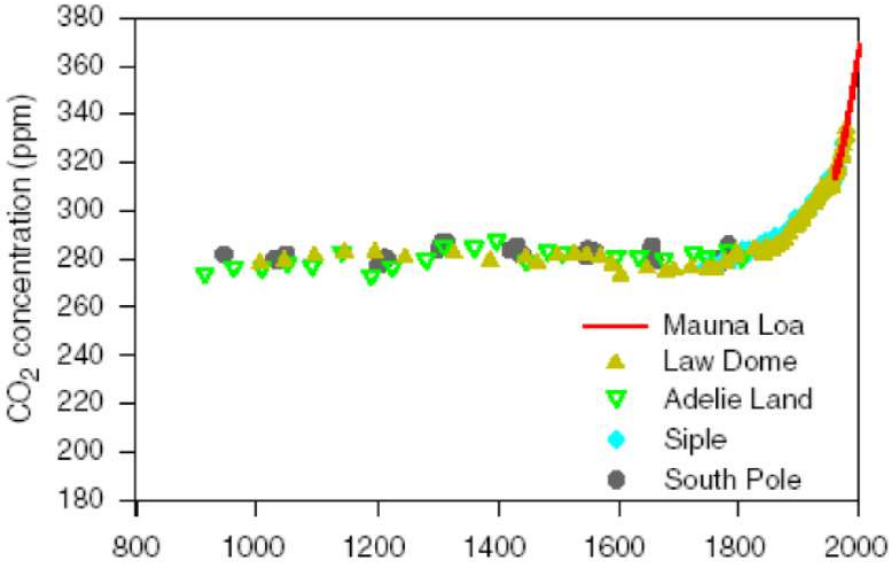

Figure 1.3 - CO_2 concentration increase over the centuries in the atmosphere.

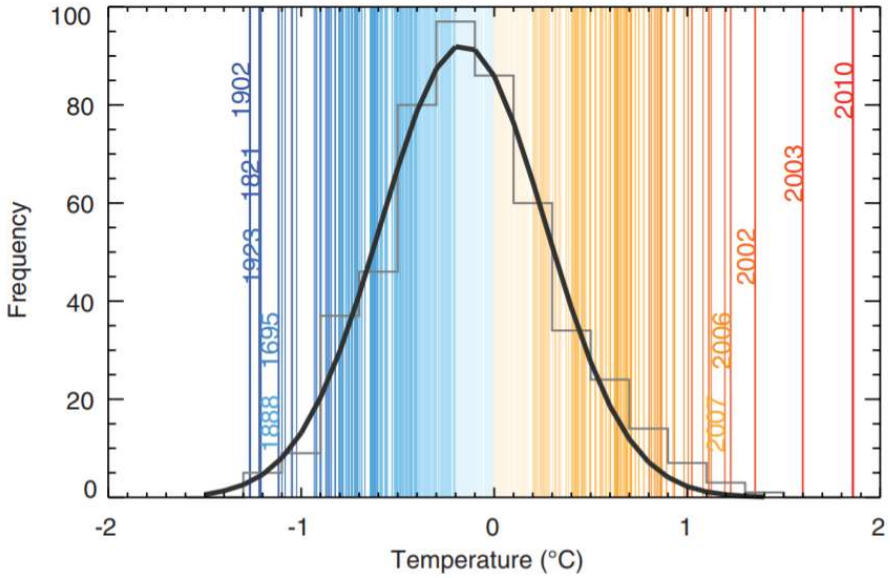

Figure 1.4 - European summer temperature variation in the last century.

The European region is a worldwide leader in acting against climate change and promoting sustainable development. In order to achieve the long-term goal set by Paris Agreement all members are asked to take action independently, following European directives. The most recent one is the new Renewable Energy Directive (RED II, or simply Directive), entered into force the 24th of December 2018. The Directive promotes the development of renewable energy in the next decade through an EU-wide renewable energy binding target of at least

32% share of the primary energy consumption by 2030, to be achieved collectively by the Member States. In order to do so, the Directive includes a number of sectoral measures promoting further deployment of renewable sources in the electricity, heating and cooling, and transport sectors, with the overall aim of contributing to reducing GHG emissions, improving energy security, reinforcing Europe's technological and industrial leadership in renewable energy and creating jobs and growth [4].

Transport is the sector that relies most on fossil fuels accounting for around one third of Europe´s primary energy consumption. The most effective way to reduce the share of fossil fuels in this sector without upsetting too much the industry depending on it, is to produce the same fuels from renewable sources.

Biofuels might be suitable for this purpose, but most of them are produced out of crops and that means huge land utilization for large-scale production. Food and livestock feed demands would need to be satisfied either through intensification of current production or by bringing non-agricultural land (mainly woodlands that are very important carbon storage systems) into production. For that reason in RED II the concept of Indirect Land Use Change (ILUC) is introduced as important mean of characterization: high ILUC risk biofuels are the one produced from crops and wood (direct combustion), low ILUC risk biofuels or advanced biofuels are the ones produced from organic waste and synthetic processes.

Following RED II, the Member States must require fuel suppliers to supply a minimum of 14% of the energy consumed in road and rail transport by 2030 as renewable energy; anyway, limits are set on high ILUC-risk biofuels, bioliquids and biomass fuels. These limits affect the amount of such fuels that each Member State can count on to achieve its national targets, when calculating the overall national share of renewables and the share of renewables in transport. These limits consist of a freeze at 2019 levels for the period 2021-2023 (with an overall maximum set at 7% of the 2020 final consumption of energy in road and rail transport) and a gradual decrease from the end of 2023 to zero by 2030. In parallel, the promotion of advanced biofuels and biogas (low ILUC risk) is reinforced via a specific binding target of a minimum 3.5% share for 2030, with two intermediary milestones (0.2% in 2022 and 1% in 2025) [4].

Stationary power production targets are set for each country, taking into account their starting point and overall potential for renewables. These targets range from a low of 10% in Malta to a high of 49% in Sweden and peaks of 50% in Denmark for 2020.

Moving from programmable fossil fuel-based energy production to intermittent renewable energy sources requires drastic modification of the energy system: the higher the share of intermittent renewables (solar photovoltaic and wind above all), the more flexible and interconnected the energy system needs to be, allowing to store energy also for long periods.

Energy can be stored in different ways: as potential energy in pumped hydro, through compression of air, as thermal energy, in batteries, in form of hydrogen or other synthetic fuels.

- Pumped hydro storage consists in the conversion of electricity into potential energy, pumping water to an upper reservoir. This is done during periods of low demand and high availability of electric energy, when its price is low; when needed, the water can be released and the potential energy is transformed back into electricity.
  The plants can rely on Francis groups operated both in pumping and turbine operation, or on pumps coupled with turbines. The specific energy costs of these plants are very high, being mainly related to construction. Operation is competitive only when the difference in price of electricity sold and bought is sufficiently high. In addition, despite the very long life of such plants, the operative yearly hours are limited being strongly dependent on the capacity of the basin (from 1 MWh up to 10 GWh of storable energy), as well as on electricity price. The roundtrip efficiency that can be achieved in electricity-electricity conversion can be as high as 70-85%.
- Compressed air energy storage is cheaper compared to pumped hydro since the main share of specific costs is represented by turbomachinery. The storage capacity depends on the volume of compressed gas, which also influences capital costs. Considering an electric efficiency of more or less 85% for both gas turbine and compressor, a max 70% roundtrip efficiency can be achieved. Thermal management is an issue: compression implies an increase in temperature in the gas, which would not be immediately exploited by the turbine and therefore wasted. The opposite happens during expansion: the gas is not hot and the energy conversion process only relies on pressure. As a consequence of that, the turbine is not exploited at its maximum potentiality and efficiencies are actually lower because of low temperature operation. A heat exchanger can be installed to improve turbine operation, contributing to a decrease of roundtrip efficiency and an increase of investment cost. Energy can be stored for an indefinite amount of time, but the energy density is not that high to allow very big capacities without exceeding too much with capital cost.
- Thermal energy storage main problem is that energy cannot be stored for a long period. Despite the insulation and the high thermal capacity of thermal energy storage materials (both fluids and solids), heat is slowly rejected to ambient: usually storage time never exceeds 8-10 hours for large scale plants. For that reason, these systems are mainly used to increase operative hours of concentrated solar power (CSP) plants. Since heat is stored during the day from the excess collected solar thermal power that is not transferred to the power block, a roundtrip efficiency (electricity-to-electricity) is not defined.
- Batteries are very efficient electrochemical systems, the roundtrip efficiency achieved can be as high as 90% for Li-ion batteries and 80% for vanadium redox flow batteries. The main problem of batteries are costs, related mostly to raw materials: these technologies are already mature and a lot of research and development is necessary to further decrease the costs. In addition to that, storage time is an issue since the battery would start discharging itself after long periods.

Batteries are suitable for short term energy storage applications, grid balance above all, but not at all the best solution for long term.

- Water electrolysis conversion efficiency (based on hydrogen lower heating value) can be as high as 65% and 70% for alkaline and PEM (Polymer Electrolyte Membrane) electrolysers, respectively. Solid oxide technologies working at higher temperature seem the most promising for future commercial applications. Also considering the fuel cell operation to generate electricity by converting hydrogen, a roundtrip efficiency of roughly 33% can be achieved for alkaline, 40% for PEM and 65% for solid oxide cells.
  Costs are still high, but with a big margin of improvement thanks to research and development. The main advantage of producing hydrogen from water electrolysis or synthetic fuels from steam and CO_2 co-electrolysis combined with further chemical synthesis, is represented by the high energy density of these fuels and the possibility to store them for an indefinite amount of time.

Figure 1.5 summarizes the performance parameters of energy storage technologies not related to electrolysis [5]. Despite the lower round-trip efficiency compared with the other energy storage technologies, electrolysis still represents a very promising solution to store energy for the next years. Research and development are improving both performances and durability of these systems as well as decreasing the costs, which are expected to be very competitive by 2030. A more detailed cost analysis is presented in paragraph 1.1.2.31.1.3.5.

Technology	Top Power [MW]	Top Energy [MWh]	Energy Density [Wh/kg]	Response time	η_{round}
Pumped hydro	3000	10^4	0.3	min	70-85%
Compressed air	300	10^3	10–30	min	60%
Thermal energy storage	20	10^1	70	min	-
Flywheel energy storage	20	5	11–30	ms	85%
Advanced lead acid	10 – 40	10^1	25-50	ms	75-85%
Sodium sulfur	34	10^1	150-120	s	85-90%
Sodium nickel clorine	1	6	95-120	s	85%
Lithium ion	16	20	100-200	ms	95%
VRFB	2–100	6-120	10–50	ms	85%

Figure 1.5 - Summary of performances of the different energy storage systems, except for electrolysis.

Figure 1.6 represents in a chart the discharge times and the power of different energy storage technologies [5]. The possibility to store highly energetic fuels or hydrogen for an indefinite time at low cost makes electrolysis and co-electrolysis the first choice for seasonal storage, allowing their spread and integration with the electrical system of intermittent renewable energy sources.

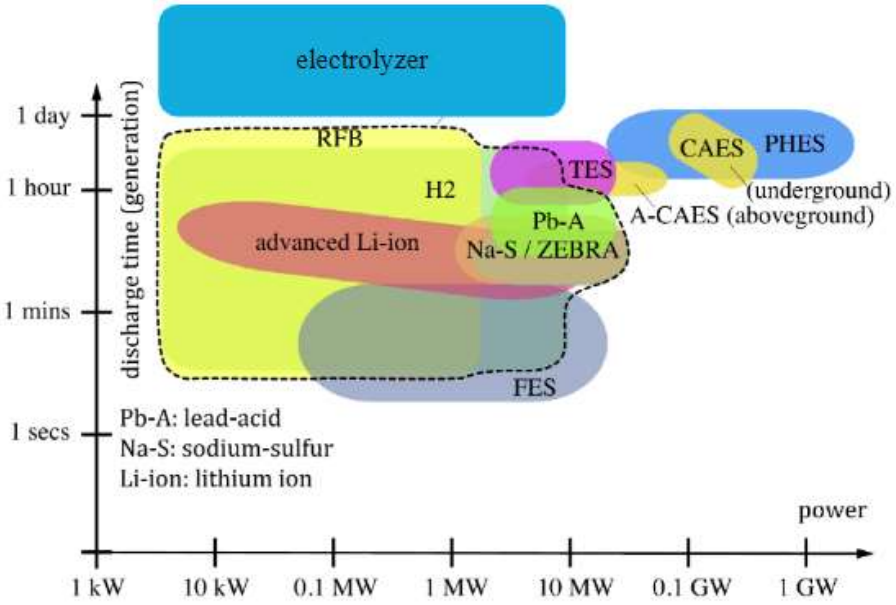

Figure 1.6 – Power comparison among different energy storage technologies.

In addition to that, hydrogen is a very important good, necessary for ammonia production (very energy intensive industry and with an important market mainly related to fertilizers), for oil-refinery industry and for synthetic fuels production. Road and rail transport sector would benefit from large-scale adoption of electrolysis, since advanced synthetic fuels would help to follow European directives in decarbonisation.

On a European scale, analyses show that 1600 GW electrolysis and 7500 TWh of chemical storage may be needed to completely decarbonise heavy-duty transport such as trucks, ships and planes [6]. The infrastructure as well as distribution systems would need to be revolutionized, together with the electrical grid, but this would be necessary anyway to reduce the dependence on fossil fuels.

Technological, economic, social and political challenges are to be faced to achieve sustainable development and to limit climate change, and only through cooperation among all the countries this could be achieved. Dealing with technology and energy industry, electrolysis will play for sure a central role and, among all the technologies, solid oxide cells are the ones that are most promising in terms of performances and cost.

1.1.2 Introduction to electrolysis

Hydrogen is a very versatile energy carrier with many possible utilizations, which can help to face up various critical energy challenges. Hydrogen is the most abundant element in the universe, but its exhaust velocity is so high that it is not retained in the Earth's atmosphere. However, underwater exudations of natural hydrogen have recently been discovered, as well as the existence of geological structures from which large flows of natural hydrogen are

released. Despite this, hydrogen used in the industrial sector is currently produced from fossil and renewable sources through several synthesis methods [7].

Nowadays it is mainly used in the chemical (ammonia and ethanol synthesis) and refining sectors and it is obtained especially from fossil fuels, as it is possible to understand in Figure 1.7 (data taken from reference [7]). The most widely used methods, based on mature technologies, are steam reforming of natural gas and partial oxidation of hydrocarbons. These processes produce large amounts of greenhouse gases and are therefore not environmental friendly: they account for 6% of global natural gas use and 2% of coal consumption and they are responsible for 830 Mt per year of CO_2 emissions [8].

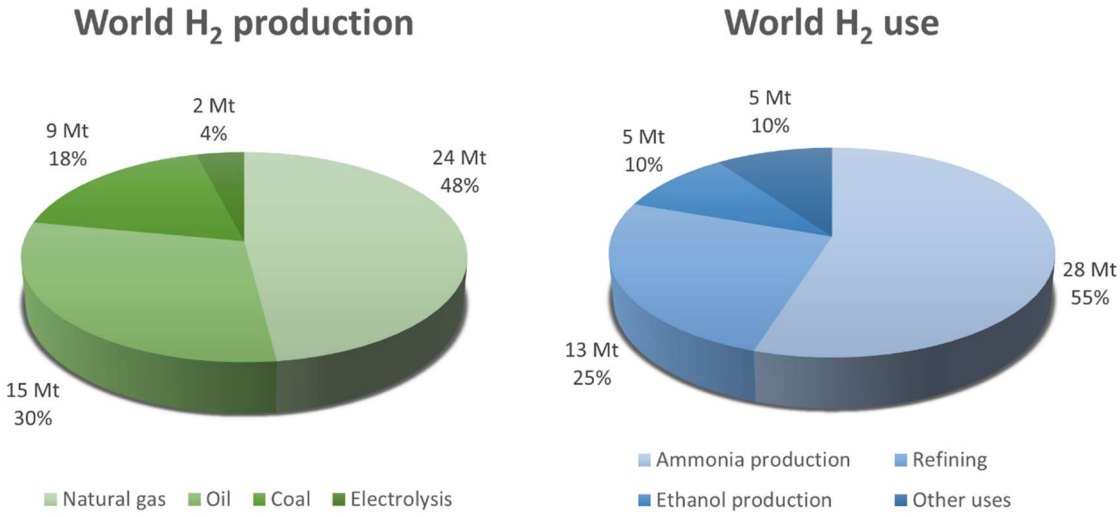

Figure 1.7 - Sources for hydrogen production and main sectors consuming it.

For this reason, methods for producing hydrogen from renewable sources have been developed in recent years, making a significant contribution to sustainable development.

Clean hydrogen, being produced from renewables, nuclear or fossil fuels with CCUS (Carbon Capture, Utilisation and Storage), can help to decarbonize many sectors, including long-range transport, chemical industry and metallurgy.

Water electrolysis has proven to be a very valid solution, since it allows the production of hydrogen from a common abundant good. Moreover, thanks to electrolysis, hydrogen can support the integration of intermittent renewable energy sources in the electricity system, being one of the very few options for storing electricity even over months.

Electrolysis is an example of hydrolysis process, consisting in the splitting of water molecules into hydrogen and oxygen. Other examples of hydrolysis processes are:

- Thermochemical water splitting: this process uses high-temperature heat (500 °C – 2000 °C), from concentrated solar power or from nuclear power reactions waste heat, to drive a series of chemical reactions producing hydrogen. The chemicals

used in the process are reused within each cycle, creating a closed loop that consumes only water and produces hydrogen and oxygen [9].

- Water photolysis: this process consists in water splitting through solar radiation promoted by a photo catalyst, *i.e.* a species that absorbs photons and triggers the redox elementary steps required to break water in H_2 and O_2 [10].

Among these technologies, only electrolysis has found commercial large-scale applications. Electrolysis consists in splitting water molecules through the passage of a direct current in an appropriate device, driving the thermodynamically non-spontaneous decomposition of water into its constituting elements, H_2 and O_2.

At the current state of the art, the main electrolysis technologies are three:

- Alkaline electrolyser;
- PEM electrolyser;
- Solid Oxide Electrolysis Cells (SOEC).

Until few years ago alkaline electrolysers were the only available option, so today most of the plants producing H_2 from electrolysis are based on this technology. Recently also PEM electrolysers started to have a significant growth, thanks to the similarity with PEM fuel cells (commercially available) and because they are more suitable to deal with intermittent power generation. SOEC technology was under development as an interesting alternative to ordinary alkaline electrolysis during the 1980s [11]. Due to low fossil fuel prices the development of SOEC was stopped around 1990. During the last decade intensive research in Solid Oxide Fuel Cell (SOFC) technology has taken place world-wide. SOFC improvements, together with the increase in fossil fuel prices and the general interest in hydrogen as energy carrier, have revived the SOEC technology [12]. Indeed solid oxide electrolysis cell technology has witnessed tremendous improvements during the past 10 to 15 years; it is attractive especially because of the unrivalled conversion efficiencies, the cheap materials and the possibility to perform co-electrolysis of steam and carbon dioxide.

1.1.2.1 Alkaline electrolyser

A traditional alkaline electrolyser is composed by four main elements, as can be seen in Figure 1.8: two electrodes, a separator, and the electrolyte.

The electrodes have both structural and catalytic functions. The solid negative charged electrode is usually made of graphite, the positive one of iron and cobalt; both of them contain also nickel as catalyst. The electrolyte is a solution of potassium hydroxide (KOH) that allows the transport of OH^- ions. The separator is a porous media, either polymeric or made of cellulose, that allows the passage of the liquid electrolyte; the pores are very small in order to reduce the transport of bubbles (O_2 or H_2), formed on the electrodes surfaces. Oxygen and hydrogen are collected on the upper part of the system simply exploiting gravity.

The electrochemical reactions occurring in an alkaline electrolyser are:

- negative electrode (cathode) → $4\,H_2O + 4\,e^- \rightarrow 2\,H_2 + 4\,OH^-$

- positive electrode (anode) → $4\,OH^- \rightarrow 2\,H_2O + O_2 + 4\,e^-$

In case of alkaline electrolysers, the ions promoting the reaction are hydroxide ions (OH^-), that move from negative to positive side (from cathode to anode).

The electrochemical reactions take place at the so-called Triple Phase Boundary (TPB). TPBs are the parts of the electrode where gaseous phase (reactants), liquid phase (electrolyte) and solid phase (catalyst) interact; this means that the simultaneous occurrence of gaseous, electronic, and ionic species is essential for the reaction to proceed. It is then evident that the TPB is of great importance since it determines the overall cell performance.

The main problem of this technology is the risk of gas mixing: if hydrogen and oxygen get in contact, an explosive mixture could be formed. This is above all a safety problem, but it also implies a loss of efficiency, since less products would be formed. In order to minimize mixing, besides having small pores in the separator, there is a significant gap (in the order of millimetres) between the two electrodes, called inter-electrode gap. In this way, the presence of bubbles in proximity of the separator is reduced. On the other hand, this large gap implies a higher ion transport loss, because the OH^- ions have to cross a longer path to move from cathode to anode.

A second type of alkaline electrolyser is under development: the so-called zero-gap configuration. In this case, on both sides, a flow-field and a porous GDL (Gas Diffusion Layer) are used to distribute the liquid electrolyte over the whole surface of the two electrodes with porous structure. The electrodes are both in contact with the separator: a polymeric membrane called Anion Exchange Membrane (AEM), which is still not available. The mixtures exiting the device are rich of H_2 and O_2, respectively on cathode and anode side. This configuration allows to have a better separation of the two sides, hence lower gas mixing risk, and much lower ion transport losses thanks to the absence of inter-electrode gap [13].

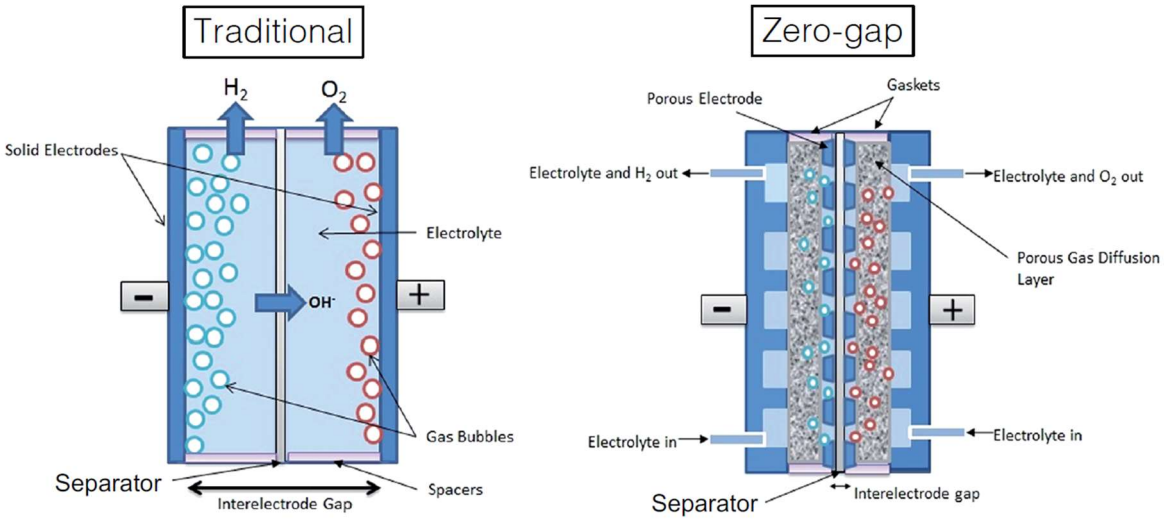

Figure 1.8 - Scheme of a traditional and a zero-gap alkaline electrolyzers.

The main advantage of alkaline electrolysers is that they are a consolidated technology, which nowadays allows them to be the cheapest option from a commercial point of view. The most expensive materials adopted are nickel, used as catalyst, and steel (since the pH is high) for the current collector.

The main limits of this devices are two: they cannot operate at low loads or at high pressures. During partial load operation, H_2 production is reduced with respect to full load operation, but oxygen crossover (movement of O_2 through the membrane, from anode side to cathode side) is not affected, because it is related to oxygen dissolved in the liquid electrolyte that does not depend on the current density. If the amount of oxygen that mixes with hydrogen becomes higher than a certain limit, an explosive mixture can be formed, this is why alkaline electrolysers cannot be operated at current density lower than 40% of the nominal one. Crossover is also the reason why alkaline electrolysers cannot be operated under pressurised conditions, indeed high pressures would enhance the mixing of oxygen and hydrogen.

1.1.2.2 PEM electrolyser

A PEM electrolyser has a more complex structure. Referring to Figure 1.9 [14] representing a scheme of a PEM electrolyser, water flows through a titanium flow-field on the positive side and, thanks to a titanium diffusion layer, it is distributed homogeneously over the positive electrode (anode), made of titanium as well (resistant at high potentials) with either iridium or ruthenium oxides as catalyst. The electrolyte is a polymeric membrane (the backbone is a very stable polymer called Teflon, to which sulfuric groups are attached), designed to transport H^+ ions. The negative electrode is made of graphite, containing a low amount of platinum particles as catalyst (Pt loading is low because the reaction occurring is very fast). Both electrodes also contain ionomer particles, made of the same polymer used for the membrane, to allow the transport of H^+. The hydrogen produced on the negative electrode and the water transported with it flow through the titanium diffusion layer and are collected by a titanium flow-field on the cathode side. The electrochemical reactions occurring in a PEM electrolyser are:

- negative electrode (cathode) → $4\,H^+ + 4\,e^- \rightarrow 2\,H_2$
- positive electrode (anode) → $2\,H_2O \rightarrow O_2 + 4\,H^+ + 4\,e^-$

In case of PEM electrolysers, the ions promoting the reaction are hydron ions (H^+), that move from positive to negative side (from anode to cathode). The triple phase boundary in case of PEM technology is composed by reactants (gaseous phase), a polymeric phase (ionomer) and platinum as solid phase.

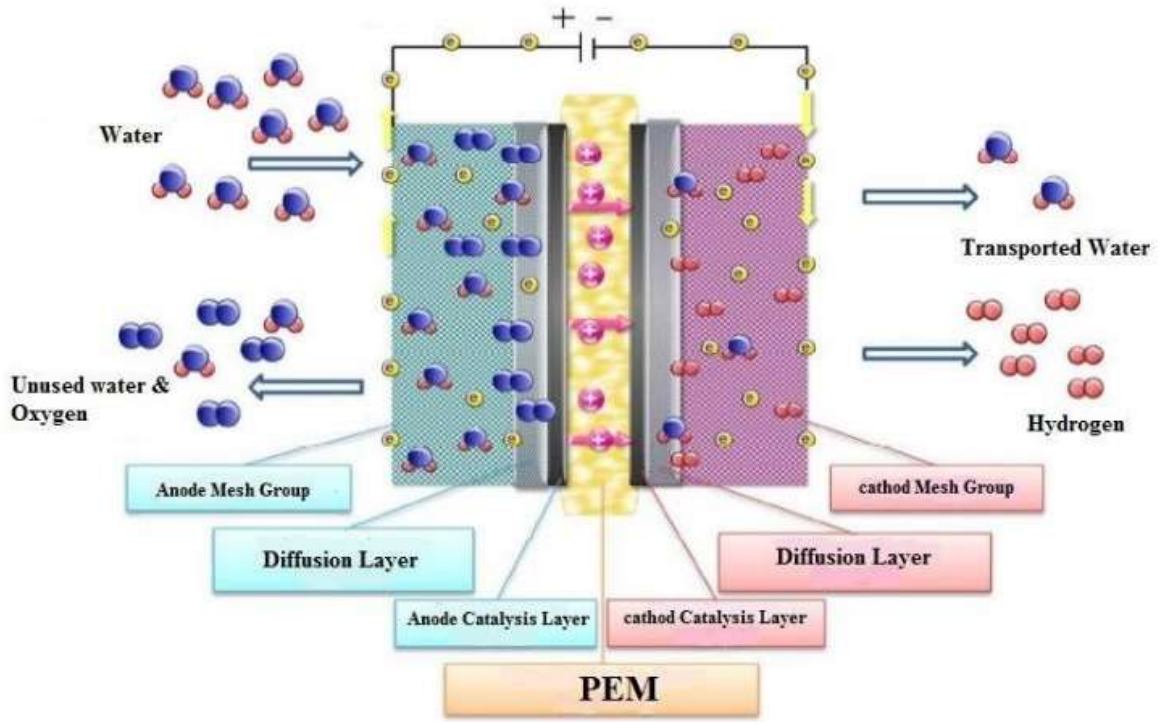

Figure 1.9 - Scheme of a PEM electrolyser.

The main advantages of PEM electrolysers with respect to the alkaline technology are:

- Higher achievable current density, thanks to lower losses related to water mass transport, since it is always available for the reaction being always present in the ionomer;
- Possibility to pressurize the anode compartment to obtain high pressure hydrogen, thanks to the low crossover;
- Higher hydrogen purity, since oxygen crossover is very low and hydrogen is not mixed with a liquid electrolyte (H_2 just needs to be separated from water);
- Large partial load range, thanks again to the low crossover. Alkaline electrolysers cannot be operated at current density lower than 40% of the nominal value, PEM electrolysers instead can reach lower values (10%) and this allows to follow better the dynamic operation of RESs.

PEM electrolysers represent a quite consolidated technology, but there is still room for improvement, especially because costs related to titanium-based contact elements are still very high, and because iridium oxide suffers a significant degradation.

1.1.2.3 Solid Oxide Electrolysis Cells

A solid oxide electrolysis cell is composed by three main elements, as shown in Figure 1.10 [15]: two porous solid electrodes and a dense ceramic electrolyte capable of conducting oxide ions (O^{2-}).
Usually an YSZ (Yttria-Stabilized Zirconia) ceramic structure is used as electrolyte, obtained

doping zirconium oxide (ZrO_2) with yttrium oxide (Y_2O_3) in order to have oxygen vacancies able to transport oxide ions when temperature is sufficiently high. The most common option adopted for the steam/hydrogen electrode is Ni-YSZ cermet (ceramic structure composed by YSZ and metal structure composed by nickel), which function is to move both electrons and oxide ions. For less-demanding applications, oxygen electrodes based on abundant Sr-doped $LaMnO_3$ (LSM, Lanthanum Strontium Manganite) may be used, while higher-performing applications require electrodes based on mixed conductors, such as lanthanum-strontium-cobalt ferrite (LSCF) or lanthanum-strontium cobaltite (LSC). Thin layers of gadolinium-doped ceria (CGO) are commonly used to prevent reaction between the oxygen electrode and the acid electrolyte. This layer has to be thin and very dense to reduce ohmic resistance.

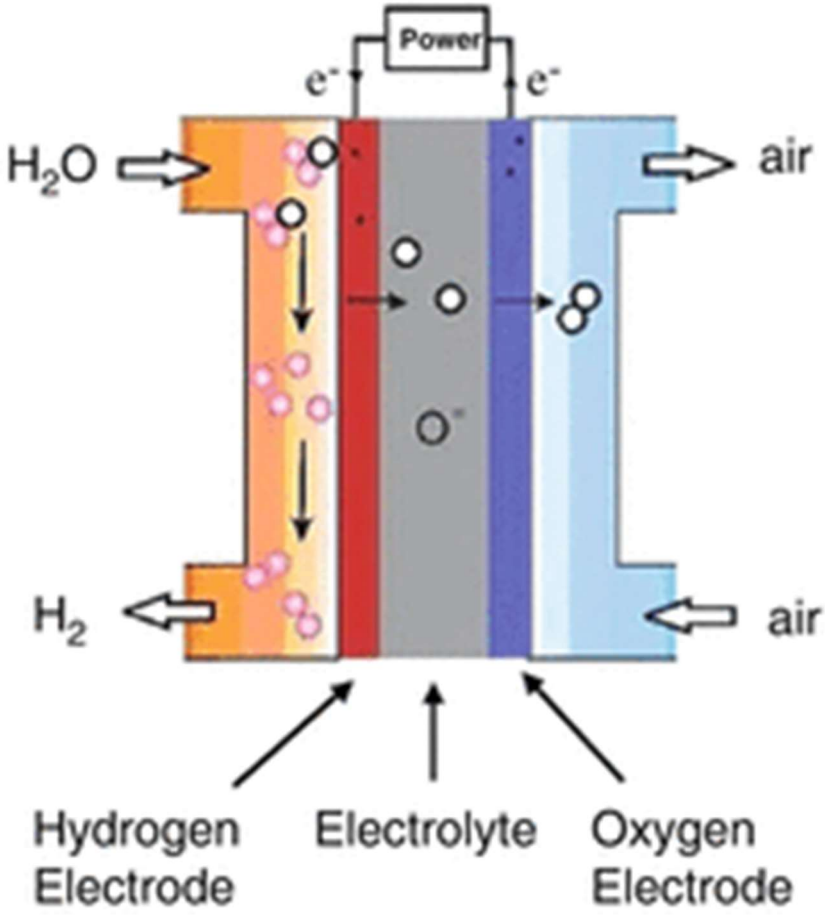

Figure 1.10 - Scheme of a solid oxide electrolysis cell.

In addition to hydrogen, SOECs can produce carbon monoxide from carbon dioxide or syngas ($H_2 + CO$) through co-electrolysis of H_2O and CO_2, allowing the production of green hydrocarbon fuels through different synthesis processes. These products can also be obtained operating at a pressure higher than the atmospheric one. High pressure is beneficial because the unit can be more compact and the products require less energy to be further compressed

for storage. The main electrochemical reactions occurring in a SOEC (operating co-electrolysis of steam and carbon dioxide) are:

- negative electrode (cathode) → $2\,H_2O + 4\,e^- \rightarrow 2\,H_2 + 2\,O^{2-}$
  $2\,CO_2 + 4\,e^- \rightarrow 2\,CO + 2\,O^{2-}$
- positive electrode (anode) → $2\,O^{2-} \rightarrow O_2 + 4\,e^-$

In case of solid oxide electrolysers, the ions promoting the reaction are oxide ions (O^{2-}), that move from negative to positive side (from cathode to anode). The triple phase boundary in case of SOEC technology is composed by a gaseous reactants and two solid phases, reaction catalyst and oxide ion conducting structure.

1.1.3 Focus on Solid Oxides Cells

Solid oxide cells can be operated both as fuel cells or electrolyzers without changing the materials and the structure of the cell. SOECs are based on designs thought for SOFC mode that have been studied extensively for more than 20 years [16].

Their main characteristic is the high operating temperature (600 °C – 1000 °C), leading to more favourable thermodynamics and faster kinetics, making this technology more efficient compared to competing ones. Solid oxide cells for electrolysis application have attracted increasing interest recently due to the unrivalled power-to-gas efficiency and capability of co-electrolysis of H_2O and CO_2 for syngas (H_2 + CO) production.

1.1.3.1 SOEC classification

Solid oxide cells can be designed and classified in different ways. Dealing with their geometrical design, they can be distinguished between planar, tubular and flat-tubular cells; currently the planar design dominates the field. Another way to distinguish different types of cells is considering which layer has support function.

This has traditionally been the electrolyte. One of the advantages of the electrolyte-supported design is that it is fairly robust, but the high operating temperature (> 800 °C), needed to achieve a sufficient transport of oxygen ions with a thicker electrolyte, requires more expensive materials for balance of plant and stack components. An alternative option is to have a ceramic fuel electrode as substrate for the cell. This would allow a thinner electrolyte, and as a consequence lower operating temperature and the use of cheaper materials. One of the challenges with the ceramic-supported design (commonly named anode-supported referred to SOFC mode) is that it is more sensitive to the oxidation of the fuel electrode. Another option is the use of a porous metallic substrate and the deposit of all the electrochemical active layers over it. This also allows to operate at even lower temperatures and offers some cost saving by replacing ceramics with steel. The challenge with this technology is to limit the corrosion of the substrate [16].

Figure 1.11 summarizes the three mentioned options of supports of solid oxide cells, reporting also their typical operating temperatures.

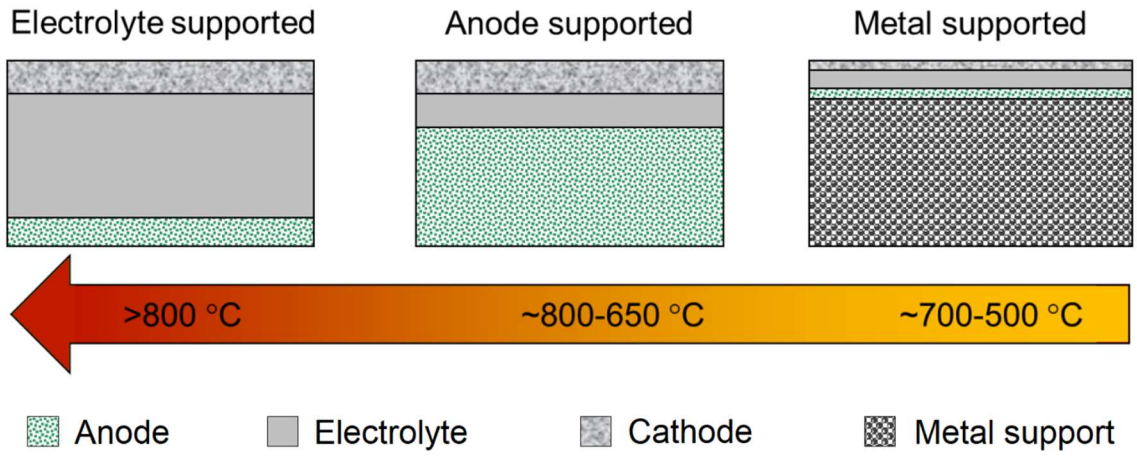

Figure 1.11 - Schemes of different SOC's structures and their typical operating temperatures (here the term anode is referred to SOFC mode).

1.1.3.2 Advantages of the technology

The main advantages of solid oxide cells compared to other electrolysis technologies are:

- Very high conversion efficiency, thanks to the favourable thermodynamics and fast kinetics at high temperatures, especially if combined with other thermodynamic cycles. This is evident from Figure 1.12 [17].
- Ability to produce, in addition to hydrogen, also carbon monoxide from carbon dioxide and syngas from co-electrolysis of H_2O and CO_2.
- Excellent reversibility between SOEC mode for fuel production and SOFC mode for power generation, which makes SOC very attractive also for grid balance applications [18].
- SOECs can be thermally integrated with a range of chemical syntheses, enabling production of syngas, gasoline and methanol from recycling of captured CO_2.
- SOEC technology is based on scalable production methods and abundant raw materials, such as nickel, zirconia, and steel, all of them not precious metals; indeed, noble metals are not required to catalyse the reaction, thanks to high operating temperatures [19].

The scale at which electrolysis cells will have to be deployed in future energy scenarios necessitates that any viable electrolysis technology should be based on Earth-abundant materials, which is the case for the commonly used SOEC. In most cell designs, the electrolyte is made of YSZ and both yttria and zirconia are abundant materials. Solid oxide cells providing 1 TW of power for 24 hours in fuel cell mode would require just 1 month worth of global ZrO_2 production and 21 months worth of Y_2O_3. To put these numbers into

perspective, 24 hours of 1 TW of power generated using Li-ion batteries would require Li corresponding to ~160 years of Li production referred to 2012, and 24 hours of 1 TW of power provided by a PEM fuel cell system would require 53 months worth of global Pt production [19].

Finally, it is possible to operate the cells at partial load maintaining very high conversion efficiency. Once the system is started and has reached operative temperature, it can follow the energy fluctuations very well just by changing the input current: this makes SOEC technology particularly interesting to be coupled with intermittent RES (it is possible for instance to follow wind profiles).

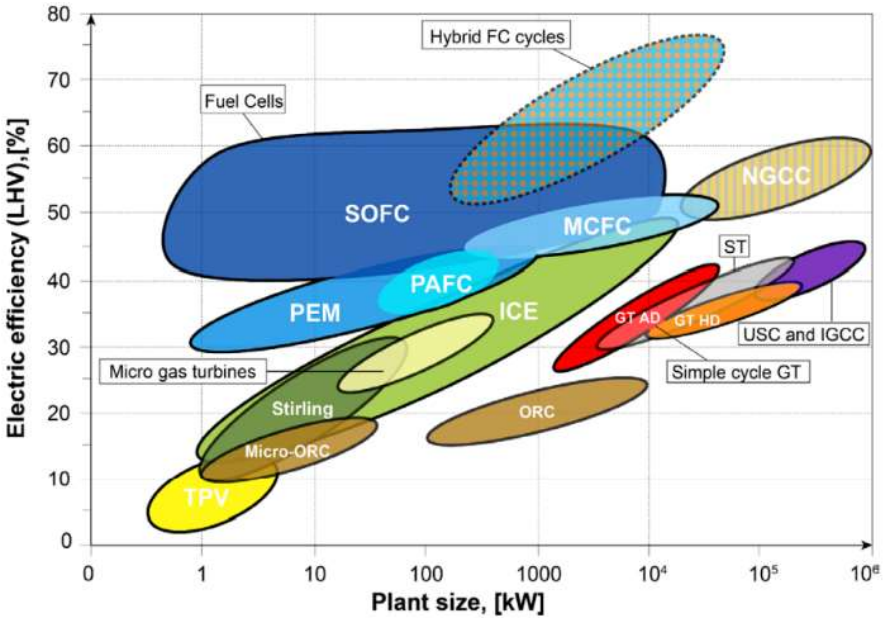

Figure 1.12 - Efficiency comparison among stationary power generation units based on natural gas.

1.1.3.3 Thermodynamics of SOECs

Elevated temperatures are necessary to reach sufficient ionic conductivity. The high operating temperature is an important feature of SOEC technology, giving rise to its two main advantages over competing alkaline and PEM electrolyzers, which typically operate from 60 °C to 160 °C: more favourable thermodynamics and faster kinetics [19].

SOEC is by far the most efficient type of H_2O and CO_2 electrolysis and this is due to basic thermodynamics of water/steam and carbon dioxide. This is observable in Figure 1.13, which shows a thermodynamic diagram at atmospheric pressure [20].

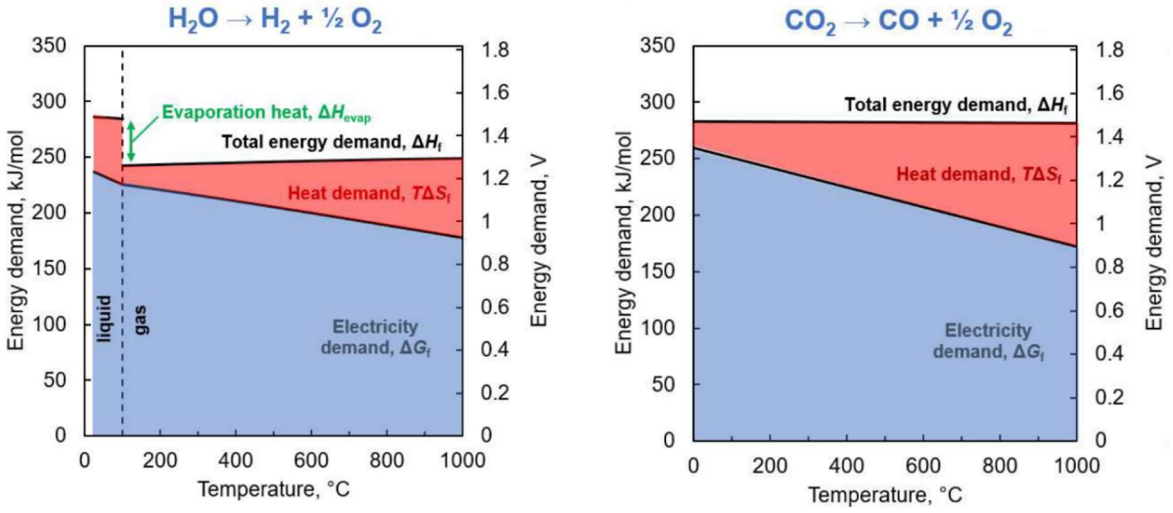

Figure 1.13 - Total energy demand (ΔH), electrical energy demand (ΔG) and thermal energy demand (TΔS) for steam and carbon dioxide electrolysis, computed at 1 atm changing the temperature.

It is possible to see that the effect of a temperature increase is a decrease of the electricity demand, while the heat demand becomes higher. The explanation of this behaviour can be found simply from thermodynamics. The electrical energy demand of the system can be considered equal to the Gibbs free energy of the electrolysis process (ΔG), defined as difference between the enthalpy of the reaction (ΔH) and the losses due to irreversibility ($T\Delta S$), as equation (1.1) reports.

$$\Delta G = \Delta H - T\Delta S \tag{1.1}$$

Increasing the temperature the total energy that is necessary to perform the electrolysis process (ΔH) slightly increases, while the heat demand ($T\Delta S$) becomes higher, resulting in a decrease of ΔG. This means that working at high temperature the electrolyser requires much less electricity. On the other hand, the high-temperature source needs to provide more heat, so it has higher electric consumptions. Anyway, since the high-temperature source is a component much less expensive than the cell, using high-temperature electrolysis may turn into an economic advantage. Moreover, the heat source could be the electrolysis stack itself: if the current density and consequently the cell voltage are sufficiently high, the internal heat generation due to losses could be sufficient to cover the heat demand. In this case, the electrolysis stack operating at high temperature could work with a lower amount of electric energy and with no need of an external heat source, leading to very high overall electrical efficiencies.

A comparison of the two charts in Figure 1.13 reveals that thermodynamics of CO_2/CO and H_2O/H_2 are quite similar in terms of ΔG values (electricity demand) in the temperature range from about 700 °C to 900 °C. This makes SOECs suitable to perform co-electrolysis of mixtures of steam and carbon dioxide.

In Figure 1.13 the relation between the two y-axes is direct, since energy can be related to the electric potential through Faraday´s constant F (the right axis values are simply obtained by dividing the left ones by $2F$; 2 comes from the exchange of two electrons per mole of reactants in the reactions). This relation will be better explained in equations (1.3) and (1.4).

The cell potential-temperature plane can be divided into three zones by the "equilibrium voltage line" and the "thermoneutral voltage line", as shown in Figure 1.14 [21].

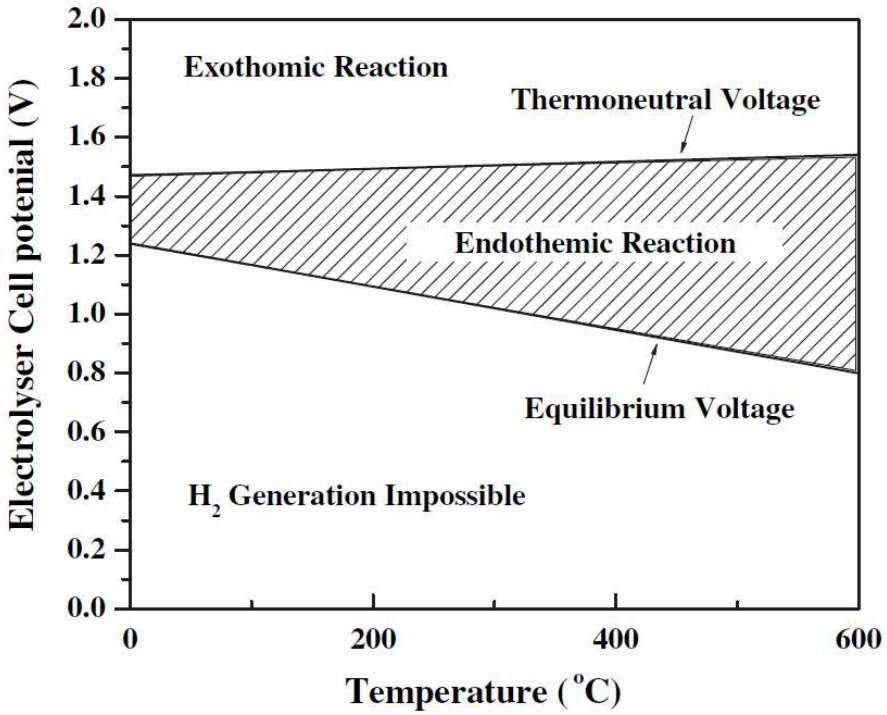

Figure 1.14 - Cell potential for hydrogen production by liquid water electrolysis as a function of temperature.

If considering water splitting, the equilibrium voltage is the minimum voltage required to dissociate water by electrolysis, below which this process cannot proceed. It can be computed knowing the Nernst law (1.2), here reported referred to a general electrochemical reaction.

$$E_N = \frac{\Delta G^0}{n_{e^-}\, F} + \frac{\mathcal{R}\, T}{n_{e^-}\, F}\, ln\left(\prod\nolimits_i {a_i}^{\nu_i}\right) \tag{1.2}$$

Where:

- E_N is the equilibrium electrode potential (Nernst potential);
- ΔG^0 is the standard Gibbs free energy of the electrochemical reaction;
- n_{e^-} is the number of electrons involved in the electrochemical reaction;
- F is the Faraday's constant ($F = 96485\ A\ {mol_{e^-}}^{-1}$);

- $\mathcal{R}$ is the universal gas constant ($\mathcal{R} = 8.314\ J\ mol^{-1}\ K^{-1}$);
- T is the temperature (expressed in kelvin, K);
- a_i are the activities of the several i components involved in the electrochemical reaction;
- ν_i are the stoichiometric coefficients of the several i components involved in the electrochemical reaction.

Considering ideal mixtures of ideal gases, the activity of each species (a_i) is equivalent to its partial pressure (p_i). At standard pressure (1 bar), at $p_{O_2} = 1$ bar and at $p_{H_2}/p_{H_2O} = 1$, the equilibrium voltage (E_{eq}) of the electrolysis cell (fed just with water) can be simply written as in equation (1.3).

$$E_{eq,w.s.}(\mathrm{T}) = {E_N}^+ - {E_N}^- = \frac{\Delta G^{0\,+}}{2\,F} - \frac{\Delta G^{0\,-}}{2\,F} + \frac{\mathcal{R}\,T}{n_{e^-}\,F}\,ln\frac{{p_{O_2}}^{0.5}\,p_{H_2}}{p_{H_2O}} = \\ = \frac{\Delta G^{0\,+}}{2\,F} - \frac{\Delta G^{0\,-}}{2\,F} = \frac{{\Delta G^0}_{w.s.}(T)}{2\,F} \tag{1.3}$$

${\Delta G^0}_{w.s.}$ is the Gibbs free energy of water splitting reaction and it is a function of temperature (in the equation the symbols + and – refer to positive and negative electrode respectively).

The same reasoning can be done for carbon dioxide reduction (1.4).

$$E_{eq,c.d.r.}(\mathrm{T}) = {E_N}^+ - {E_N}^- = \frac{\Delta G^{0\,+}}{2\,F} - \frac{\Delta G^{0\,-}}{2\,F} + \frac{\mathcal{R}\,T}{n_{e^-}\,F}\,ln\frac{{p_{O_2}}^{1/2}\,p_{CO}}{p_{CO_2}} = \\ = \frac{\Delta G^{0\,+}}{2\,F} - \frac{\Delta G^{0\,-}}{2\,F} = \frac{{\Delta G^0}_{c.d.r.}(T)}{2\,F} \tag{1.4}$$

In both cases, the equilibrium voltage decreases with increasing temperature, because it follows the same trend of ΔG.

The thermoneutral voltage instead is the minimum voltage that has to be applied to the high-temperature electrolysis cell in order to generate internally the heat necessary to supply the reaction demand. Water splitting is an endothermic reaction, requiring heat at constant temperature (oppositely to the case of H_2 oxidation, which is exothermic). In SOFC mode the process is highly exothermic, while in SOEC operation whether heat is produced or consumed in the overall process depends on the applied voltage. When operating the SOEC above thermoneutral voltage (e.g. 1.29 V for steam electrolysis and 1.47 V for CO_2 electrolysis) the whole process will be exothermic, while below thermoneutral voltage it will be endothermic [18].

As the equilibrium voltage is related to the reaction's Gibbs free energy, the thermoneutral voltage could be expressed as a function of the enthalpy variation, as in equations (1.5) and (1.6).

$$E_{tn,w.s.}(\mathrm{T}) = \frac{\Delta H_{w.s.}(T)}{2\,F} \tag{1.5}$$

$$E_{tn,c.d.r.}(\mathrm{T}) = \frac{\Delta H_{c.d.r.}(T)}{2\,F} \tag{1.6}$$

The internal losses produced by a cell working at E_{tn} provide the heat required for the endothermic electrolysis process to occur at a given current density and temperature. In this case it is not necessary to supply any external heating (or cooling) of the cell, apart from the heat necessary to compensate the heat loss to the surroundings, which Dönitz et al. found to be 7% for a system with a stack temperature of 995 °C [22]. If the cell voltage is in the interval $E_{eq} < E_{cel} < E_{tn}$, it is necessary to supply heat in order to keep the requested cell temperature, while if $E_{cel} > E_{tn}$ the cell would heat up and therefore it would need cooling [20].

Figure 1.15 shows ranges taken from the literature of voltages and current densities for different kind of electrolysis technologies, on the left for water electrolysis and on the right for CO_2 electrolysis. Lower cell voltage translates directly into lower operational costs (lower electricity demand per quantity of produced gas), while higher current densities are associated with lower capital costs (fewer electrolyzers needed to achieve the required capacity for gas production). The economic motivation for wider adoption of SOEC technology remains high, being clear from Figure 1.15 that a higher temperature allows to have lower voltages and higher currents. From the right chart it is clear that high-temperature operation is even more favourable for CO_2 electrolysis.

When both thermodynamics and kinetics are considered, temperature-related efficiency gains are far higher [19]: a solid oxide electrolysis cell operated at thermoneutral potential for the splitting of steam (1.29 V) reaches an electrolysis current density of ~ 1.5 A/cm^2, whereas a PEM electrolyser operated at thermoneutral potential for the splitting of liquid water (1.47 V) reaches a current density of ~ 0.5 A/cm^2 at similar gas compositions (see the left chart of Figure 1.15). PEM electrolyzers are typically operated at higher potentials (1.6 V to 1.7 V), reaching current densities of ~ 1 A/cm^2. The difference in thermoneutral potentials is directly related to the heat of evaporation, ΔH_{evap}.

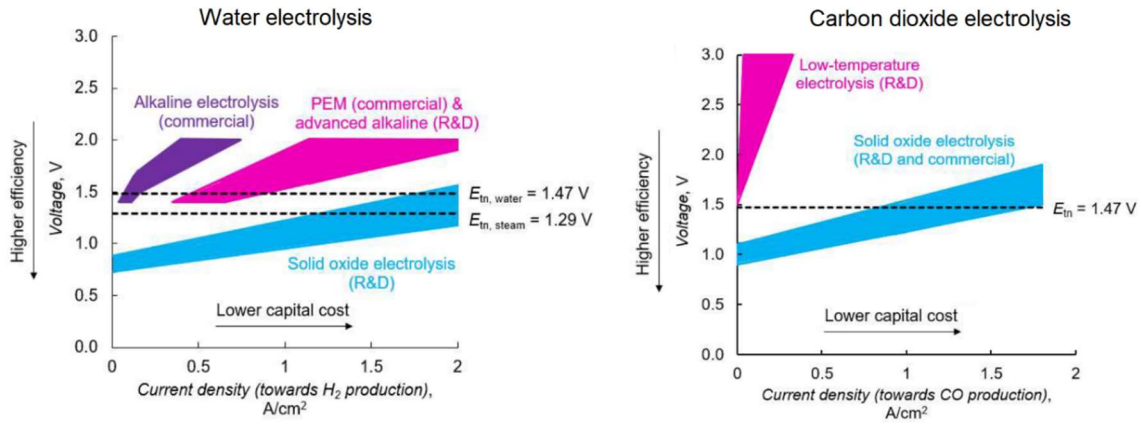

Figure 1.15 - Typical ranges of cell voltages as function of current density from the literature, for SOEC and low temperature water and CO_2 electrolysis cells.

The other thermodynamic parameter that affects SOECs operation is pressure. If the cell works under pressurized conditions, slightly higher electricity must be supplied because of ΔG increase, as shown in Figure 1.16. Pressurization is also technologically complex, due to the challenge of keeping separated hydrogen and oxygen. Anyway, high pressure is beneficial for the compactness of the unit and because hydrogen would be already at a closer pressure for storage (typically at 30-50 bar), avoiding the installation of a big compressor after the electrolyser.

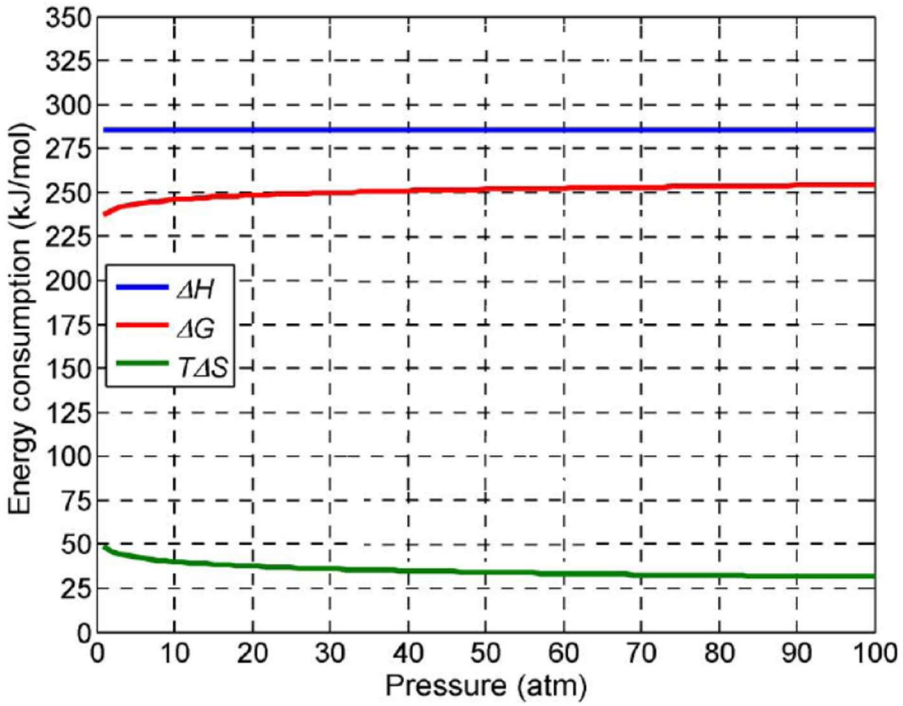

Figure 1.16 - Total energy demand (ΔH), electrical energy demand (ΔG) and thermal energy demand (TΔS) for steam and carbon dioxide co-electrolysis changing the pressure.

1.1.3.4 Problems, recent advancements and goals in research and development

The biggest disadvantage of SOEC technology is related to the mechanical stability of its components. In order to reach the very high operating temperatures, the ceramic cells cannot be warmed up too quickly, because the materials would be subjected to extremely high thermal and mechanical stresses that would break the layers. This means that SOECs require very long transients for start-up and shutdown, so research is mainly focused on studying cells with a lower amount of ceramic materials.

A solution could be found in Metal Supported Cells (MSC) that have been recently developed and tested, with promising first experimental results. Whereas conventional SOFCs are typically heated to operating temperature over a few hours to minimize temperature gradients and thermal shocks, MSCs can tolerate very large temperature gradients (> 100 °C/cm) and extremely rapid thermal cycling [23].

In a recent study published in 2020 by Hagen et al. [24] two different MSCs were tested. The difference between the two cells was in the anode backbone materials: one based on FeCr-ScYSZ and the other one based on FeCr-titanate. The tests were carried out comparing the performances of the two, both with hydrogen and methane as fuel. The results were promising in terms of long-term stability, achieving 3000 h operation with hydrogen as fuel. The main problem in terms of performances using methane-containing fuel is related to the nickel active sites for internal reforming. In order to improve the catalytic activity of the two type of metal supported cells, especially for methane reforming operation, nickel loading can be increased through more infiltration cycles or higher nickel content in infiltrating solutions. Another option is to introduce catalytically active stack components such as contact/gas distribution layers (for example metal foams have been studied for this purpose having large surface area). Tests were carried out only under fuel cell operation for these systems until now. One of the purposes of this project is to give a characterization of metal supported cells operated in electrolysis mode.

The performance of state-of-the-art solid oxide cells has improved a lot with respect to the first designs and long-term durability has been increased by a factor of ∼100 [19]. A lifetime of 5 years with high fuel production rate is considered a requirement for broad commercialization [12] and the main decay processes occur in the fuel electrode. In a study published in 2019, aimed to investigate long term degradation of solid oxide cells operated in electrolysis (4400 h), emerged that degradation occurs mainly at fuel electrode. The principal phenomena responsible for such decay are loss of contact between Ni and Ni grain, due to Ni agglomeration or migration, and nano-ZrO_2 precipitation from Zr dissolved in Ni bulk. In addition, the formation of small cavities inside YSZ grains, cracks along the grain boundary close to electrolyte-oxygen interface, and oxygen electrode delamination have also been reported. The reason for this has been mainly attributed to the high oxygen activity close to electrolyte-oxygen electrode interface. In order to prevent the formation of these cavities, better performing oxygen electrodes, based on strontium doped lanthanum cobaltite

(LSC) or strontium and cobalt co-doped lanthanum ferrite (LSCF), could help to decrease the over-potential at high current densities.

The tests reported showed that in order to achieve goals in durability without a significant loss in performance, the fuel electrode must be further improved in particular to prevent loss of percolation between Ni-Ni grains. Long-term durability tests were not performed for metal supported cells in SOEC mode, and it would be particularly interesting to assess degradation phenomena related to the active layers.

The electrochemical performance of SOEC stacks is determined not only by the activity of the cells, but also by the performances of other stack's components: metallic interconnections, glass sealings and flow channels. The properties of each of these components change during long-term operation (interconnects corrode, glass crystalizes, electrodes coarsen and accumulate impurities, and elements inter-diffuse) strongly affecting the whole system´s performance: particularly, silica-containing impurities can block the electrocatalytically active sites, causing degradation and increasing polarization resistance. Glass is usually replaced by other sealing non-crystalizing materials for single cells tests, for example gold, but it is commonly present in commercial stacks being cheaper.

In conclusion, research in improved processing methods is allowing to reduce thickness and to enhance mechanical properties of the cells, making them more and more suitable for the coupling with intermittent RES. Metal supported cells have potential advantages, but their negative electrode has to be improved if it is desired to directly convert hydrocarbons. Fuel electrode is the most stressed part from the electrochemical point of view in the cell-system, therefore it is plausible that it would remain the main cause for loss of performance for the metal-supported as well as for the ceramic-supported cells. Oxygen electrode as well as the electrolyte are not very problematic, there is margin for improvement but the current state-of-the-art solutions already provide solid performances. At stack level, improving durability and reducing costs have been the goals ever since the first SOECs were tested in the late 1980s; going forward, the performance metric to be maximized should not be durability, but rather the amount of gas produced over the stack´s life [25]. Figure 1.17 shows hydrogen production capacity projections worldwide until 2022 [19].

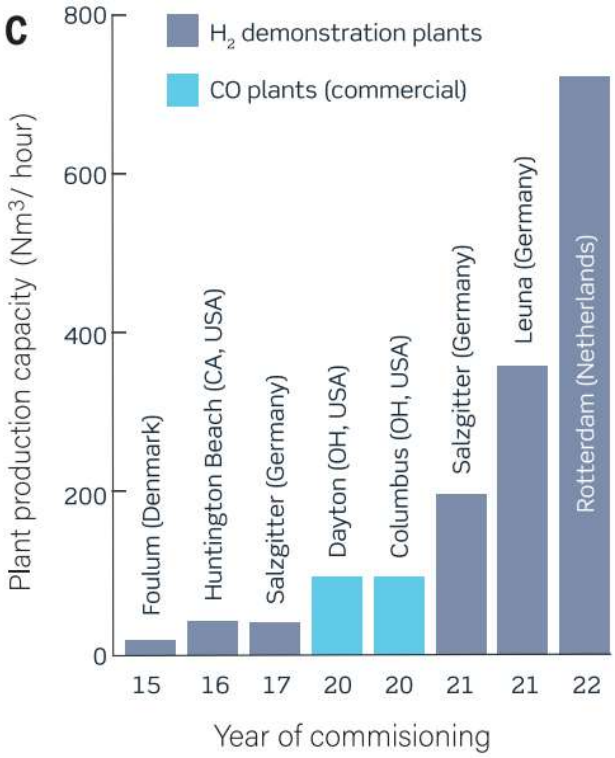

Figure 1.17 – Hydrogen production capacity projections until 2022.

1.1.3.5 Economic overview and future scenarios for green hydrogen

Together with technological boundaries, economy plays a very important role allowing the spread of a technology. Storage costs for chemical energy as hydrogen, methane in caverns, or other high energy density fluids, are today at the level of less than 1 €/kWh (excluding conversion costs), while the cost of battery storage is expected to remain considerably higher, being nowadays around 150 €/kWh and expected to be around 80-100 €/kWh by 2030 (optimizing the number of cycles over the life of the battery) [19].

In order to allow the spread of hydrogen as mean of energy storage, infrastructure renovation is essential but it would imply an important additional cost, especially at the beginning of the transition; this will be however essential to allow a sustainable future and, on the long run, it will allow to have a more efficient and well-integrated energy supply system. In addition to that, production costs need to be competitive and SOEC technology will not become the electrolysis technology of choice unless the total cost of ownership (cost of 1 kg of H_2) is brought down to a lower level than the one achievable by alkaline or PEM electrolyzers.

Interest in fuel cells is increasing world-wide and Asia is the region which shipped more units in the recent years, as Figure 1.18 (left chart) shows [26]. Japan in particular is pushing toward micro-residential CHP (Combined Heat and Power) systems as well as in transport sector, which still remain the dominant in terms of shipped units. North America follows, having experienced the biggest increase in installed power in the recent years, as it is possible

to see in Figure 1.18 (right chart) [26]. Europe demand and capacity are expected to grow significantly in this decade, both in transport and stationary power fields.

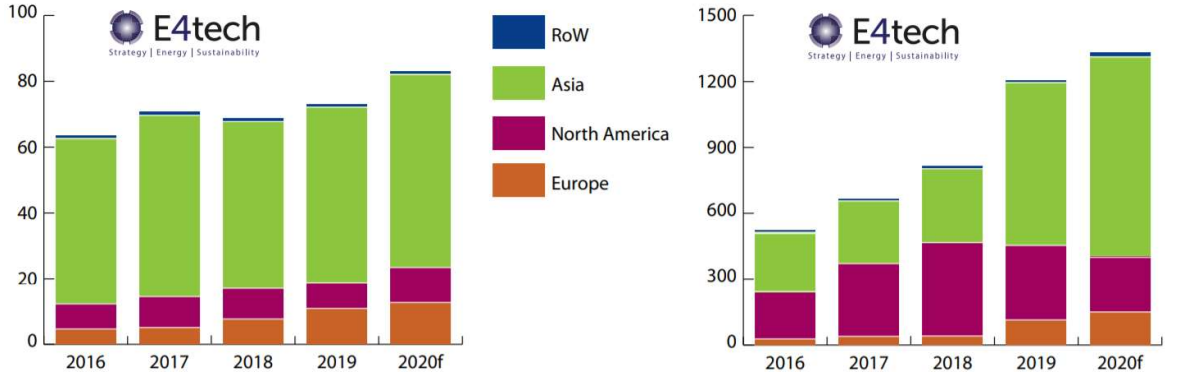

Figure 1.18 – On the left, fuel cells shipments by region (1000 units); on the right, installed MW of fuel cells by region.

In the recent years research and development are improving a lot performances and costs of Alkaline and PEM cells, which are starting to become competitive with respect to small scale thermal power generators, achieving the milestone of 1000 €/kW (small diesel generators of few MW cost around 900 €/kW).

Figure 1.19 shows fuel cell installation by application and type of technology [26]. It is appreciable that PEM remains the dominant one in the market (right chart) mainly because of its potentiality in the transport sector (left chart), which is still the leading application. Most of the effort comes from Toyota and Hyundai cars (750 MW in 2019).

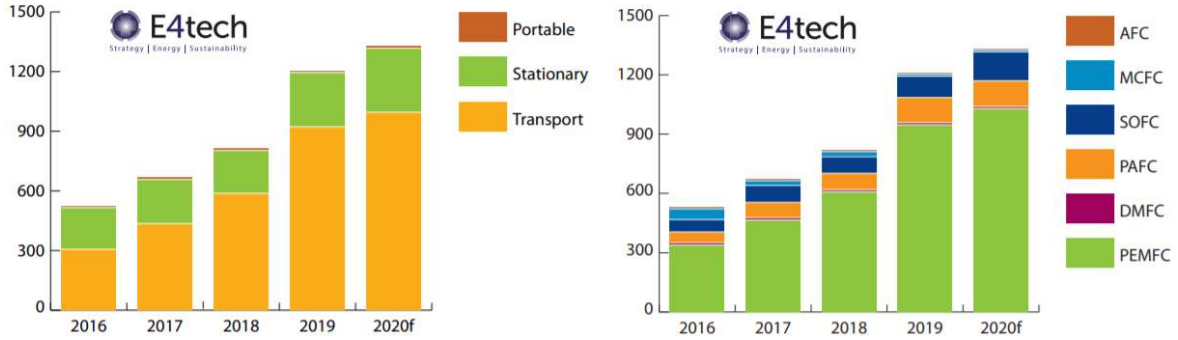

Figure 1.19 – Fuel cell installations in MW by application (left) and by type (right) 2015-2019.

Solid oxide technology nowadays is very expensive. The average cost of a stack is 4000-8000 €/kW, much higher with respect to Alkaline and PEM technologies, which costs are respectively around 700 €/kW and 1000 €/kW. The main contribution to costs is in the bipolar plates for PEM (accounting 51% of total cell cost) and in anode and cathode for Alkaline (accounting respectively 24% and 24% of total cell cost) [27]. These costs mostly rely on materials, hence, despite there is still room for improvement, is not possible to reduce

the costs too much. Expected costs by 2030 are around 760 €/kW and 580 €/kW for PEM and Alkaline technologies, respectively [27].

SOEC technology is based on abundant not noble materials and, thanks to the more recent developments in such technology, like the use of metal supports, these cells are expected to become cheaper thanks to improvements in production technologies and to scalability of the production. In particular, if research and development will allow to reduce degradation and achieve higher life duration (expected to be more than 60000 h), the costs will drastically decrease both for capital investment (lower cost and longer life) and operation expenses (halving them from 2-2,5 to 1-1,5 €/kWh) [17]. In this scenario costs can drop to levels lower than 500 €/kW, allowing such technologies to spread widely in the market [28].

Finally, considering the production of synthetic fuels, a recent techno-economic assessment of power-to-gasoline conversion found a price for gasoline of 2,25 €/l, with several assumptions in terms of efficiency [29], and a price for electric power of 81,6 €/MWh. Likewise, a targeted price of less than 2 €/l was announced for a demonstration project with a production capacity of 8000 tons of liquid fuel per year.

For power-to-X energy conversion processes the price of electricity will play the major role in influencing the price of the product, in a scenario in which long life durability of stacks and lower CAPEX and OPEX will be achieved.

1.2 SOC state-of-the-art: components, materials, processing

In this section the main components of solid oxide cells will be analysed, focusing on the working principles and the key aspects to guarantee high performances. Many designs and materials for each component have been investigated in the years: the state-of-the-art technologies will be presented, going more into details with the most promising technologies and the choices behind the cells that have been tested for this project's purpose.

The main aim of this work is to investigate the behaviour of solid oxide cells operated in electrolysis at low temperatures, comparing a state-of-the-art ceramic-supported cell with a metal-supported one. The electrodes will be referred univocally as fuel electrode or negative electrode (anode for fuel cell operation and cathode for electrolysis operation) and oxygen electrode or positive electrode (cathode for fuel cell and anode for electrolysis mode). The two types of cell tested are structured as follows.

- Ceramic-supported solid oxide cell: Ni-YSZ-based (nickel yttria stabilized zirconia) cermet as negative electrode and support structure, YSZ as electrolyte, LSC-CGO (strontium doped lanthanum cobaltite and gadolinium doped ceria) composite oxygen electrode, LSM (lanthanum strontium manganite) positive current collector layer.
- Metal supported solid oxide cell: LSFNT (lanthanum strontium doped titanate) negative electrode layer deposited on a FeCr metal support, ScYSZ (scandia yttria

co-doped stabilized zirconia) electrolyte, LSC positive electrode and current collector layer.

The aim is to provide a general understanding of the main phenomena characterizing each active layer that is present in the tested cells, and compare them with some of the most common or promising materials and designs.

1.2.1 Electrolyte

In solid oxide cells the electrolyte must meet precise requirements: high ionic conductivity and low electronic conductivity are key aspects, together with electrochemical stability both in reducing and oxidizing conditions. In addition to that, mechanical stability at the operative temperatures is essential to allow the realization of a thin layer, reducing as much as possible ion-transport related losses.

Historically fluorite structure has been the main choice but in the recent years many other materials have been investigated, mainly to help reducing the operative temperature. Among fluorite-oxide-structured, doped ceria is the most promising, allowing a good ion conductivity at lower temperatures (800 – 600 °C). Also many other materials such as perovskites, brownmillerites and hexagonal-structured oxides have been investigated, obtaining remarkable results.

In this section the focus will be on fluorite-structured electrolytes, since these are the ones present in tested cells. YSZ (yttria doped stabilized zirconia) is the electrolyte of the ceramic-supported cell, while ScYSZ (scandia yttria co-doped stabilized zirconia) is the electrolyte of metal-supported ones. Also ceria will be discussed, even if such electrolyte is not used in the experimental activity, being helpful to understand some concepts which apply also to zirconia but are easier to appreciate in such systems. In addition to that, it is a very actively investigated technology being promising in furtherly reducing operative temperatures.

Nernst in 1890s first observed oxide ion conductivity in ZrO_2 containing 15 wt% Y_2O_3 (yttria stabilized zirconia), and in 1937 Baur and Preis realized the first SOFC using this electrolyte [30]. The dependence of ion conductivity with temperature has been investigated in the years also for different materials and, despite YSZ is not the best material in terms of conductivity, it is made of very abundant elements, it is cheap, easy to process and particularly it has a low electron conductivity.

The fluorite-oxide structure (general formula MO_2), shown in Figure 1.20 [31], is formed by tetravalent metal cations such as Zr^{4+}, Ce^{4+} and Th^{4+}, occupying the regular sites of a face-centered cubic structure, whereas oxygen ions occupy the eight tetrahedral interstitial sites leading to a large number of octahedral interstitial voids.

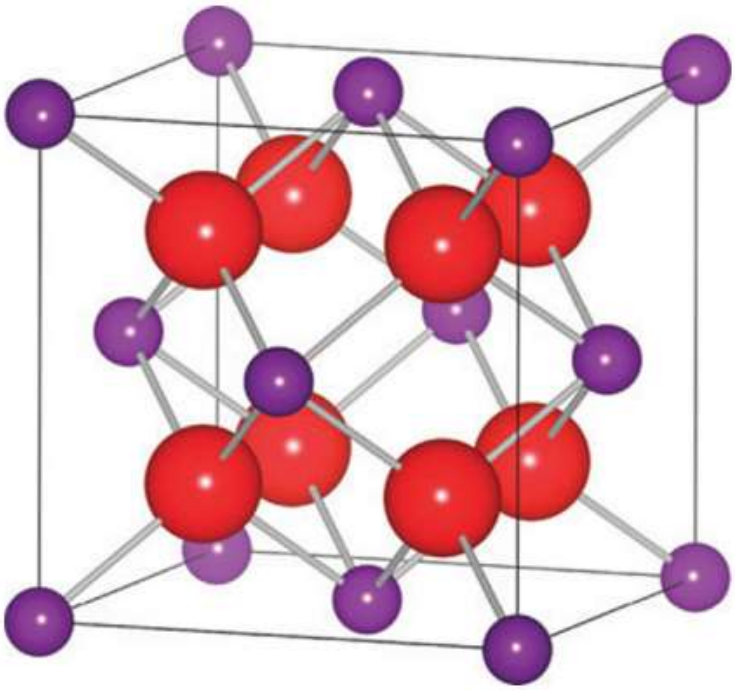

Figure 1.20 - Cubic fluorite structure (red spheres are oxygen ions, purple spheres are M^{4+} cations).

Zirconia (ZrO_2) only forms the fluorite structure at high temperatures [32], but with the addition of divalent or trivalent (i.e. aliovalent) cations, such as Ca^{2+}or Y^{3+}, the structure can be stabilized at lower temperatures. Ceria (CeO_2) also adopts the fluorite structure and its stability does not strictly require doping.

Oxide ion conductivity is given by point defects, either vacancies or interstitial oxide ions, in the oxygen tetrahedral structure. These defects are essential to allow the ions to move through the crystal by occupying an equivalent site with a minimum of hindrance. Thermodynamic equilibrium sets the intrinsic defect concentration that is very low in most oxide materials, for that reason extrinsic defects are generated by the addition of aliovalent substitutional cations.

The presence of a soluble aliovalent ion (dopant), such as Y^{3+}, in an ionic structure creates localized charges that are compensated by an increase in concentration of vacancies or interstitial defects to maintain electro-neutrality. In crystalline structures formed by multivalent cations like ZrO_2, charge compensation can also occur by the formation of electronic defects, implying an increase in electronic conductivity. Doping is essential to achieve targets in ion conductivity but requires many attentions in production processes to limit the rise of electron conductivity.

1.2.1.1 Ionic conductivity analysis

Yttria (Y_2O_3) dissolution in zirconia (ZrO_2) can be written in Kröger–Vink notation (1.7), highlighting that for each additional mole of yttria an oxygen vacancy ($V_O^{\bullet\bullet}$) is formed and

the electric-neutrality condition gives the concentration of the vacancies, linearly dependent to the substitution level (1.8).

$$Y_2O_3 \xrightarrow{ZrO_2} 2Y'_{Zr} + 3O_O^x + V_O^{\bullet\bullet} \tag{1.7}$$

$$[V_O^{\bullet\bullet}] = \frac{1}{2}[Y'_{Zr}] \tag{1.8}$$

The ionic conductivity (σ) can be expressed as function of the number of charge carriers (n) and their thermally activated mobility (μ) and charge (q) through equation (1.9). It is possible to relate the conductivity to the concentration of the vacancies [33], as expressed in equation (1.10), where the fraction of mobile oxide ions is the product of the fraction of vacancies ($V_O^{\bullet\bullet}$), and the fraction of occupied oxygen sites (1 - $V_O^{\bullet\bullet}$) moduled by a pre-exponential constant A. E_a is the activation energy for the conduction process, R the gas constant, T the absolute temperature.

$$\sigma = nq\mu \tag{1.9}$$

$$\sigma T = A[V_O^{\bullet\bullet}](1 - [V_O^{\bullet\bullet}]) \exp\left\{\frac{E_a}{RT}\right\} \tag{1.10}$$

According to the model, the maximum conductivity should occur at an oxygen vacancy concentration of 50% (by site fraction), but experimental data show an important behaviour deviation from the model: the maximum occurs at much lower concentrations and changes by changing the type of trivalent cation. This phenomenon occurs both with zirconia [34] and ceria systems [33], [35], [36] and numerous attempts have been made in the years to explain it.

The content of dopant that gives the highest conductivity decreases increasing the radius of substitutional ion: the concentration of mobile oxide ion vacancies is affected by the elastic strain energy, which is related to the size mismatch between the host and substituted cations. For zirconia, Sc^{3+} has the closest ion radius to the host ion Zr^{4+} and shows the highest conductivity and the highest substitutional content at the maximum conductivity; while other ions with bigger radius (Dy^{3+} and Gd^{3+} for instance) show a lower conductivity and a maximum concentration of 8%mol, as shown in Figure 1.21 [34].

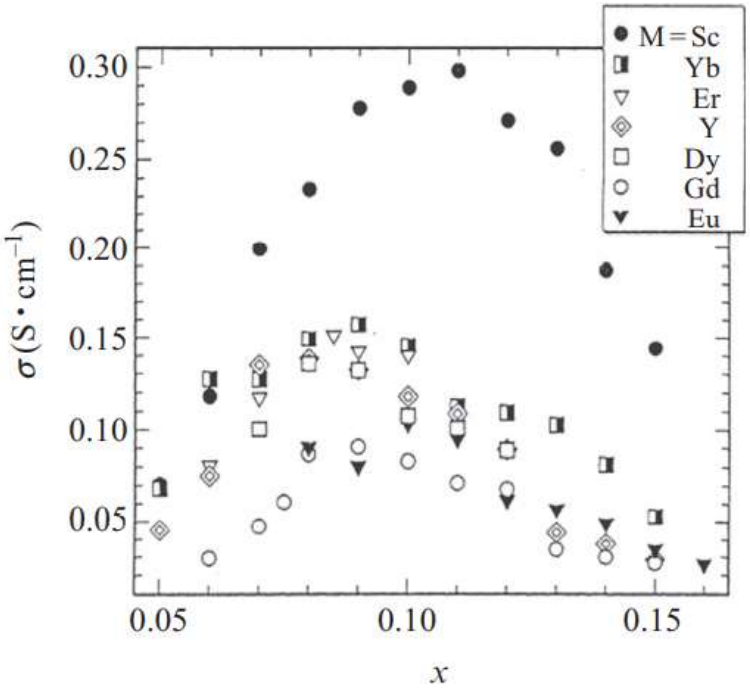

Figure 1.21 - Electrical conductivity dependence on composition for ZrO_2 – M_2O_3 at 1000 °C.

Conductivity dependence on ionic radii mismatch has been observed in the CeO_2 system, in which a wider range of substitutional ions is possible. The interaction between oxide ion vacancies ($V_O^{\bullet\bullet}$) and aliovalent cation (M'_{Ce}) may form a defect pair like in reaction (1.11) or even higher-order clusters, for instance a trimer in reaction (1.12).

$$V_O^{\bullet\bullet} + M'_{Ce} \leftrightarrow \{V_O^{\bullet\bullet} M'_{Ce}\}^{\bullet} \tag{1.11}$$

$$V_O^{\bullet\bullet} + 2M'_{Ce} \leftrightarrow \{M'_{Ce} V_O^{\bullet\bullet} M'_{Ce}\}^{x} \tag{1.12}$$

An isolated pair is more likely to occur given the random distribution of aliovalent cations [37], however recent studies showed that depending on the dopant and its concentration, complex cluster can be formed [38]. In the case of simple pair formation (for the sake of simplicity), at very low aliovalent concentration the equations (1.13) and (1.14) apply.

$$[\{V_O^{\bullet\bullet} M'_{Ce}\}^{\bullet}] \gg [V_O^{\bullet\bullet}] \tag{1.13}$$

$$[V_O^{\bullet\bullet}] = \frac{B}{T} \exp\left\{\frac{\Delta H_a}{RT}\right\} \tag{1.14}$$

The effect of the binding enthalpy (ΔH_a) of an associated ion significantly affects the concentration of vacancies, especially at low temperatures, when association is almost complete as shown in equation (1.14) – B is a constant. Concentration of vacancies and their migration is thermally activated and the ionic conductivity is affected by binding enthalpy.

Many attempts have been made to try to minimize binding enthalpy. Only recently, through more sophisticated atomistic [39] and density functional theory (DFT), it was possible to understand that the minimum occurs when the host and aliovalent cation ionic radii are close to each other. Particularly, when the aliovalent cation is slightly larger than the host, lattice relaxations result to be minimized and with it the energy related to such structure. In addition to that, a switch in the position of the oxygen vacancy from the nearest neighbourhood to the next-nearest one helps decreasing lattice binding energy, as it is possible to observe in Figure 1.22 [39].

DFT calculations of Andersson and colleagues [40] showed that it is not possible to find a cation with the optimum radius, and in order to obtain the optimum it was suggested to use a combination of dopants. This opened the way for co-dopant studies which anyway showed a minimal improvement in conductivity [41], [42], [43], [44].

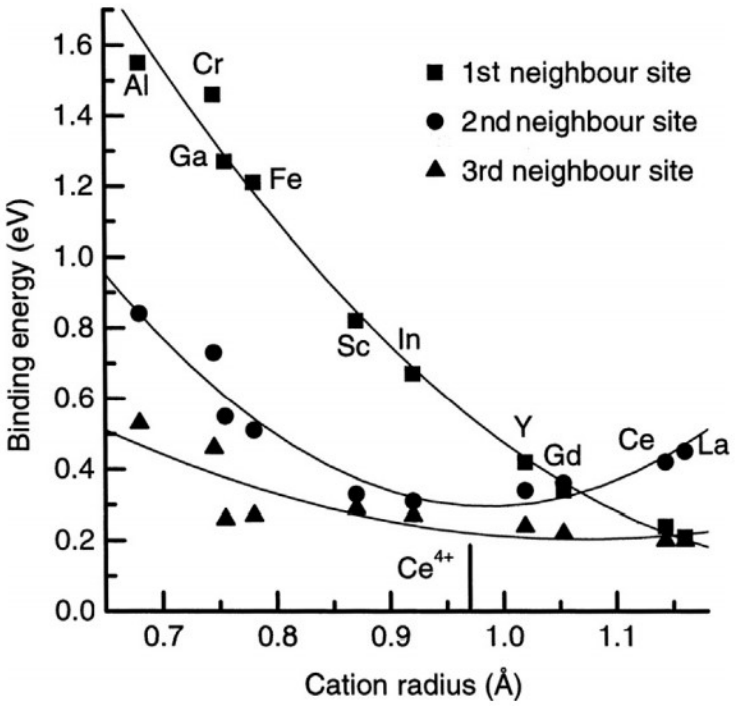

Figure 1.22 - Binding energies of M^{3+} cations with an oxygen vacancy in ceria.

In zirconia systems it is harder to observe experimentally the influence of aliovalent cation radius on lattice relaxation energy, however atomistic simulations confirmed that the system behaves similarly to ceria [45]. The general conclusion is that the matching of the dopant

radius with the host one is the main aspect to take into account in order to achieve higher ion conductivity in solid oxide ion conductors.

1.2.1.2 Fluorite-structure-based ion conductors

Zirconia crystalline structure changes with the temperature exhibiting three polymorphs: at ambient temperature the structure is monoclinic, up to 1170 °C it is tetragonal, and it becomes cubic fluorite above 2370 °C. The addition of a dopant such as yttria can stabilize both tetragonal and cubic structure at ambient temperature and the performances in terms of ionic conductivity are affected by its concentration. An addition of about 8%mol gives a conductivity of 0.14 Scm^{-1} at 1000 °C. Being zirconium and yttrium abundant, cheap and easy to process materials, such systems are still the most used in commercial application for solid oxide cells.

With the interest going towards lower operating temperatures (600 – 800 °C), scandia-stabilized zirconia (ScSZ) has been extensively studied showing good initial conductivity (σ =0.28 Scm^{-1}) at 10-11%mol at 950 °C. ScSZ is a polyphase system containing both cubic and rhombohedral structures: the second one, implying a lower conductivity, is more stable below 550 °C, when an important decrease in conductivity is appreciable, and after ageing on long term exposure to high temperature. Indeed, Hearing et al. observed a decrease of conductivity from 0.28 Scm^{-1} to 0.12 Scm^{-1} keeping the cell at 1000 °C for 1000 h. On the other hand YSZ showed no ageing effect at same conditions [46].

In order to stabilize the cubic structure, even at lower temperatures or during long periods, co-doped systems have been investigated: ceria (1%mol) and scandia (10%mol) co-doping for instance showed good conductivity, good stability and no visible ageing [47]. Other solutions that have been tried included co-substitution with other trivalent cations, such as holmia, ytterbia, and yttria. The last one in particular is the solution adopted for the realization of the electrolyte of tested metal supported cell.

Literature is not comprehensive on the topic, since different research groups studied many different materials. However, in Spirin et al. [48] paper a comparison with other experimental data obtained by different groups is present, so it will serve as main reference.

The addition of 1-3 mol% yttria to 8-10 mol% ScSZ solid solution stabilizes the cubic structure even below 550 °C. Total molar concentration of dopant species does not excess 10-11 mol%: $xY_2O_3 - (10 - x)Sc_2O_3$ is the generic crystal, but additional impurities can be present.

Experimental data obtained by Spirin showed that the conductivity in such systems has a linear trend that depends on the concentration of yttria, with the slope moduled by the temperature, showing also that the elastic strain energy of the crystalline structure is directly proportional to the co-dopant content. This is shown in Figure 1.23, where pure scandia is on the left, yttria-scandia co-doped in the middle and pure yttria on the right side. The inset shows activation energies of two different powders differing in molar fraction composition,

and the linear correlation for one of the two [48]. Increasing the molar percentage of yttria, the conductivity at a given temperature decreases from the maximum value obtained with ScSZ to the minimum value related to YSZ. In addition, it was also observed that the presence of yttria crystals helps to prevent the polymorphous transition occurring below 550 °C. Figure 1.24 compares data obtain by Spirin et al. with past experimental activities reported in the literature, dealing with the dependence of ionic conductivity on temperature. It is appreciable that adding yttria to ScSZ prevents the rhombohedral transition, by observing that there is no sudden conductivity drop at 550 °C with ScYSZ, spotted instead for ScSZ.

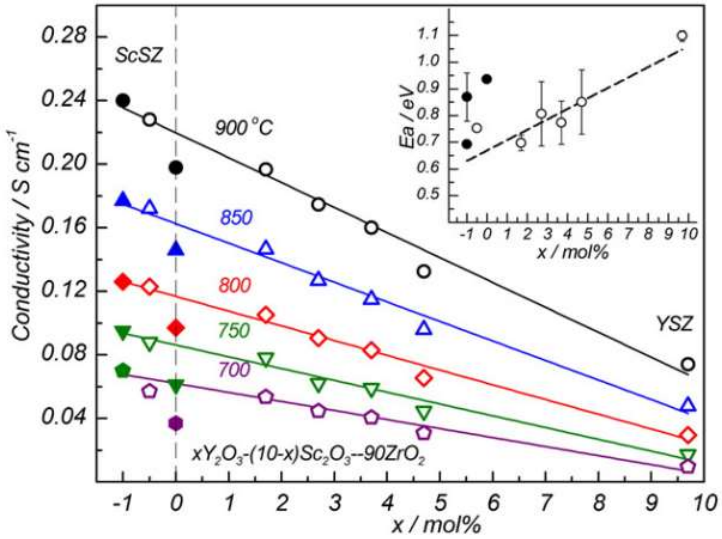

Figure 1.23 - Conductivity isotherms as function of scandia and yttria concentration in zirconia crystalline structure.

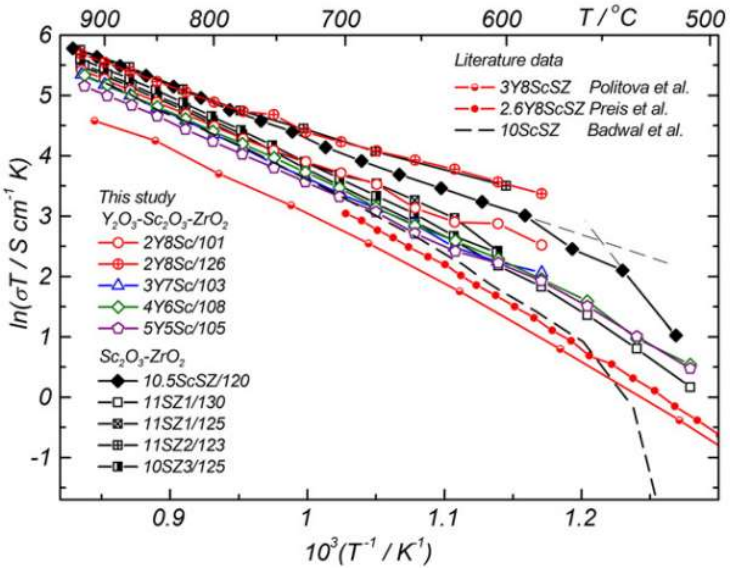

Figure 1.24 - Arrhenius plot of the total conductivity at different temperatures for different ceramic powders. In black: ScSZ; in colors: ScYSZ with different yttria content and sintered at different temperatures. It is also present a comparison with other experimental data from the literature.

Another important aspect that was observed is the dependence of the performances with sintering temperature. It is possible to see it in the left legend of Figure 1.24 as the number following the powder name, with a zero missing. These electrolytes are produced by co-precipitation route to form two agglomerated powders (10YSZ and 10ScSZ) that are subsequently transformed in nano-powders through laser evaporation method, ultrasonically dispersed in isopropanol and finally blended with zirconia [49]. Sintering temperature was addressed as one of the variables that influences performances in terms of conductivity and durability: a lower sintering temperature (1010 °C compared to 1300 °C) allows the formation of a denser crystalline structure, with a slightly lower conductivity and grain dimension (1 vs 7 μm), which is less susceptible to changes over long periods of operation.

An alternative to operate at lower temperature is to adopt ceria, which has the same cubic fluorite structure as zirconia. Ceria can be doped adding Gd^{3+}, Sm^{3+} and La^{3+}, and the maximum conductivity can be observed around 10%mol Gd_2O_3 ($\sigma = 3.6 \cdot 10^{-2}\ Scm^{-1}$ at 700 °C and $\sigma = 3.8 \cdot 10^{-3}\ Scm^{-1}$ at 500 °C).

An issue with ceria-based electrolytes is that the conductivity is affected by oxygen partial pressure. Figure 1.25 shows the dependence of a ceria-based electrolyte conductivity on oxygen partial pressure [50]. Close to the fuel electrode, where p_{O_2} is lower, the crystalline structure partially reduces leading to an increase in electronic conductivity in an important volume portion of the electrolyte.

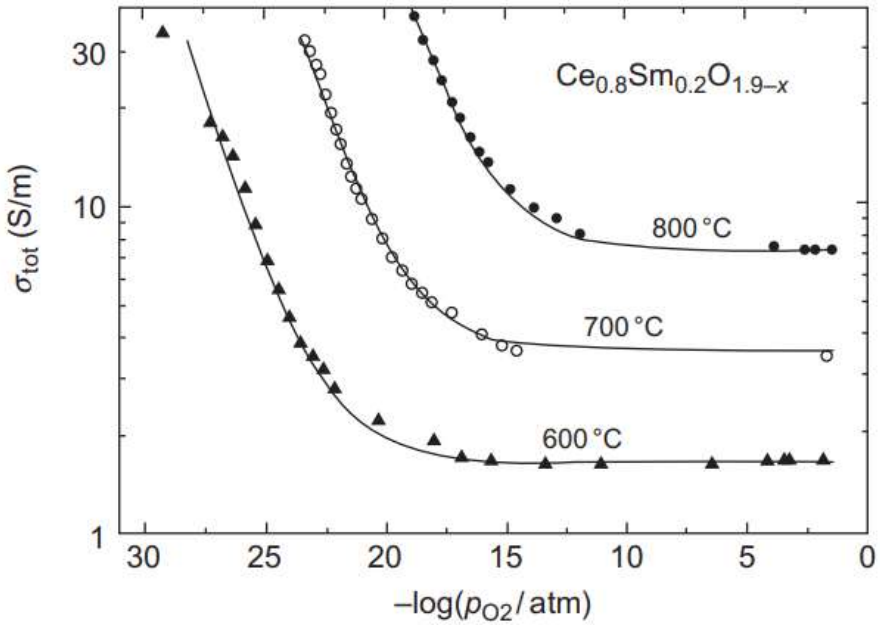

Figure 1.25 - Total electrical conductivity of $Ce_{0.8}Sm_{0.2}O_{1.9-x}$ at different temperature as function of oxygen partial pressure.

This dependence can also be seen as a bigger difference between the open circuit voltage and the theoretical one: in addition to non-idealities, there will always be a minimum current flowing for ceria-based systems.

Efficiency calculations based on Gibbs free energy performed by Godickemeier and Gauckler [51] showed that to achieve better performances the cell should be operated around 550 – 600 °C. At these temperatures they achieved an efficiency of about 60% (SOFC mode), higher than the 50% value obtained at 800 °C where electronic leakages are more consistent. If higher temperature of operation is required the phenomenon can be limited by coating the fuel electrode side of the electrolyte with a thin zirconia layer [50].

1.2.2 Fuel electrode

The fuel electrode is the part of the cell which most influences the lifetime of the system, being the most stressed from the electrochemical point of view: the partial pressure of oxygen varies between inlet and outlet in an appreciable way, both during oxidation of the fuel (hydrogen or hydrocarbons) in SOFC operation and reduction of water or CO_2 in SOEC operation. For practical and economic reasons, the electrode is usually sintered in air; however, when oxidation can become an issue, this process can be carried out also in hydrogen atmosphere as in the case of metal supported cells. The best solution is to make a material that is stable under both oxidizing and reducing conditions. Along with good electronic and ionic conductivity and catalytic activity, electrochemical stability is essential for the system to achieve lifetime and performance goals.

An advantage of the higher operative temperature with respect to other electrolysis technologies, is the enhanced kinetic of the reactions that allows to use cheaper materials. On the other hand, many more stability requirements are to be satisfied in order to avoid microstructural changes (metal sintering above all) or structural damages to the system (cracks) due to different thermal expansion coefficients of the different components.

The critical part of fuel electrode is the TPB (triple phase boundary) which needs careful microstructural engineering and realization processes. Adequate electronic conductivity is essential to obtain a resistance low enough to get the electrons out of the cell. For good performances, it is usually considered that the total electrode resistance should be less than 0.15 Ωcm^2 (including electronic, ionic and chemical resistances) [52]. Considering the porous nature of the electrodes that increases the resistance, the conductive material would have to have a conductivity higher than 100 S/cm. Reducing extra contact points with careful microstructural engineering and with a good design of the current collector, this could be relaxed to about 1 S/cm [53].

In the last century, when solid oxide cells were first studied, materials have been chosen to have a sufficient electronic and ionic conductivity, and the high temperatures would make them good catalysts. However, both ionic and electronic conductivity is uncommon in materials; for that reason, given the increase of interest in such technologies, the recent year's research and development is more oriented to multiple phase electrodes to enhance the performances. The best solution is to mix an electronically conductive phase with the ionic conductor (MIEC – mixed ionic electronic conductor) which usually is the same material present in the electrolyte.

Since the high operative temperatures also allows the utilization of hydrocarbon fuels, a brief introduction to the technology, relative problems and possible solutions will be presented. This project's purpose is not to test hydrocarbon fuels or CO_2 electrolysis, hence the topic will be discussed without going deep into details. In the literature were found more papers dealing with SOFC operation mode, anyways the same carbon-related problems affecting the cells would be present also in the reverse mode, perhaps with different dynamics.

1.2.2.1 Ni-YSZ fuel electrode

Historically single-phase materials have been investigated, such as graphite, iron oxide, platinum groups and transition metals [54]. Nickel spiked among all for its higher electrochemical stability against corrosion and its catalytic action toward hydrogen oxidation and water reduction.

A problem remained the thermal expansion mismatch with stabilized-zirconia (electrolyte material), and the grain growth and aggregation at high temperature that eventually obstructs the porosity of the electrode, eliminating the three-phase boundaries required for cell operation. For that reason, Spacil introduced the nickel–zirconia cermet electrode [55] and it remained the most important solid oxide cell fuel electrode design in the last 50 years. The association of nickel, the best transition metal option, with the yttria-stabilized-zirconia ceramic material of the electrolyte, allows to reduce the difference of thermal expansion with respect to the electrolyte. The function of the ceramic phase in the composite is essentially structural, to retain the dispersion of the metal particles and the porosity of the electrode during long-term operation. Moreover, it also allows oxide-ion mobility. The combination of nickel, providing electronic conductivity and electro-catalytic action, resulted in the realization of the first composite electrode.

This configuration (electrode supported) allows to have a reduced thickness of the electrolyte (no more than 15 μm), hence a lower ohmic resistance. The actual electrode itself only needs to be 10–15 μm thick as the electrochemistry generally takes place very close to the electrolyte interface [56]: through the separation of current collector and support functions in more advanced designs, the thickness of the fuel electrode can also be reduced from 200 μm to 10-15 μm, decreasing the demand for electrical conductivity.

In conventional Ni-YSZ manufacture, nickel is usually processed as nickel-oxide, allowing to maintain lower production costs and the compatibility with ceramic process routes and temperatures involved [57].

To make the cell electrochemically active it is necessary to reduce the nickel to its metallic form by introducing gradually the fuel. The specific nickel reduction procedure followed for the tests carried out during this project, will be discussed in detail together with the whole experimental procedure.

Nickel reduction can be very fast and the method of initial introduction of the fuel gas together with the morphology and size ration of the Ni/NiO and YSZ powders given by the

manufacturing process, play a very important role in the definition of the future cell performances [58].

The procedure allows to activate the catalyst, as well as to form more cavities enhancing the effectiveness of diffusion phenomena: the reduction of the nickel oxide provides extra porosity to the fuel electrode which undergoes a significant volume reduction. It is very important that the process is gradual and that the ceramic cermet remains structurally stable during this volume change, since any issue compromising the integrity of the supporting ceramic structure would negatively affect cell's future performances or eventually lead to system failure. Figure 1.26 shows a representation of Ni coarsening effects during negative electrode redox cycling [59]: image (a) shows the as-sintered anode before reduction, image (b) the immediate-reduced state, image (c) the coarsening of the Ni particles, that leads to a volumetric growth during re-oxidation (d) causing formation of cracks in the overlying electrolyte.

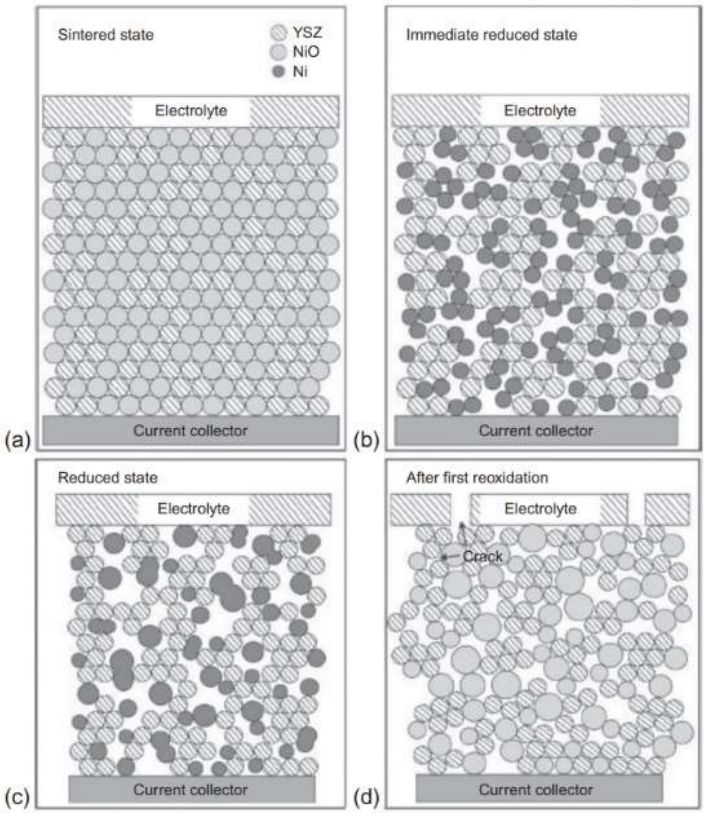

Figure 1.26 - Diagrammatic representation of effects of Ni coarsening during anode redox cycling.

Once nickel is reduced, it is essential to always feed the cell with a fuel that can be oxidized (clean hydrogen is the best choice) otherwise the oxygen in the atmosphere would oxidize nickel back to NiO. This would be relevant particularly if the cell is operated at ambient pressure, allowing the air to easily get in contact with the cell because of any imperfect sealing. If this occurs, there would be a very rapid change in volume in the cermet

microstructure, which can produce cracks leading to leakages, electrodes gas mixing, performance decays and eventually cell or system failure. This phenomenon is of course more significant in anode-supported cells with respect to electrolyte supported ones, given the support function of the electrode exposed to damages [60].

In addition to that, nickel particles have the tendency to coarsen at high temperatures, eventually changing the particle distribution with respect to the YSZ structure (even with the presence of YSZ to minimize this process, it occurs very fast) [61]. This inevitable phenomenon is the most addressed for the cell performance decay, leading to a loss of catalytic surface, electronic-conductive contacts, and porosity obstruction.

Despite many attempts have been made to stabilize this effect, it remains a major weakness in Ni-based anode-supported cells. Significant control systems are required to limit the phenomenon, for instance using purge gases, which would add complexity and cost [62].

The combination of advanced ceramic with non-cermet materials and different production processes opens the way to alternative candidate materials for the fuel electrode that alone would not meet electronic conductivity requirements [63]. In addition to the use of a composite electrode to gain both electronic and ionic conductivity, a small amount of catalyst may be added to the surface of the anode after it has been sintered, via impregnation for instance, to improve the electrode behaviour.

1.2.2.2 LSFNT composite fuel electrode

High operative temperatures are fundamental to achieve good ionic conductivity in the electrolyte and to guarantee a thermodynamic and kinetic advantage, however as solid oxide cells technology is maturing there is an interest in reducing it. To guarantee the commercial spread of such systems, stack elements materials must be cheap, hence target temperatures are below 750 °C.

A fuel electrode support strategy that has been well studied over the last years is the metal-supported cell. In this concept, the mechanical support element is a porous metal on the fuel side of the cell. Both planar and tubular designs have utilized this approach, with the former being more prevalent. State of the art cells are based on either gadolinia-doped ceria or yttria-scandia co-doped zirconia thin electrolyte, aiming to operate in the intermediate temperature regime of 500–750 °C. In particular, the ceria-based systems target the lower temperature range below 600 °C and the zirconia-based systems the higher, up to 700–750 °C. The main advantages of this approach are the reduced materials costs, allowing for instance the use of ferritic stainless steels in the stack interconnect, the improved mechanical robustness and, of course, the high conductivity given by the metal support [64].

Since such technology is still in its early development phase, support literature is not very comprehensive and different research groups are focusing on different materials. Energy Conversion and Storage department of Danmarks Tekniske Universitet (DTU) is very active

in testing new solutions, which in the last years led to the study of the so called LSFNT fuel electrode in collaboration with St. Andrews University [65].

The electrode is composed by a thin layer of site-deficient Lanthanum doped Strontium Titanate ($La_{0.4}Sr_{0.4}Fe_{0.03}Ni_{0.03}Ti_{0.94}O_3$) providing the porous structure in which the electrocatalyst (Ni-CGO) is infiltrated, supported on a porous FeCr structure.

The LSFNT negative electrode is very attractive for metal-supported cells for different reasons: it is easier to process with respect to conventional Ni-YSZ, being more compatible with the supporting metal structure and sintering procedure, and it is more tolerant to redox, coking and sulphur (particularly important if operated with hydrocarbons), enabling higher performances and stability in high steam content atmosphere.

Other options were studied previously with particular interest in perovskite structures: modified $SrTiO_3$ materials have been extensively explored being very stable and having high conductivity ($\sigma > 100\, Scm^{-1}$). LSFNT however became more interesting showing lower processing difficulty as well as better adhesion properties with all the functional layers (support structure, electrolyte and electrocatalyst) and higher ionic and electronic conductivity. In addition, the electrocatalyst coating did not give islandic formations as on $SrTiO_3$, demonstrating to be more suitable for LSFNT.

At DTU Energy three different LSFNT based fuel electrodes were studied, differing by composition: 95% LSFNT – 5% ScYSZ (composition of the fuel electrode of the MSC tested in this project, here referred as A), 55% LSFNT – 40% FeCr – 5% ScYSZ (referred as B) and 20% LSFNT – 60% FeCr – 20% ScYSZ (referred as C). In all of them a percentage of the same material present in the electrolyte (ScYSZ) is present to strengthen the adhesion with this component. In the 95% LSFNT – 5% ScYSZ electrode, electronic conductivity is given by LSFNT while ionic conductivity and electrocatalytic activity are provided by the infiltrated Ni-CGO. Compositions B and C also have FeCr porous structure which gives rise to electronic conductivity, and option C particularly, which has 20% of ScYSZ, is supposed to be the best performing in terms of ionic conductivity.

However, performances reported by Nielsen et al. [65] show that between B and C there is not substantial difference in terms of peak power density and area specific resistance, suggesting that a high percentage of ScYSZ is not useful to enhance conductivity. On the other hand, the porosity of the structure seems to be the most important factor, influencing the amount of electrocatalyst that can be deposited during infiltration cycles and its distribution. Structure A has the densest microstructure, followed by B and C: it is possible to observe in Figure 1.27 [65] that the smaller the dimension of the pores, the more concentrated will be the electrocatalyst (Ni-CGO is in white). A possible explanation is related to capillary forces playing a central role during the infiltration cycle: electrocatalyst concentration increases in water during the evaporation and the capillary forces will drive highly concentrated solution to the smallest pores as the process continues.

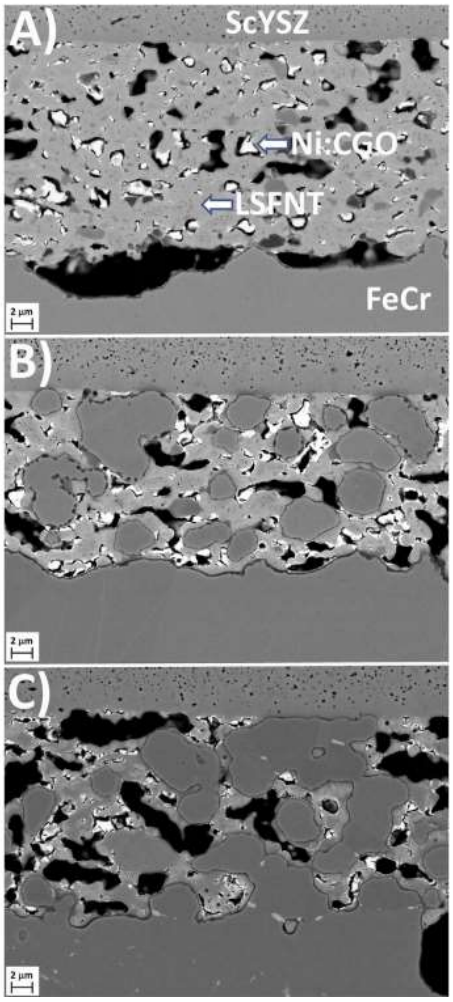

Figure 1.27 - Cross sectional SEM of the three infiltrated backbone fuel electrode compositions (A, B, C) studied by Nielsen et al.

LSFNT strength in adhesion with the metallic support is the presence of exsoluted Fe and Ni nanoparticles, which have high sintering activity and the possibility to inter-diffuse at the interface. On the other hand, from the electrochemical point of view it is not beneficial to have exsoluted Ni and Fe nanoparticles, since a nanostructured electrocatalyst coating is subsequently infiltrated. For that reason, there is a limit in catalyst loading after which agglomeration and undesirable Ni particle growth can occur.

As already said, composition A is the less performing among the three studied by Irvine et al. because of an uneven distribution of the catalyst. Despite that, its performances are good compared with state-of-the-art Ni-YSZ electrodes and considering that LSFNT technology is in an early design stage, margins of optimizations are possible.

1.2.2.3 Implication of hydrocarbon use on fuel electrode

One of the main reasons why solid oxide cells are very interesting is fuel versatility: the high operating temperature allows the oxidation of simple hydrocarbons (particularly methane,

but also butane and decane in more advanced designs) in SOFC mode. However, this makes cell design and material choice more challenging: there are more problems related to impurities, always present in hydrocarbons flows, and to unwanted side reactions that might occur, such as carbon cracking and cooking.

To directly oxidize the species according to the reaction (1.15) without any problem, the electrode material and microstructural design have to be carefully engineered [66]. Research and development are very active on this front but for this project's purpose there is no interest in going too much into details.

$$CH_{4(g)} + 4O^{2-}_{(i)} \rightarrow CO_{2(g)} + 2H_2O + 8e^- \tag{1.15}$$

Hydrocarbon fuels are usually reformed to obtain smaller molecules, ideally CO and H_2 (steam reforming (1.16) and water gas shift (1.17) both occur) that will be easily oxidized by the electrode. The reforming can be external, internal (inside the cells themselves), or both external and internal. The hydrocarbons typically are not reformed with pure steam, but with the addition of small amounts of O_2/air, which partially oxidizing the species helps the process.

$$CH_{4(g)} + 2H_2O_{(g)} \leftrightarrow CO_{(g)} + 3H_{2(g)} \tag{1.16}$$

$$CO_{(g)} + H_2O_{(g)} \leftrightarrow CO_{2(g)} + H_{2(g)} \tag{1.17}$$

Steam reforming is an endothermic process, therefore it can exploit the waste heat from the fuel cell to drive the reaction. Both the CO and H_2 produced from reforming can be used in SOFCs, but the electrode needs to catalyse the oxidation of both CO (1.18) and H_2 (1.19).

$$CO_{(g)} + O^{2-}_{(i)} \leftrightarrow CO_{2(g)} + 2e^- \tag{1.18}$$

$$H_{2(g)} + O^{2-}_{(i)} \leftrightarrow H_2O + 2e^- \tag{1.19}$$

The kinetics of reaction (1.18) are typically more sluggish than the hydrogen oxidation reaction, and often this reaction is bypassed by the faster water–gas shift reaction (1.17). In this case CO reacts with the water coming from the feed or from hydrogen oxidation, to form more H_2, which is then converted in the faster hydrogen oxidation reaction [67]. Therefore, to enhance the kinetic, hydrocarbon fuels are normally introduced with extra water (usually with a minimum steam to carbon ratio of 2) over a steam reforming catalyst, where reactions (1.16) and (1.17) take place [68].

Care needs to be taken in the design and control of the fuel mixture to ensure that the speed of the endothermic reformation reactions does not lead to localized cooling of the inlet of the cell, which could create thermal and mechanical stresses leading to cracking and failure [69].

In addition to that, the reforming reactions also compete with cracking (1.20) and Boudouard (1.21) reactions.

$$CH_{4(g)} \rightleftharpoons C_{(s)} + 2H_{2(g)} \tag{1.20}$$

$$2CO_{(g)} \rightarrow CO_{2(g)} + C_{(s)} \tag{1.21}$$

Although nickel is an excellent hydrogen oxidation and methane steam reforming catalyst, it also catalyses the formation of carbon filaments from hydrocarbons under reducing conditions. The mechanism involves carbon dissolution into the metallic bulk [70], and the precipitation of graphitic carbon from some facet of Ni particles lifting off the surface. Figure 1.28 shows an example [71]. While thermodynamic calculations are often used to predict carbon formation favoured conditions, carbon fibres can be formed even when carbon is not thermodynamically predicted [72]. A sufficient amount of steam has to be present in order to avoid carbon formation on nickel surface [73].

Figure 1.28 - SEM image showing carbon filament with catalyst particle at its end.

One approach to overcome the limitations of nickel-based electrodes with hydrocarbon fuels, is to increase the oxidation activity of Ni/YSZ cermets adding an oxide-based oxidation catalyst. For instance, stable operation on dry methane has been reported at 650 °C in an

SOFC using an yttria-doped ceria interlayer between the YSZ electrolyte and the Ni/YSZ cermet anode. Ceria is a well-known oxidation catalyst and increases the activity of the anode for the electrochemical oxidation in SOFC mode [74]. In addition, it is possible to replace nickel with copper as current collector and in this case ceria acts as primary catalyst promoting the direct oxidation of the fuel. The Cu/Ce O_2/YSZ anode system is particularly interesting and has been shown to be effective for the direct utilisation of a variety of hydrocarbon fuels [75].

External reforming still remains an advantageous route, allowing to use well developed state-of-the-art cells, to control better the reforming process and to avoid solid carbon formation inside the electrode. The actual processes taking place inside solid oxide electrodes fed with hydrocarbons (in SOFC mode) or electrolyzing CO_2 are very complex and yet not very comprehensively explained. R&D is very active on this front, particularly for the highly efficient use of conventional fuels and their production through CO_2 electrolysis.

Sulphur compounds are present in many real-world fuels, either as a natural impurity in biogas, diesel and coal gas, sometimes at significant levels, or introduced as a deliberate additive, for instance as odorants in natural gas supplies for leak detection. Due to the operational temperatures employed in SOFCs, most sulphur compounds will be converted to H_2S by the time they reach either the support or the fuel electrode itself. H_2S would react rapidly with the electrode surface, even at ppm levels, blocking reactions sited for both steam reforming and fuel oxidation, and severely degrading Ni catalyst performances [76].

Exact mechanisms occurring are still under investigation, what is certain is that sulphur-related degradation is often a two-stage process with an instantaneous drop followed by a slower longer-term continuous decay in performances [77]. It is possible to remove the sulphides from the metal surface (which formation is thought to be the main blocking cause [78]), operating a partial recovery, but still the performances will not fully recover and eventually lead to a system failure. The only way to avoid sulphur-related problems is to purify the inlet gas, since materials which can be considered less affected by this problem have not been developed yet, adding complexity to the plant and costs.

1.2.3 Oxygen multi-layer electrode

Desirable features for the oxygen electrode are ionic and electronic conductivity, chemical and mechanical stability, compatibility with other cell components and catalytic activity. The last one in particular is crucial, since oxygen association (or dissociation) requires a relatively high overpotential and is responsible for the major electrochemical energy conversion efficiency loss.

The high temperature of operation allows not to use precious metal catalysts. Historically many types of oxides, such as indium and zinc oxides, have been investigated [79] but, as seen for the other active layers, a single material which satisfies all the requirements does not exist. Several mixed ionic electronic conductors (MIEC) have been developed more recently, with particular focus on fluorite-structured oxides (see electrolyte section) and

perovskites. Among fluorite-structured oxides, gadolinium-doped ceria (or cerium-doped gadolinia, the dopant is the specie with the lower molar fraction), usually referred as CGO or GDC, is particularly interesting and it is present in the tested cells. Regarding perovskite structures, lanthanum-strontium doped cobaltite (LSC) and lanthanum-strontium manganite (LSM) are the two most adopted materials, also present in the tested cells.

1.2.3.1 Perovskite lattice structure and oxygen non-stoichiometry

The perovskite structure is formed by three elements: large cations A^{n+} (with a positive n charge), small cations $B^{(6-n)+}$, and the oxide ions O^{2-}. The general formula is ABO_3, and the elements are ideally arranged to form a cubic lattice, as shown in Figure 1.29 [80]: the $B^{(6-n)+}$ cation is in the center, surrounded by six oxide ions forming an octahedron, whereas A^{n+}cations have twelve oxide-ion coordinates and they form the outer cubic structure.

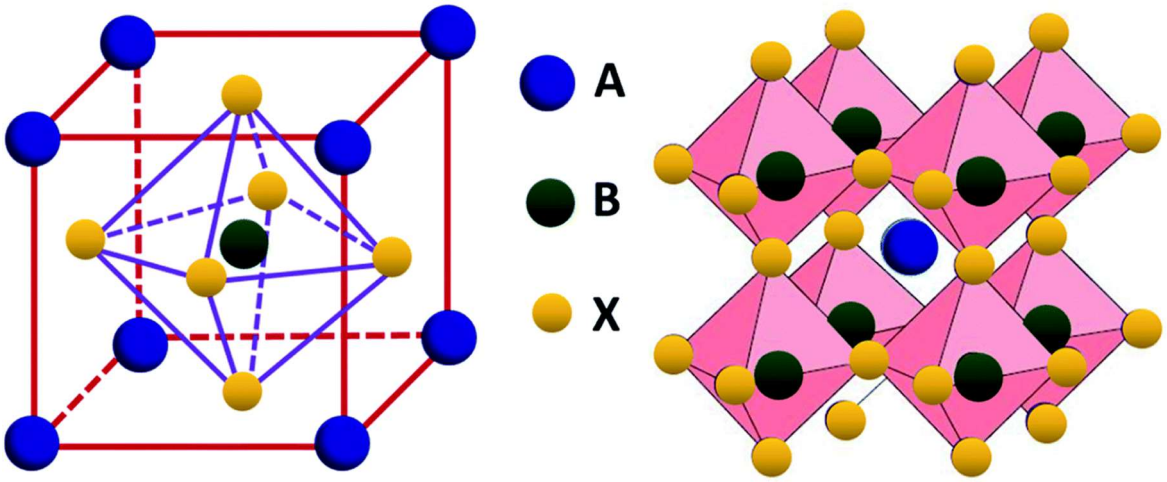

Figure 1.29 – ABO_3 perovskite cubic structure schematic representation. A cations in blue, B cations in black and oxygen ions in yellow.

Cations size determines the presence of orthorhombic or rhombohedral lattice distortions. A way to assess this is through Goldschmidt tolerance factor (1.22), where r_a, r_b and r_o are the effective radii of A, B and O^{2-} ions.

$$t = (r_a + r_o)/\sqrt[2]{r_b + r_o} \tag{1.22}$$

The closer the tolerance factor to one, the higher the probability to have a cubic structure. In addition to that, the temperature determines phase transitions, with the cubic structure generally stable at higher temperatures as seen for the fluorite structure.

The valence state of transition metal in B-site can be changed by doping aliovalent cations in A-site or B-site. For instance, in $LaMO_3$ (M is the transition metal cation), the doping with strontium Sr^{2+} in the La^{3+} A-site increases the average valence number of the M ion in B-site over 3, and the generated positive charge can behave either as a small polaron, for example in LSF (lanthanum strontium ferrite), or as a hole like in LSC [81], [82].

Under reduced oxygen partial pressure, these quasiparticles allow the formation of oxygen vacancies and the properties of B-site cations influence the equilibrium constant of vacancies ($V_O^{\bullet\bullet}$) formation reaction (1.23).

$$O_O + 2h \rightarrow V_O^{\bullet\bullet} + \frac{1}{2}\, O_2 \tag{1.23}$$

Many works attempted to create a model relating oxygen non-stoichiometry to oxygen partial pressure and temperature, to fit experimental data and better understand how all the elements interact in the lattice structure. For this project's purpose it is not considered necessary to go further in detail, however the references for Mizusaki et al. [83] and Lankhorst et al. [84] works are given.

Particularly interesting from the oxygen non-stoichiometry point of view, lanthanum-strontium manganite ($La_{1-x}\, Sr_x MnO_{3-\delta}$), among transition metal perovskites (for instance compared to $La_{1-x}\, Sr_x CoO_{3-\delta}$), presents an oxygen excess region in addition to the oxygen defect one at high oxygen partial pressure, as Figure 1.30 shows [85].

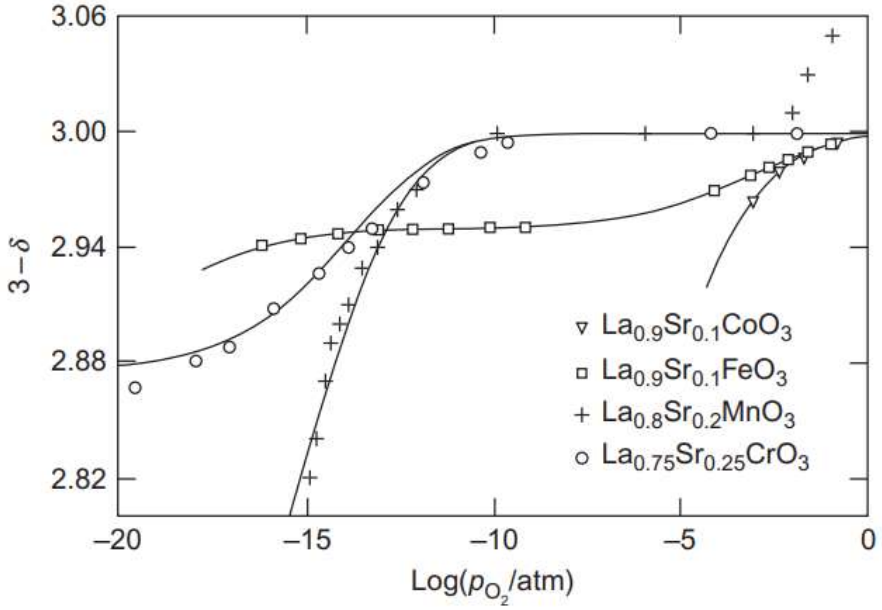

Figure 1.30 - Comparison of oxygen non-stoichiometry dependence on partial pressure for different LSM structures (M is a general transition metal).

Attempts to explain and model the phenomenon are reported in Van Roosmalen and Cordfunke [86], Yokokawa et al. [87] and Mizusaki et al. [88] works. Isothermal dilatometry revealed that oxygen incorporation in the oxygen excess region induces the formation of new crystal lattices, suggesting that the excess is given by cation vacancies formations rather than oxygen interstitials, and this is crucial in defining thermo-chemo-mechanical properties [89].

1.2.3.2 Mixed ionic-electronic conductivity and oxygen transport

Electronic conductivity is given by localized charge carriers in the transition metal ions (Mn, Fe and Co in LSM, LSF and LSC systems respectively, which are common perovskites used as oxygen electrodes) and it is affected by the operating temperature, dopant content and oxygen partial pressure.

All these variables influence the lattice structure: in general in lanthanum-based perovskites the higher the temperature, the content of doping strontium and the oxygen partial pressure, the higher both ionic and electronic conductivity. The temperature allows the transition between semiconductor-conductor behaviours of the material, directly enhancing the energetic level of the electrons in the external shells as well as promoting the stabilization of cubic lattice structure. The presence of strontium, along with a higher oxygen partial pressure, are responsible for lattice deformation and charge localization as previously explained. This general behaviour can be integrated with a much more detailed analysis assessing all microstructural and lattice-energy related changes for different systems [82], [88], [90], not relevant for this project's purpose.

Electrode performances do not rely only on ionic and electronic conductivity but also on mass transport phenomena: gaseous oxygen is adsorbed on the surface of the particles and dissociates in oxide ions, which diffuse through the lattice structure toward the electrolyte.

The match between the different rates of oxygen diffusion, adsorption and transport through the lattice has to be maximized in order to reduce total electrode related losses. A porous structure with a wide surface area enabling the oxygen incorporation reaction is crucial for performances. The lattice structure providing mixed ionic and electronic conductivity allows fast bulk diffusion paths, but this is only possible if oxygen diffusivity is sufficiently high to match the oxygen incorporation reaction rate.

Different research groups assessed oxygen diffusion coefficients in different electrode materials through different techniques, for instance through isotope ${}^{16}_{8}O/{}^{18}_{8}O$ exchange experiment or electrical conductivity relaxation experiment. Kilner et al. [91], Wang et al. [92], and Kudo et al. [93] contributed to a comprehensive understanding of oxygen diffusivity and ionic conductivity in a variety of perovskite materials.

The key aspect to be considered is that a higher oxygen diffusivity enables a thicker portion of the electrode to take part in oxygen adsorption, reducing the overall electrode reaction resistance (in one-dimensional approximation, the reaction resistance decreases with the square root of the diffusion resistance). In addition to that, the diffusivity can be related to

oxygen vacancy concentration (see aforementioned works [83] - [88]) in a sub-stoichiometric oxide (for instance LSC or LSM at moderate oxygen partial pressure – see Figure 1.30) and particularly the two are proportional when vacancy concentration is small (vacancy mobility would be constant).

LSM systems show lower diffusivity, especially at lower temperatures, with respect to cobalt or iron containing perovskites (LSC and LSF), due to smaller vacancy concentration with oxygen diffusion coefficients scattered over one order of magnitude [94]. On the other hand, LSM has a very good electric conductivity and that is why it is sometimes used as thin additional current collector layer.

1.2.3.3 Chemical stability and compatibility with cell components

Transition metals in B-sites (referring to Figure 1.29) are very well established in perovskite structures thanks to the geometrical matching with A-site ions (similar dimensions lead to a tolerance factor (1.22) close to unity).

However, perovskite structures present two main issues: chemical instability at the interface with the zirconia-based electrolytes and thermal expansion mismatch with electrolyte and fuel electrode.

The lanthanum oxide (La_2O_3) present in the lattice structure can react with zirconia (ZrO_2) present in the electrolyte, forming lanthanum zirconate ($La_2Zr_2O_7$) and side products according to the following reactions (M is the transition metal and MO_n is its binary oxide).

$$LaMO_3 + ZrO_2 \rightarrow \frac{1}{2}La_2Zr_2O_7 + MO + \frac{1}{4}O_{2(g)} \tag{1.24}$$

$$LaMO_3 + ZrO_2 \rightarrow \frac{1}{2}La_2Zr_2O_7 + \frac{1}{2}M_2O_3 \tag{1.25}$$

$$LaMO_3 + ZrO_2 + \frac{1}{4}O_{2(g)} \rightarrow \frac{1}{2}La_2Zr_2O_7 + MO_2 \tag{1.26}$$

During fabrication at high temperature, reactions (1.24), (1.25) and (1.26) become important due to the large entropy change, while during operation at lower temperatures, since the electrolyte is an ion conductor, the oxygen potential at the interface between electrolyte and electrode becomes the driving force and determines the rate and severity of the process [95].

Different ways have been explored to mitigate the problem, at first an A-site-deficient lanthanum manganite was studied ($La_{1-x}MnO_3$) since it is not reactive with zirconia, however it also implied an appreciable decay in performances. Composite electrodes of mixed LSM and YSZ, which react during fabrication and then stabilize, showed an improvement, but still not sufficiently to validate it as a good design.

Lanthanum cobaltite ($LaCoO_3$) is predicted to be stable below 900 °C by thermodynamic calculations, but to make it suitable for ionic conductivity strontium doping is necessary (LSC), leading to a high reactivity and to the possibility to form $SrZrO_3$ also at 600 °C.

Both LSM and LSC are not suitable to interface the electrolyte, but they have very interesting performances in terms of mixed ionic and electronic conductivity; to allow their use, more recent studies pointed out the use of a thin ceria-based (CeO_2) protective layer in between the electrode and the positive electrolyte, since ceria has a less acidic nature and hence lower reactivity toward the perovskite. Ceria-based oxygen electrodes (CGO for instance) have been intensively investigated particularly for the use at intermediate and low temperatures, showing very good oxygen ionic conductivity (better than perovskites) because of the fluorite structure, but lower electronic conductivity. CGO is known to be reactive with zirconia at temperatures higher than 1300 K, giving a solid solution less conductive than YSZ, but not dramatically. Such temperature can be reached only during fabrication processes and to avoid that the active layers are sintered separately: after the realization of the fuel electrode and adhesion through sintering with the electrolyte, the CGO barrier layer is deposited together with the oxygen layer and finally the cell would be laminated and sintered again at temperatures lower than 1100 K.

The use of a multi-layer electrode allows to integrate strength and weaknesses of the different materials, allowing better performances. In addition to that, temperature management during fabrication processes is essential to achieve optimal porosity and electrochemical properties.

Another aspect to be taken into account is chemical stability during long term operation: the potential gradient given by the oxide ions flow toward the electrolyte can act also on the cations of the lattice structure. Despite the cations are much less mobile than the oxide ones, during long period of operation the portion of the electrode closer to the electrolyte may alter its structure and the components may separate. This phenomenon, called *kinetic decomposition* or *kinetic de-mixing,* is inevitable, irreversible and leads to a decrease in performances. Different materials with different cations have different behaviours: LSC shows more stability over long periods than LSM, for that reason is the best one to be applied closer to the CGO barrier layer. On the other hand LSM has higher electronic conductivity, for that reason it may be used as additional current collector layer, realized with bigger pores allowing the oxygen to diffuse and be adsorbed mainly in the LSC structure. An example is reported in Figure 1.31.

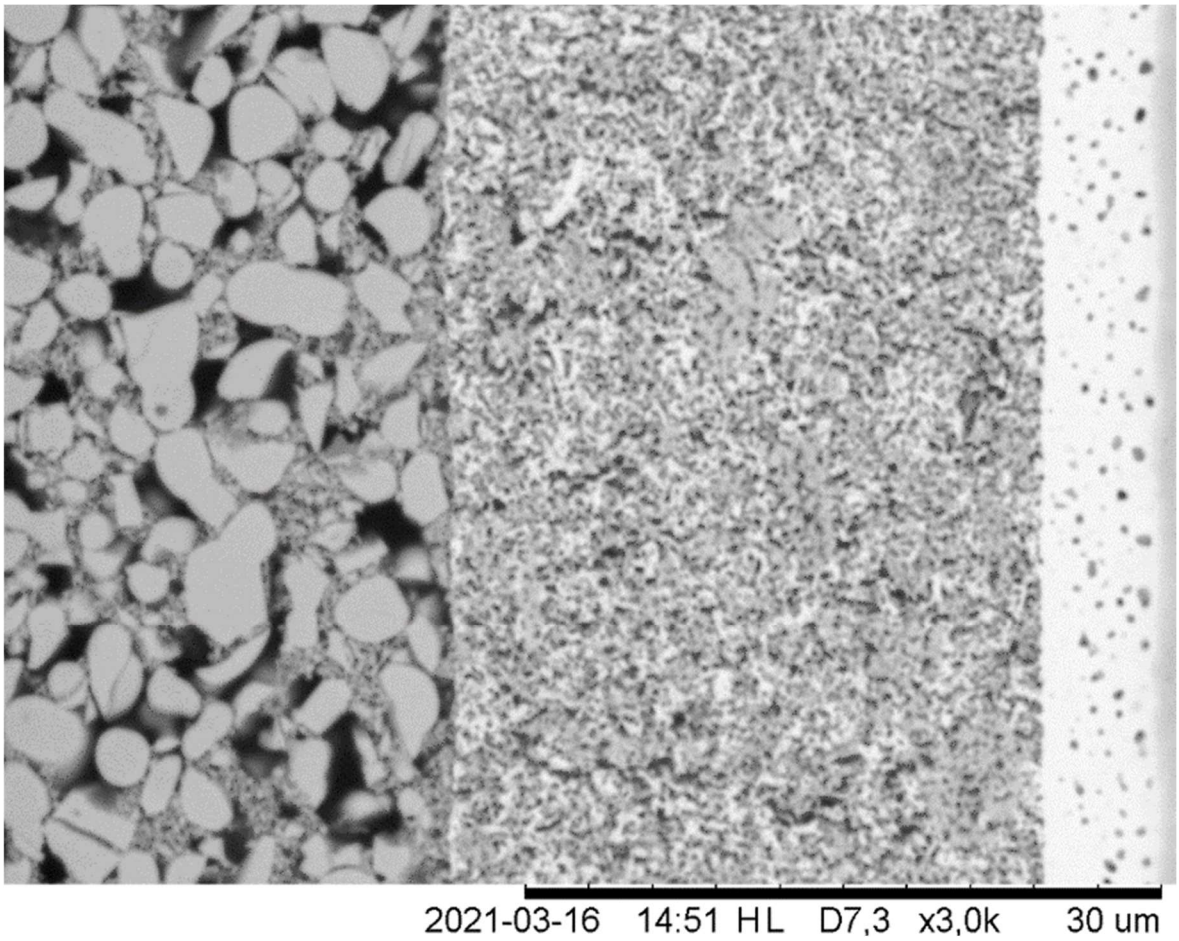

Figure 1.31 - SEM microscopy of LSC-CGO composite oxygen electrode. From left to right: LSM current collector layer, LSC-CGO composite electrode layer and compact CGO barrier layer.

Thermal expansion coefficients mismatch between the electrode and the other cell components is important to be minimized in order not to mechanically stress the cell. The electrolyte in particular is very delicate and cracks may easily form, leading to gas leakages, changes in feed composition and performance decay.

The oxygen electrode is composed by different materials having different expansion coefficients with respect to the electrolyte, in addition to that also the different lattice structure plays a role in the thermal mismatch-associated problems. The perovskite structure has a higher expansion coefficient than the fluorite one due to a more important deformation related to oxygen vacancies formation. The process is also enhanced by higher temperatures, which increase the ionic conductivity.

Different solutions have been studied and the most remarkable ones are two, both implying the integration of the properties of perovskite and fluorite structure. As shown in Figure 1.32 [96], the first one is the realization of a porous CGO backbone support structure, in which LSC is subsequently infiltrated through aqueous solutions; the second one is the realization of a composite LSC-CGO electrode by screen printing a mixture of the two powders (solution adopted in the oxygen electrodes of the tested cells – see Figure 1.31).

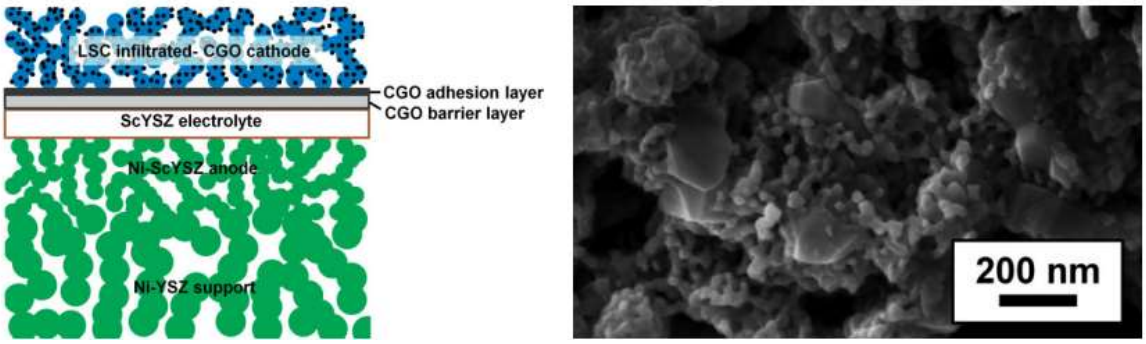

Figure 1.32 - On the left, schematic representation of a Ni-YSZ supported solid oxide cell with LSC infiltrated-CGO oxygen electrode. On the right, microscopy image of the oxygen electrode cross section.

A composite LSC-CGO electrode (realized through tape casting and acquous infilitration) has lower performances in terms of mixed ionic-electronic conductivity with respect to the pure LSC, but the loss is payed back by a more stable system that allows operation for a longer period.

Aqueous infiltration offers several advantages with respect to the more conventional fabrication techniques: the size of the electrocatalyst can be controlled through heat treatment and atmosphere; cell sintering profile can be optimized with more freedom; infiltration helps to reduce the thermal expansion mismatch between the conventional MIEC used as oxygen electrodes (typically above $15 \cdot 10^{-6}\ K^{-1}$) and the other layers (in range $10 - 12 \cdot 10^{-6}\ K^{-1}$), it helps to control the catalyst load and concentration very carefully at the same time, and finally it is a fast process. The number of infiltration cycles, as well as heat treatment temperature, determines different interactions phenomena affecting performances between the backbone structure and the electrocatalyst phase. A first insight has been given by the work of Samson et al. [96] from the Department of Energy Conversion and Storage of DTU, and further research is expected.

Compatibility of the oxygen electrode with the interconnects is also important. Many alloys have been investigated as metallic interconnects and almost all of them contain chromium, which forms the protective oxide scale. Chromium containing species easily react with other oxides. Chromium poisoning strongly depends on the combination of active layer materials. The most severe degradation was observed in LSM/YSZ systems. In pure LSM lattice structure the oxide ion diffusivity is low, and the oxygen potential appears exclusively in proximity of the triple phase boundaries. The electrochemical gradient generates a driving force for chromium-containing species, which attack the active sites and give rise to a performance decay. Other systems such as LSCF have a more delocalized active sites distribution, and the degradation can be less severe since the deposition on one site can be compensated by the activation of another site. The temperature influences the content of chromium that can be found in the electrode, but the degradation was observed to be more severe at low temperatures and in presence of water vapour [97].

To avoid reactions with Cr-containing species in the active layer, the oxygen electrode can be coated with dense electrically conductive oxides (LSM for instance), which would act primarily as Cr-getters and current collectors.

Chapter 2
Methodology for electrochemical characterization

The main tools to characterize electrochemical devices used in this project are polarization curves – also referred to as i-V curves – and Electrochemical Impedance Spectroscopy (EIS). In this section their meaning and interpretation will be analysed, focusing on solid oxides cells particular features, along with other useful parameters to compare operative conditions (steam utilization) and performances (electric efficiency).

2.1.1 Polarization curves

Polarization curves show the electric energy, in terms of potential difference between the two sides of the cell, associated to a specific current that can be produced or absorbed during fuel cell or electrolysis operation mode respectively. An example of polarization curve in electrolysis is showed in Figure 2.1.

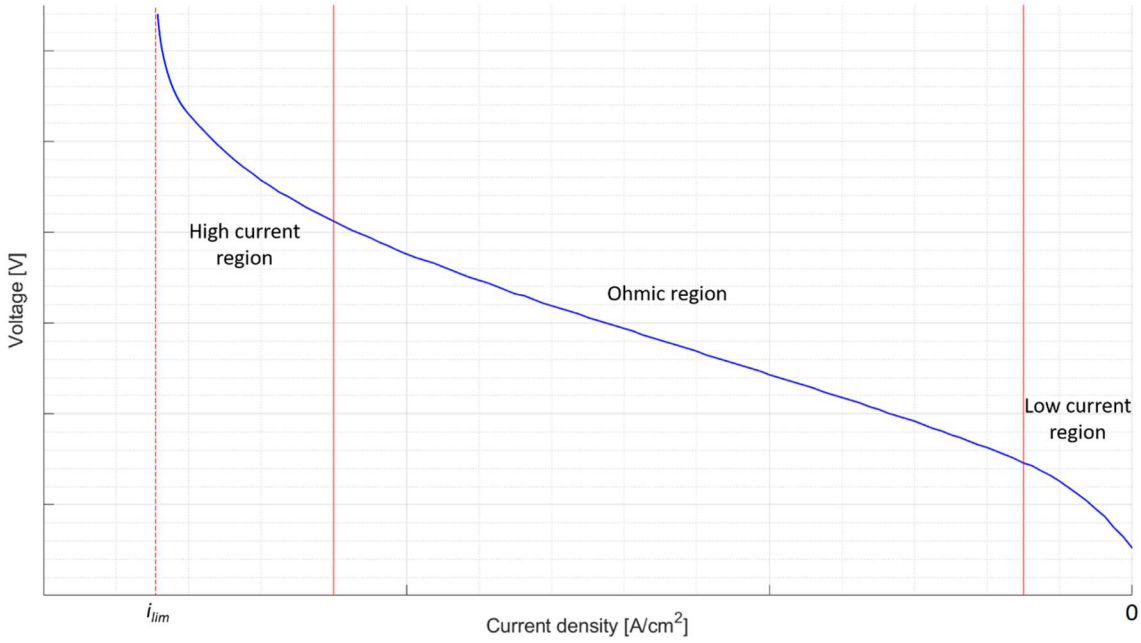

Figure 2.1 - Example of polarization curve in electrolysis mode.

This particular shape is the result of losses occurring in the cell when equilibrium conditions do not apply, hence when current is flowing. The losses can be simply divided in three contributions, related to negative electrode, electrolyte and positive electrode. The loss given by the electrolyte has ohmic nature, while the losses associated to the electrodes account both for activation of the reactions and concentration of the reactants at the triple phase boundary. The polarization curve can be typically divided in three sections: at low current density activation phenomena give the main losses contribution, the central region can be referred to as ohmic region because of the linearity of the curve and a non-linear part at higher current density which is associated to the limitations given by reactant concentration. Different operating conditions imply a change in the range of current densities related to the three regions.

Important information that can be extracted from such curves are the value of measured Open Circuit Voltage (OCV) and the Area Specific Resistance (ASR). The OCV is the voltage measured at zero current and gives information about data reliability if compared to the theoretical value calculated from Nernst equation, which computing procedure is presented in Appendix A. Such deviations give an indication of any unexpected operating temperature or feed gas composition changes, which can be caused by leakages of different nature (for instance gas supply unit problems, imperfect sealing in the test set-up and cracks in the cell). The accepted OCV deviation between measured value and the theoretical one is about 10 mV, based on past experimental observation, which accounts for non-idealities of the system as well as small differences in temperature and feed composition with respect to the nominal ones.

The ASR is an important parameter used to assess cell performances. It represents the total cell's resistance (expressed in Ωcm^2) including all the different voltage loss contributions, and it is measured in the i-V plane as the slope of the polarization curve at a specific current. The ASR can be computed as the derivative of the i-V curve at the current of interest, as shown in equation (2.1).

$$ASR = \frac{dV}{di} \tag{2.1}$$

Reactant starvation is a condition that occurs when the electric current, supplied in SOEC mode or drained in SOFC mode, is close to the physical conversion limit imposed by the amount of fed reactant. Indeed, flow rate of reactant and current are related according to Faraday's law (2.2).

$$I = n_i \, F \, \dot{N}_i \tag{2.2}$$

Where:

_ $I\ [A]$ is the electric current;

_ $n_i \left[\frac{mol_{e^-}}{mol_i}\right]$ are the moles of electrons involved in the reaction per mole of component i;

_ $F = 96485\ \frac{C}{mol_{e^-}}$ is the Faraday's constant;

_ $\dot{N}_i \left[\frac{mol_i}{s}\right]$ is the molar flow rate of the component i.

In the i-V plane reactant starvation can be visualized as an important change of the curve's slope increasing the current (absolute value), which tends to the asymptote set by the so-called limit current density. In case of electrolysis operation, it is common to talk about steam starvation, being H_2O the reactant.

Moreover, from polarization curves data it is possible to obtain the power curve, where power density can be simply computed as product between voltage and current density.

2.1.2 Electrochemical impedance spectroscopy

The Electrochemical Impedance Spectroscopy (EIS) is a tool used to measure the impedance of a system, which depends on the AC frequency. Working in steady state all the different phenomena occurring inside an electrochemical cell cannot be differentiated, because they overlap and contribute to the total resistance of the system. Instead, analysing the cell in AC regime, these phenomena can be distinguished: faster ones, for instance the movement of charged species, are observable at high frequencies, where the slower ones, like temperature effects related to heat losses, would not be spotted.

Frequency response analysis can be interpreted considering that ohmic phenomena are the fastest, occurring at very high frequencies, they are followed by kinetic ones, spotted at medium frequencies, and by mass transport related phenomena identified at the lowest frequencies.

In general, EIS is performed as follows:

1. The cell is operated in steady state condition, i.e. constant current density (can be zero or not) and voltage.
2. Over this steady state a very small sinusoidal current density (i_{AC}) with frequency f is applied.
3. The voltage response (ΔV_{AC}) is measured; it is a sinusoidal wave with same frequency f and a phase shift with respect to i_{AC} (the response is pseudo-linear because the oscillation is very small, so the frequency does not change). Figure 2.2 shows how the current density and voltage trends appear.

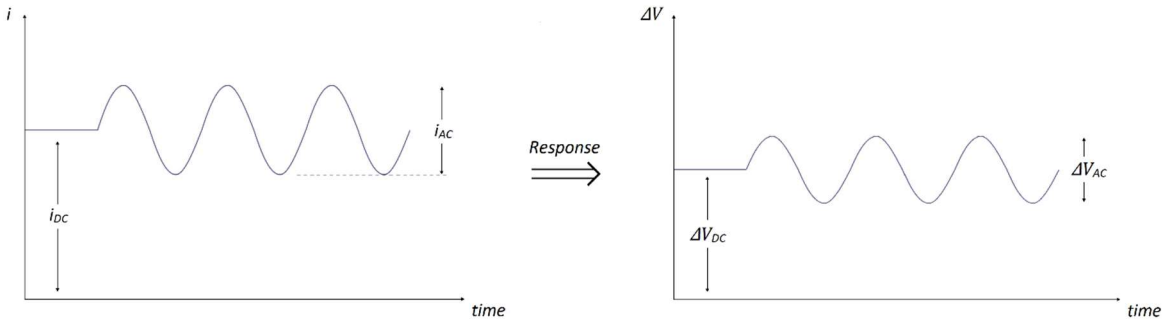

Figure 2.2 - Current and voltage response during EIS.

4. The impedance (complex number) is computed as

$$\bar{Z}(f) = \frac{\overline{\Delta V}_{AC}(f)}{\bar{\imath}_{AC}(f)} = Z_{Re} + i\, Z_{Im} \tag{2.3}$$

5. The voltage measurement and the impedance calculation are repeated with different values of f, in order to obtain a spectrum of impedances.

From the impedance spectrum two main information can be obtained, plotting the so called Bode plots: Real/Imaginary impedance vs Frequency. The imaginary part of the impedance results negative, because the cell behaviour is mostly capacitive, so in the vertical axis is reported the opposite of Z_{Im}.

- In the imaginary impedance plot each peak is associated to a certain physical phenomenon.
- In the real impedance plot, the ohmic resistance (lowest value, at high frequency) and the ASR (highest value, at low frequency) can be extracted.

Figure 2.3 shows an example.

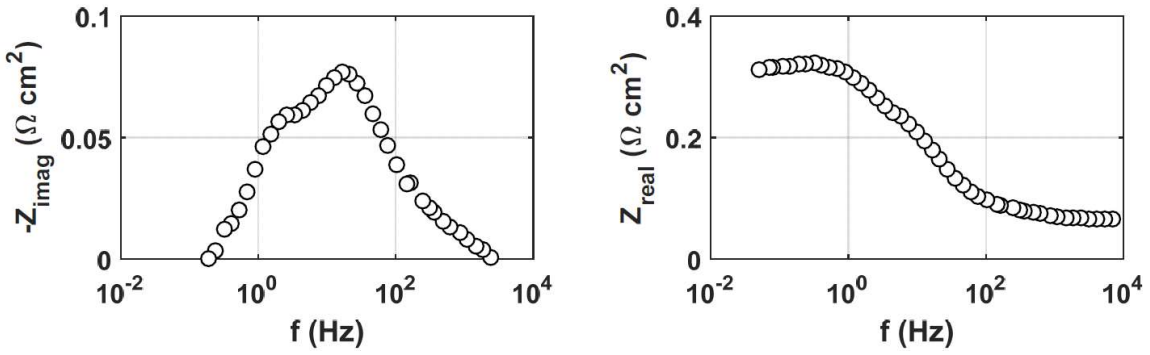

Figure 2.3 - Example of Bode plots.

This two information can be summarized through the Nyquist plot: Real impedance vs Imaginary impedance. Here every point represents a measurement performed at a different frequency. Figure 2.4 shows an example.

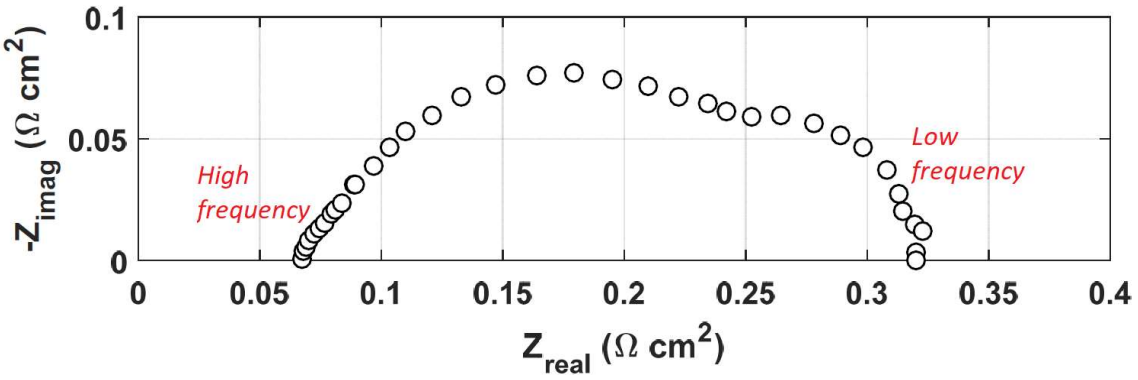

Figure 2.4 - Example of Nyquist plot.

EIS takes into account all contributions of phenomena of different nature occurring in all the layers, and different studies that can be found in the literature model each particular process with a semicircle which peak is at a specific frequency. The overlapping of such semicircles can generate different shapes in the Nyquist plot, spotted by changing layers materials and operative conditions (for instance temperature, feed compositions and current density).

It was decided not to adopt any model to analyse the EIS curves, but only to distinguish ohmic and polarization contributions; the already mentioned ASR is their sum. This simple approach does not allow to separate all the contributions of the different phenomena. Anyway, analysing the Bode plots it is possible to assess which specific frequency ranges are related to processes occurring in a particular layer.

Particularly, EIS data can be interpreted by comparing the imaginary part of Bode plots while changing the operative conditions: peaks in the curves obtained as differences of two imaginary impedances recorded at different conditions help identifying which part of the frequency spectrum is related to the active layer more affected by such parameter change. For instance, the differences between different steam-to-hydrogen ratios would help to identify which frequencies are related to phenomena occurring at the negative electrode, as well as give information about which feed produces a lower imaginary impedance. It is important to take into account that a higher current, at which EIS is performed, slightly shifts peak related to different phenomena to lower frequencies.

Figure 2.5 shows how ohmic and polarization resistances are extracted from Nyquist plot.

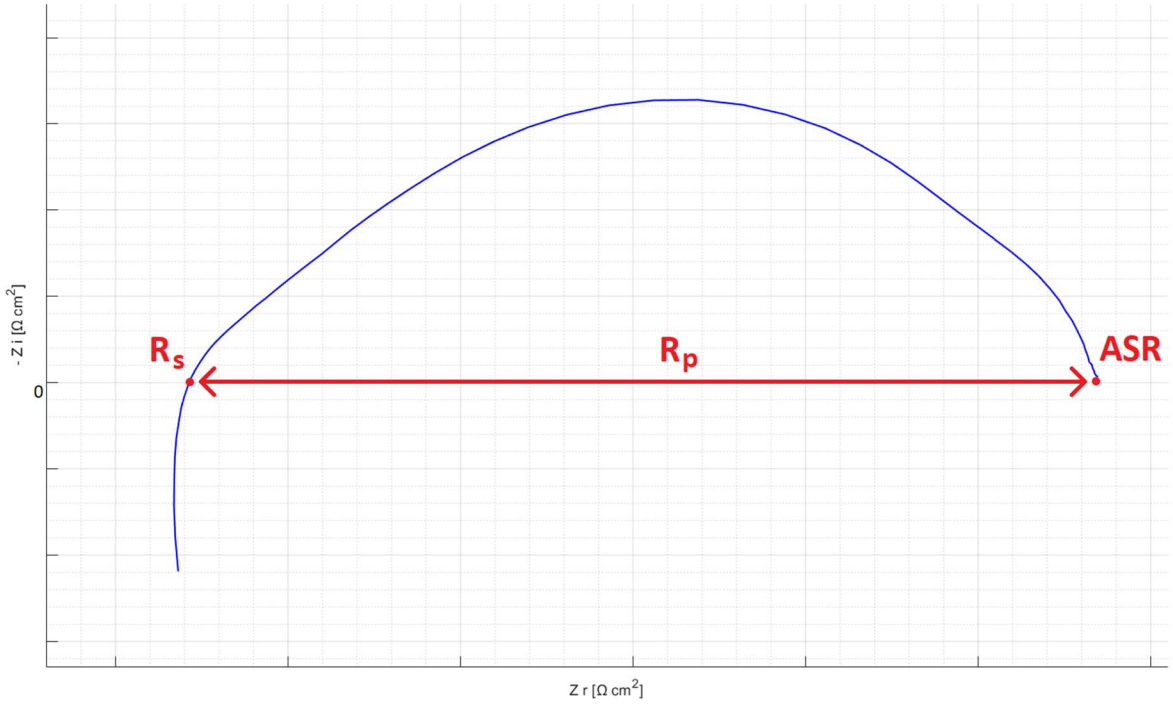

Figure 2.5 – Resistances contribution interpretation from EIS.

The ohmic resistance (resistance to conduction of ions in the electrolyte, conduction of electrons in the electrode and contact resistances), also referred to as serial resistance (R_s), corresponds to the real impedance recorded at very high frequency. It can be considered either the point of the curve at the highest frequency or the one corresponding to a null imaginary part. The difference between these two approaches is almost negligible and for this project it has been chosen to follow the second way.

The ASR, as already anticipated, corresponds to the derivative of the i-V curve at a chosen DC current. This can be explained observing that during the EIS, at low frequency the current, and as a consequence the voltage, oscillates slowly. Consequently, this operating regime can be approximated as a sequence of steady states: the current and voltage change very slowly, simply moving along the polarization curve. In this case the impedance, computed as in equation (2.3), at very low frequencies can be approximated as the ratio between the voltage and the current changes (non-complex values), and since the oscillations are small this ratio can be furtherly approximated as the derivative of the polarization curve (see Figure 2.6).

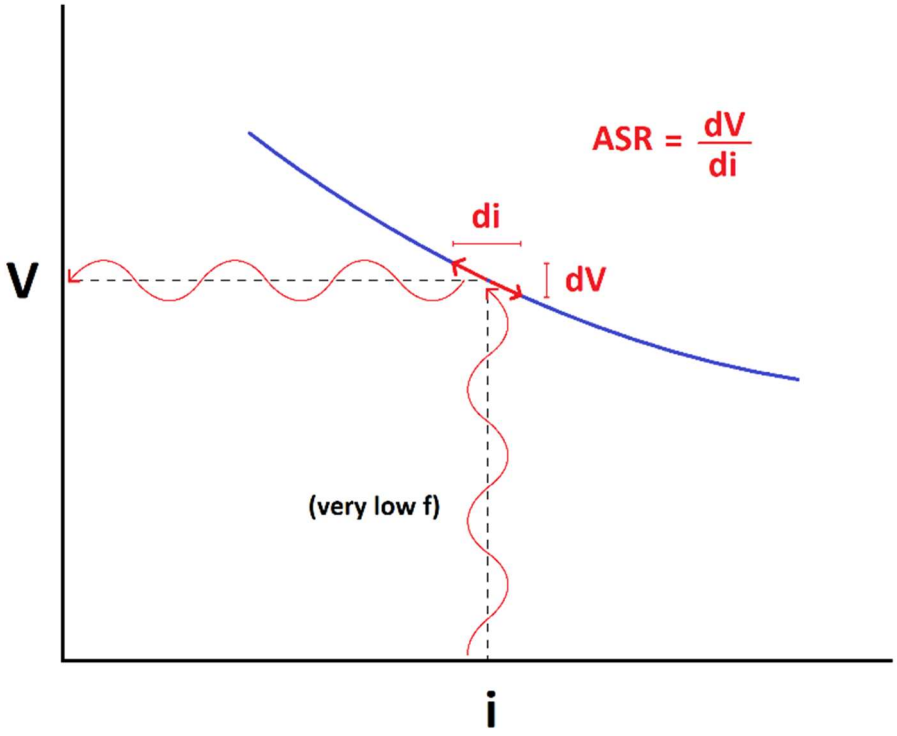

Figure 2.6 - Definition of ASR from i-V curve.

The dependency of ASR on current density must be taken into account especially if a performance comparison is done between polarization curves with different shapes. An example can be observed in Figure 2.7.

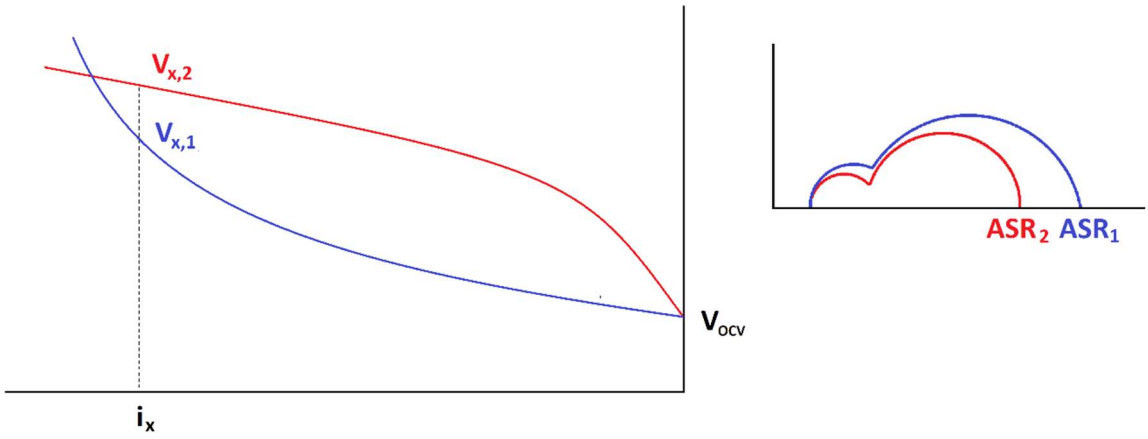

Figure 2.7 - Different Nyquist plot depending on i-V curve's shape.

Here the blue polarization curve is representative of a better performing electrolysis cell, since at same current densities the needed voltage is lower with respect to the red curve. Anyway, if an impedance spectroscopy is performed at high current (here simply called i_x), the Nyquist plot would display a different outcome: the ASR of the red curve would result

lower than the ASR of the blue curve, indicating that at this high current density the cell represented by the red curve is the best one. This is partly true, but just in terms of resistance, while considering the voltage the blue curve remains better than the red one.

This simple example allows to understand the importance of a careful interpretation of the results. To characterize the cells in neutral conditions by means of a meaningful ASR value, for this project it was decided to record the EIS at OCV.

2.1.3 Steam utilization

The fuel utilization is a parameter used to quantify the amount of reactant fed to the cell that is actually converted by the electrochemical reaction. In the electrolysis case, it is more reasonable to talk about steam utilization (SU). It is defined as the ratio between the amount of water converted into hydrogen and the total amount of water fed to the negative electrode (2.4).

$$SU = \frac{\dot{V}_{H_2O,converted}}{\dot{V}_{H_2O,fed}} \tag{2.4}$$

The volume flow rate (measured in normal cubic meters) of steam fed to the cell can be found with equation (3.9) that will be presented in Chapter 3, while the volume flow rate of steam that actually participate to the reaction can be found from Faraday's law, expressed in equation (2.2).

Knowing the current, it is possible to obtain the molar flow rate of steam consumed. It can be simply converted in volume flow rate assuming that the steam behaves as an ideal gas and knowing that 1 normal cubic meter contains 44.618 moles of an ideal gas.

With the values of current adopted in electrolysis mode in this project, the amount of converted water results always lower than the total amount supplied, with all the several fuel mixture compositions. This means that the steam utilization is always lower than unity, or in other words that the cell is never operated close to starving conditions.

2.1.4 Electric efficiency

Efficiency is defined as useful output divided by the needed expense. In case of water electrolysis the useful product is hydrogen and, since water splitting is an endothermic reaction, as explained in section 1.1.3.3, the expense consists both in electric energy and heat. The efficiency then can be expressed as in equation (2.5).

$$\eta_{el} = \frac{H_2\ heating\ value}{Electric\ power + Heat} \tag{2.5}$$

The thermoneutral voltage for splitting liquid water is about 1.47 V, and practical PEM and alkaline electrolysis cells usually operate above it, in the range of 1.6-2 V [98]. Consequently, in realistic PEM and alkaline electrolyzers, the extra heat generated due to internal losses typically covers the heat requirement and the efficiency can simply be computed considering electricity as input.

In case of SOECs the things are different because they operate at high temperatures with steam, so the thermodynamics is significantly different. The thermoneutral voltage for steam electrolysis is about 1.29 V, and it is very likely that a SOEC operates below it, thanks to the very good thermodynamics and kinetics due to the high temperature. In this case the heat requirement must be supplied by an external source and it should be considered in the efficiency calculation, since it is part of the total energy input. This is also the case of the cells analysed in this project, since during the characterizations they have been operated almost always below 1.29 V, being the maximum limit for i-V curves recording set at 1.3 V.

The total energy input (ΔH) needed by the cell can be expressed in volts with the thermoneutral voltage, using equation (1.5). The efficiency in this case becomes:

$$\eta_{el} = \frac{LHV_{H_2}}{\Delta H} = \frac{LHV_{H_2}}{2FE_{t.n.}} \tag{2.6}$$

Computing the efficiency in this way would give a result independent on the cell or on the operating point, since all the terms in equation (2.6) are known constants. Using different cells operated at different operating conditions and different currents, the shares of absorbed electricity and supplied heat would change, but the total energy given as input to the cell would be the same.

For this analysis, in order to have an efficiency representative of the specific performances of each cell, it has been evaluated as ratio between the energy stored in the obtained hydrogen and the electricity absorbed (2.7). In this way just the conversion electricity-to-hydrogen is considered.

$$\eta_{el} = \frac{H_2 \text{ energy}}{Electric\ energy} \tag{2.7}$$

The efficiencies calculated with this approach using the data obtained during fingerprints will result higher than 100%, because the voltage is lower than the thermoneutral value and heat is not considered. Instead, the efficiencies calculated in durability tests conditions will have more reasonable values, since the only energy input comes from the electricity, being the cell voltage always above the thermoneutral value.

The chemical energy contained in hydrogen can be found simply multiplying its lower heating value by the amount of gas produced. Instead the electric power can be calculated as

the product between the cell voltage and the current, which can be expressed with the Faraday law (2.2). The expression for the electric efficiency can be then developed as shown in equation (2.8)

$$\eta_{el} = \frac{\dot{N}_{H_2}\,\mathrm{LHV}_{H_2}}{2\,F\,\dot{N}_{H_2}\,V_{cell}} = \frac{\mathrm{LHV}_{H_2}}{2\,F\,V_{cell}} \tag{2.8}$$

Where:

_ $\dot{N}_{H_2}\left[\frac{mol}{s}\right]$ is the molar flow rate of hydrogen produced by the cell;

_ LHV_{H_2} is the hydrogen lower heating value, equal to 119.96 MJ/kg [99], that converted in molar basis is 239920 J/mol;

_ $F = 96485\ \frac{C}{mol_{e^-}}$ is the Faraday's constant;

_ V_{cell} is the cell voltage.

Chapter 3
Experimental activity

The following chapter is dedicated to a detailed description of the experimental activity. Firstly, the cells used for this project will be described focusing on their structures, dimensions and production processes. Both ceramic and metal-supported cells were available for testing at DTU Energy laboratory, their realization was not part of this work but it is described for sake of completeness, together with the devices used to perform the tests. The procedure followed for assembling the cells test-house and installing it in the test station is then defined, and in the end tests structure as well as microscopy investigation steps will be presented.

3.1 Tested cells

The electrochemical cells that have been operated for this study are solid oxide cells manufactured at DTU Risø National Laboratory. First, two nominally identical ceramic-supported cells were tested: one was used as a reference cell, so it was only exposed to initial reduction; the other one instead went through initial and final performance characterizations, before and after long-term durability test. Then, two metal-supported cells were tested in the same way: initial characterization, durability test, final characterization. Figure 3.1 shows how the two kinds of cells look before being tested.

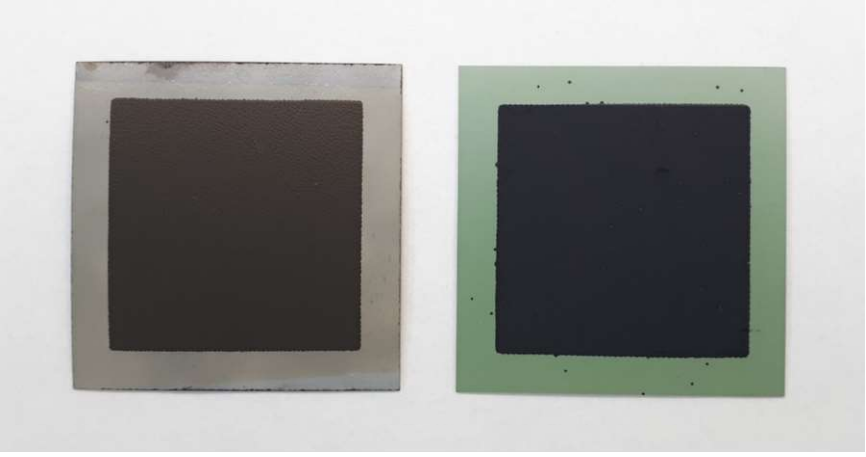

Figure 3.1 - On the left, tested metal-supported cell; on the right; tested ceramic-supported cell.

3.1.1 Ceramic-supported cells

The first tests were performed with the state-of-the-art ceramic-supported cell. The support consists in a ceramic structure which is also an active layer..

The planar cell consists of:

- A cermet fuel electrode, made of a ~300 µm thick Ni-YSZ porous mechanical support, with a percentage of doping Y_2O_3 in the ZrO_2 structure equal to 3%mol, and a ~20 µm thick Ni-YSZ active layer, denser than the support, with a percentage of doping Y_2O_3 equal to 8%mol. Ni has been mixed with YSZ (Yttria Stabilized Zirconia) to form the slurry before tape casting, in form of nickel oxide. This allows simpler compatibility with the ceramic process routes and temperatures involved in the formation of the cell layers [100]. NiO has to be reduced to its metallic form before the operation;
- A ~10 µm thick YSZ electrolyte, with a percentage of doping Y_2O_3 equal to 8%mol;
- A ~5 µm thick $Ce_{0.9}Gd_{0.1}O_{1.95}$ (CGO, Gadolinium-doped ceria) inter diffusion barrier layer, made by screen printing;
- A ~25 µm thick composite $La_{0.6}Sr_{0.4}Co_{1.05}O_{3-\delta}$ (LSC, Lanthanum Strontium Cobaltite) - CGO oxygen electrode (the LSC/CGO weight ratio is 40/60);
- A ~20 µm $La_{0.8}Sr_{0.2}MnO_3$ (LSM, Lanthanum Strontium Manganite) current collector.

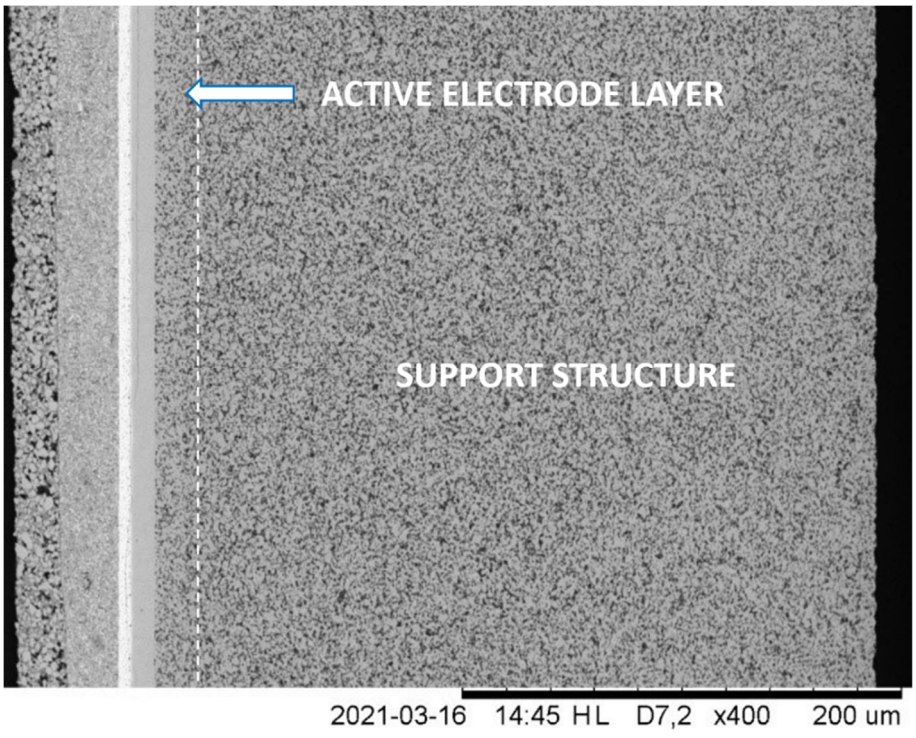

Figure 3.2 - SEM microscopy of the LSC-CGO cell; from left to right: LSM current collector, LSC-CGO oxygen electrode, CGO barrier layer, YSZ electrolyte, Ni-YSZ active fuel electrode, Ni-YSZ mechanical support.

The cell area is 5.3 x 5.3 cm^2, with an active electrode area of 4 x 4 cm^2, hence 16 cm^2 (Figure 3.3) and its total thickness is ca. 380 μm.

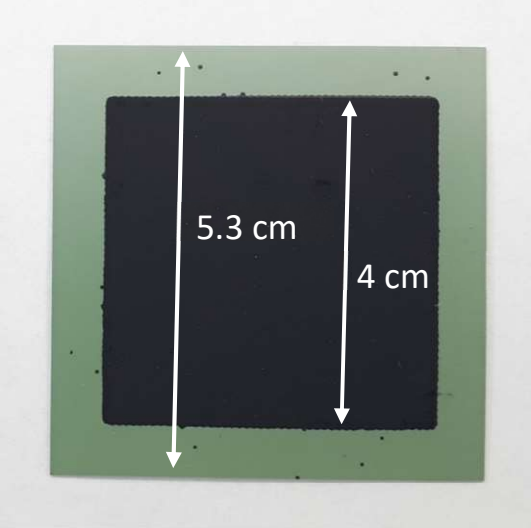

Figure 3.3 - Cell dimensions.

The production starts by tape casting the support layer of the fuel electrode. Tape casting, schematically shown in Figure 3.4, is a technique to produce thin ceramic sheets from ceramic slurry that is casted in a thin layer onto a flat surface and then dried and sintered.

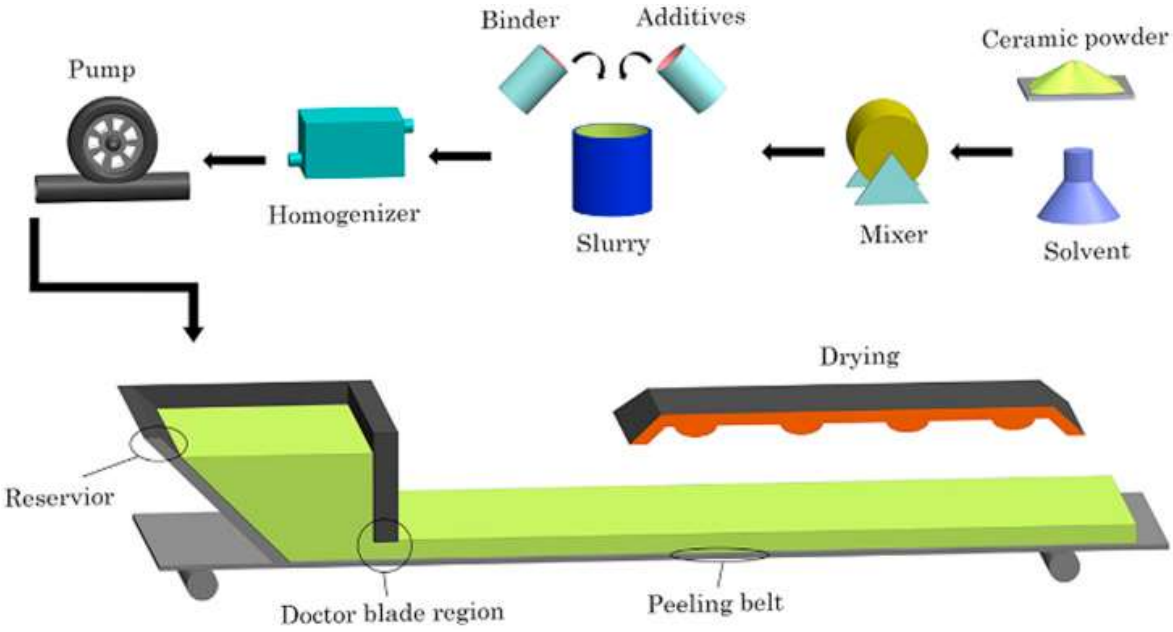

Figure 3.4 - Schematic diagram showing the tape casting process.

Afterwards, the active fuel electrode is tape casted as well. The Ni-oxides will be reduced to their metallic form before operation, as explained in sub-section 3.4.1. The electrolyte and the CGO barrier are then tape-casted over the other layers.

At this point the half-cell is laminated and sintered, in order to obtain a more compact and bonded structure. Lamination is the process of manufacturing a material from multiple layers using heat and pressure, so that the composite material achieves improved strength, stability and other properties [101]. Instead, sintering is the process of compacting and forming a solid mass of material through heat, without melting it to the point of liquefaction; the atoms in the material diffuse across the boundaries of the particles, fusing the particles together and creating one solid piece [102]. This process also allows to form pores thanks to the presence of pore-formers in the slurry.

The oxygen electrode is realized by screen printing a mixture of 40% LSC and 60% CGO on top of the half-cell and sintering the whole cell. LSC provides the required electric conductivity, while CGO provides ionic conductivity (and also a small contribution in electric conductivity). Moreover, since LSC and CGO have different thermal expansion coefficients, an electrode made of just LSC would expand in a different way respect to the CGO barrier layer, causing mechanical stresses inside the cell; the use of this composite material allows to have a thermal coefficient of the oxygen electrode more similar to the one of the barrier layer, solving this problem.

Finally, the LSM current collector is screen printed over the oxygen electrode. It works as an extra contact layer with the function of improving the capture of the electrons, since the CGO present in the electrode is not a very good electric conductor.

3.1.2 Metal-supported cells

As explained in paragraph 2.2.2.2, DTU Energy has developed during years different types of metal supported cells based on LSFNT fuel electrode. The cell that has been tested for this project is the one with composition equal to 95% LSFNT / 5% Sc-YSZ. Despite this is the less performing cell (at least in fuel cell mode) among the ones produced at DTU, the choice of using it for this study came from the fact that it is the less expensive and the easiest to be produced. The manufacturing at Risø National Laboratory was slowed down by the Covid situation and the MSCs available in the laboratory were very limited in number, so the pragmatic decision of select the less valuable cell was taken. Anyway, the test performed with this cell was the first of its kind, so the results obtained from it are still noteworthy.

As the LSC-CGO cell, the used LSFNT-MSC is a planar cell with a total section of 5.3 x 5.3 cm^2, an active area of 16 cm^2 and a total thickness of ca. 395 μm, structured as follows:

- a ~335 μm thick metal support made of a ferritic stainless-steel alloy ($Fe_{22}Cr$);
- a ~20 μm thick fuel electrode backbone layer, comprising of an electronically conducting ceramic component ($La_{0.4}Sr_{0.4}Fe_{0.03}Ni_{0.03}Ti_{0.94}O_3$, LSFNT) and various vol.% of FeCr and ScYSZ particles;

- a ~12 µm thick electrolyte based on ZrO_2 co-doped with Sc_2O_3 and Y_2O_3 (from here on referred to as ScYSZ);
- a ~1.5 µm thick $Ce_{0.9}Gd_{0.1}O_{1.95}$ (CGO) barrier layer to prevent inter-diffusion and reactions between electrolyte and oxygen electrode;
- a ~25 µm thick $(La_{0.6}Sr_{0.4})_{0.99}CoO_{3-\delta}$ (LSC) oxygen electrode.

The metal support and the fuel electrode layer were tape casted individually and then laminated, together with the tape casted electrolyte layer. The tape casting slurries consisted of, besides the metal and/or ceramic powders, an organic system containing solvent, binder, plasticizer and other additives (such as pore formers) needed for the fabrication of porous dense layers. The LSFNT material was fabricated with solid state route and supplied by the company *KCERACELL*. The laminated layers comprising the half cell (metal support, anode backbone layer, and electrolyte) were air de-bonded to remove the organics from the tapes. The de-bonding step was followed by a co-sintering step, using a proprietary procedure, above 1100 °C in a reducing atmosphere (H_2/Ar) [65].
Subsequently, in order to enhance its catalytic activity, the anode backbone was infiltrated with aqueous metal nitrates of Ni, Ce and Gd to form the Ni-CGO electro catalyst upon subsequent heat treatment. The ratio of Ni to CGO was 10:90 by weight. After three cycles of infiltration, the electro catalyst loading was 0.008–0.010 g/cm^2 resulting in ca. 0.8–1.0 mg/cm^2 of Ni [24]. Figure 3.5 shows the layers and microstructures of the second cell after the tests. The small gap between CGO and LSC layers is attributed to current collector detach and polishing procedures for microscopy sample preparation.

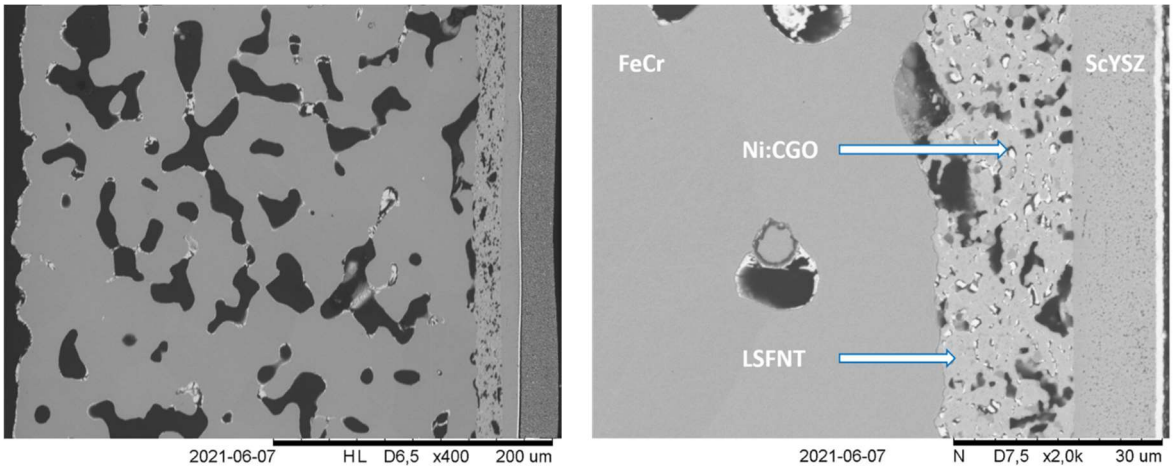

Figure 3.5 - SEM microscopy of LSFNT-MSC. In the left image, from left to right the layers are: FeCr porous support, LSFNT negative electrode, ScYSZ electrolyte, CGO thin barrier layer, LSC positive electrode. The right image is a focus on the negative electrode at higher magnification.

After the integration of the electro catalyst, the CGO barrier layer was deposited above the electrolyte using physical vapour deposition. Finally, the LSC layer was deposited using screen printing. The whole cell has to be sintered in situ during start-up of the test to achieve good contact between all the layers, prior to the electrochemical testing, as will be described

in sub-section 3.4.2. This is necessary since the metallic support and negative electrode were manufactured in pure hydrogen atmosphere to prevent metal oxidation, while the positive electrode is sintered in air. Therefore, the sintering processes has to be carried out in two different atmospheres for the two sides of the cell and this is possible once the cell is installed in the test-house.

Figure 3.6 summarizes the phases of the LSFNT-MSC's manufacturing process [24].

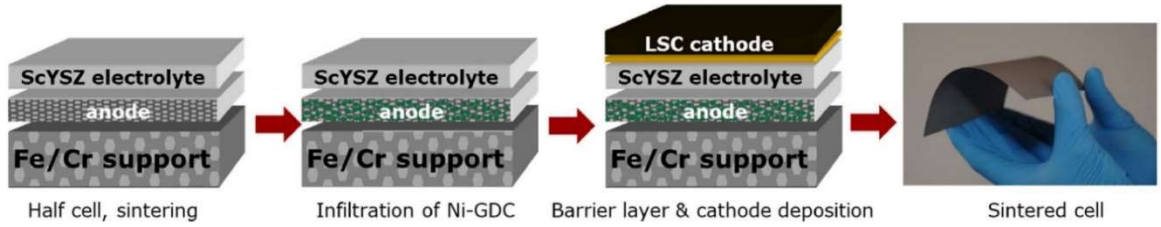

Figure 3.6 - Illustration of the phases in the fabrication of the LSFNT-MSC used in this study (here "anode" and "cathode" are referred to fuel cell mode).

3.2 Laboratory equipment and measures

Both the ceramic and metal-supported cells have been tested in the electrochemistry laboratory located in the new DTU Energy facility in Lyngby campus, which is an excellence in the field of solid oxide cells research and development. After a quick introduction to all the pieces of equipment used for this project purpose, the measurement procedures will be explained.

3.2.1 Test station

The test stations that are present in this laboratory are specifically designed to perform experiments on solid oxide cells: some of them are used to test full cells, others are arranged to study half cells, for examples just anodes of solid oxides fuel cells, others can host stacks. These machines are commonly called "rigs" and are either assembled by DTU or provided by the company *HORIBA FuelCon*. The test rig's model used for this project is the *FuelCon Evaluator-C*, with test stand number 70517. The common name adopted in DTU laboratory to refer to the specific machine used is rig46.

The test rig is controlled by means of *FuelWork* software. The instructions to carry out an experiment can be implemented through code scripts in Visual Basic language, and are sent to the rig's control system through a GPIB communication bus.

The heart of the rig is the furnace, where the cell to be tested is positioned, installed inside a specific in-house developed test-house that will be described later. This furnace can reach very high temperatures, up to 1100 °C. A picture of the furnace present in the rig that was used is shown in Figure 3.7.

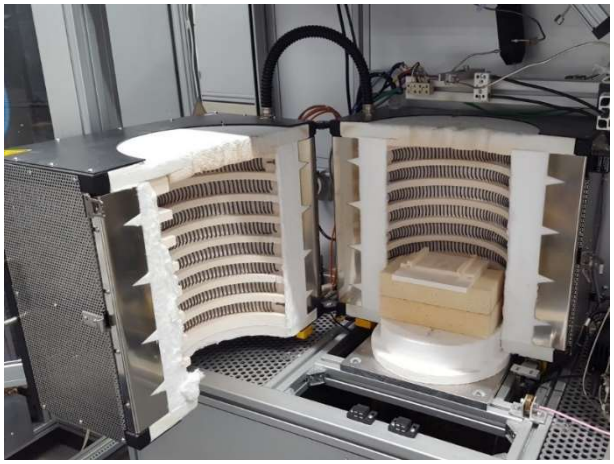

Figure 3.7 - Rig 46's furnace.

The gas supply unit (air, oxygen, hydrogen, methane and other gases) is placed behind the rig. The fluids lines are equipped with ball valves, solenoid valves, filters, pressure sensors, pressure regulators and mass flow controllers. All gas flows are preheated inside the furnace and, if needed, steam can be produced burning hydrogen and oxygen in the channel feeding the cell test-house.

Power is supplied to the cell through a circuit placed under the furnace, which consists mainly in a power supply unit and a load. Figure 3.8 shows how these components are installed in rig 46.

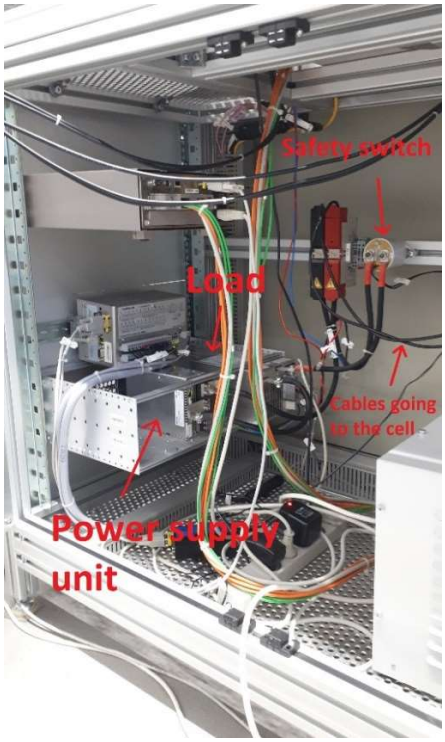

Figure 3.8 - Rig 46's power supply.

The power supply module is a *Cosel600F-3R3*, which can produce a DC output voltage up to 3.3 V; its specifications can be found at the reference [103]. The load instead is a *FuelCon TrueData-LOAD Model: 100A/35V/600W* and the datasheet can be found at the reference [104]; its function is to absorb the excess power flowing in the circuit: when the cell is operated as a fuel cell, it has to absorb both the power produced by the supply module and by the cell, instead in electrolysis mode the load has to absorb the power produced by the supply module minus the one absorbed by the cell.

This layout implies that the current can circulate just in one direction, so the cell's current collectors must be connected to the power cables differently depending on the operation mode (fuel cell or electrolysis cell) as shown in Figure 3.9. In fuel cell mode the positive terminal of the power supply module is connected to the negative electrode of the cell while in electrolysis mode the positive terminal of the power supply module is connected to the positive electrode of the cell.

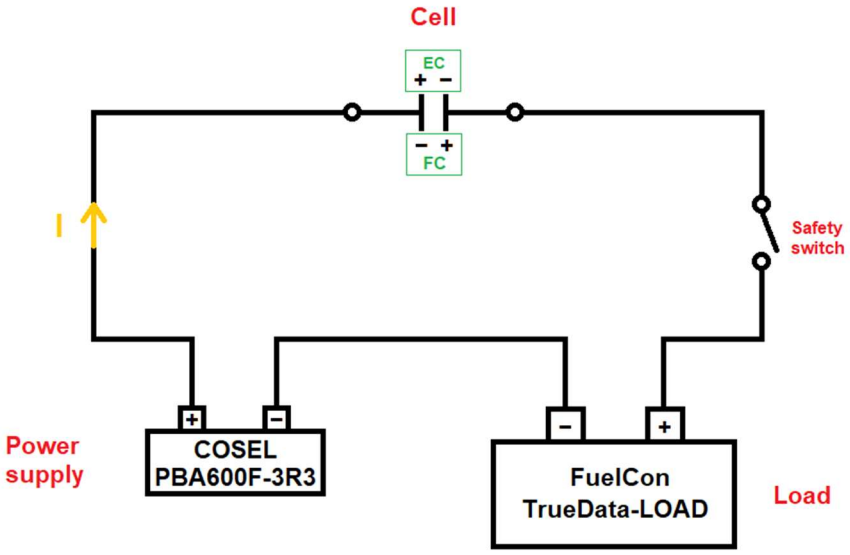

Figure 3.9 - Rig 46 simplified power supply's electrical scheme.

The test rig is equipped with a measurement system that collects all the signals coming from the sensors: thermocouples, oxygen partial pressure sensors and voltage measurements sensors are all connected to the measurement system via a TC panel inside the rig itself.

The thermocouples are used to monitor the operative conditions and to apply safety measures. In particular, a thermocouple is used to measure and control the furnace temperature, three thermocouples are placed inside the test house and measure the gas flows temperatures (inlet of the fuel electrode, outlet of the fuel electrode, inlet of the oxygen electrode), two thermocouples are placed in contact with the cell and measure the surface's temperature at inlet and outlet on the positive electrode side. Temperature is one of the parameters which mostly affects cell behavior, for this reason good thermal management is

essential to obtain reliable results. The only way to perform thermal control is setting furnace temperature, while cell temperature changes accordingly and can only be monitored.

Two oxygen sensors, placed inside the test house's channels at the fuel inlet and at the outlet, measure the partial pressure of oxygen to estimate fuel conversion and to check whether any leakage has occurred [105].

The electric potential is measured in 4 points: inlet and outlet of the fuel electrode, inlet and outlet of the oxygen electrode. This allows to measure the cell voltage (potential difference between the two electrodes) and the in-plane voltages along the electrodes (potential difference between inlet and outlet of the same electrode); an in-plane voltage that is not null indicates an uneven distribution of the current across the electrode. Particularly important is the measurement of the cell voltage, since it allows to record the polarisation curve of the cell. For this project, i-V curves recording has been simply performed changing the current each 4 seconds by small steps (0.2 A), from the value of 0 A to a maximum value (positive for fuel cell mode and negative for electrolysis mode) and then going back to 0 A, while recording the cell voltage. This means that all the i-V curves registered are constituted by two "branches", one descending and one ascending, that are not perfectly overlapping because of the unavoidable slight hysteresis phenomenon and uncertainty of the measurements. For a better visualization of the curves, just one of the two branches (the ascending one) has been plotted and analysed, as it will be possible to see in the chapter dealing with the results. The current has always negative sign because the convention is to consider a positive current during fuel cell mode.

3.2.2 Frequency response analyser and EIS

The frequency response analyser is a device that allows to perform Electrochemical Impedance Spectroscopy (EIS).

Frequency response analysers measure the real and imaginary impedance response characteristics with respect to frequency of the device under test, by applying a frequency swept sine wave to it and examining its response signal [106].

The frequency response analyser adopted for this project is a *Solartron 1255B*, produced by the company *Solartron Analytical.* Technical information about this device can be found at the reference [107]. Its operation can be controlled by the *Elchemea 6.2* software (developed at DTU Energy by Søren Koch and Karin Vels Hansen), through a computer connected to the frequency analyser via a GPIB communication.

The 1255B Solartron version is the simplest and cheapest available on the market since it is not provided with a current generator for the excitation signal, that is instead obtained with a voltage generator. So the way the value of the cell impedance is obtained is different from the procedure described previously. This device receives in input two voltage measurements: the cell voltage and a voltage measured at the terminals of a resistor, from now on referred to as "shunt resistance", whose value is known.

Figure 3.10 shows a scheme of the ports of the used Solartron 1255B.

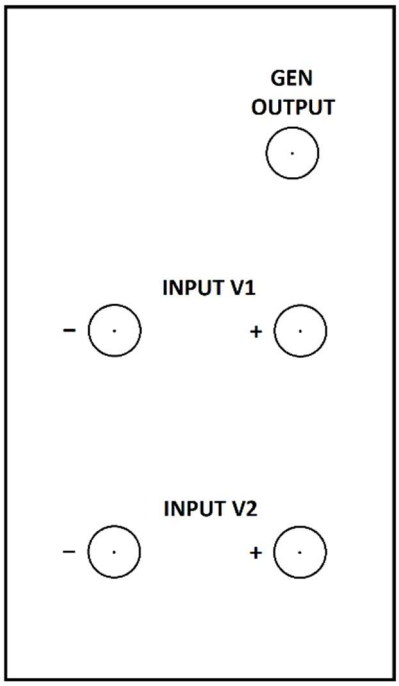

Figure 3.10 - Solartron 1255B ports.

“Gen output” is the excitation signal generated by the Solartron, “Input V1” is the voltage measured at the electric terminals linked to the cell (after DC cancellation) and “Input V2” is the shunt resistance’s voltage drop (after DC cancellation). DC cancellation consists simply in the subtraction of the mean DC voltage value from the sine-wave in order to get a wave oscillating around zero. A visual representation is shown in Figure 3.11.

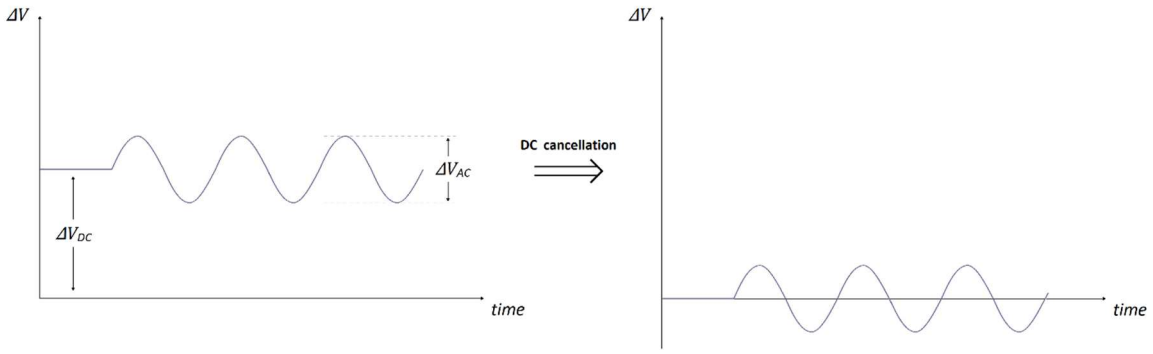

Figure 3.11 - DC cancellation.

The raw data created by the Solartron during EIS recording do not represent impedance values (they are not measured in ohm), but are simply the result of the ratio between the two

input signals V1 and V2. To obtain the actual value of the cell impedance two corrections have to be made, as explained in the following. Figure 3.12, representing how the Solartron wires are connected, can help understanding the way of calculating it.

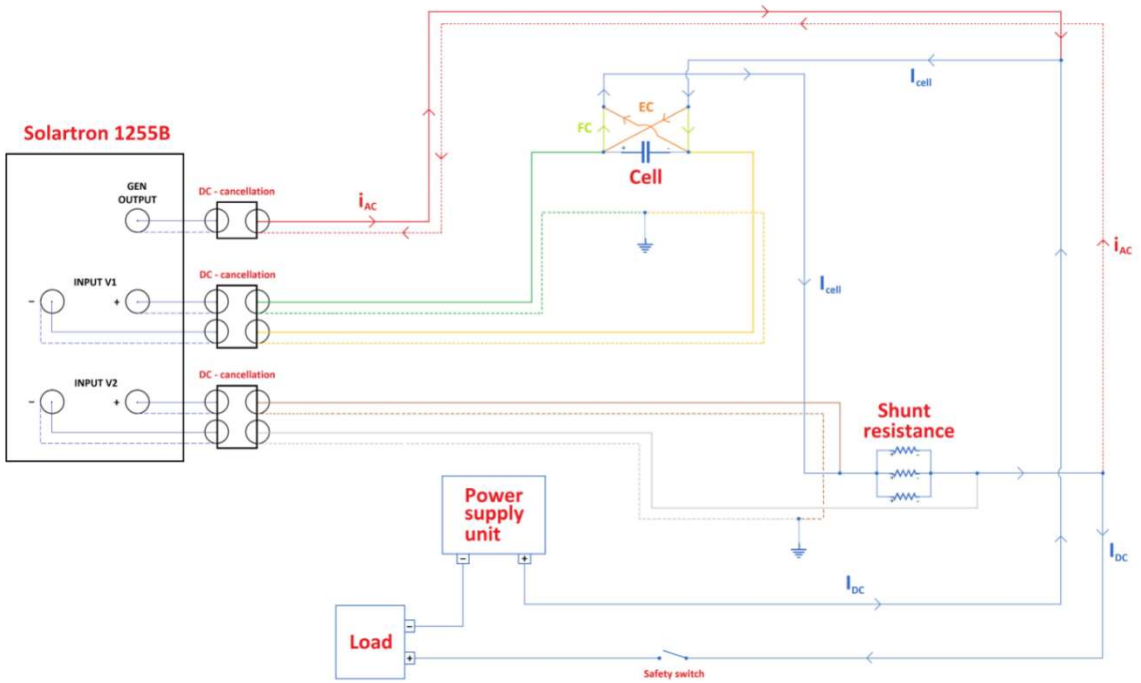

Figure 3.12 - Simplified scheme representing the Solartron connections.

In Figure 3.12 the blue lines represent the main circuit supplying current to the cell. The colored ones instead are the wires connected to the Solartron's ports; they all are single-wire shielded cables, the shield is represented by the dotted line. As already explained previously, the wires have to be connected differently if the cell is operated in electrolysis mode or fuel cell mode, as it is possible to see also in the scheme above.
The shunt resistance is a parallel connection of three resistors of 100 mΩ, so the overall value is 33.3 mΩ, as can be simply computed following the steps (3.1) and (3.2).

$$\frac{1}{R_{tot}} = \frac{1}{R_1} + \frac{1}{R_2} + \frac{1}{R_3} \tag{3.1}$$

$$R_{tot} = \frac{1}{\frac{1}{R_1} + \frac{1}{R_2} + \frac{1}{R_3}} = \frac{1}{\frac{1}{100\ \text{m}\Omega} + \frac{1}{100\text{m}\Omega} + \frac{1}{100\text{m}\Omega}} \cong 33.3\ \text{m}\Omega \tag{3.2}$$

The steps to obtain the corrected cell impedance are shown below (be aware that all the following formulas are based on complex math).

1. According to Ohm's law, the cell impedance is:

$$\bar{Z}_{cell} = \frac{\overline{\Delta V}_{cell}}{\bar{I}_{cell}} \tag{3.3}$$

2. The current flowing in the cell can be found knowing the impedance value of the shunt resistor (it is not an ideal resistor, so its impedance is not fully resistive but has also an imaginary part) and the voltage drop across it:

$$\bar{I}_{cell} = \frac{\overline{\Delta V}_{shunt}}{\bar{Z}_{shunt}} \tag{3.4}$$

   The shunt impedance has to be known.
3. The expression for the cell impedance becomes:

$$\bar{Z}_{cell} = \frac{\overline{\Delta V}_{cell}}{\overline{\Delta V}_{shunt}} \bar{Z}_{shunt} \tag{3.5}$$

4. The input V1, as already stated, is the voltage measured at the electric terminals linked to the cell, but it does not represent the actual cell voltage, because it also includes the voltage drop in the cables installed between the cell's current collectors and the electrical terminals. The cell voltage can be found subtracting from the measured voltage (from now on called $\overline{\Delta V}^{*}_{cell}$) the small surrounding voltage drop (from now on called $\overline{\Delta V}_{short}$, since its contribution can be simply measured by making a short circuit at the spot where normally the cell is placed, as will be explained later):

$$\overline{\Delta V}_{cell} = \overline{\Delta V}^{*}_{cell} - \overline{\Delta V}_{short} \tag{3.6}$$

5. Substituting the expression for $\overline{\Delta V}_{cell}$ in the one for $\bar{Z}_{cell}$, the final expression for the cell impedance can be found:

$$\bar{Z}_{cell} = \left(\frac{\overline{\Delta V}^{*}_{cell}}{\overline{\Delta V}_{shunt}} - \frac{\overline{\Delta V}_{short}}{\overline{\Delta V}_{shunt}} \right) \bar{Z}_{shunt} \tag{3.7}$$

The first term, $\frac{\overline{\Delta V}^{*}_{cell}}{\overline{\Delta V}_{shunt}}$, is the result given by the Solartron and represents the ratio between the input V1 and the input V2 (after DC-cancellation) when the cell is in position. The second and the third terms are the two needed corrections.

$\frac{\overline{\Delta V}_{short}}{\overline{\Delta V}_{shunt}}$ is the so-called "short circuit correction" and represents the result given by the Solartron when the cell is not present and instead of the electrochemical device a short circuit is implemented. $\bar{Z}_{shunt}$ is the so-called "shunt correction" and represents the shunt resistor's impedance; it cannot be measured with a *Solartron 1255B*, a *Solartron 1260* is needed because it is equipped with an input for measuring currents, allowing to compute the impedance of a general electric component simply as the ratio between a voltage and a current. Here the procedure to measure $\bar{Z}_{shunt}$ is not described, not being relevant for the purpose of the work; the values of the shunt impedance mounted in rig 46 were calculated previously and saved in a database.

Figure 3.13 shows an example of EIS of a shunt resistor of 50 mΩ [108]: the resistance (real part of the impedance) is very close to the rated value and the reactance (imaginary part) is not zero.

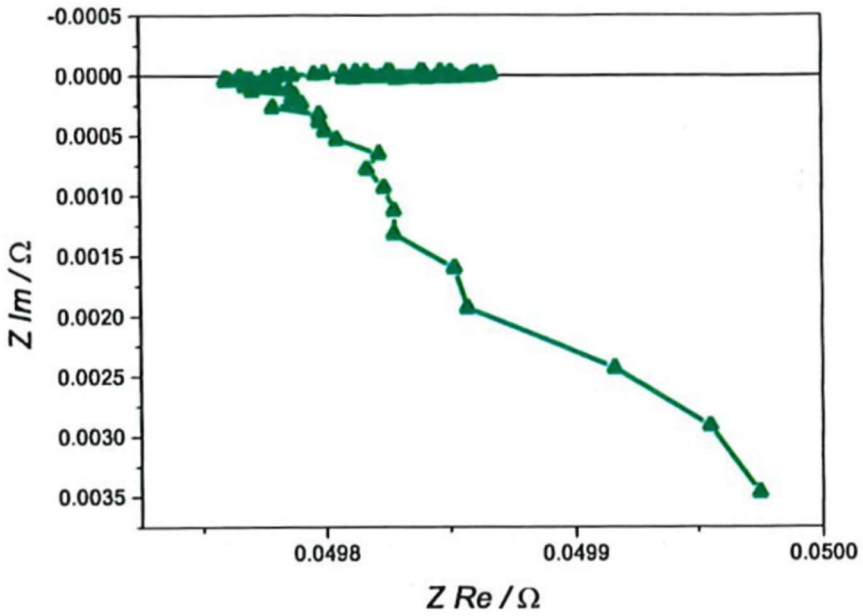

Figure 3.13 - Nyquist plot of a shunt resistance (in this case, it consisted of two 100 mΩ resistors connected in parallel, so the overall resistance should be ideally 50 mΩ).

Figure 3.14 illustrates an example of change in the Nyquist plot by applying the two correction steps [108].

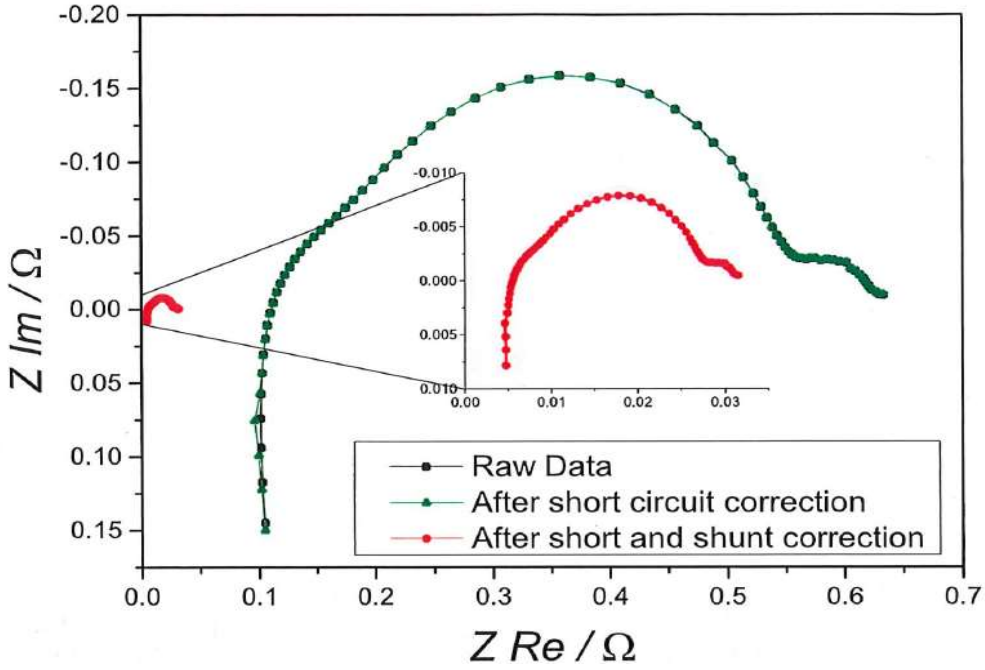

Figure 3.14 - Nyquist plot change after the two corrections.

It can be noticed how most of the influence on the whole correction comes from the shunt correction, while the short circuit correction produces an almost negligible change, since the resistance of the cables is very low.

3.2.3 Scanning electron microscope

The microstructure of the two cells was analysed performing Scanning Electron Microscopy (SEM) imaging with backscattered electrons, using a *Hitachi TM3000* tabletop scanning electron microscope, equipped with a field emission gun and an energy-dispersive X-ray spectrometer. Technical information about this device can be found at reference [109].

The TM3000 was used not only for imagining, but also for performing Energy Dispersive Spectrometry (EDS), a technique used to quantify the amount of different chemical components in the observed specimen, in this case the cell. The working principles of electron microscopy and EDS are not analysed in this report, not being strictly related to the purpose of the project.

X-ray spectrometry always produces images affected by a background noise: the maps of element distribution show the presence of the elements in the entire surface investigated, hence only high concentrations of points are indicative of the presence of such element and only a qualitative analysis can be performed.

3.3 Assembly and installation of the cell test-house

All the experimental activities performed on solid oxides cells at DTU laboratory start with the preparation of the cell test house. The mounting procedures that have been followed in this project are the same for both the ceramic and the metal supported cells.

For electrochemical testing, the cell was sandwiched between gas distribution layers, current collector layers and the alumina cell test-house blocks, in which gas supply channels and holes for wires for current pick-up and voltage probing were fabricated. Figure 3.15 shows a picture of the test house before the cell installation.

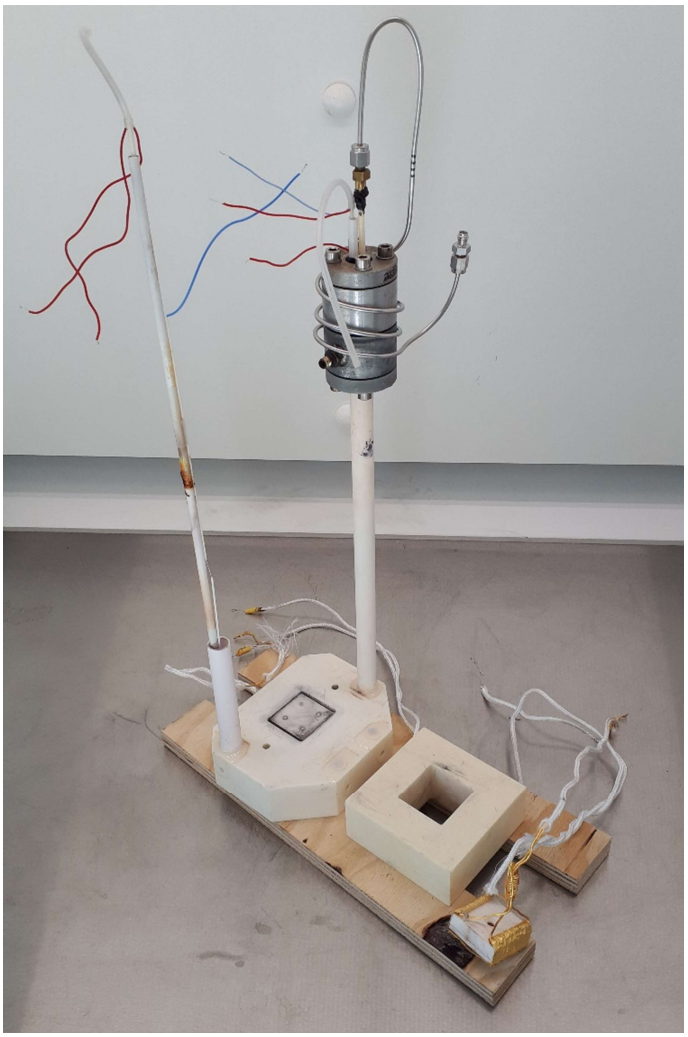

Figure 3.15 - Cell test-house.

The bottom alumina block has the function of directing the gas flowing at the fuel electrode side. In case of SOFC mode, this electrode has to be fed with hydrogen, while during SOEC mode water is the reactant necessary for the reaction. Since during testing both operational mode can be required, the solution that has been adopted is to feed the negative electrode of

the solid oxide cell with a mixture of hydrogen and oxygen in any case: the O_2 level is always lower than the stoichiometric amount needed to burn all the H_2, so the gas mixture that gets to the electrode's surface is always made of hydrogen and steam. The bottom part of the alumina test house presents a built-in channel for the H_2-O_2 mixture in inlet, a hollow (with a depth of 0.80 mm) for placing the current collector and the gas diffusion layers, through which the gas flows and reaches the cell's surface, and another channel for the outgoing H_2O-H_2 mixture. In the hollow there are six platinum contacts, four of them are connected to gold wires for current pick-up and the other two are voltage probes, connected to as many platinum wires. The wires come out from under the block.

The upper block of the test house is divided into two parts: a bigger piece with a square hole and a small piece, that has to be placed inside it. The smaller part has the function of directing the gas flowing at the positive electrode side, indeed on its base it presents a flow distributor constituted of milled trenches. Moreover, the flow distributor is covered with two layers made of gold: the first one is thick and has the function of current collector (it is connected to a gold wire for current pick-up, but also to two platinum wires that serve as voltage probe), the second one is a thin mesh that works as a diffusion layer, indeed it is in contact with the cell. In this project, the gas fed to the oxygen electrode through the upper alumina block was either pure oxygen or air. It is delivered to the middle of the cell and flows from the centre to the sides, perpendicularly with respect to the flowing direction of the gas at the negative electrode. The larger piece instead is just needed to hold the smaller piece in position; moreover, it provides weight to compact the cell and the underlying additional layers.

Before proceeding with the assembly of the test house, it is necessary to clean it and remove any residue left on it from previous tests. It is important to have a surface where to place the cell and the additional layers as flat as possible to avoid mechanical stress and because eventual debris could influence the results.

The first step of the mounting procedure consists of covering with a conductive paste, made mostly of platinum, the platinum contacts present in the hollow on the upper surface of the test house. These contacts are connected to the wires for current pick-up and voltage probing installed inside the bottom alumina block. The Pt paste improves the electrical contact between these wires and the current collector of the cell's negative electrode, that is the first layer placed inside the hollow: it is made of nickel, has a thickness of 0.11 mm and an area of 4 x 4 cm^2. Figure 3.16 shows the test house after the application of the Pt paste and after the positioning of the Ni plate.

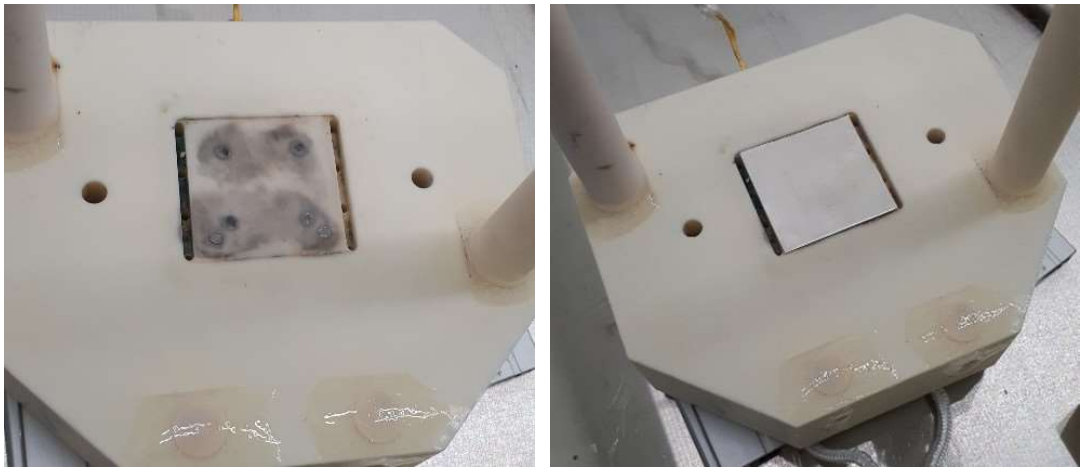

Figure 3.16 - Test house with Pt paste (left) and Ni plate (right)

The next step is to place around the hollow a thin (0.11 of thickness) “frame” made of gold, that will have the function of sealing the lower side of the cell, to avoid gas leakages. On top of the Ni current collector two more layers with the same surface area are placed. They both are nickel meshes used as gas diffusion layers; the first one is corrugated and is 0.56 mm thick, the second one is flat and is 0.24 mm thick. These layers are shown in Figure 3.17.

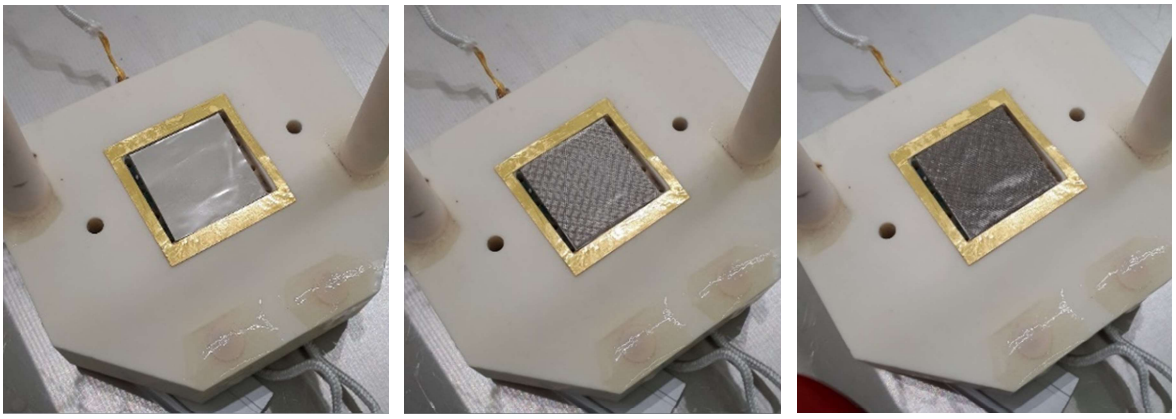

Figure 3.17 - Test house with gold sealing (left), first Ni mesh (center), second Ni mesh (right)

The sum of the thicknesses of the nickel layers (plate, corrugated mesh, flat mesh) is equal to the sum between the hollow’s depth and the gold sealing’s thickness, in this way the upper surface results homogeneously high. Indeed, on top of these layers the metal supported cell is placed, and a flat surface is required under it in order to have a gas distribution as uniform as possible on the whole area. Figure 3.18 shows the several additional layers and their thicknesses, while in Figure 3.19 the ceramic supported cell is shown in its position (with the metal supported cell the same applies).

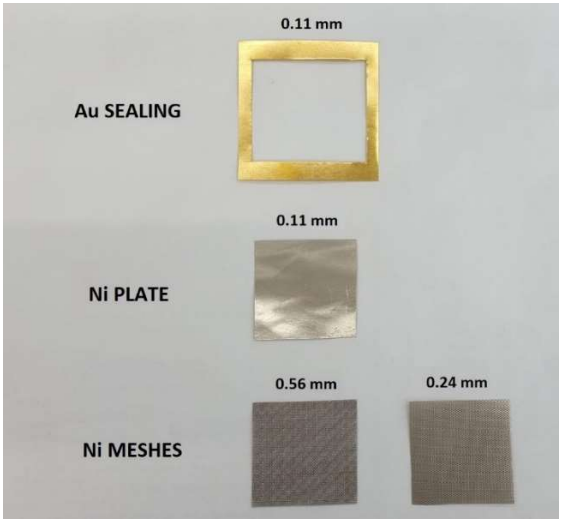

Figure 3.18 - Several additional layers.

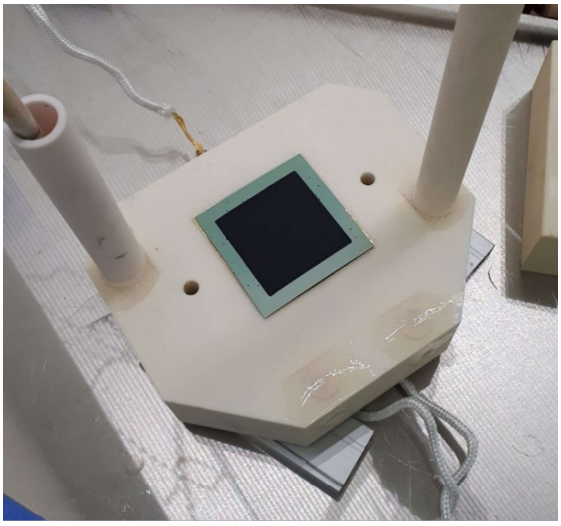

Figure 3.19 - Test house with the cell in position.

Once the cell is in position, the square holed alumina block is placed above it, leaving exposed inside the hole only the active surface of the upper electrode. At this point it is possible to insert the second part of the upper test house block, already covered with the gold layers, inside the square hole. Figure 3.20 shows how the test house looks like after these two last steps.

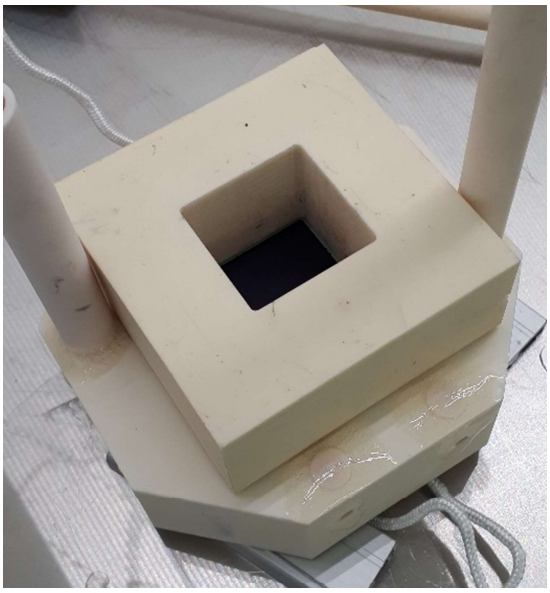

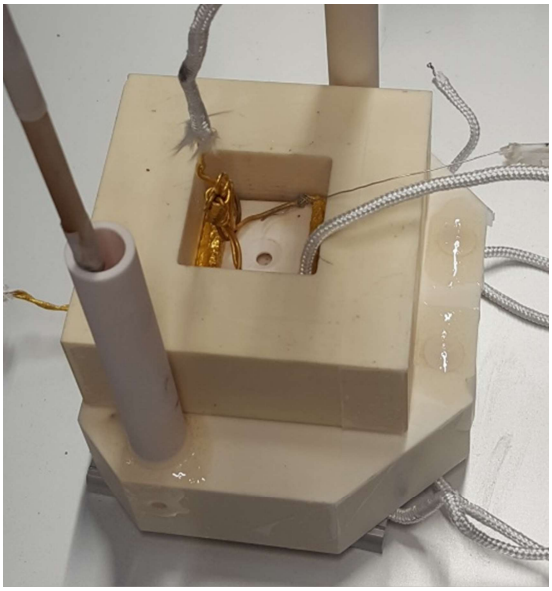

Figure 3.20 - Test house with upper alumina block (left: just the first piece; right: both pieces).

Now the test house is ready to be placed inside the rig's furnace and to be connected to the fluid supply unit's pipes and to all the sensors' wires. A detailed drawing of the test house cross section, also including the cell, the additional layers, the gas flows, the sensors, the wires, the probes, is given in Figure 3.21*;* instead, Figure 3.22 shows the views of the two

cell house's pieces, presenting in particular the directions of the gas flows and the positions of the Pt contacts for current pick-up and voltage probing in the bottom alumina block.

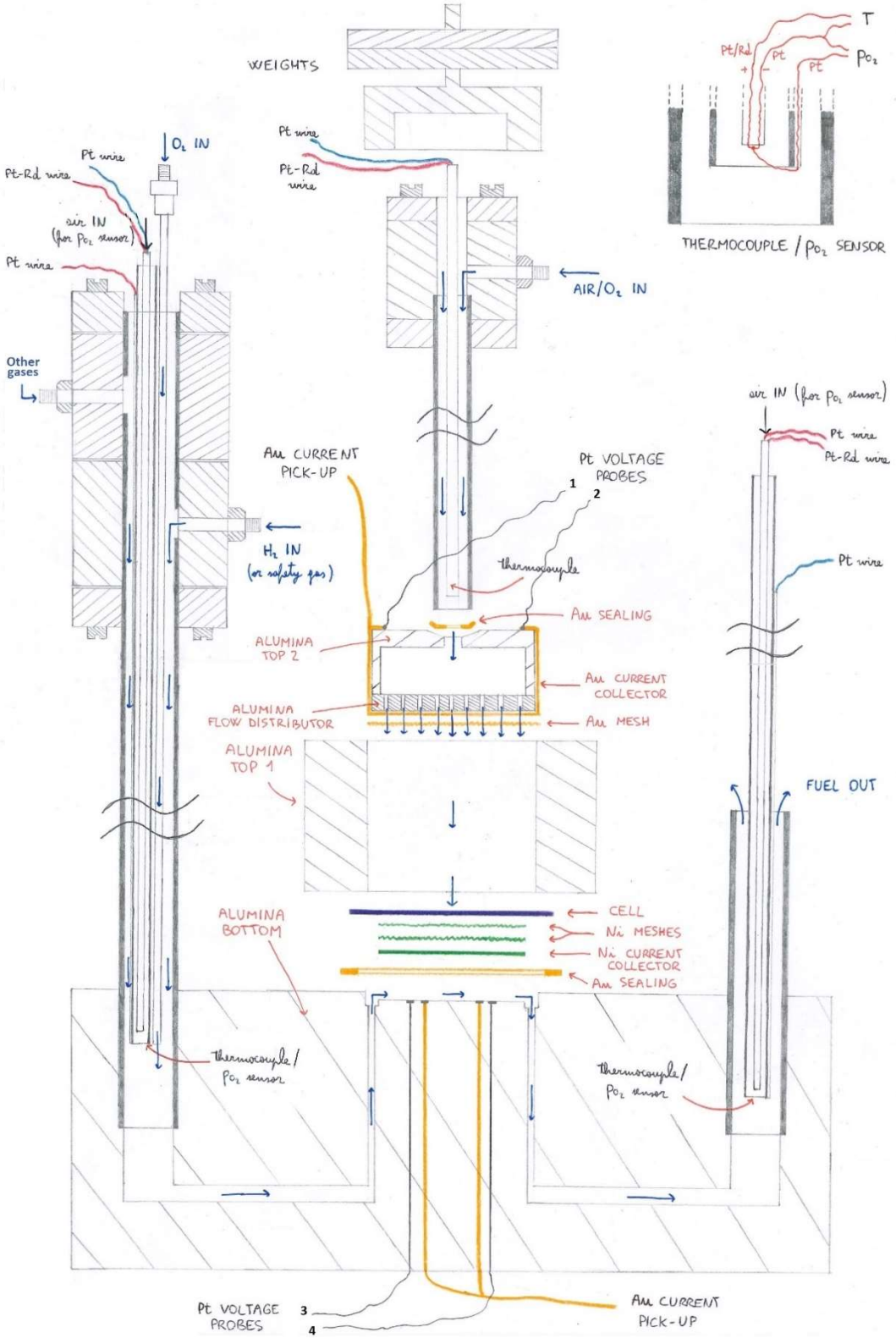

Figure 3.21 - Cross section of the test house.

The flow called “other gases” refers to all the fluids different from oxygen and hydrogen that can be fed to the negative electrode of the cell. For example, nitrogen was used during test’s start-up, as will be explained in sub-section 3.4.1. The four voltage probes were used to monitor the cell voltage and the in-plane voltage along the electrodes. The cell voltage was measured between probes 1 and 3. The positive electrode in-plane voltage was measured between probes 1 and 2, and the negative electrode in-plane voltage was measured between probes 3 and 4. The numbers are the ones shown in Figure 3.21.

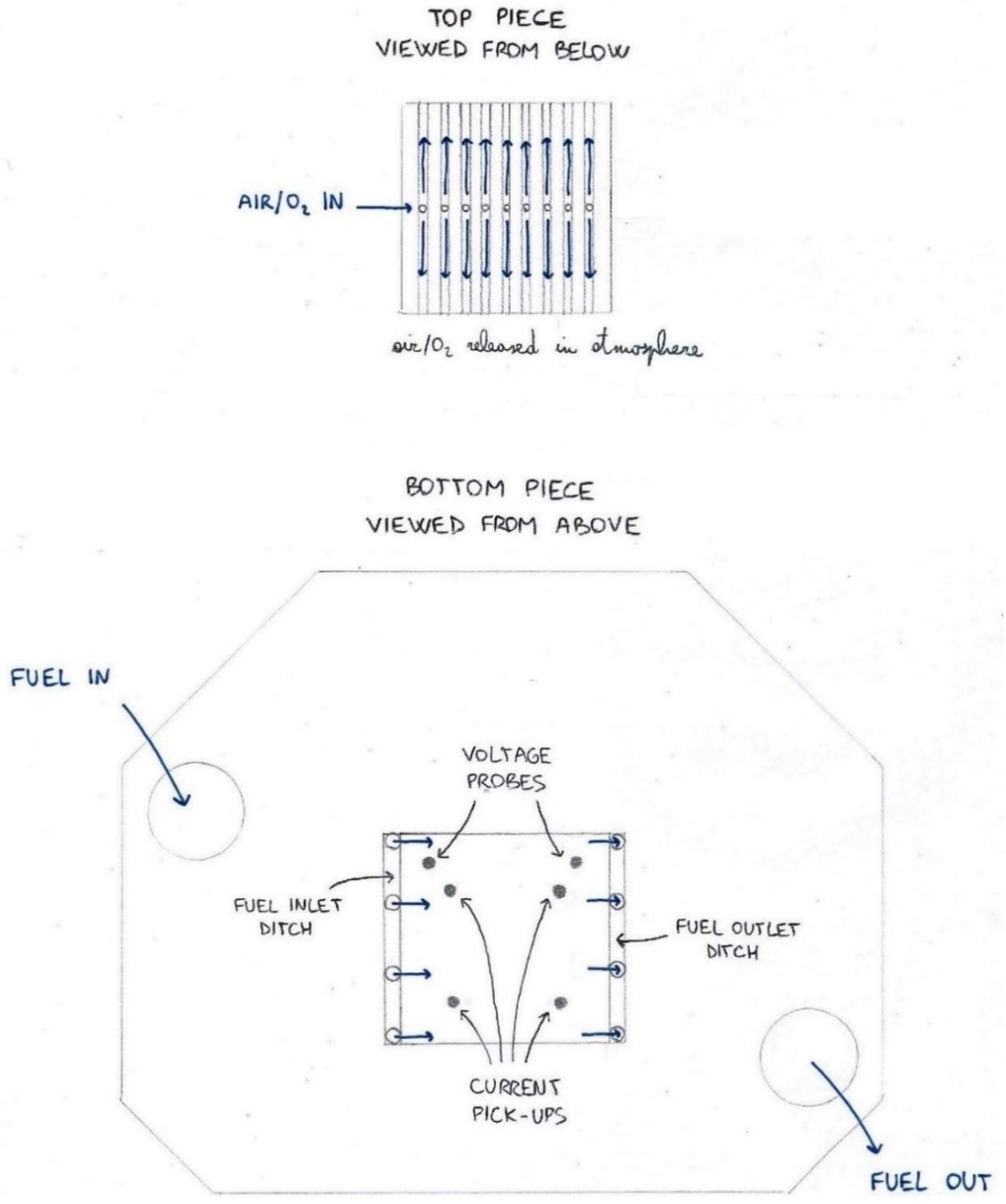

Figure 3.22 - Views of the test house.

The test house must be place inside the furnace and an alumina pipe for air/oxygen feeding is connected to the upper part of the test house, using a small gold ring as sealing (it is shown in Figure 3.21).

The next step consists simply in the connection to the test house of all the gas-feeding pipes (oxygen, hydrogen, air), all the sensors' wires (thermocouples and oxygen sensors), the four voltage probes and the two current wires. Furthermore, two thermocouples (for measuring the cell's center and corner temperatures) must be placed in contact with the cell, while another thermocouple must be positioned inside the furnace to register its temperature. Finally, a weight load of 4 kg is put on top of the central alumina pipe in order to compact the cell and the additional layers. At this point it is possible to close the furnace door and to start the test.

3.4 Structure of the experiments

For sake of measurement comparability with past experimental activities, the tests performed on the solid oxides cells at DTU's laboratory follow a standardized protocol developed by DTU Energy researchers in the years. This protocol is consolidated for state-of-the-art cells, therefore it was followed to test the ceramic-supported technology, while for the metal-supported one changes were required to limit corrosion-related issues. Even if this project's purpose is mainly aimed on the investigation of SOEC operation and degradation phenomena assessment, during fingerprints the cells were tested also in fuel cell mode. This allowed the comparison with previous tests performed with the similar cells and, as consequence, to assess the validity of the obtained results. Moreover, it was also required to enrich DTU's tests database.

In general, the cells are firstly activated through thermal and electrochemical processes. Then a first characterization, also referred to as "fingerprint", is carried out to assess initial cell's performances under different operating conditions (electrolysis and fuel cell operation modes, different temperatures and different gas compositions). After that, the test of interest – in this case a galvanostatic operation for 500 hours – is performed, followed by a final characterization aimed to evaluate the change in cell's performances.

Independently on the operating mode (SOFC or SOEC), both hydrogen and steam have always been fed to the negative electrode during the characterizations, changing their ratio accordingly to the standardized compositions as follows. The steam that flows to the cell is the product of hydrogen combustion. The chemical reaction is shown in equation (3.8).

$$H_2 + \frac{1}{2}\, O_2 \rightarrow H_2O \tag{3.8}$$

This means that each molecule of oxygen reacts with two molecules of hydrogen to give one molecule of water. Therefore, the flow rates of steam and hydrogen that reach the cell surface are calculated as shown in equations (3.9) and (3.10).

$$\dot{V}_{H_2O} = 2\,\dot{V}_{O_2,fed} \tag{3.9}$$

$$\dot{V}_{H_2} = \dot{V}_{H_2,fed} - 2\,\dot{V}_{O_2,fed} \tag{3.10}$$

Where:

_ $\dot{V}_{H_2O}$ is the volume flow rate of steam obtained by the combustion process;

_ $\dot{V}_{H_2}$ is the volume flow rate of hydrogen reaching the cell;

_ $\dot{V}_{H_2,fed}$ is the volume flow rate of fed hydrogen;

_ $\dot{V}_{O_2,fed}$ is the volume flow rate of fed oxygen.

The percentage composition of the mixture obtained after the combustion is simply computed has in equations (3.11) and (3.12).

$$\%\,H_2 = \frac{\dot{V}_{H_2}}{\dot{V}_{H_2} + \dot{V}_{H_2O}} \tag{3.11}$$

$$\%\,H_2O = \frac{\dot{V}_{H_2O}}{\dot{V}_{H_2} + \dot{V}_{H_2O}} \tag{3.12}$$

To perform a durability test in electrolysis mode, being H_2O the reactant, a pure steam feed would be the expected choice. Instead, hydrogen is always present to prevent nickel oxidation (enhanced by thermodynamic operative conditions), that would imply a loss in catalytic surface and hence performance. In real operative conditions, recirculated hydrogen would be present in the feed as well to help prevent excessive degrading.

It is not desired to operate at high steam content in metal-supported cell because the Cr_2O_3 scale on the FeCr surface could no longer offer the required protection to the metallic support, resulting in corrosion. This is based on knowledge from previous SOFC tests. For this reason a 50% steam – 50% hydrogen composition is chosen for the MSC's durability test. The same feed composition was adopted for the ceramic-supported cell's durability test to have a fair comparisons of the results. In addition to that, the 50% steam - 50% hydrogen composition is the most reliable if any leakage occurs. Imperfect sealing and cracks, that may form in the crystalline structure of the cell after long operation or repeated stresses

(electrochemical and thermal), could allow leakages formation. This would imply a change in steam-to-hydrogen ratio at the negative electrode (and consequently a small change in cell temperature), that would be more severe as the ratio of the two gets far from unity.

The positive electrode is fed either with oxygen or air during EIS and polarization curves recording to assess the performances of such electrode, instead during durability test it was always fed with air. Oxygen is a product of electrolysis and it is not necessary to allow the reaction, however a gas flow is useful to sweep up the products and increase reaction rate. In addition to that, it is also useful for the thermal management of the cell and the stack in real operations: maintaining as constant as possible the operative temperature is very important and a cooling gas would be necessary especially if the voltage is higher than the thermoneutral voltage.

3.4.1 Ceramic-supported cell's test procedure

The Ni-YSZ/LSC-CGO cells present a fuel electrode that appears green, as can be seen in Figure 3.1, because nickel in the YSZ's ceramic structure is in form of Ni-oxides. Nickel must be reduced to its metallic form to exploit its catalytic activity toward hydrogen oxidation and evolution.

The first step was the heating up of the furnace, to perform nickel reduction at high temperature. Keeping the current at zero, the cell was fed with 20 l/h of air to the positive electrode and 20 l/h of nitrogen to the negative one, while the furnace was heated up from ambient temperature to 850 °C, with a heating rate of 1 K/min. The furnace temperature has been changed with such rate during all the transients, to avoid thermal stresses that would cause the inevitable break of the cell's ceramic structures. At the end of the heat up a stabilization time is necessary to let the cell voltage stabilize at more or less 150 mV, that is the theoretical OCV value obtained with these gases' compositions and temperature, and to let the cell reach the temperature of 850 °C.

When the right values of cell's voltage and temperature were obtained, it was possible to proceed with the reduction phase. The positive electrode kept receiving 20 l/h of air, while the flow at the negative electrode side was switched to 20 l/h of the so-called safety gas, a mixture composed by 5% hydrogen and 95% nitrogen. Hydrogen is the species that, oxidizing, is responsible for nickel oxides reduction. These conditions were held for 2 hours, after which the safety gas flow was stopped and replaced with 20 l/h of pure hydrogen, while on the other side 40 l/h of air were fed. After 1 hour under these operating conditions, the reduction procedure was completed and the cell was ready to be tested. The name "safety gas" is commonly used to refer to this particular mixture because it is automatically fed to the negative electrode in case of any control system failure, to prevent nickel oxidation.

The first ceramic-supported cell was only exposed to reduction, to have a lattice structure reference for degradation phenomena assessment. Instead, the second ceramic-supported cell's test followed the entire protocol.

The initial fingerprint was composed by 100 different tests, in particular 60 i-V curve recordings (30 in fuel cell mode and 30 in electrolysis mode) and 40 electrochemical impedance spectroscopies.

The test started in fuel cell mode and the hydrogen-steam mixtures that have been adopted for cell testing, together with the respective amount of hydrogen and oxygen flows fed to the test house, are shown in Table 3.1. All the flow rates reported in this work are referred at normal conditions (atmospheric pressure and 0 °C), but for sake of simplicity they will be simply expressed in litres per hour.

Table 3.1 - Fuel electrode gas compositions used in fuel cell mode during the fingerprint.

H_2 fed [l/h]	O_2 fed [l/h]	H_2 - H_2O to the cell %mol
24	0.5	95.8 – 4.2
24	2.5	79.2 – 20.8
24	6	50 - 50

For sake of simplicity, these compositions will be referred to approximating their values as: 96% H_2 – 4% H_2O, 80% H_2 – 20% H_2O, 50% H_2 – 50% H_2O.

Starting with a furnace temperature of 850 °C, the cell was fed first with a fuel mixture of 96% H_2 – 4% H_2O, then with 80% H_2 – 20% H_2O and finally with 50% H_2 – 50% H_2O. Oxygen and hydrogen flows were changed gradually, to not cause stresses inside the cell. For each of these three fuel compositions, the cell was tested feeding the positive electrode first with 140 l/h of air and then with 140 l/h of pure oxygen. For each combination, first an i-V curve recording and then an EIS (at open circuit voltage) were performed.

Everything was repeated at furnace temperatures of 800 °C, 750 °C, 700 °C, and 650 °C.

After the first half of the fingerprint in fuel cell mode, the cell's wires were swapped to operate in electrolysis mode. The only differences with respect to what has been described so far are the ones listed below.

- The furnace temperature was kept first at 650 °C and then increased to 700 °C, 750 °C, 800 °C, 850°C.
- The fuel mixture compositions adopted were the ones reported in Table 3.2. These compositions will be referred to approximating their values as: 80% H_2 – 20% H_2O, 50% H_2 – 50% H_2O, 10% H_2 – 90% H_2O. For obtaining the last mixture reported in Table 3.2 (10% H_2 – 90% H_2O), instead of using a flow rate of hydrogen equal to 24 l/h and increase the flow of oxygen, it was preferred to maintain an oxygen flow rate of 6 l/h and decrease the hydrogen to 13.4 l/h. This was decided to not have a total flow rate too high, indeed 24 l/h of hydrogen would have required more or less 10.8 l/h of oxygen.

Table 3.2 - Fuel electrode gas compositions used in electrolysis mode during the fingerprint.

H_2 fed [l/h]	O_2 fed [l/h]	H_2 - H_2O to the cell % mol
24	2.5	79.2 – 20.8
24	6	50 - 50
13.4	6	10.4 – 89.6

- The EISs were performed just at 10% H_2 – 90% H_2O, since with the other compositions they had already been recorded during the fingerprint in fuel cell operation. Indeed, since the EISs were recorded at null DC current, there is no difference between the two operation modes.

As already explained in sub-section 3.2.1, the i-V curves were recorded changing the current by small steps from the value of 0 A to a maximum value, consequence of the limits in maximum/minimum cell voltage set in *FuelWork,* and then going back to 0 A. In electrolysis mode a maximum cell voltage of 1.3 V was set, instead in fuel cell mode the minimum value was set to 0.65 V. These two limits are provided by DTU test protocol and are needed to maintain the cell in safe conditions.

Before every EIS, the cell was left resting for more or less 10 minutes to let the voltage stabilize after the i-V recordings. During spectroscopy, the cell impedance was recorded at 74 different frequencies, ranging from almost 100 kHz to about 100 mHz.

After the first fingerprint, a 500-hours electrolysis-mode durability test was performed. The adopted operating conditions were the following ones: furnace temperature of 650 °C, hydrogen flow rate to the negative electrode of 12 l/h, oxygen flow rate to the negative electrode of 3 l/h (to obtain a fuel gas composition of 50% H_2 and 50% H_2O), air flow rate to the positive electrode of 50 l/h, current of 4 A (0.25 A/cm^2).

Electrochemical impedance spectroscopies were performed twice a day for the first 100 hours, then three times per day for the next 140 hours, finally four times per day for the last 260 hours. This schedule was decided while proceeding with the test, to better track the observed degradation rate.

At the end of the durability test, the final fingerprint was carried out. Starting from electrolysis mode at 650 °C, the same tests performed during the initial fingerprint were repeated. At the end of the last recordings at 850 °C, it was decided to stop the tests because looking at the results it was clear that the cell got broken, so it was not worth to keep going. This will be clarified in next chapter, where the results are discussed and analysed.

At this point the furnace was slowly cooled down to ambient temperature with a rate of 1 K/min, feeding the cell with 20 l/h of safety gas to the fuel electrode and 20 l/h of air at the oxygen electrode.

Figure 3.23 summarizes how the whole test was performed, showing the temperature's trend, the different phases and the operating modes.

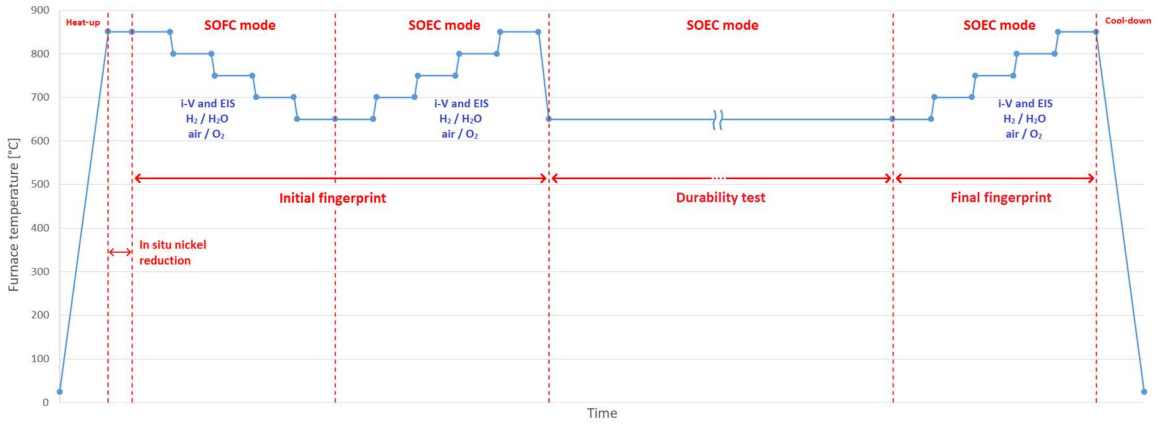

Figure 3.23 - Ceramic-supported cell's test structure.

3.4.2 Metal-supported cell's test procedure

During manufacturing at DTU Risø National Laboratory of the metal-supported cell, the LSC and CGO layers were just deposited above the half-cell, without being sintered. Therefore, before being able to proceed with the experimental activity, the cell necessitated to undergo a firing process in order to obtain a strong and effective bond between all the layers.

Keeping the current at zero, the cell was fed with 40 l/h of air to the positive electrode and 20 l/h of safety gas to the negative electrode, while the furnace was heated up from ambient temperature to 800 °C, with a heating rate of 1 K/min. A metal-supported cell could withstand faster thermal transients with respect to the other technology, anyway the temperature was changed very slowly not to risk damaging the alumina test-house. Once the set temperature was reached, the flow of air was increased to 140 l/h while the safety gas stream was shut down and replaced with 24 l/h of pure hydrogen, necessary to not oxidize the metal support. These conditions were held for 5 hours. At the end of this sintering phase, the temperature was immediately lowered to 750 °C. Indeed this kind of cells cannot operate at very high temperatures as the ceramic-supported cell, since the corrosion of the metal support is very severe above 750 °C.

Metal-supported cell characterization, as already anticipated, did not follow the standardized protocol, that was adjusted to limit corrosion of the metallic structure. Moreover, in order to reduce the thermal transients as much as possible and to save time, instead of carrying out all the tests first in fuel cell mode and then in electrolysis mode (as done with the ceramic-supported cell), the MSCs have been operated in these two modes alternately. In the following, the structure of the first fingerprint for the first MSC tested is presented, feed

compositions are obtained with the same feed flow rates already reported in Table 3.1 and Table 3.2.

- At 750 °C the cell was tested just in fuel cell mode, with a mixture fed to the fuel electrode of 96% H_2 – 4% H_2O and 80% H_2 – 20% H_2O, while the oxygen electrode was fed just with air in both cases. Electrolysis mode was not performed, since it was thought that at this high temperature the metal support would have excessively suffered corrosion, given the large amount of steam fed to the cell. For the same reason, the mixture 50% H_2 – 50% H_2O was not used even in SOFC mode. In addition, pure oxygen was not fed to the positive electrode to avoid possible leakages of O_2 to the fuel side (leakages are always present because the gold sealing is not 100% effective), since it would react with hydrogen producing more water. With air instead the magnitude of such leakages would be lower.

  For each composition, both i-V curve recording and EISs were performed.
- The furnace temperature was then lowered to 700 °C and the cell was tested in fuel cell mode (i-V and EIS at 0 A). The fuel mixtures adopted were 96% H_2 – 4% H_2O, 80% H_2 – 20% H_2O and 50% H_2 – 50% H_2O. For each fuel composition, both air and pure oxygen were fed at the positive electrode.
- At this point the current cables were swapped and the cell was tested in electrolysis mode at the same furnace temperature. Just i-V curve recordings were carried out, since EIS had already been performed in fuel cell mode. The fuel mixtures adopted were 80% H_2 – 20% H_2O and 50% H_2 – 50% H_2O; the mixture with 90% steam was not tested because the amount of water would have been too high. At the positive electrode, both air and pure oxygen were adopted.
- The furnace temperature was then decreased to 650 °C and the cell was tested in electrolysis mode (I-V and EIS at 0 A), adopting the same gas compositions presented in the previous point.
- Finally, the cables were swapped again and fuel cell mode was tested at the same furnace temperature. The gases used are the same presented at the second point of this list. EIS was carried out just with the mixture 96% H_2 – 4% H_2O, since with the other compositions it was already recorded in electrolysis mode.

At the end of the initial fingerprint the cables were swapped again and the long-term test in electrolysis mode started.

The same durability test performed with the ceramic-supported cell was repeated with the first MSC: 650 °C for the furnace temperature, 12 l/h as hydrogen flow rate to the negative electrode, 3 l/h as oxygen flow rate to the positive electrode, 50 l/h as air flow rate to the positive electrode, 4 A for the electric current.

As in the previous test, electrochemical impedance spectroscopy was performed twice a day for the first 100 hours, then three times per day for the next 140 hours, finally four times per day for the last 260 hours.

Observing the results obtained during the first characterization, it was clear that something unexpected related to metal oxidation happened, as will be explained in section 4.2. For the final fingerprint was then decided to operate the cell just at 650 °C to limit the corrosion effects that were noticed during the operation so far. The tests performed were the same ones described previously: i-V curves recording and EIS at 0 A in electrolysis mode, with a composition of the fuel electrode's feed first equal to 80% H_2 – 20% H_2O and then to 50% H_2 – 50% H_2O, both with air and pure oxygen to the positive electrode. After swapping the cables, fuel cell mode was tested, first recording both i-V curves and EIS with 96% H_2 – 4% H_2O to the negative electrode and with both air and pure oxygen to the positive electrode, and then recording just i-V curves with 80% H_2 – 20% H_2O first and then 50% H_2 – 50% H_2O to the negative electrode, both with air and pure oxygen to the positive electrode.

The furnace was then slowly cooled down to ambient temperature with a rate of 1 K/min, feeding the cell with 20 l/h of safety gas to the negative electrode and 20 l/h of air at the positive electrode.

Figure 3.24 summarizes the whole test structure.

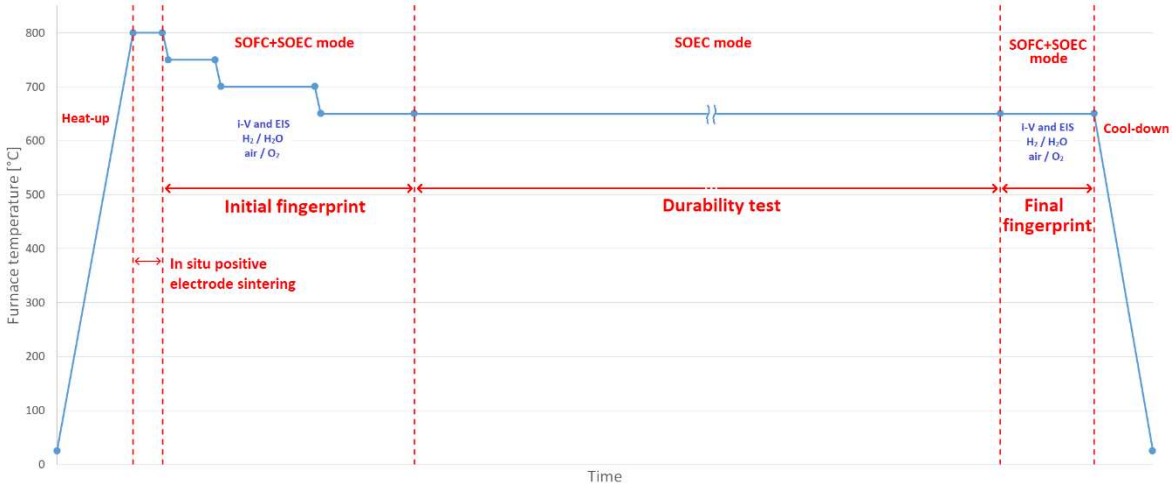

Figure 3.24 – First metal-supported cell's test structure.

After having analysed the results obtained from the first MSC experiment, it was decided to repeat a second test with an identical cell, changing the structure of the first fingerprint. The data from the first test showed that most likely the metal support went through oxidation during SOFC mode, so for the second test it was attempted to keep the operating conditions as safe as possible. In particular, the temperature was kept at lower values (just 700 °C and 650 °C) and the operation in fuel cell mode was limited.

First the cell was operated in electrolysis mode at 700 °C, using the same gas compositions and procedures adopted with the first MS cell. Then at the same temperature SOFC mode was tested, just with air to the positive electrode and the mixture 96% H_2 – 4% H_2O to the

negative one. Subsequently, the furnace temperature was lowered to 650 °C and SOFC mode was tested as done with the previous cell, followed by SOEC mode.

For the durability test, it was decided to push harder the cell using a current of 8 A (0.5 A/cm^2). The other operating parameters were not changed: 650 °C for the furnace temperature, 12 l/h as hydrogen flow rate to the negative electrode, 3 l/h as oxygen flow rate to the negative electrode, 50 l/h as air flow rate to the positive electrode.

The second fingerprint consisted of both SOEC and SOFC mode testing at 650 °C, while at 700 °C just SOEC mode was performed.

Finally, the cell was cooled down with a rate of 1 K/min, feeding 20 l/h of safety gas to the negative electrode and 20 l/h of air at the oxygen electrode.

3.5 Microscopic investigation

Microstructure analysis was carried out after testing to examine the possible causes of degradation. Fragments from different parts of the cell were investigated: inlet, outlet and centre (inlet and outlet are referred to the fuel electrode; here, as shown in Figure 3.22, the gas flows from one side of the cell to the other one, while at the oxygen electrode the gas is fed to the middle of the cell and flows towards both sides). Figure 3.25 shows where the segments of cell that have been observed (two pieces for the inlet, one for the centre, two for the outlet) were taken from.

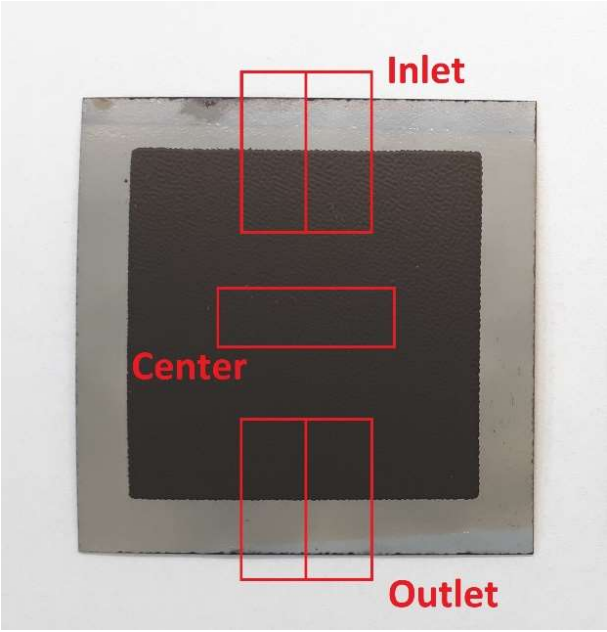

Figure 3.25 - Segments of the cell observed with the scanning electron microscope.

The cell was simply cut and the fragments were inserted in a plastic holder specifically realised for sample preparation, as it is possible to see in Figure 3.26.

Figure 3.26 - Holder for cell's fragments.

The cell samples were then vacuum embedded in Struers epoxy resin (Epofix). The cross-sections were ground using SiC paper and polished using 6 μm, 3 μm and 1 μm diamond paste. Finally the sample was carbon coated to eliminate surface charging, in order to obtain a better resolution with the scanning electron microscope. Figure 3.27 shows how a sample ready for microscopy appears.

Figure 3.27 – Sample ready for microscopy.

The investigation proceeded by checking the entire available sample surface with a magnification of x400 to identify the regions where to focus. Several pictures of the cells fragments were taken at inlet, outlet and centre with a magnification of x1500, allowing to see all the layers and appreciate any structural change, and a magnification of x2000 focusing

only on the fuel electrodes and electrolytes since are the parts more affected by degradation phenomena.

EDS was performed in the most significant areas detected by SEM, particularly for the inlet and the outlet of the cell, starting from an image acquisition at a magnification of x1500 which allows to map the element distribution in all the different layers in a qualitative way.

Chapter 4
Results analysis

In this chapter the test results will be analysed and discussed. Each cell technology is characterized by the interpretation of polarization curves and EIS, which provide an indication about the whole cell-system behaviour. Firstly, the ceramic-supported technology will be analysed, followed by the metal-supported one. The dependence of the operative parameters on the polarization and EIS curves for both technologies is initially shown and, after this characterization, data are used also to identify any problems which occurred during the tests and the reliability of the results is discussed. In the following sub-sections durability test results are analysed focusing on voltage and resistance contributions evolutions over time, allowing to assess the possible causes of degradation, verified afterwards by means of SEM and EDS investigation. A final comparison of the performances at low temperature between the two technologies investigated is presented in the end.

The differences between the measured cell's temperatures and the nominal ones (taken as reference for the representation of the results), were always monitored and it was checked that they never differ by more than 5 °C.

It is important to highlight that the tests were also affected by unforeseen events, such as: a programmed DTU network shutdown, a power outage in the laboratory, master computer shut down, a malfunctioning of the Solartron, a leakage of hydrogen from the test-house, and a failure of the main hydrogen supply unit of the laboratory. These problems and their impact on the tests will be explained in the related results sections, anyway the results are not considered compromised.

4.1 Ceramic-supported technology

This section is dedicated to the results for the ceramic-supported cells. Particular importance is given to their electrolysis performances evaluation at low temperatures, since the specific combination of materials which compose the cells used for this project were never tested at such operative conditions.

4.1.1 Cell characterization

A first analysis on the OCV deviations (to know the theoretical values, refer to Appendix A) obtained during the first fingerprint, reported in Table 4.1, shows significant deviations when using a 90% steam composition in the feed, while at 20% and particularly at 50% steam – condition of the durability test – the deviations are acceptable. Furthermore, the difference between the measured OCV values and the theoretical ones increases with the temperature. This parameter was constantly checked and never differ in a way that would justify such OCV deviations, hence a change in feed composition is thought to be the cause for this increase across the first characterization test.

This immediately suggested the presence of a small leak, which is always very likely to occur since the mounting and the realization of all the current collectors and gas diffusion layers (see section 3.3) is made by hand. However, the test was not considered compromised and was thus continued.

Table 4.1 - OCV deviations [mV] from theoretical values for all the i-V curves registered in electrolysis mode with the ceramic-supported cell, at different temperatures and steam content, for air and oxygen. Green: acceptable deviation; red: unacceptable deviation (more than 10 mV).

	650 °C		700 °C		750 °C		800 °C		850 °C	
20%	5	6	5	6	5	7	6	8	9	11
50%	4	5	5	6	5	6	5	6	7	9
90%	9	13	11	14	14	16	17	22	23	34
	Air	O_2	Air	O_2	Air	O_2	Air	O_2	Air	O_2

Figure 4.1 shows the polarization curves registered at the different temperatures with 50% steam – 50% hydrogen fed at the negative electrode and air fed to the positive one, where the slope of the curves decreases by increasing the temperature. It is clear this parameter is the one that mostly influences cell's performances. All results and theoretical OCV values - always shown in all polarization curves as small segments at zero current - are reported referring to nominal temperatures and feed compositions. The relative ASR measured at a current density of 0.25 A/cm^2 are reported in Table 4.2.

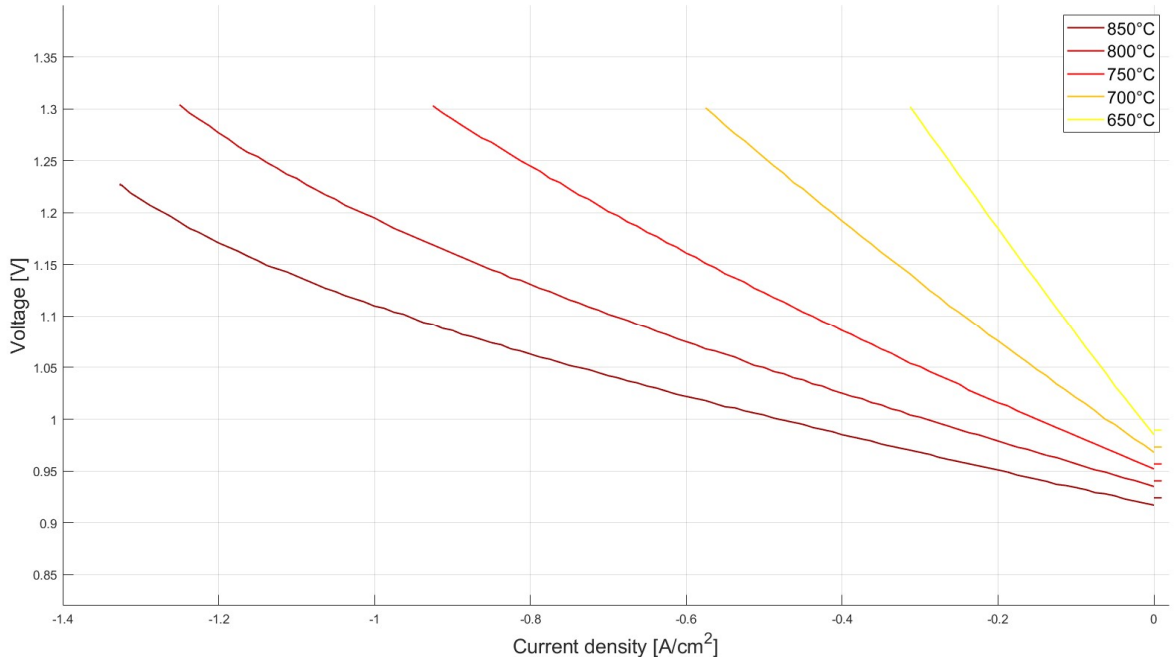

Figure 4.1 - Ceramic-supported cell's polarization curves at different temperatures with theoretical OCVs, feeding 50% steam content to the negative electrode and air to the positive one.

Table 4.2 – Ceramic-supported cell's ASR measured at 0.25 A/cm^2 at different temperatures, feeding 50% steam content to the negative electrode and air to the positive one.

Temperature [°C]	650	700	750	800	850
ASR [Ωcm^2]	1.036	0.567	0.360	0.220	0.160

In Figure 4.1 is also appreciable how Rig46 power supply demonstrated to be limited for the registration of polarization curves at high currents, since the curve at 850 °C does not reach the limit voltage set by the script (1.3 V). Instead, the current ramp was reversed by the maximum current that was reached only in the program, while the real one remained constant when the total power supplied to the cell was around 26 W. Such high currents were not expected to be reached in the following tests, for this reason and not to incur in unexpected events, the power supply was not substituted.

Figure 4.2 shows the polarization curves at different steam partial pressures with air fed to the positive electrode, at a temperature of 850 °C. In Table 4.3 the area specific resistances, calculated at a current density of 0.65 A/cm^2 and referred to 50% and 90% steam content and 850 °C, are shown. No important differences between the two steam compositions were spotted in the ASR values, but only a different OCV value accordingly to Nernst equation. In Figure 4.2, with a 20% steam – 80% hydrogen mixture fed to the negative electrode, the effect of steam starvation can be appreciated. The bending up of the curve relative to this phenomenon can be appreciated because of a lower limit current density imposed by this composition, around 0.75 A/cm^2 according to (2.2). The presence of this limit is more

appreciable at high temperatures, since the lower overall resistance allows to reach higher currents before the limit voltage triggers the end of the measurement.

Changing the feed to the positive electrode with oxygen the same trends were observed, the only difference was in the OCV values. The curves registered with oxygen are not reported since they would not add relevant information at this point of the analysis.

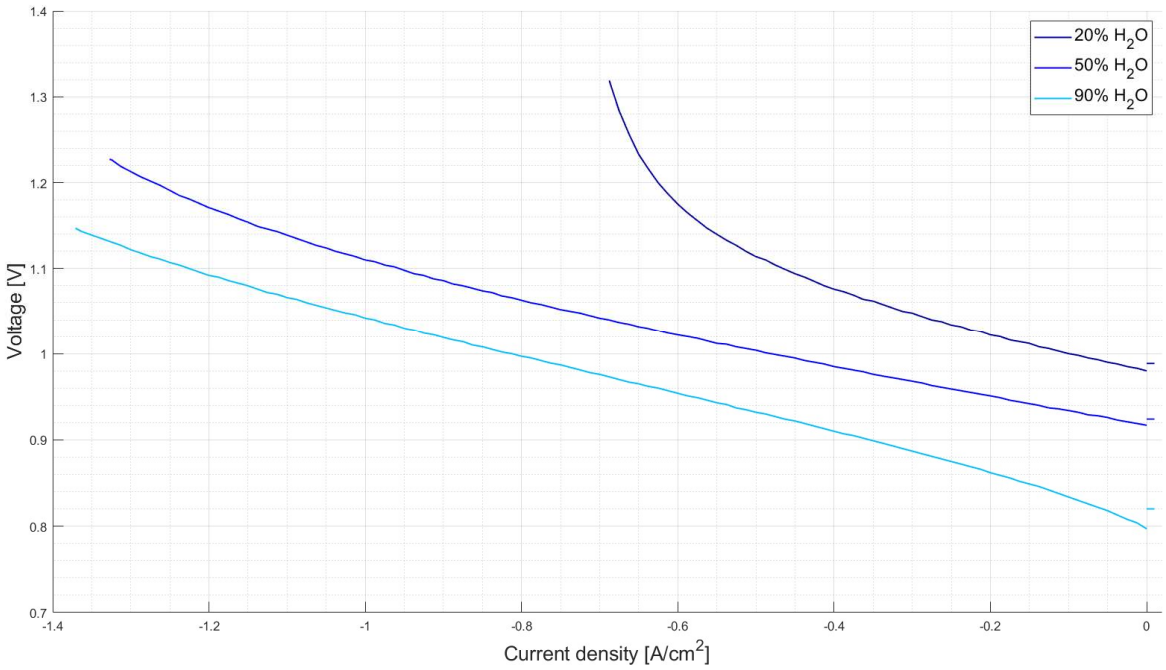

Figure 4.2 - Ceramic-supported cell's polarization curves at different steam contents to the negative electrode with theoretical OCVs, operating at 850 °C and feeding air to the positive electrode.

Table 4.3 – Ceramic-supported cell's ASR measured at 0.65 A/cm^2 at different steam contents to the negative electrode, operating at 850 °C and feeding air to the positive electrode.

Steam content [%]	50	90
ASR [Ωcm^2]	0.208	0.216

Analysing the Nyquist plot obtained at 50% steam – 50% hydrogen mixture at the negative electrode and air at the positive one, at the different temperatures presented in Figure 4.3 the same considerations about the influence of the temperature on the total resistance can be done. Particularly, EIS allowed to highlight the ohmic contribution. The nature of the electrolyte is responsible for this behaviour: a higher temperature increases the concentration of oxygen vacancies in the lattice structure, enhancing ionic conductivity. Changing feed compositions at fixed temperature no changes were appreciated in ohmic resistance.

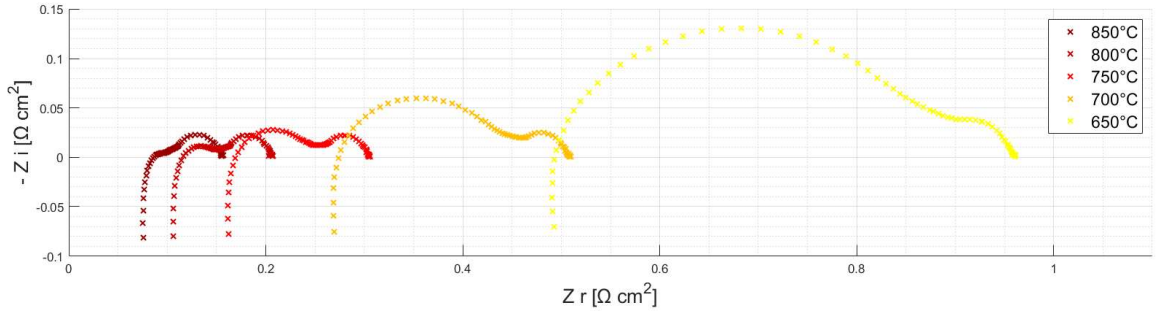

Figure 4.3 - Nyquist plot obtained at 50% steam at the negative electrode, air fed at the positive one at all the temperatures.

The dependence of ohmic resistance with such parameter was interpolated through an exponential function, shown in Figure 4.4; this is in accordance with the literature review presented in paragraph 1.2.1.2. The precise values of serial resistances at the different temperatures are reported in Table 4.4.

In addition, also the polarization resistance seems to be affected by the temperature, presenting a minimum at 850 °C.

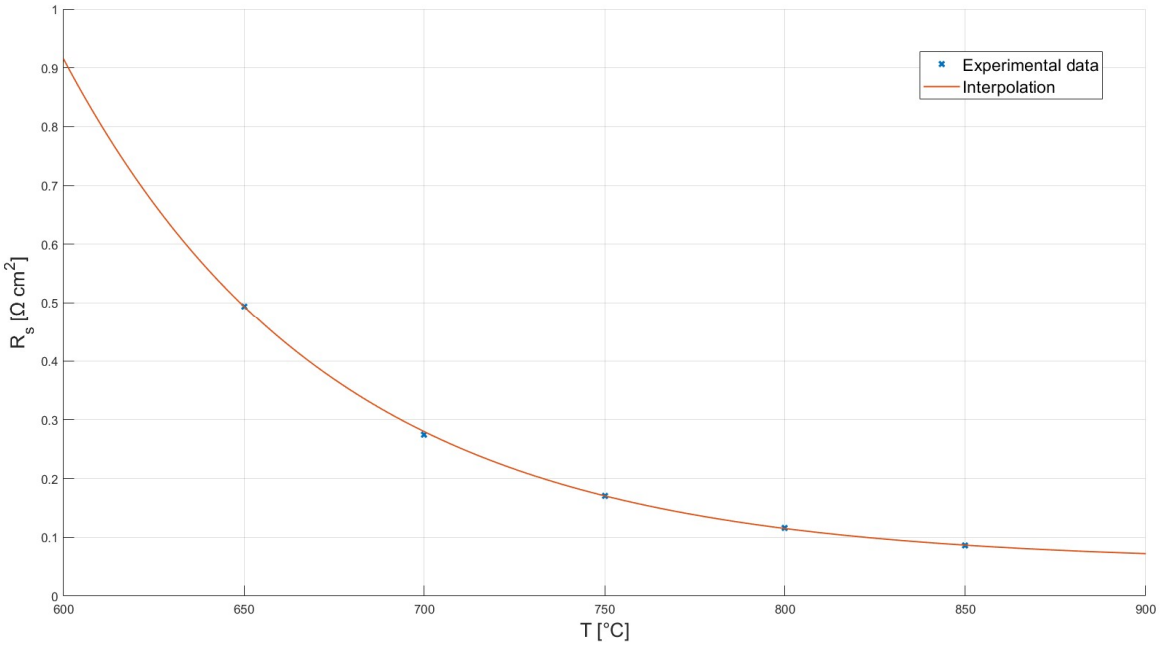

Figure 4.4 - Exponential interpolation of the serial resistance dependence on temperature for the ceramic-supported cell.

Table 4.4 – Serial resistances values for the ceramic-supported cell at the different temperatures.

Temperature [°C]	650	700	750	800	850
R_s [mΩcm^2]	494	275	170	115	86

The dependence of cell's responses to steam partial pressure change can be analysed by means of Bode plots investigation. Figure 4.5 shows the differences between 4% steam content in the mixture fed to the negative electrode, with 20%, 50% and 90% steam contents, at 650 °C and 850 °C with air fed to the positive electrode.

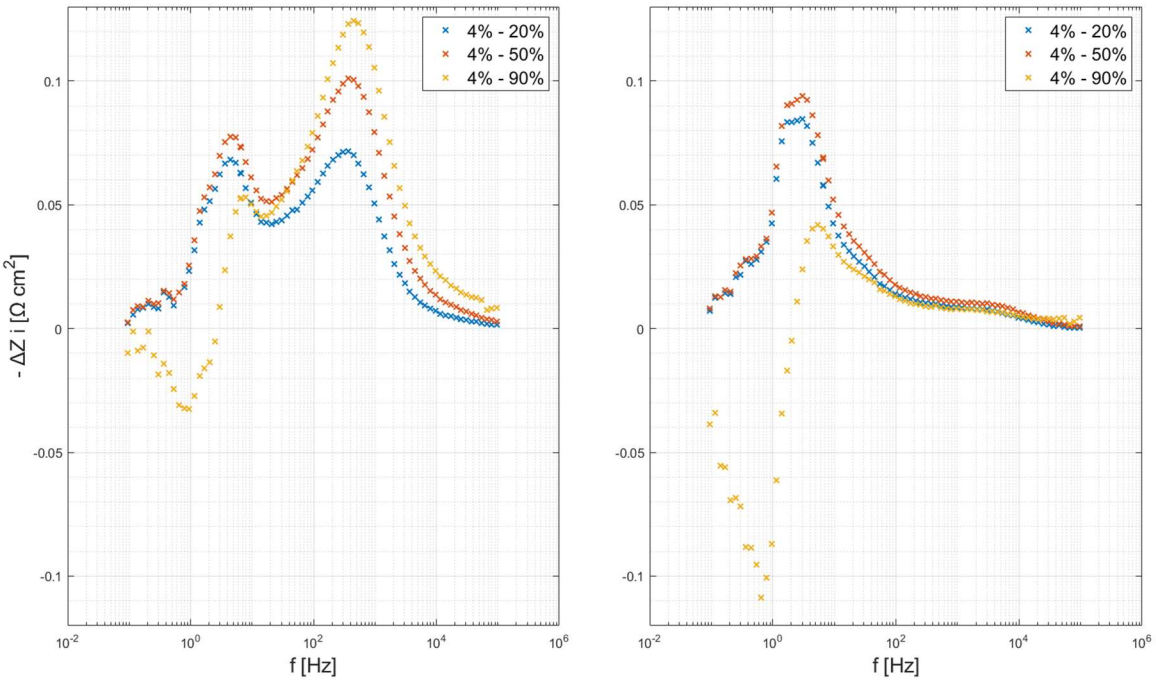

Figure 4.5 - Ceramic-supported cell's differences of imaginary impedances in Bode plots between different steam contents in the negative electrode's feed, at OCV, 650 °C (left) and 850 °C (right).

Such change affects especially low frequencies at 850 °C and both medium and low frequencies at 650 °C. The low frequency region is generally associated to gas conversion, hence appreciable changing feed composition. The yellow curve showing the difference between 4% and 90% steam compositions is clearly affected by a flow feed noise: a conversion process would produce a clear arc, while in this figure, at low frequencies, is possible to appreciate an irregular trend due to fluctuations of the real flow fed, more appreciable when steam and hydrogen are unbalanced. This particularly is highlighted by the difference in impedance between the two most unbalanced feed compositions.

Figure 4.6 shows the differences of imaginary impedances between the different temperatures at the same negative electrode feed composition, in this case at 50% and 90% steam, with air at the positive electrode. Peaks at medium frequencies can be observed both changing the temperature (Figure 4.6) and steam particularly at 650 °C (Figure 4.5), hence it is likely that the phenomena affected by these two parameters in this frequency range are of the same kind. Temperature affection suggests that the kinetics of the reaction can be involved. The influence of steam partial pressure, observed in the evident peaks around 400

Hz at 650 °C and in the small ones around 1100 Hz at 850 °C, suggests that such phenomena are related to the negative electrode.

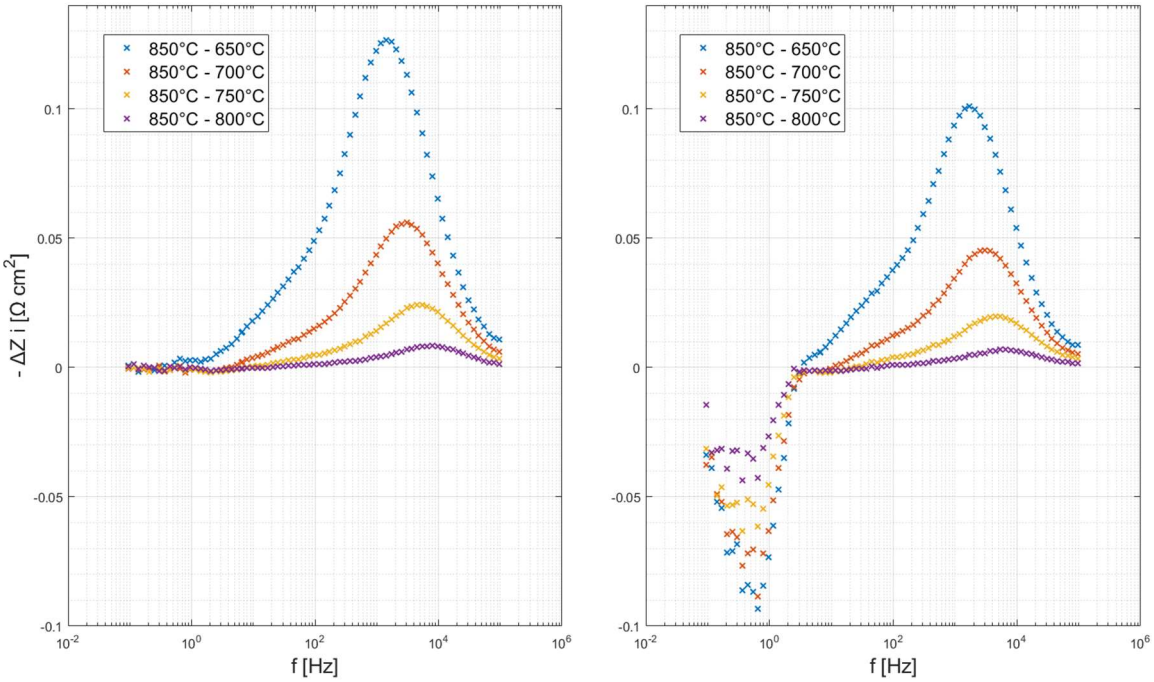

Figure 4.6 - Ceramic-supported cell's differences of imaginary Bode plot between different temperatures, at OCV, 50% (left) and 90% (right) steam content in the negative electrode's feed.

Kinetics of the reaction is enhanced by temperature – going toward higher temperatures, the kinetics is faster and the peak in the imaginary impedance difference chart is lower and shifts toward higher frequencies – and when such parameter is lower also the influence of steam partial pressure can be observed, as shown in Figure 4.5 at 650 °C. In this figure, it is appreciable that the higher the steam content in the negative electrode feed, the lower the impedance at the frequency associated to such electrode. Increasing from 4% to 90%, and taking as first term of the subtraction the impedance recorded at 4% steam, the difference increases, meaning that the maximum impedance corresponds to a feed mixture with 4% steam.

This observation leads to the conclusion that nickel catalytic activity has a dependence on the steam content. This is also confirmed by Budiman et al., which studied the dependence of hydrogen oxidation reaction on steam in anode supported SOFCs [110]. They concluded that the presence of OH^- on the Ni metal surface possibly enhances hydrogen oxidation reaction (HOR) rate, and the same happens with the evolution reaction (HER) occurring in SOEC mode.

Figure 4.7 shows the difference between air and oxygen feed, registered at 650 °C with 50% steam – 50% hydrogen mixture fed to the negative electrode. The curve was obtained subtracting the imaginary impedances recorded with air with the one recorded with oxygen.

A higher impedance recorded with air is due to EIS recording at OCV: in SOFC mode, operated during positive current fluctuations, oxygen is a reactant and its presence favour the reaction. The peak observed at around 20 Hz allows to identify the frequencies probably related to the conversion processes occurring in the positive electrode.

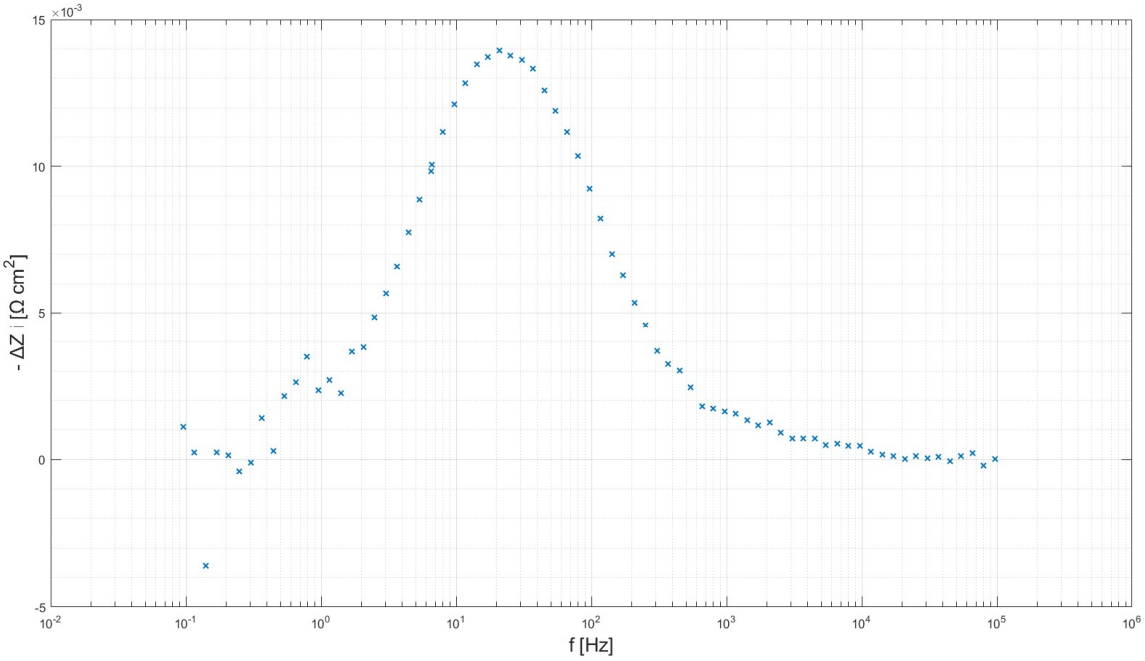

Figure 4.7 – Ceramic-supported cell's difference of imaginary Bode plot obtained subtracting the impedance recorded with air from the one obtained with oxygen at the positive electrode, at OCV, 650 °C, 50% steam content to the negative electrode's feed.

The impedance differences in the low frequency region observed changing temperature for the 90% steam composition, observed in Figure 4.6, suggest that something unexpected happened: at the same feed composition no differences should be spotted in the gas conversion region, as observed for the 50% steam composition. This suggests that the feed composition is changing since that frequency range has been demonstrated to be related to changes in steam partial pressure (shown in Figure 4.5). This observation, combined with the OCV deviations in Table 4.1, allowed to detect a leakage which effect is more visible at higher temperatures and at steam-to-hydrogen ratios in the feed far from unity.

Figure 4.8 shows the Nyquist plot obtained at 50% and 90% steam fed to the negative electrode, with both air and oxygen at the positive one at the different temperatures.

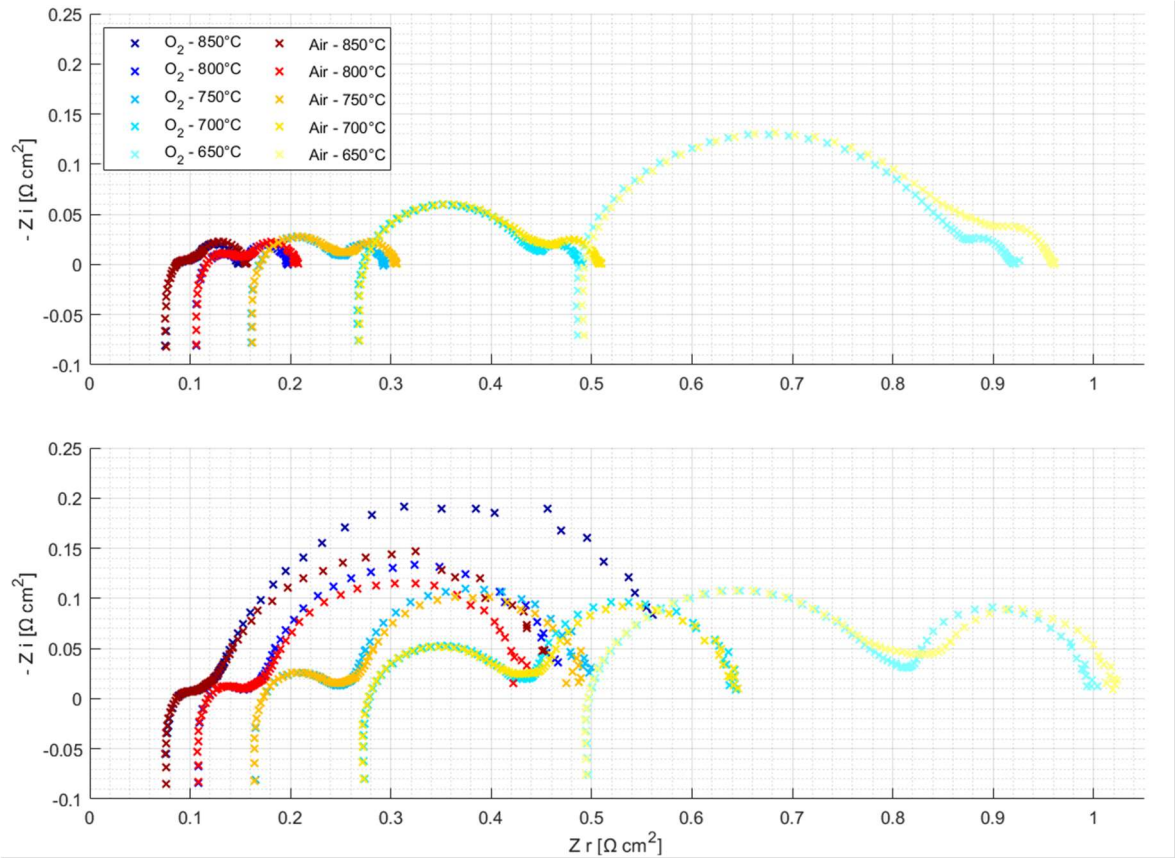

Figure 4.8 - Nyquist plots of the ceramic-supported cell, first fingerprint at all the temperatures with 50% (above) and 90% (below) steam content with both air and oxygen at the positive electrode .

During EIS registration the current fluctuates around zero making the cell operate alternately in fuel cell (when current is positive) and electrolysis mode (when it is negative). At 50% steam 50% hydrogen composition the concentration of both reactants for the two modes (steam for SOEC and hydrogen for SOFC) is the same, hence as a general behaviour a minimum in the dimensions of the low frequency arc, related to gas diffusion losses (gas conversion is always directly related to diffusion), is observed. Going towards a higher steam or hydrogen content implies a lack of reactant for one of the two operation modes, hence an increase in mass transport resistance. As a consequence, leakages are more easily detected at unbalanced conditions, 90% steam for instance.

For the same reason also the presence of air and oxygen fed to the positive electrode influences the dimension of the low frequency arc: being oxygen a reactant in SOFC mode the low frequency arc should be always smaller with respect to the one recorded in with air. This is not what is observed at higher temperatures and steam content in Figure 4.8, on the contrary an increase is spotted suggesting higher gas conversion. The cause of that is assessed to be related to a leak of oxygen toward the fuel electrode, which produces a higher steam content in the mixture fed to the negative electrode.

Furthermore, the leakage presence is confirmed analysing Figure 4.9 that shows two polarization curves recorded with air and oxygen fed at the positive electrode at 850 °C, with

20% steam – 80% hydrogen mixture fed to the negative electrode. With a leak of air towards the fuel electrode, the steam content would increase less with respect to a leak of pure oxygen, implying a lower limit current density due to a lower H_2O concentration.

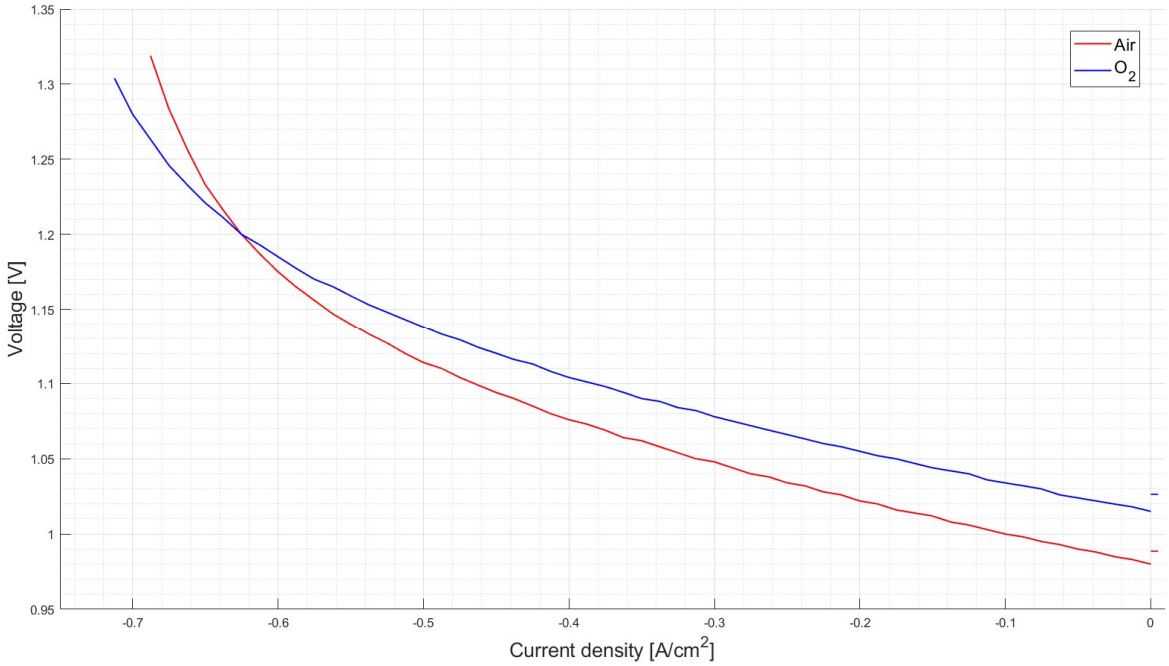

Figure 4.9 - Ceramic-supported cell's polarization curves with theoretical OCVs, at 850 °C, 20% steam fed to the negative electrode, air vs oxygen to the positive electrode.

Considering the test structure in sub-section 3.4.1, the 90% steam composition at 850 °C was tested at the very end of the first characterization. Referring to these conditions and looking at the OCV deviations in Table 4.1 and at Figure 4.8, where an important increase of the low frequency arc can be appreciated at these conditions, it is clear that the leakage got more severe while proceeding with the characterization. Perhaps a possible cause, along with electrochemical stress, can be attributed to the multiple temperature ramps.

4.1.2 Durability test

Figure 4.10 shows the time evolution of cell voltage during the 500-hours galvanostatic test at 0.25 A/cm^2, with 50% H_2 + 50% H_2O supplied to the negative electrode at a flow rate corresponding to a 28% steam utilization and air supplied to the positive electrode as sweep gas. The notches along the curve are due to the EISs recorded during the whole duration of the durability test to progressively follow and analyse cell degradation. The voltage profile presents some irregularities and discontinuities due to unforeseen events: between the 110 and 165 hours of operation there have been communication issues between the Solartron and the master computer, after a programmed DTU network shutdown; in two moments the hydrogen flow was automatically stopped and replaced by safety gas, as a consequence first

of an uncontrolled master computer's shut down and then of a power outage in the laboratory; between the 400 and 420 hours no EIS were recorded because of a malfunctioning of the Solartron. Fortunately, the outcome of the test was not affected, thanks to automatic safety measures present in the FuelCon rig test station.

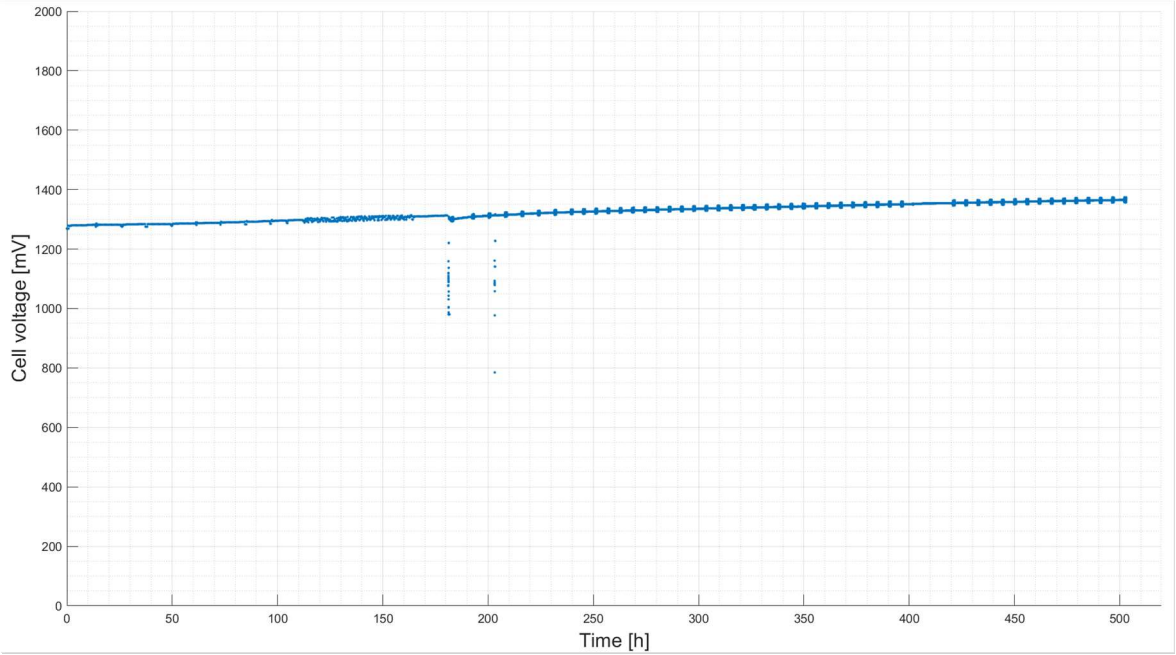

Figure 4.10 - Cell voltage profile of the ceramic-supported cell during durability test.

The cell voltage change has turned out to be quite linear, starting from the initial value of 1280 mV and ending at 1365 mV. The increase during the 500 hours is equal to 85 mV, resulting in an average degradation rate of 13.28% per 1000 hours.

These voltage values correspond to electric efficiencies, computed as in equation (2.8), equal to 97.13% at the beginning of the 500 hours and 91.08% at the end. The electric efficiency decreased with an average rate of 12.1 percentage points per 1000 hours.

The Nyquist plots of the EISs recorded during durability test are shown in Figure 4.11. The colour of the curves turns from blue to red as time passes. The real impedance has been divided in its two main components and Figure 4.12 shows the trend of the ohmic and polarization contributions during time.

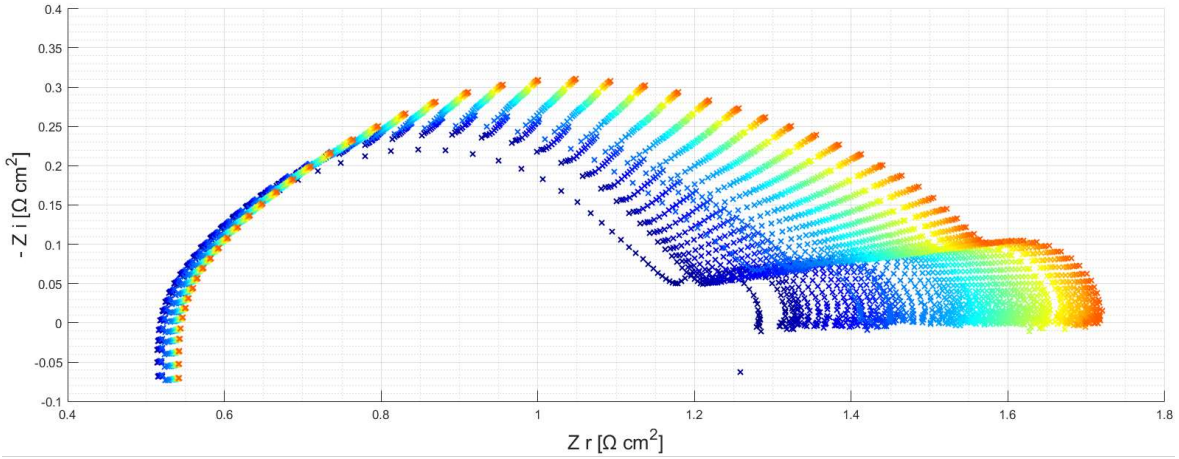

Figure 4.11 - Nyquist plots during durability test for the ceramic-supported cell. The evolution is followed changing colour from blue to red

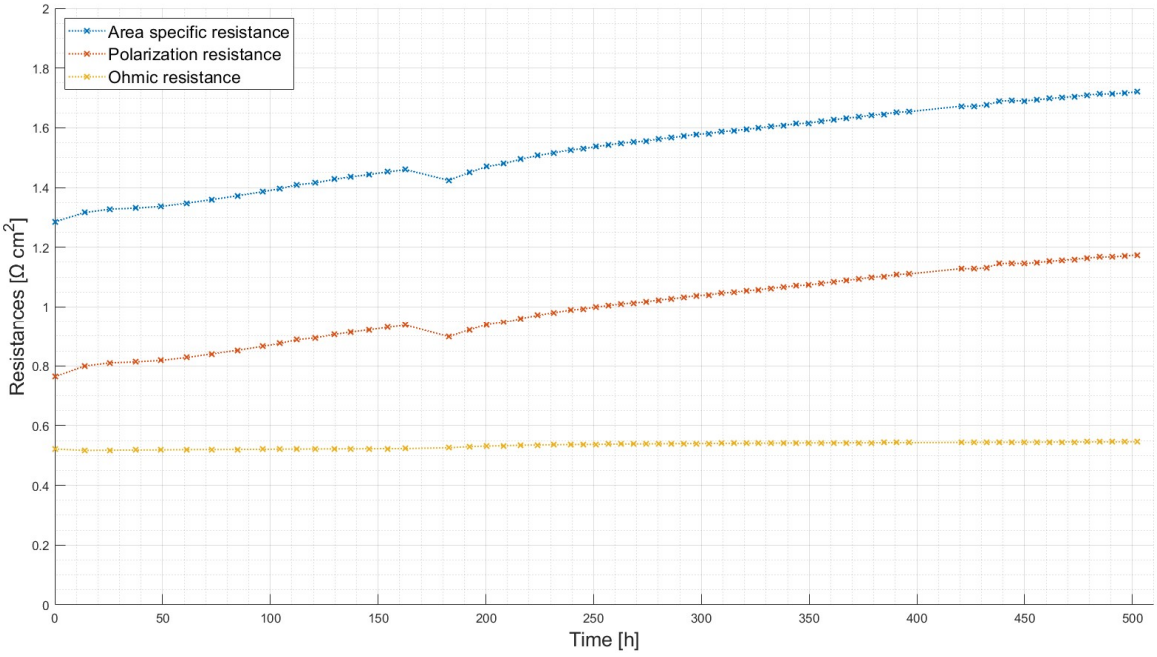

Figure 4.12 - Trend of R_s, R_p, ASR during durability test for the ceramic-supported cell.

The values of the several resistances at the beginning and at the end of the durability test are reported in Table 4.5. Observing the data, it is clear how the cell's performance loss was mainly due to an increase in the polarisation resistance, and checking Figure 4.11 it is possible to attribute most of this change to the medium-frequency arc, while the low-frequency arc change is less important but still not negligible. From the literature it is known that the electrode that suffers most degradation is the negative one [18], so it is expected that the observed worsening would be related to it as well. The serial resistance was pretty stable during the long-term test, suggesting that the electric contact between the several layers did not deteriorate too much.

The area specific resistance (obtained from the EIS at 4 A) changed from an initial value of 1.286 Ωcm^2 to a final value of 1.720 Ωcm^2. The increase during the 500 hours is equal to 0.434 Ωcm^2, resulting in an average degradation rate of 67.5% every 1000 hours.

Table 4.5 - Resistance contributions of the ceramic-supported cell before and after durability test at 0.25 A/cm^2.

	R_s	R_p	ASR
Start of the test	0.522 Ωcm^2	0.764 Ωcm^2	1.286 Ωcm^2
End of the test	0.546 Ωcm^2	1.174 Ωcm^2	1.720 Ωcm^2
Change	+ 0.024 Ωcm^2	+ 0.410 Ωcm^2	+ 0.434 Ωcm^2
Percentage change	+ 4.60%	+ 53.66%	+ 33.75%

Figure 4.13 shows the difference of imaginary impedance along the long-term test, taking as reference the first curve registered. As before, the colour turns from blue to red as time passes. This graph indicates that during durability test the impedance was mainly affected in the medium-frequencies region. In particular, the peaks of the curves are in the range of few hundreds of hertz (between ca. 100 and 500 Hz). As demonstrated by the analysis on steam dependence of cell's performance at 650 °C (see Figure 4.5), this is the frequency range where processes involving the negative electrode take place. It is therefore thought that the increase in medium-frequency arc observed during the durability test is associated to degradation of such electrode, and probably it is related to a loss of active surface (this is in accordance with the literature [18]).

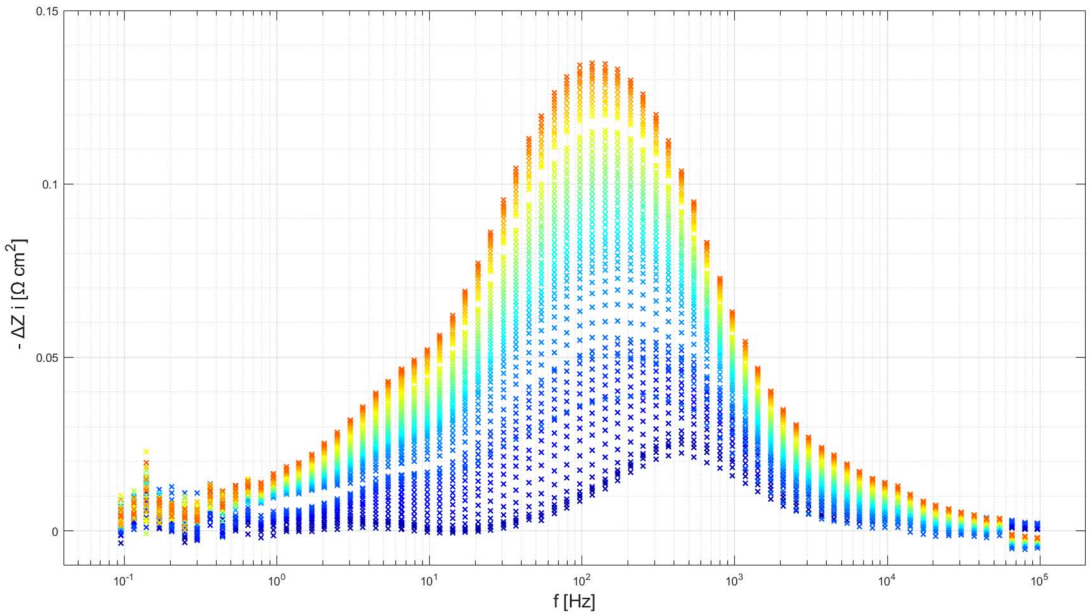

Figure 4.13 - Ceramic-supported cell's differences of imaginary Bode plot during durability test (the reference is the first EIS recorded, the evolution is followed changing colour from blue to red).

From Figure 4.13 it is also possible to identify a less important change of impedance at low frequencies, around 7 Hz. This is consistent with the increase of low-frequency arc observed in Figure 4.11, and it suggests a worsening of gas conversion that can be attributed to a porosity change (hindering diffusivity) or to an uneven degradation of the negative electrode. Indeed, if part of the Ni-YSZ electrode deactivated during the durability test, less steam flowing through the flow paths in the degraded area would be converted, resulting in a by-pass of reactant.

The decrease in performance is also evident comparing the results obtained from the final fingerprint with the ones recorded before the long-term test at same operating conditions. Figure 4.14 and Figure 4.15 represent respectively the polarization curves and the EIS Nyquist plots at OCV, recorded during the first and the final cell characterization, hence before and after the durability test, at a furnace temperature of 650 °C, a negative electrode gas composition of 50% H_2O - 50% H_2 and air as sweep gas at the positive electrode side.

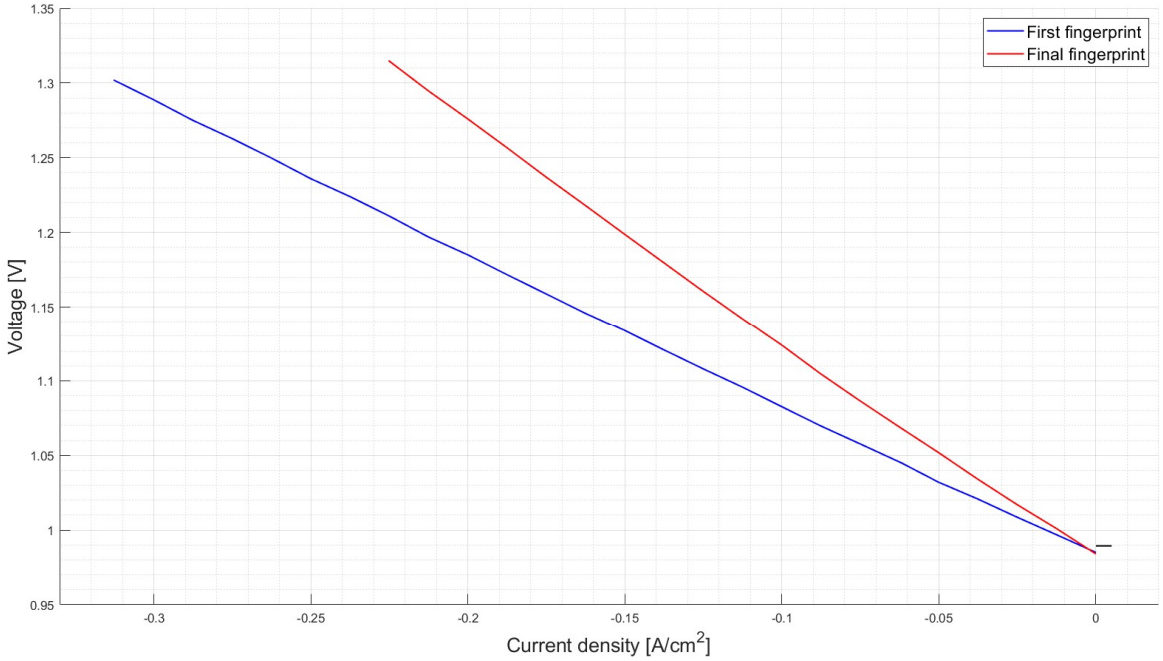

Figure 4.14 - Polarization curves of the ceramic-supported cell recorded during first and final fingerprint - 650 °C, 50% steam content, air.

In Figure 4.14 it is also possible to observe how both polarization curves present almost the same OCV value before and after durability test (just 1 mV of difference). This proves that the leakage that was identified remained stable during the durability test that can be considered not compromised. However, it is likely that in part it also contributed to the increase in both ohmic and polarisation resistances.

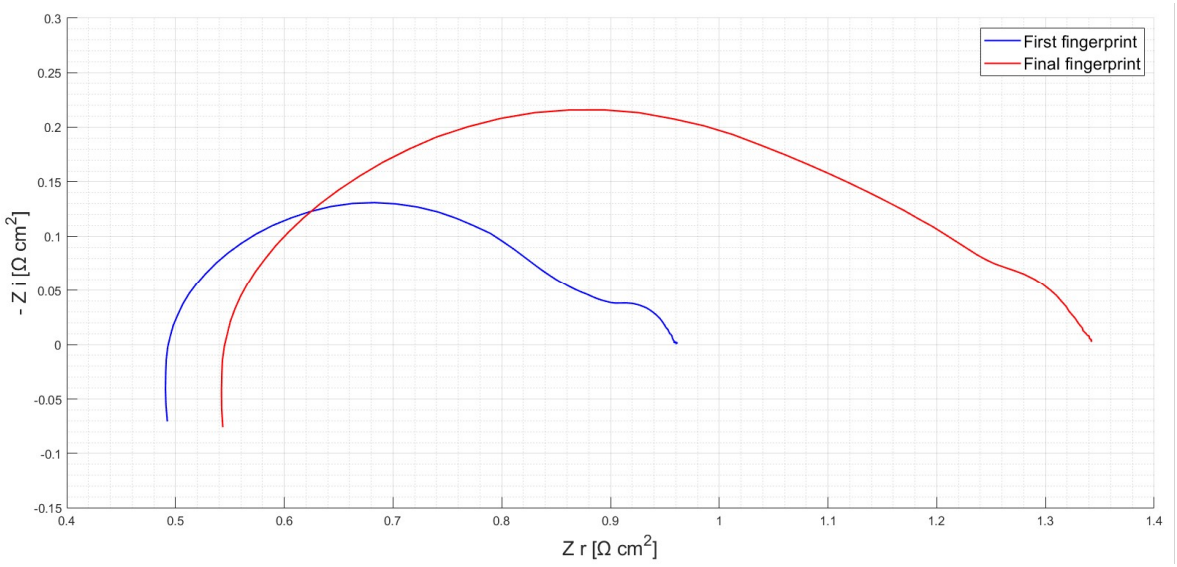

Figure 4.15 - Nyquist plots at OCV of the ceramic-supported cell recorded during first and final fingerprint - 650 °C, 50% steam content, air.

The values of ASR, referred to the polarization curves in Figure 4.14 and computed at 0.2 A/cm^2, are reported in Table 4.6.

Table 4.6 – ASR values of the ceramic-supported cell at 0.2 A/cm^2, before and after durability test - 650 °C, 50 % steam content, air.

	ASR at 0.2 A/cm^2 [Ωcm^2]
Before durability	1.044
After durability	1.554
Percentage change	+ 48.9%

In Table 4.7 the values of ASR extracted from the EIS recorded at OCV during first and final fingerprints at durability test's temperature and feeds are reported, together with their percentage change.

Table 4.7 – ASR values of the ceramic-supported cell extracted from EIS at OCV, before and after durability test - 650 °C, 50 % steam content, air.

	ASR at OCV [Ωcm^2]
Before durability	0.96
After durability	1.34
Percentage change	+ 39.6%

It is possible to conclude that the increase of area specific resistance measured at 650 °C, with 50 % steam content to the negative electrode and air to the positive one, resulted in the order of 40% if measure at OCV and around 49% when measured at 0.2 A/cm^2.

During the final characterization in SOEC mode, at high temperatures and steam contents, recorded OCVs started to show important deviations from the theoretical values and the Nyquist plots started to have an unnatural trend at low frequencies, suggesting that a lot of oxygen was reaching the negative electrode changing drastically the steam content. At this point the test was stopped because the structure of the cell was considered compromised, as would have been further registered data.

4.1.3 Microscopy analysis

After dismounting the cell from the alumina test-house, degradation and cracks were clearly visible. Figure 4.16 shows the cell before mounting (A) and after the test (B,C). The first difference that can be appreciated is the colour of the support: before the test nickel was oxidized (light green) and after it appeared in the reduced metallic form (light grey). In addition to that, the nickel present at the cell inlet remained in its metallic form, while at the center and at the outlet it went back to its oxidized state (Figure 4.16 - C). Such severe oxidation was not observed in previous test samples and it is probably due to the formation of the big crack, which broke the cell at the end of the final characterization. Nickel oxidation clearly started from the center, but during the durability test it was not considered to be as severe as it appears in Figure 4.16 - C.

As already said, durability results are considered trustworthy; however, SEM and EDS analysis at the center and at the outlet of the cell are not reliable to assess durability degradation causes.

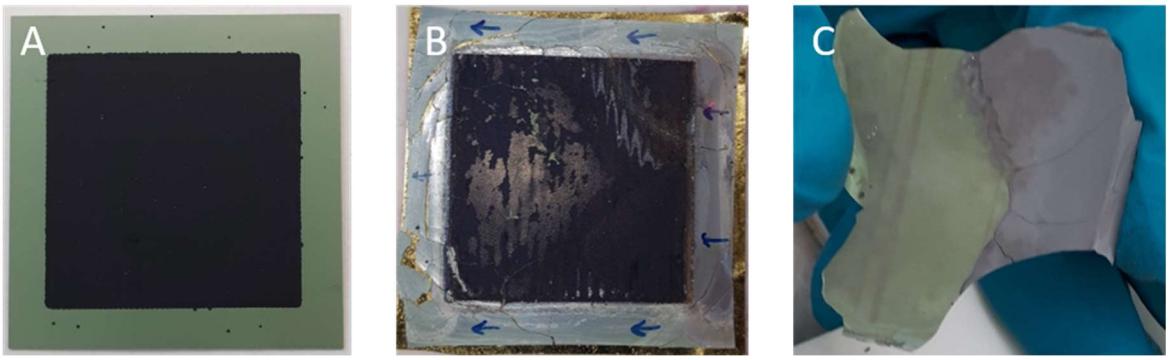

Figure 4.16 - Cell appearance before and after the test: positive electrode and support before the test (A), positive electrode and support after the test (B) and ceramic support - negative electrode side - after the test (C). The arrows on the support structure in image B represent the fuel gas flow's direction.

Figure 4.17 shows a view of the whole cell section at the outlet, where a volume increase in the negative electrode due to the presence of nickel oxides in the crystal lattice produced

cracks perpendicular to the layers, which propagated from the LSM current collector to the electrolyte.

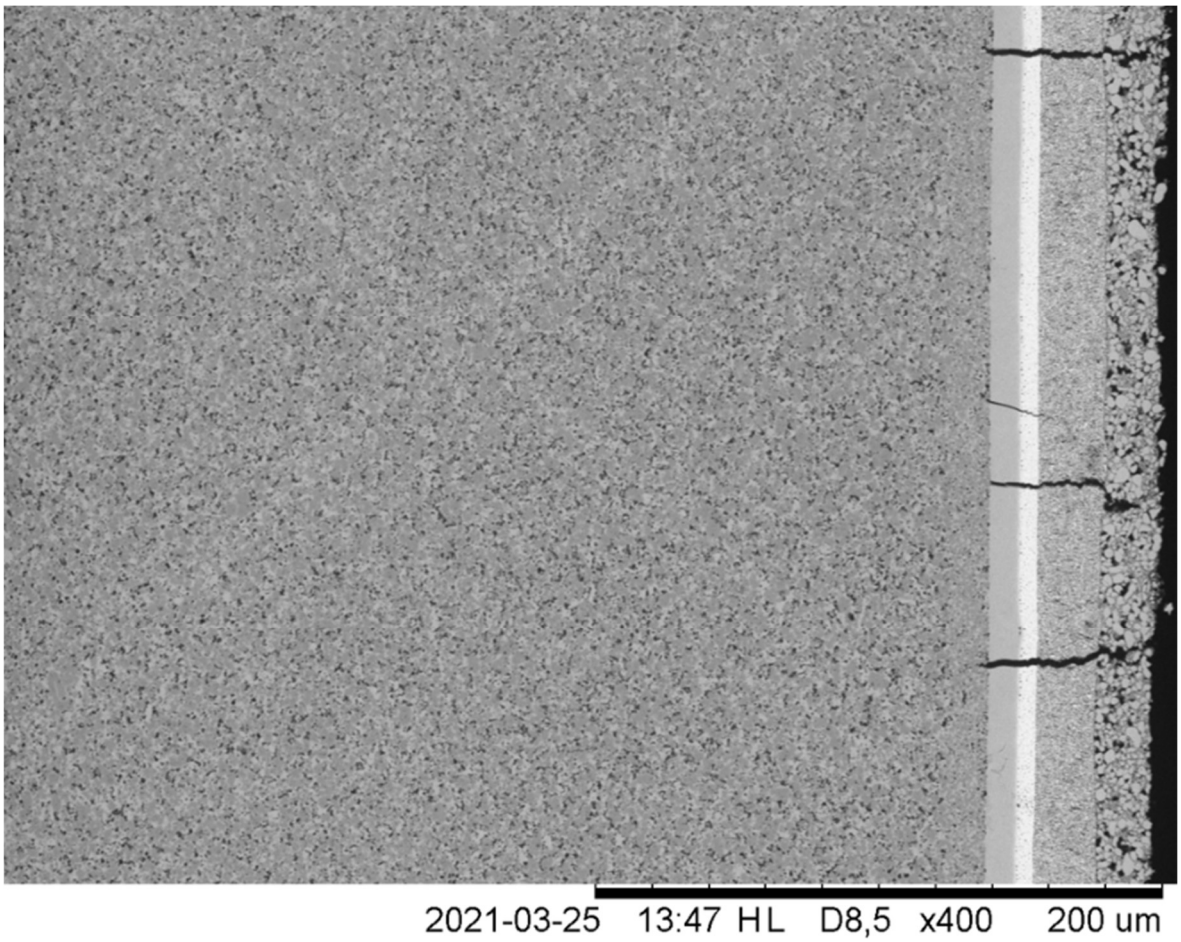

Figure 4.17 – Perpendicular cracks formation at the outlet of the tested cell.

Figure 4.18 shows inlet (1) and outlet (2) comparison between two identical Ni-YSZ ceramic-supported cells: the upper one (A) was only reduced and taken as reference, while the bottom one (B) is the cell tested.

The EIS analysis during durability test suggested that degradation phenomena were related mostly to polarization resistance increase, and SEM and EDS investigation helped in understanding the causes.

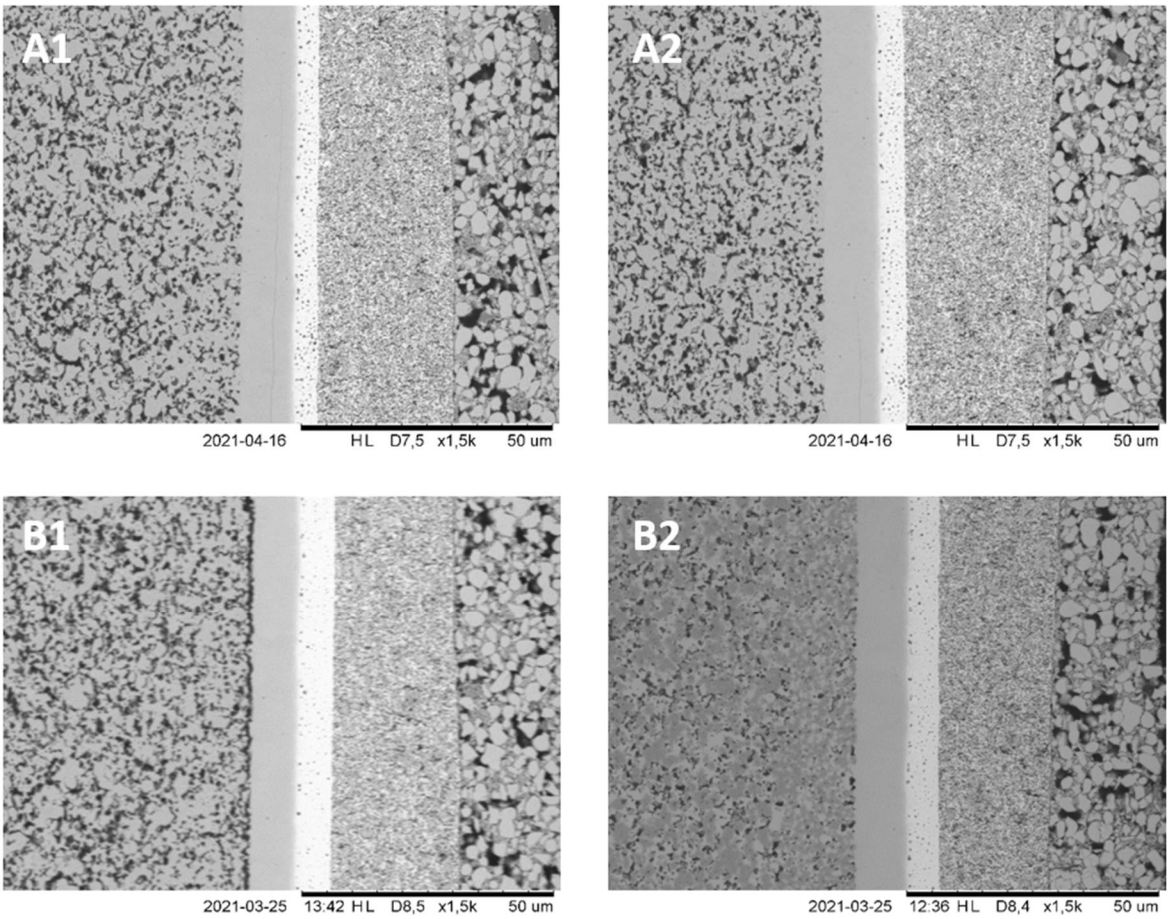

Figure 4.18 - SEM of reference ceramic supported cell, only reduced, at the inlet (A1) and outlet (A2) and tested cell at the inlet (B1) and outlet (B2). The observable layers from left to right are ceramic support and thin active layer close to the electrolyte, electrolyte, CGO barrier layer, LSC oxygen electrode and LSM current collector.

The interface between negative electrode and electrolyte at the inlet is the most stressed part from the electrochemical point of view, for the higher reactant content. In Figure 4.18 – B1 it can be appreciated a loss of contact between these two layers that is probably due to severe redox reactions occurred at the end of the characterization when the cell broke. Such an important loss of catalytic and conductive surface would have produced an important ohmic resistance increase during the durability test, if this occurred at that time. This cannot be observed in the evolution of Nyquist plot reported in Figure 4.11, hence these SEM images cannot be considered reliable to assess durability degradation phenomena at the fuel electrode. However, the small increase in ohmic resistance observed with the EIS analysis is attributed to a loss of electric contact surface between negative electrode and electrolyte at the inlet that during the durability was definitely less severe than what is observed in Figure 4.16 – B1.

Catalytic surface loss was also spotted at the outlet, where nickel oxidation was probably allowed by leaked oxygen. This is clear by looking at Figure 4.18 - B2 where nickel oxides appear as intermediate grey tonality, absent in the other pictures. Checking the OCV values before and after the durability test reported in Figure 4.14, it is thought that the leak did not

affect the test, hence galvanostatic related degradation causes are not assessed to be related to this severe oxidation that most likely occurred only at the end of the final characterization.

Figure 4.19 shows nickel (A) and oxygen (B) concentrations at the inlet (2) and outlet (3) of the tested cell. Only the inlet of the reduced cell (1) is taken as mean of comparison, since there are no differences with the outlet. EDS investigation did not show any appreciable changes in distribution of the other elements present in all the layers.

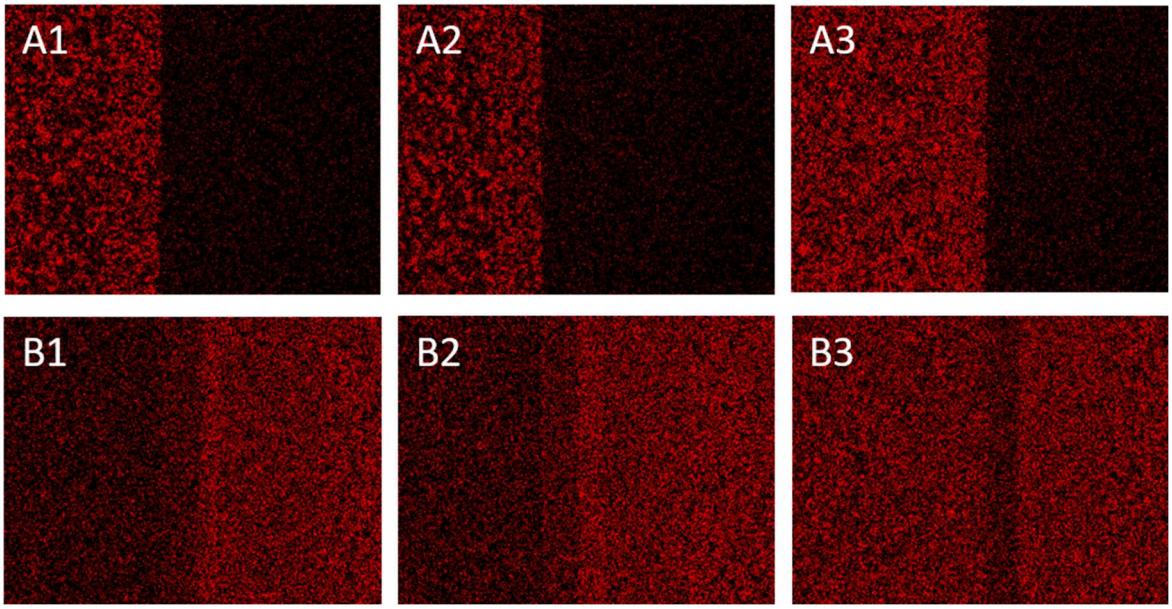

Figure 4.19 - Nickel concentration in the layers at inlet of the reference cell (A1), inlet (A2) and outlet (A3) of the tested cell. Oxygen concentration in the layers at inlet of the reference cell (B1), inlet (B2) and outlet (B3) of the tested cell. To identify the layers the reference is Figure 4.18.

After the test, in the support of the negative electrode at the inlet, nickel appeared slightly more clustered with respect to the reduced cell. This qualitative comparison based on EDS images however is not sufficient to address clearly nickel agglomeration, since the different dimensions of the clusters would be clearly appreciated only using a different microscope with a higher magnification. However, it is plausible to associate the increase of polarization resistance spotted during the durability test to a loss of catalytic surface due to the redistribution of nickel nanoparticles from the interface with the electrolyte towards the ceramic support structure, where they would agglomerate, accordingly to the literature.

Such result was observed by Sun et al., which tested a similar cell at higher temperature and current density [18], and it was considered the main degrading phenomena. Nickel migration and particle coarsening is hypothesized to be due to the formation of $Ni(OH)_x$ gas species [111], [112], [113]. This phenomenon is highly dependent on steam partial pressure, indeed its consequences were observed at the inlet of the cell where this reactant is more abundant.

In addition to that, nickel migration also implies porosity change that as a consequence is more severe closer to the electrolyte where the electrochemical potential is higher and at the

inlet where the steam content is higher. It was not possible to observe this difference in porosity and nickel concentration across the support and active electrode, since this phenomenon occurs very slowly and it would have been highlighted only by a longer degradation test. For instance, this was observed by Sun et al. [18] whose durability test was carried out for 4400 h.

The main cause for low-frequency arc increase, observed in the EIS evolution during durability test, is assessed to be related to a partial deactivation of some areas in the Ni-YSZ electrode, which reduced the TPB active surface and consequently the conversion of steam.

At the outlet, nickel appears much more uniformly distributed (see Figure 4.19 - A3) and this is probably due to the formation of oxides during the last characterization that disassembled existing clusters. The loss of contact between the fuel electrode and electrolyte here is not observed.

Figure 4.20 shows EDS oxygen counts across the layers: A is the reference cell (inlet and outlet do not present any differences), while B and C are respectively inlet and outlet of the tested cell. It is clear that oxygen concentration changed appreciably in the negative electrode and support at the outlet, while remained the same at the inlet in the electrolyte, barrier layer and oxygen electrode (this was not well appreciable by looking at the element map showed in Figure 4.19). This suggests that the negative electrode and support, where nickel is present, are the parts that would be mostly affected by any leak of air or pure oxygen toward such layers. Indeed SEM did not show any difference with respect to the reference cell in the other layers, even when the cell structure was considered compromised.

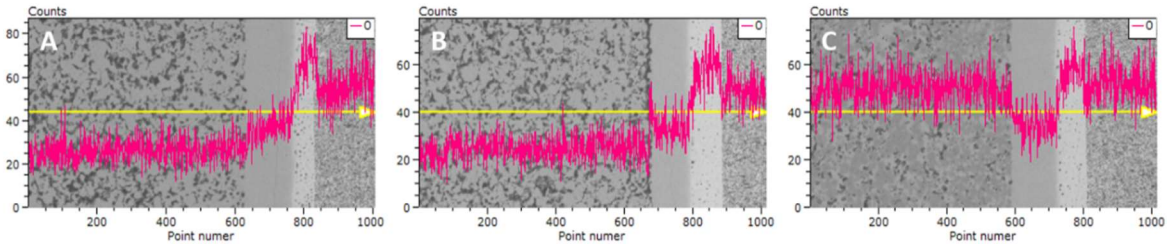

Figure 4.20 - EDS oxygen count across ceramic support, negative electrode, electrolyte, barrier layer and positive electrode. A is the reference, B and C inlet and outlet respectively of the tested cell.

In conclusion, the fuel electrode is thought to be the layer which during long term operation is affected by the main degradation phenomena. It was not possible to clearly demonstrate this assumption since the cell structure was compromised before SEM and EDS investigations. Without a leakage, the performance decay would be attributed mostly to nickel percolation and agglomeration, which would be more severe at the inlet of the cell and close to the electrolyte. This would imply an increase of the ohmic resistance but more appreciably of the polarization one. An additional loss of performance, which affects all the resistances contributions, can be also given by the formation of a crack that would allow nickel oxidation.

Finally, this test showed how ceramic supported cells are very sensitive to thermal and mechanical stresses that facilitate the formation of cracks compromising the cell. This indeed is what R&D is aiming to achieve through the development of high performing and stable metal supported cells.

4.2 Metal-supported cell

In this section the metal supported cells' tests are discussed. The lack of previous tests for this technology made test plans challenging, since it was not possible to have a clear idea about the possible behaviour of the cell under different operative conditions.

The metal support structure is very sensitive to steam presence and to high temperatures, which cause corrosion in the metallic layers. Therefore, only few operating conditions were selected. As a consequence, the cell performance assessment relies on less data, and this added a degree of difficulty in the interpretation of the results, together with the lack of literature for such recently developed technology and specific materials combination.

Data from the final characterization of the second cell tested are used as a mean to illustrate cell performances, the reasoning behind this choice will be discussed as soon as useful results for this purpose will be showed.

4.2.1 Cell characterization

Table 4.8 shows the OCV deviations from the theoretical values calculated with Nernst equation (see Appendix A). It is possible to appreciate that all the values are in the acceptable range, hence the related polarization and EIS curves are considered trustworthy.

Table 4.8 - OCV deviations [mV] from theoretical values for all the i-V curves registered in electrolysis mode with the metal-supported cell, at different temperatures and steam content, for air and oxygen. Green: acceptable deviation; red: unacceptable deviation (more than 10 mV).

	650 °C		700 °C	
20%	0	3	1	2
50%	3	0	2	1
	Air	O_2	Air	O_2

In Figure 4.21, polarization curves are reported separating the effects of temperature and different feeds in two different plots. In the left one the i-V curves recorded at 700 °C and 650 °C, with 50% steam fed to the negative electrode and air to the positive one are shown, and it can be appreciated that the temperature strongly affects cell's total resistance. On the right one instead, showing the i-V curves obtained at 650 °C with 20% and 50% steam fed to the negative electrode and both air and oxygen fed to the positive one, is also appreciable a dependence of such parameters on the polarization curves.

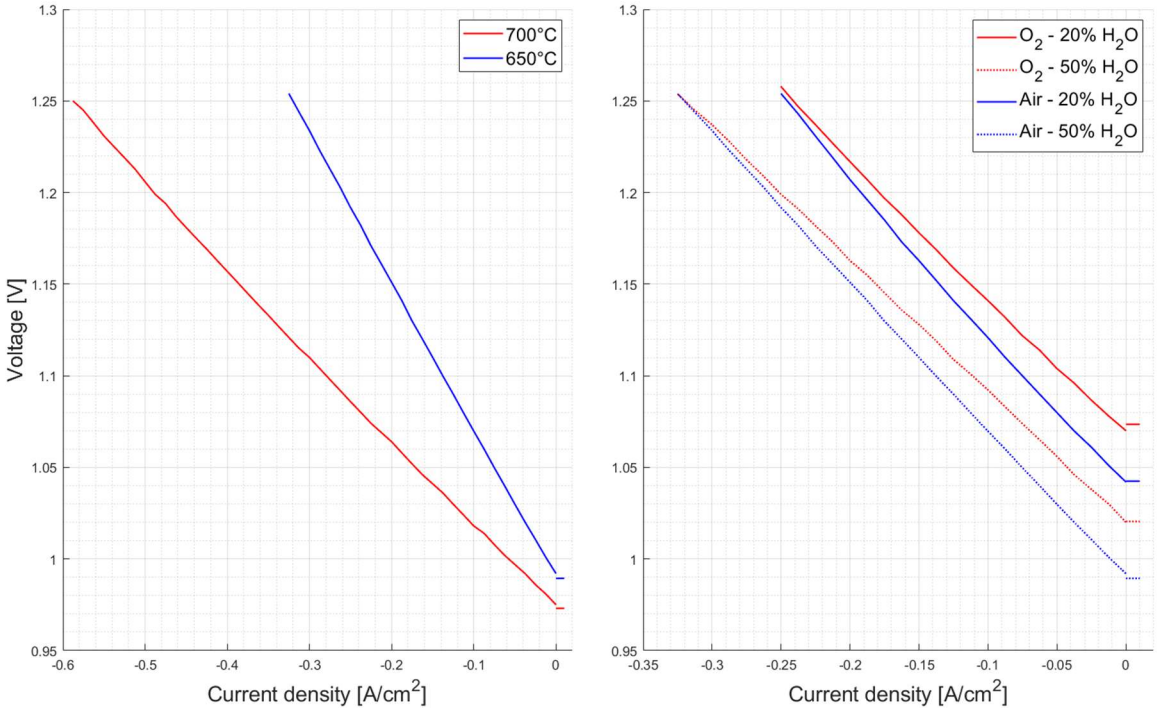

Figure 4.21 - Metal-supported cell's polarization curves with theoretical OCVs – 50% steam, air, different temperatures (left); 650 °C, different feeds (right).

Table 4.9, where all the ASR values measured for the metal-supported cell at 0.15 A/cm^2 are reported, helps to appreciate the dependence of the total resistance to the different feeds. At 650 °C particularly, the ASR increases significantly switching from oxygen to air at the positive electrode (keeping fixed temperature and steam content at the negative one) and decreasing steam content at the negative electrode (keeping fixed temperature and feed at the positive one), even if the limit current density limit is not visible from the polarization curve.

Table 4.9 – Metal-supported cell's ASR measured at 0.15 A/cm^2 at different temperatures and feeds.

Temperature [°C]	650				700			
Steam content [%]	20		50		20		50	
Positive side gas	Air	O_2	Air	O_2	Air	O_2	Air	O_2
ASR [Ωcm^2]	0.915	0.804	0.821	0.731	0.522	0.501	0.443	0.400

This evident dependence of the total resistance on all the operative parameters, can be furtherly analysed by means of EIS investigation.

Figure 4.22 highlights the differences in the imaginary impedances recorded between 650 °C and 700 °C, 20% and 50% steam partial pressure at the negative electrode and air and oxygen at the positive one, keeping fixed all the other parameters.

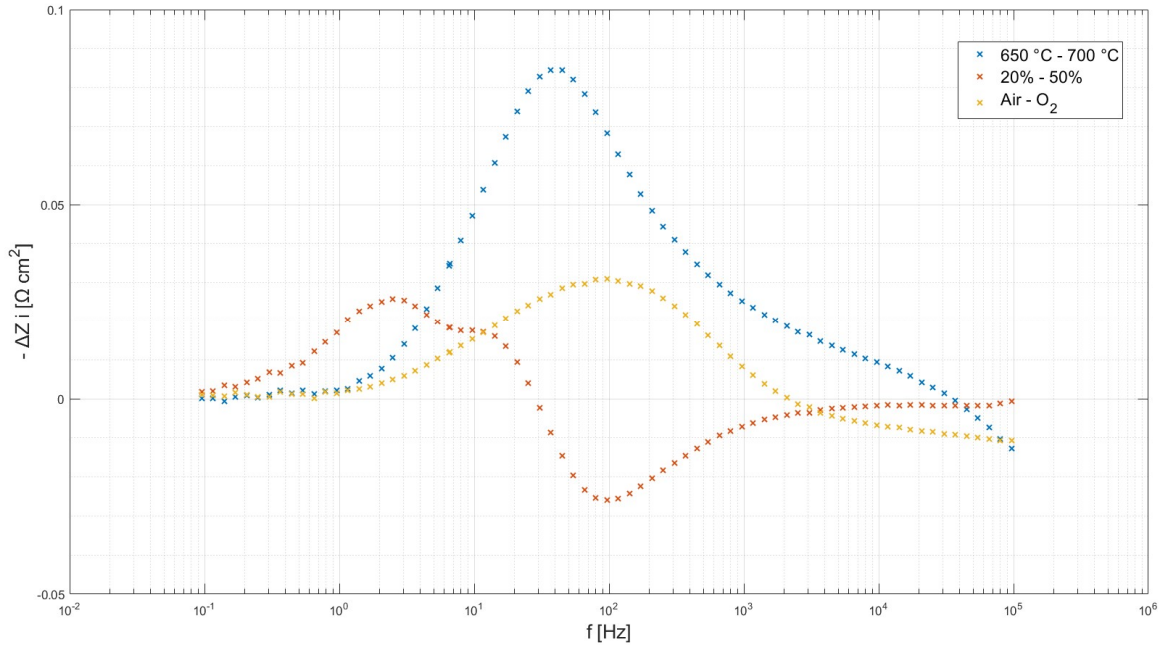

Figure 4.22 - Metal-supported cell's differences of imaginary Bode plot. Blue curve: change of temperature, with air to the positive electrode and 50% steam to the negative one. Orange curve: change of steam content at the negative electrode, with air to the positive one and temperature of 650 °C. Yellow curve: change in oxygen partial pressure at the positive electrode, with 50% steam to the negative one and temperature of 650 °C.

Temperature has mainly influence on the medium frequency region, but also at higher frequencies some effects can be observed. The central peak highlights phenomena related probably to kinetics and indeed higher impedance was registered at 650 °C. Temperature influence on high frequency region (10^5 Hz) should be investigated in Nyquist plots, since electrolyte ionic conductivity is modelled through purely real impedance.

Steam composition affects low and medium frequency regions. Dealing with the low frequency region, multiple peaks indicate that different phenomena are involved and the 50% steam composition seems to be the one that implies a lower conversion-related impedance, since the EIS curves were registered at OCV.

A negative difference at around 100 Hz between 20% and 50% steam compositions to the negative electrode, means that a lower impedance was recorded at 20%. Generally, steam enhances the catalytic activity of nickel, hence a higher steam content leads to better kinetics of the reaction. Here anyway the opposite is observed, suggesting that something unexpected occurred, hiding the actual kinetic dependence on steam partial pressure.

The impedance difference between air and oxygen at medium frequencies, and particularly the fact that oxygen implies a lower resistance, is again attributed to the EIS registered at OCV.

Distinctive behaviours of the metal-supported cells can be observed focusing on the high frequency region. Here however is not possible to talk about ohmic resistance since only the

imaginary part of the impedance is shown in Bode plots. Indeed, in such plot, steam partial pressure does not seem to influence the high frequency region, however Figure 4.23 – showing the Nyquist plots obtained at 20% (above) and 50% (below) steam composition at the negative electrode, with both air and oxygen fed at the positive electrode and at 700 °C and 650 °C – suggests the opposite. The ohmic resistance seems to be affected not only by the temperature, but slightly also by the feed composition.

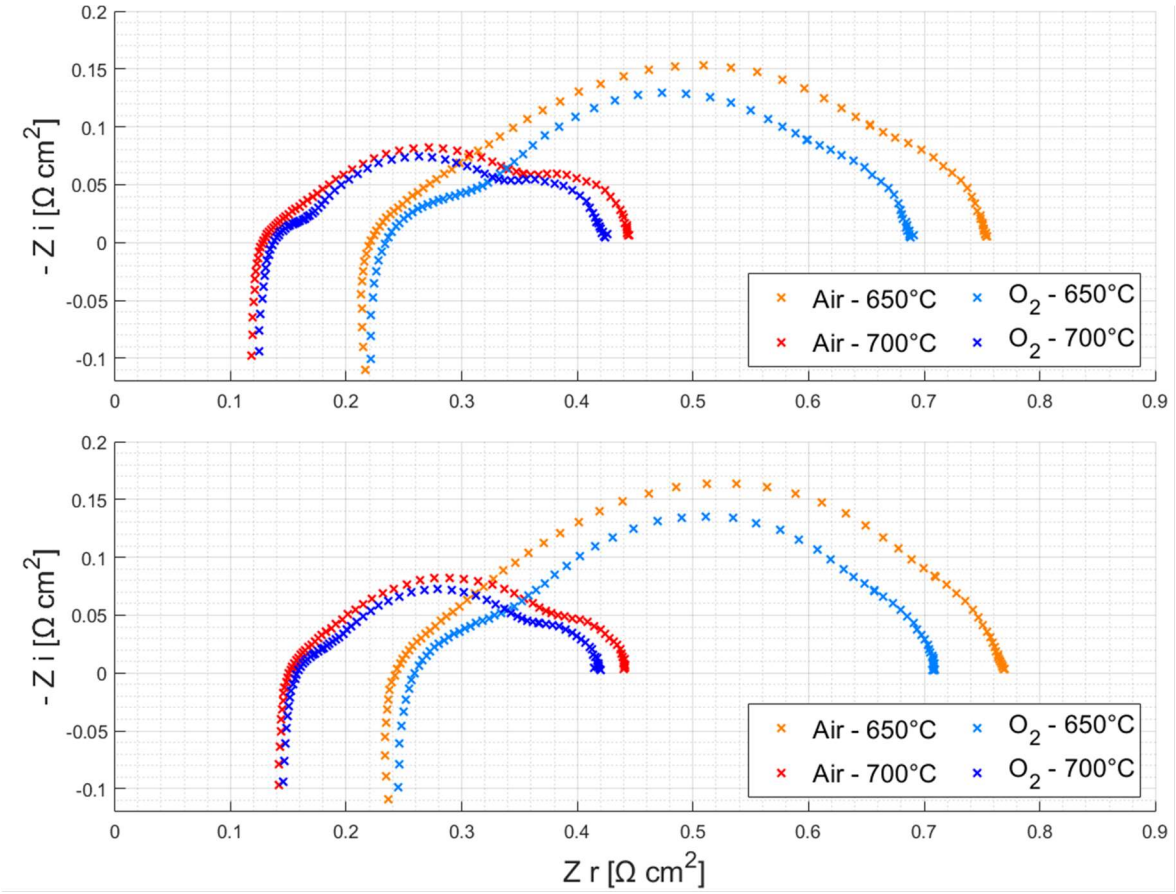

Figure 4.23 - Nyquist plots of the metal-supported cell's at 20% (above) and 50% (below) steam content.

Changing the steam partial pressure at the negative electrode, the ohmic resistance would change increasing as the steam content in the mixture fed increases. This behaviour could be attributed to metal support oxidation, which is enhanced as steam partial pressure increases, when the thermodynamic conditions are favourable. At this point, it is plausible to divide the ohmic resistance in two contributions: the main one is given by the electrolyte, which ionic conductivity strictly depends on temperature; a second share can be attributed to the metallic support's structure. This contribution is smaller but not negligible, and it mainly depends on the steam content at the negative electrode.

Looking at the evolution of the ohmic resistance over time across the whole characterization test, reported in Figure 4.24, it is appreciable how the ohmic resistance increase during the

test, seem to be more affected by time, or in other words on the number of polarization curves registered, than a change in feed compositions in any electrode. Particularly EISs and polarisation curves were always registered first feeding air to the positive electrode, and then pure oxygen, therefore, referring to the ohmic resistance with oxygen always results a bit higher than with air. This explains the apparent different ohmic resistance given by oxygen and air fed to the positive electrode shown in Figure 4.23.

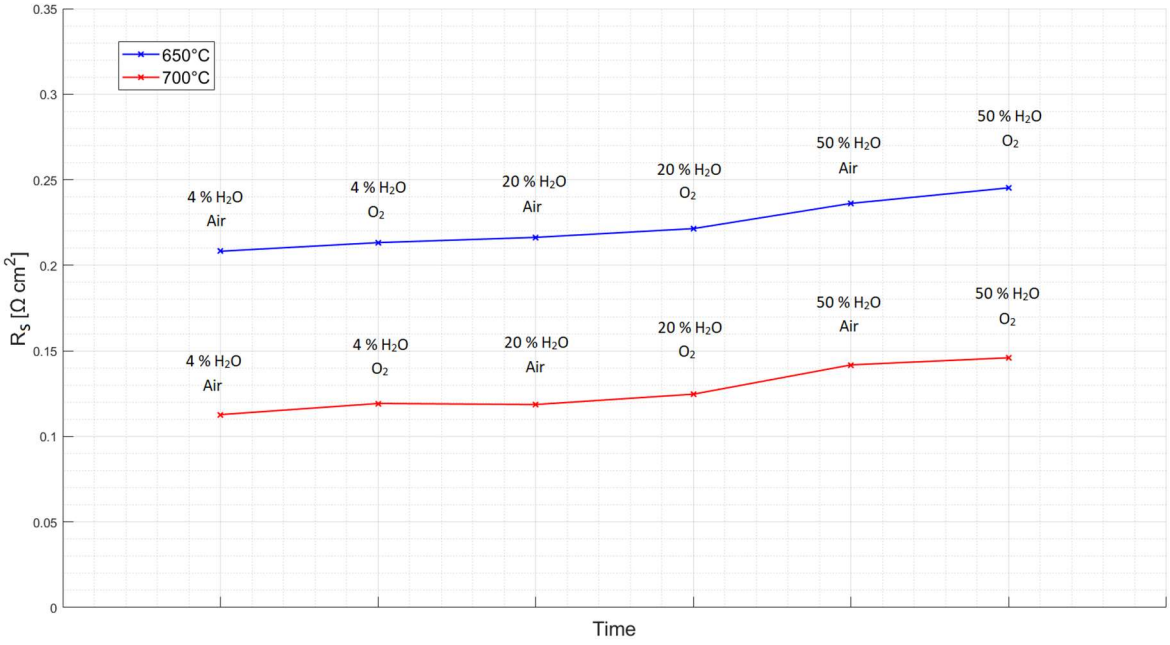

Figure 4.24 - Variation in time of serial resistance for the MSC during characterization tests.

It is thought that when current is applied during polarization curves registration, steam partial pressure is sufficiently high to determine metal support oxidation at the operative temperature. This is in accordance with the decision to limit the steam percentage in the fuel feed to a maximum of 50%, in order to prevent excessive metal oxidation. It is not possible to verify completely this assumption since two main information are missing: the exact local oxygen (steam) partial pressure inside the pores of the metallic support, and a reference for the thermodynamic oxidizing conditions of tape casted Fe-Cr alloy. Anyway, it is plausible that higher temperatures, as well as SOFC operation mode would increase the magnitude of this phenomenon.

Referring to test structure in sub-section 3.4.2, data obtained with the first tested cell during both characterizations were considered not reliable, since the characterization was also performed in SOFC mode at 750 °C.

In addition, a problem on the gas supply at the beginning of the second test caused a reduction of fed hydrogen and hence an increase in steam partial pressure. The amount of hydrogen reaching the cell was always much lower than the nominal composition required for the test, so the percentage of steam resulted to be much higher giving unwanted

compositions. This probably caused again oxidation of the metallic support. Anyway, the severity of this second oxidation was not as important as with the first cell. Before performing the second durability test, the gas supply pipe was repaired and the leakage stopped, so the results of the final characterization as well as of the durability test, can be considered trustworthy.

4.2.2 Durability test

The time evolution of cell voltage during the 500-hours galvanostatic tests, with air supplied to the positive electrode as sweep gas and a 50% H_2 - 50% H_2O mixture (total flow of 12 l/h) supplied to the negative electrode, is reported in Figure 4.25 for both the tested MSCs. The first cell was tested at a current density equal to 0.25 A/cm^2, corresponding to a steam utilization of 28%, while the second one was tested at 0.5 A/cm^2, hence with a fuel utilization of 56%.

The durability tests gave unexpected results: the cell voltage did not increase, as would be a normal consequence of degradation; instead, an activation process, implying a constant reduction of the voltage, was observed. It was decided to test the second cell with a different characterization procedure to assess the possible causes of the behaviour observed during the first test, in addition a double current density was chosen to try to observe degradation.

As happened also with the ceramic-supported cell, the profiles of both MSCs present some discontinuities due to unforeseen events: in case of the first tested cell, between the 470 and 476 hours, the current dropped to 0 A because of a temporary shut-down of the power supply unit; in case of the second cell instead, after 165 hours of operation a failure of the main hydrogen supply unit of the laboratory activated the safety gas flow, that was fed to the cell for some hours until the problem in the lab was solved. Anyway, in both cases these problems did not compromise the final results.

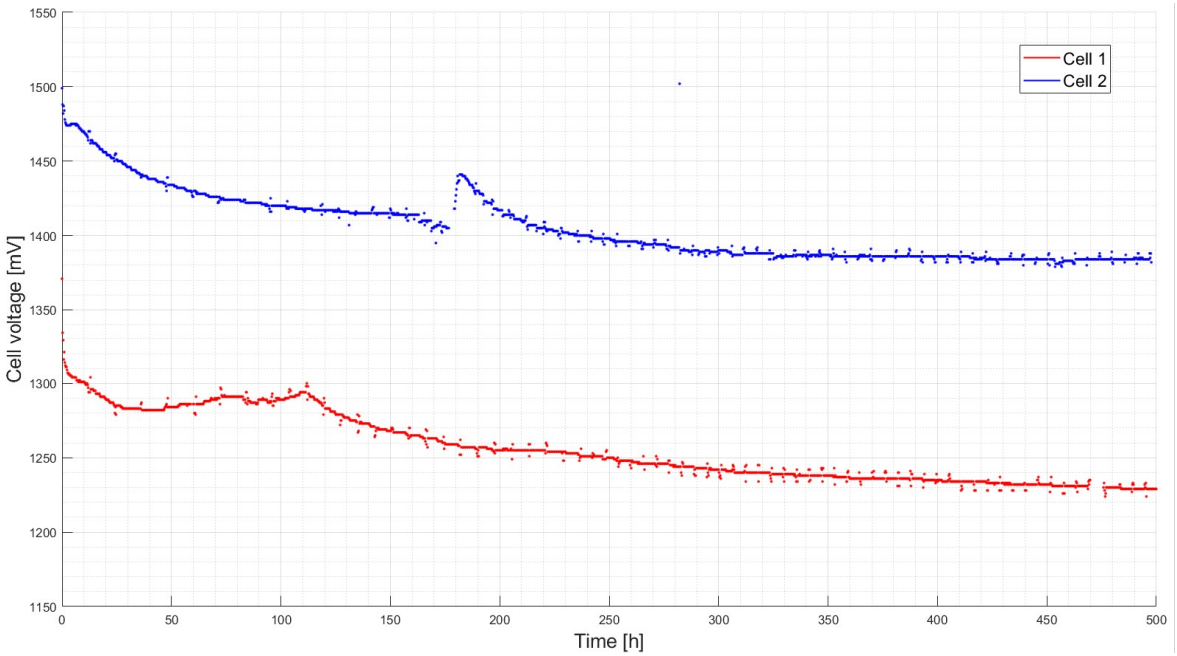

Figure 4.25 - Cell voltage profiles of the MSCs during durability test: first cell (0.25 A/cm^2) below, second cell (0.5 A/cm^2) above.

The decreasing trend with time is mainly attributed to oxidation of the metal support occurred in the first characterization tests. During durability tests, the voltage slowly decreases because in SOEC mode the reducing conditions at the negative electrode are hold constantly, allowing to slowly restore the oxidized metal support and increase its electric conductivity, visible as a reduction of ohmic resistance and cell voltage. In addition, it is thought that the thermodynamic conditions are not as favourable as during the polarization curves recording in terms of steam partial pressure, as previously explained. Particularly, with a feed containing 50% steam at the inlet, steam partial pressure at the outlet is 22% and 36% during the durability tests at 8 A and 4 A respectively, while reaches 41% at the maximum current (about 5.1 A) during the polarization curve in electrolysis. These values have been computed considering the steam converted in hydrogen through Faraday's law (2.2). Moreover, it is also thought that the oxidation process is much faster than the reduction. Indeed, during the polarization curves registration the current changes every 0.2 s and a continuous increase in ohmic resistance was observed (Figure 4.24) while during the durability test the current remained stable for a long time and the opposite trend was observed.

Despite the two durability tests were performed at different currents (one the double of the other), a similar trend in terms of voltage reduction rate was observed. However, the initial performances were better (lower voltage) and that proved the fuel cell mode affection.

With the first MSC, the cell voltage kept decreasing for the whole durability test's duration, while in the second case it decreased mainly for the first 300-350 hours, after which it started to be much more stable. This different behaviour is probably the consequence of the less

careful operating conditions adopted in the first test: during the initial characterization, the first cell was tested in fuel cell mode also at 750 °C. Again, in SOFC mode steam is a product of the electrochemical reaction, so the resulting steam content inside the metal support structure reaches very high values; moreover, the high temperature increases the severity of this oxidizing process. With the second cell instead the characterization was carried out with much more care, limiting fuel cell mode and keeping the temperature at a maximum of 700 °C. Unfortunately, the leak in the hydrogen supply pipe (which appeared during night and so could not be fixed immediately) led anyway to a presence of steam in the metal structure higher than intended, which oxidized again the metallic layer. The consequences of this unfortunate event were still less severe than in the first test, indeed in the second durability test the "healing" of the support was faster. If with the first cell the durability test had not been interrupted, but it had been continued for more than 500 hours, the voltage decrease would have been expected to stop once the reduction was completed, as observed in the second test.

As already explained in sub-section 4.2.1, the Fe-Cr metal support of the tested MSC is very sensitive to steam presence. Oxidation is very fast, indeed few minutes of operation are enough to oxidize the support, while it takes a long time to reduce it back to the initial form (in this case it is has been observed that the necessary time is in the order of hundreds of hours).

For the assessment of cell degradation, it does not make much sense to provide a value of degradation rate as done for the ceramic-supported cell. Anyway, just for sake of completeness of the discussion, the cell voltage values are here reported.

For the first tested MSC, the voltage changed from an initial value of 1371 mV to a final value of 1229 mV, resulting in a reduction of 142 mV in 500 hours. Most of this voltage reduction (58%) happened in the first 20 hours, while in the other 480 hours the decreasing trend resulted less steep.

For the second MSC, the voltage changed from an initial value of 1499 mV to a final value of 1384 mV, resulting in a reduction of 115 mV in 500 hours. Also in this case the first hours were characterized by a fast voltage reduction, that then got slower and slower until, after 350 hours, the cell voltage became pretty stable.

These voltage values correspond to electric efficiencies, computed as in equation (2.8), equal to: for the first tested cell, 90.69% at the beginning of the 500 hours and 101% at the end; for the second one, 82.94% at the beginning of the 500 hours and 89.83% at the end.

The Nyquist plots of the EISs recorded during durability test are shown in Figure 4.26. The colour of the curves turns from blue to red as time passes.

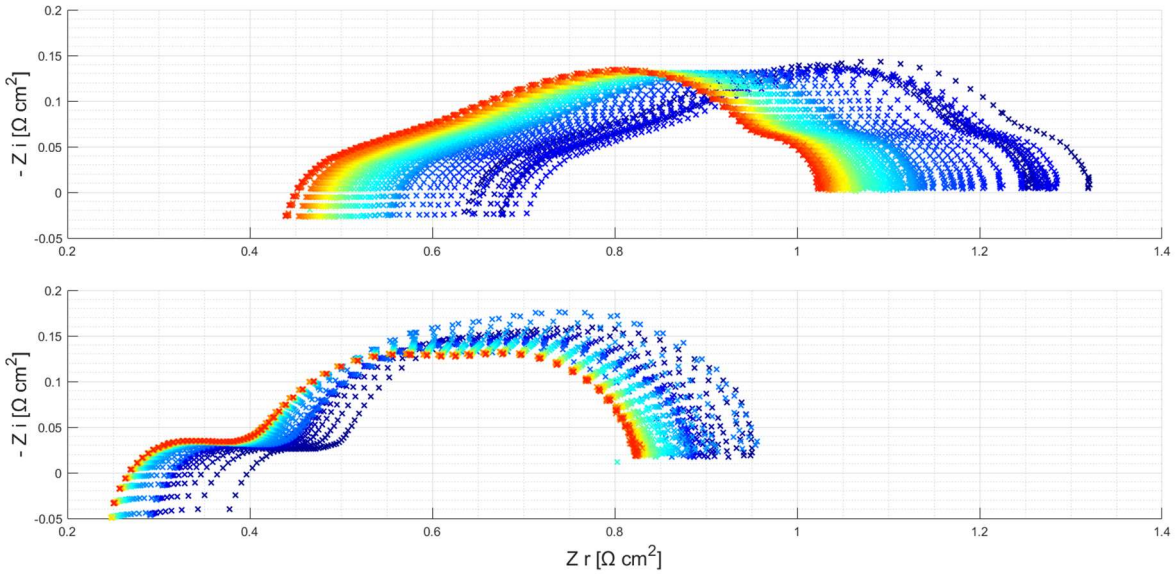

Figure 4.26 - Nyquist plots during durability tests for the MSCs: first cell (0.25 A/cm^2) above, second cell (0.5 A/cm^2) below. The evolution is followed changing colour from blue to red.

It is evident that increasing the current the shape of the curve changes substantially, while with the ceramic-supported cell this was not observed comparing the curves obtained during the characterization and the durability tests. At the end of the second MSC's durability test, while stepping down the current from 8 A to 0 A, impedance spectroscopy was performed to understand current´s influence on the shape of the curve. Figure 4.27 shows the obtained Nyquist plots.

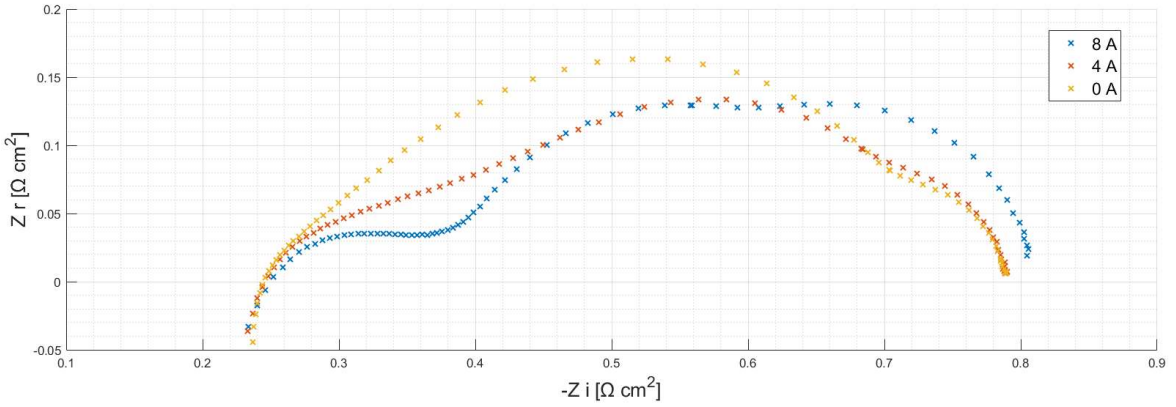

Figure 4.27 - MSC's Nyquist plots at durability test conditions (650 °C, 50% steam content, air) registered at different currents.

Increasing the electric current density, the low frequency gets bigger, since the conversion of the reactants increases. An unordinary behaviour is observed at medium frequencies: the peak of the medium-frequency arc moves towards lower frequencies as the current is raised. This means that it gets closer to the low-frequency arc, to the point that it is very complicated to distinguish them, but on the other hand, the high-frequency arc becomes more noticeable. The influence of current on the shape of the arcs was not further investigated since this

project is more focused on the assessment of degradation phenomena than in a modelling of the cell system.

Figure 4.28 shows the trend of ohmic and polarisation resistances during time, together with the ASR.

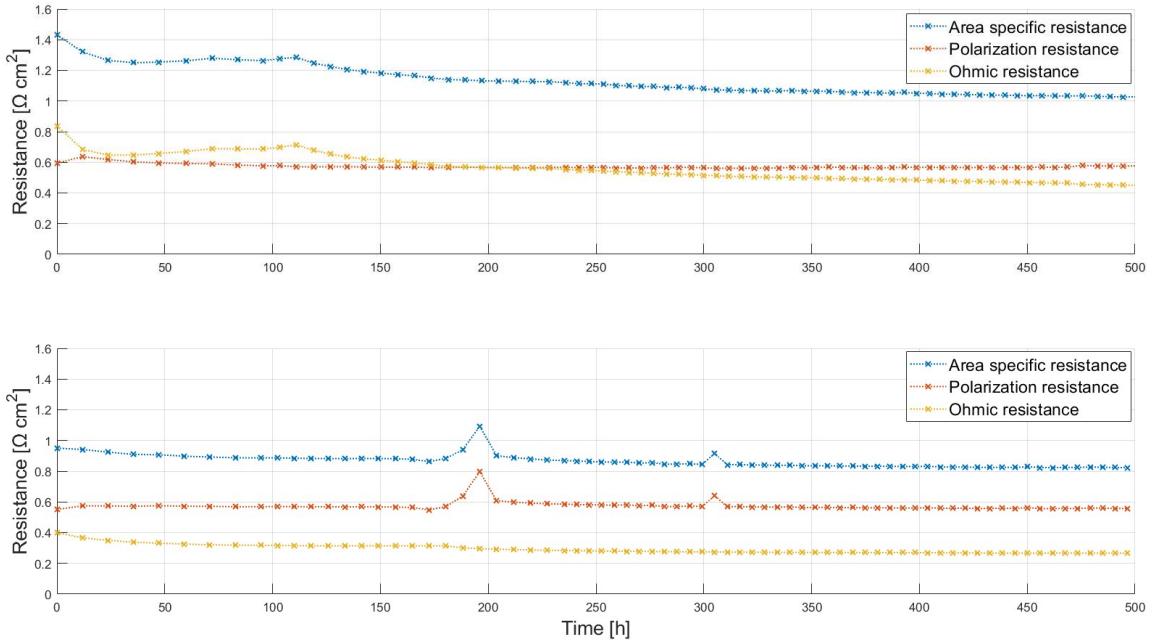

Figure 4.28 - Trend of the several resistance contributions during durability test for the MSCs: first cell above, second cell below.

These trends of resistances help understand why data from the final characterization of the second tested cell were used as a mean to illustrate cell performances in the previous sub-section, since they were registered at the lowest resistance conditions and are more indicative of the actual cell potentiality.

The values of the resistances at the beginning and at the end of the durability test, for the first and second tested MSCs, are reported respectively in Table 4.10 and Table 4.11. From these data it is confirmed that, in both cases, the ohmic resistance is the main contribution that affects the observed cell voltage change, in particular the contribution given by the metal support (that is not related to the cell's behaviour per-se, but to the unwanted oxidation), while the polarization resistance appeared to be extremely steady.

It would be interesting to perform a longer durability test, particularly it is thought that a few thousand hours (3000 h for instance) would be sufficient to appreciate degradation phenomena related to the electrodes.

Table 4.10 - Resistance contributions of the first tested MSC, before and after durability test, with a current of 0.25 A/cm^2.

	R_s	R_p	ASR
Start of the test	0.837 Ωcm^2	0.594 Ωcm^2	1.431 Ωcm^2
End of the test	0.451 Ωcm^2	0.577 Ωcm^2	1.028 Ωcm^2
Change	- 0.386 Ωcm^2	- 0.017 Ωcm^2	- 0.403 Ωcm^2
Percentage change	- 46.12%	- 2.86%	- 28.16%

Table 4.11 - Resistance contributions of the second tested MSC, before and after durability test, with a current of 0.5 A/cm^2.

	R_s	R_p	ASR
Start of the test	0.400 Ωcm^2	0.551 Ωcm^2	0.951 Ωcm^2
End of the test	0.266 Ωcm^2	0.557 Ωcm^2	0.823 Ωcm^2
Change	- 0.134 Ωcm^2	+ 0.006 Ωcm^2	- 0.128 Ωcm^2
Percentage change	- 33.50%	+ 1.09%	- 13.46%

Figure 4.29 shows the difference of imaginary impedance along the long-term test, taking as reference the first curve registered. As before, the colour turns from blue to red as time passes. In both cases, the module of impedance changes is much lower with respect to the ones registered with the ceramic-supported cell. This confirms that the magnitude of the capacitive-related degrading processes occurred during the galvanostatic test was limited.

The two graphs have difference shapes:

- At 0.25 A/cm^2 (upper plot), the frequency range mainly affected by the long operation is between 10-20 Hz. Anyway, the change occurred just in the first hours and then the impedance at these medium-low frequencies remained quite constant. This range is related to processes involving the negative electrode, as demonstrated in Figure 4.22 changing the composition of the feed to such electrode.

  Other two frequency ranges where smaller changes in impedance can be observed are at ca. 100 Hz and 30000 Hz. In the first case, the parameters having effects in this frequency range are both steam content to the negative electrode and oxygen partial pressure to the positive one (see Figure 4.22). At 30000 Hz it cannot be clearly stated which factor mainly contributes to the peak. Very high frequency range is mainly related to movement of charged species, which also might imply capacitive or inductive phenomena spotted at slightly lower frequencies. As before, the impedance change in these two ranges occurred just in the first hours. In conclusion, the considerations just made indicate that the very small initial change in polarization

resistance, observed in Figure 4.28, is related to phenomena happening in the electrodes, particularly at the negative one.

- At 0.5 A/cm^2 (plot below) the frequency range mainly affected by the galvanostatic operation is around 1-2 Hz. Again, the main parameter affecting this region of the Bode plot is the steam percentage in the negative electrode feed. The light blue lines for the second plot in Figure 4.29 should be neglected, not being representative of the nominal operating conditions (they were recorded during the failure of the main hydrogen supply unit of the laboratory). Two other small peaks are observed at around 40 Hz and 3000 Hz; the same assessments done for the case at 0.25 A/cm^2 about the involved layers, remains valid since higher currents shift the peaks of different phenomena toward lower frequencies.

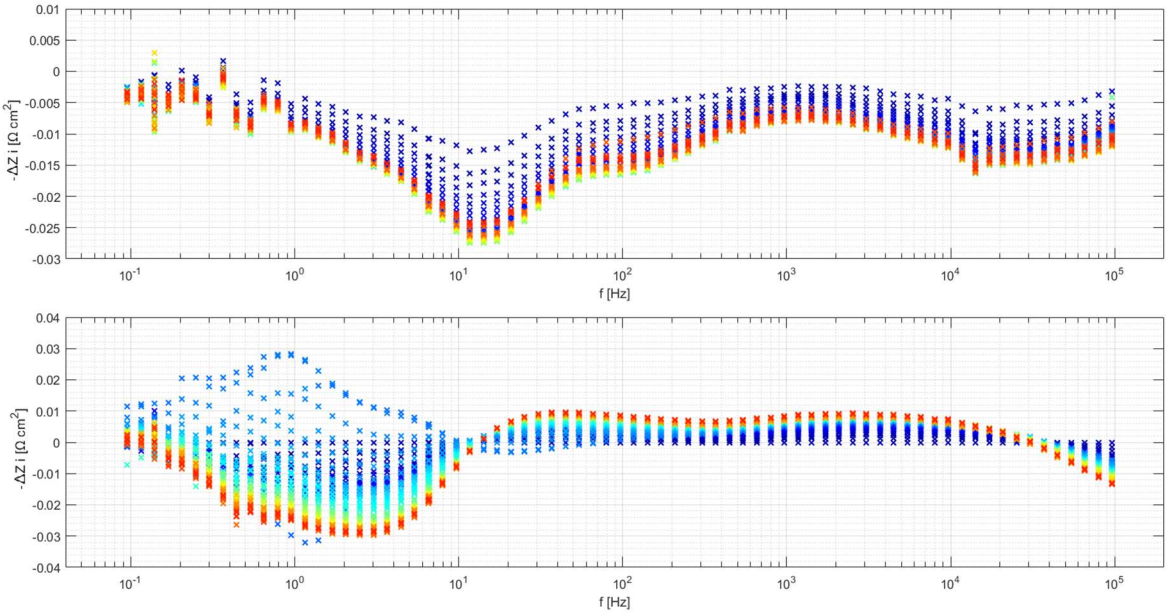

Figure 4.29 - Metal-supported cells' differences of imaginary Bode plot during durability test (the reference is the first EIS recorded, the evolution is followed changing colour from blue to red): first cell above, second cell below.

During the first test, an improvement of all processes has been spotted, being the impedance difference always negative at all frequencies. This observation, together with the ohmic resistance reduction (see Figure 4.28), proves that the initial cell conditions for the durability test, consequence of the first characterization, were so bad that all the process improved thanks to the reactivation process.

Instead, the second tested cell showed a continuous impedance improvement in the low-frequency region, demonstrated by the negative impedance differences. The initial cell conditions for the durability test were less compromised with respect to the first one, therefore the benefits of the activation process hid less the always present degrading phenomena. As a consequence, a slight electrodes degradation is observed as positive impedance difference at medium frequencies.

The change of impedance in the low-frequency region could be related to better gas conversion at the negative side, thanks to the reduction of the metal support. While the change at medium frequencies could be attributed to electrodes degradation implying a worsening of the reactions' kinetics.

The data obtained during the characterisations on the two metal-supported cells, unfortunately, cannot be used to make a reliable comparison, in terms of polarisation and EIS curves, between the pre- and post-durability test performances, as done in the previous section for the ceramic-supported cell. As already mentioned, with both the tested MSCs the data obtained during the first fingerprint are not representative because the tests where compromised in the first case by the unexpected extreme oxidation of the metal support, and in the second case by the failure of the hydrogen supply pipe.

4.2.3 Microscopy analysis

A first macroscopic investigation of the cells after dismounting did not show particular features but only the presence of metal oxides in the sides of the support structures. Figure 4.30 shows the first and second cells tested after the durability test (B and C respectively), and the first cell before the test as a mean of comparison (A); it is immediately appreciable that the oxidation was much more severe in the first cell tested, as anticipated by data analysis. A difference with the ceramic supported cell is that most of the oxygen electrode remained attached to the gold positive current collector. This is attributed to different materials used, and the consequences of that are not relevant since this electrode did not suggest any relevant degradation phenomena during the tests (also seen for the ceramic supported).

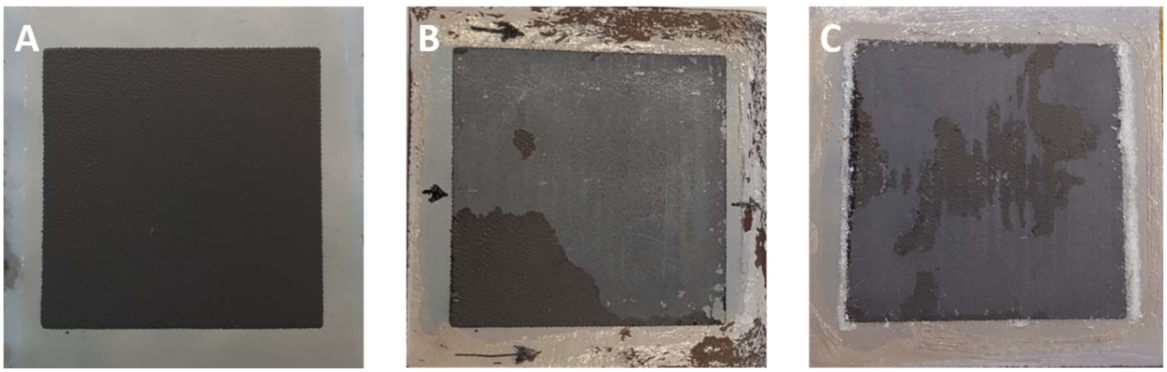

Figure 4.30 - Reference MSC before test (A); first (B) and second (C) cells after durability test.

SEM and EDS investigation was focused on addressing qualitatively the impact of current on the LSFNT fuel electrode and to confirm the presence of metal oxides in the support structures.

Unfortunately, it was not possible to have a mean of comparison with a reference cell that was only activated and did not go through a durability test, as it was done for the ceramic supported, since the availability of MSC at DTU was very limited. In addition, since such technology is recently developed, priority would be given to longer tests aimed to understand the behaviour of the cell in different operating conditions (fuel cell degradation tests, reversible fuel cell/electrolysis operations, direct hydrocarbons oxidation, CO_2 co-electrolysis, etc.).

The slight change in medium frequency resistance, observed during the second durability test at 8 A, suggested a worsening of kinetics that could be attributed to a small loss of catalytic surface. The cause could be related again to nickel migration and particles agglomeration, as happened with the ceramic supported cell; however, in the metal supported samples it was not possible to observe that by means of neither SEM or EDS. Investigating the fuel electrodes, no differences were spotted between inlet and outlet for both the cells tested at 4 A and 8 A. In Figure 4.31 only the images taken from the second cell are shown.

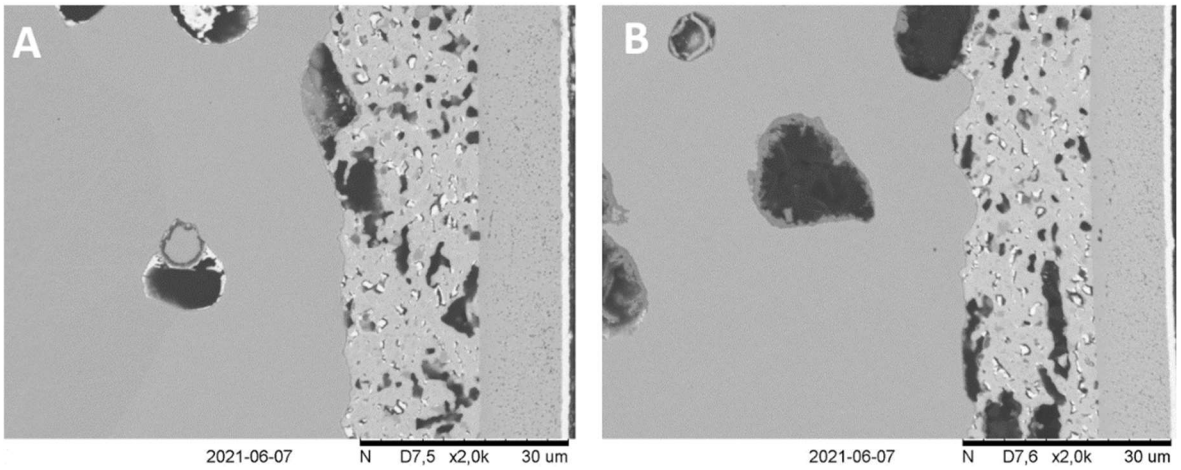

Figure 4.31 – Inlet (A) and outlet (B) SEM images of LSFNT fuel electrode of the second tested MSC. Magnification x2000. From left to right: FeCr support, LSFNT electrode, ScYSZ electrolyte and CGO barrier layer.

Metal support oxidation was confirmed by observing the pores of the metallic supports through which steam flows toward the electrode (or from the electrode in fuel cell mode). It was not possible to appreciate any microscopic difference in the magnitude of such phenomenon between the first and the second cell tested, as was expected by durability test results analysis, since both cells went through the final characterization and consequently they oxidized again.

Figure 4.32 shows two pores of the metallic support structure of the second cell tested: it is possible to observe the presence of metal oxides by looking at the SEM image (dark grey area on the pores' border) and comparing the element distribution of cerium (B) and oxygen (C). Oxygen should be present only in the infiltrated CGO, hence close to cerium, instead it is also spotted in high concentration where Ce is not present.

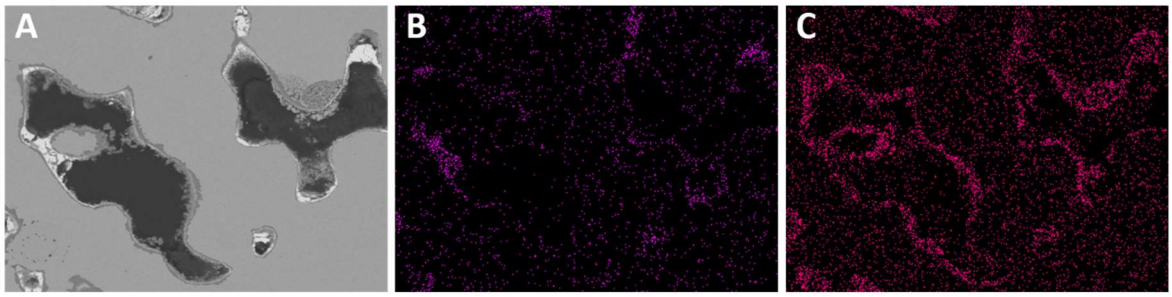

Figure 4.32 – SEM (A) and EDS (B and C) images of two pores of the second cell tested, at x1500 magnification. B and C refers to cerium and oxygen distribution, respectively.

4.3 Low temperature performance comparison between ceramic and metal-supported cells

Figure 4.33 shows polarization, efficiency and power curves for both ceramic and metal-supported technologies, obtained at 650 °C feeding air to the positive electrode and 50% steam – 50% hydrogen to the negative one.

The metal supported cell requires a lower voltage to electrolyze water at low temperatures with respect to the ceramic one, allowing to achieve higher electricity-to-hydrogen conversion efficiency and lower power demand. This is mainly due to the Sc-YSZ electrolyte, which ionic conductivity is higher than the one of the YSZ electrolyte present in the ceramic-supported cell, thanks to the presence of scandium as a co-dopant.

Resistance contributions obtained from EIS recorded at OCV for both cells, at same temperature and feeds of Figure 4.33Figure 4.29, are reported in Table 4.12.

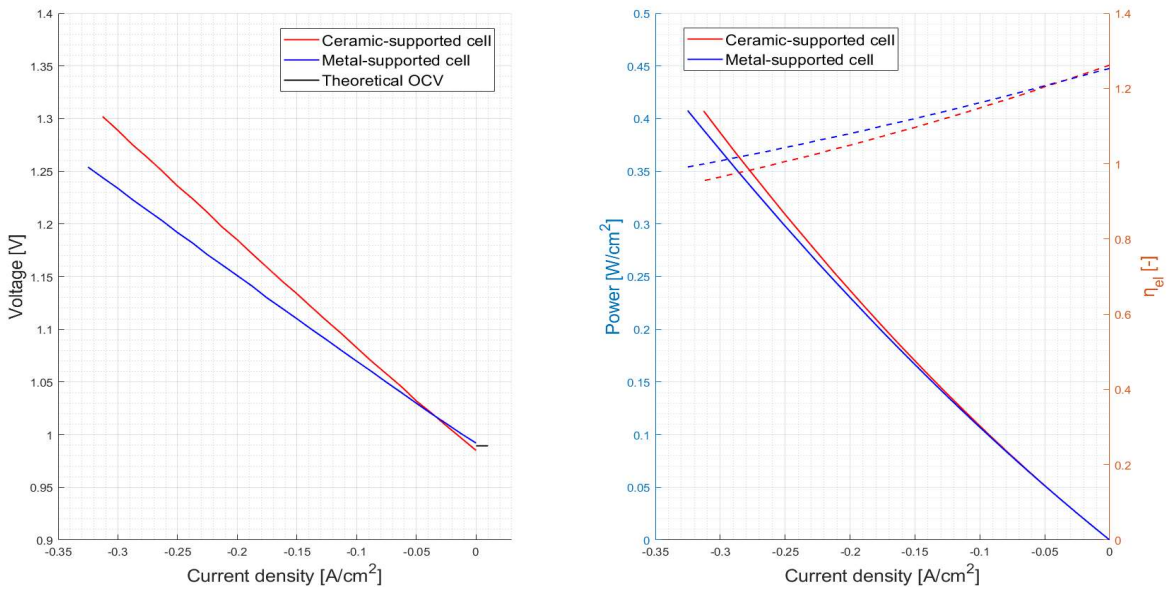

Figure 4.33 - Comparison between ceramic and metal supported cells: i-V curves (left), power (right, continuous lines) and efficiency (right, dotted lines) at 650 °C, air, 50% steam - 50% hydrogen.

Table 4.12 – Resistance contributions extracted from EIS at OCV of ceramic and metal-supported cells at 650 °C, air, 50% steam content.

Type of cell's support	R_s [mΩcm^2]	R_p [mΩcm^2]	ASR [mΩcm^2]
Ceramic	493	467	960
Metal	292	477	769

From these data, as well as Figure 4.34, showing Nyquist plots obtained at same operative conditions as Figure 4.33, it is possible to conclude that the ohmic resistance is the main responsible for the better performances, in terms of total resistance, obtained with the new technology. Besides the better conducting electrolyte, also the metallic support structure contributes to decrease the electric resistivity, being more conductive than the nickel-infiltrated ceramic structure.

On the other hand, the polarization resistance is slightly bigger in the case of the metal-supported cell compared with the ceramic one. It cannot be clearly said if the ceramic-supported electrodes are better performing than the MSC ones. However, it is important to notice that nickel loading is three orders of magnitude higher in the negative electrode of the ceramic-supported cell with respect to the MSC (3.5 g/cm^2 vs 0.8-1 mg/cm^2 for the ceramic and metal supported negative electrodes respectively), for this reason it its thought that the better performance in terms of lower polarization resistance for the ceramic supported cell, can be attributed mainly to the negative electrode.

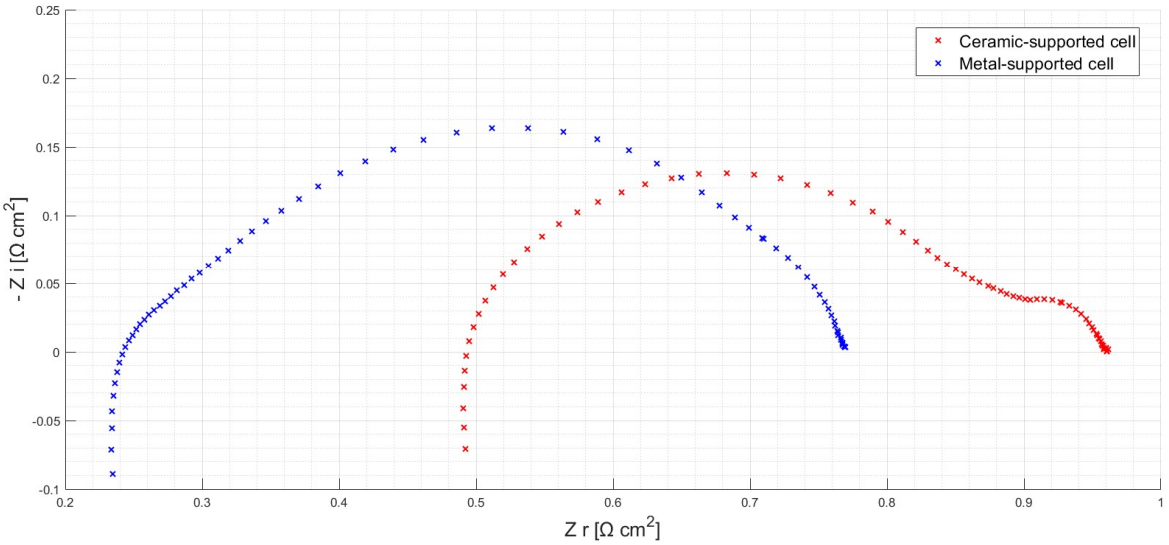

Figure 4.34 - Comparison between ceramic and metal supported cells: Nyquist plots at 650 °C, air, 50% steam - 50% hydrogen.

What is certain is that the fuel electrode-related degradation phenomena are less severe in the case of the MSC with respect to the ceramic-supported cell. Indeed, the state-of-the-art technology during the 0.25 A/cm^2 durability test showed an increase in polarization

resistance equal to 53.66% of the initial value, while at same current density the metal-supported cell's polarization resistance remained very stable (actually, the measured values show that it decreased of 2.86%).

Chapter 5
Conclusions and outlook

Both the ceramic and the metal-supported cells showed good performances at 650 °C in terms of voltage required to electrolyse steam, the latter in particular demonstrated to be the best solution for this temperature thanks mainly to the different electrolyte. The metallic support structure also contributes to decrease ohmic resistance. On the other hand, the Fe-Cr alloy proved to be very sensitive to steam presence at the pore's interface with fed gases, going through a rapid oxidation when the right thermodynamic conditions apply, and reducing back to its metallic form during galvanostatic operation in electrolysis mode.

The ceramic supported cell gave good results in terms of degradation when compared to a very similar cell tested by Sun et al [18] (same layers except for the oxygen electrode which in this case was LSCF-CGO, instead of LSC-CGO). In this test particularly, at 800 °C with a current density of 1 A/cm^2, the cell showed in the first 200 hours a degradation rate equal to 52% of initial cell voltage per 1,000 h. Ceramic-supported cells are designed to work at high temperatures, anyway the degradation observed with the cell tested for this project was consistent with the one observed by Sun et al. Indeed, the degradation rate measured in the galvanostatic test performed at 650 °C was 13.28% of initial cell voltage per 1,000 h with a current density equal to 0.25 A/cm^2, that is more or less one quarter of the degradation rate observed at a four times higher current density (1 A/cm^2). The main difference between the two cases is that at 650 °C the degradation rate remained constant for the whole duration of the durability test (500 hours), while at 800 °C after just 200 hours the cell started to reactivate and showed stable performance for about 900 hours, while for the following 3300 hours the overall cell voltage degradation was 1.9% per 1,000 h. It can be stated that at higher temperature this type of solid oxide cell behaves better, requiring a lower electric energy input for electrolysis, however a longer durability test should be performed also at 650 °C to verify if a reactivation process would occur as well. If the cell would prove to be stable also at 650 °C, the best operating conditions should be assessed trading off electricity and heat energy demand, as well as cost and lifetime of the stack.

The degradation observed can be attributed to nickel migration and loss of triple phase boundary surface especially at the inlet of the cell, where the electrochemical stress is more severe. Moreover, uneven degradation of the Ni-YSZ electrode would give rise to an uneven distribution of current, contributing to furtherly enhance the degradation of such area.

No appreciable degradation was observed at the oxygen electrode. This cell demonstrated to be very sensitive to temperature changes. Indeed, the cause of the crack that compromised the cell structure at the end of the second characterization is attributed to the multiple temperature ramps performed.

Meaningful electrolysis tests to compare the results obtained with the metal-supported cells were not found in the literature. It is very interesting to highlight that this particular material combination was designed for fuel cell mode, but the cell proved to be very stable if operated in electrolysis.

The metal supported cells tested showed very promising results in terms of active layers electrochemical stability in electrolysis conditions. It is plausible that Ni catalytic particles are more stable in the LSFNT lattice with respect to the YSZ crystalline structure, hence migration and loss of catalytic surface is more limited. In addition it also appeared, by comparing the two durability tests with the MSCs, that electrode degradation (spotted as a polarization resistance change) is not much affected by the current densities adopted during the tests. Further tests are required to verify this assumption, for instance increasing more the current and avoiding completely a characterization in fuel cell mode, to understand better the evolution of cell performance in electrolysis mode.

However, such cells demonstrated to be very sensitive to steam presence, especially if operated in SOFC mode: metallic support oxidation is thought to be the main phenomenon that hinders actual cell's potentiality, hence R&D should be focused on finding the best solution to overcome this issue. Further tests are required to achieve a more comprehensive cell behaviour knowledge; however, the tests performed during this work helped to develop a safer characterization protocol for metal-supported cells.

The tests performed for this project's purpose allowed to highlight the main features of commercially available and recently developed solid oxide cell's technologies. The ceramic supported cells showed their weakness: thermal stresses can severely compromise lattice integrity, which in the worst case can lead to a system failure. SOEC are meant to be coupled with intermittent renewable energy sources hence the more dynamic their operative conditions would be, the better for the management of the whole system. During the development of this work it was not possible to assess degradation and performance evolution across a reversible operation test. For instance, this could be done taking as electric input for SOEC mode the current profile produced by a wind farm or a photovoltaic field, and as output for SOFC mode the profile of the uncovered energy demand for a utility which would rely completely on renewable sources. For this reason, this kind of test is highly recommended for future studies and experimental activities, particularly focusing on the metal supported technology. Indeed MSCs, besides all the advantages related to the better performances at lower operating temperature (stack and energy costs), were thought to follow a more dynamic temperature profile and to achieve higher stack power densities for the coupling with big plants thanks to higher tolerance on thermal and mechanical stresses.

A comparison with more mature Alkaline and PEM technologies can be done only in a qualitative way, since the operating conditions are very different and the performance parameters – efficiencies for instance – are defined in a different way. In addition, solid oxide cells (especially metal-supported ones) are a recently developed technology, hence it is not possible to have precise information about production costs, and their impact on energy market can only be speculated. Consolidated Alkaline and PEM technologies are not expected to reduce their specific costs too much in the coming years. In particular it can be expected a reduction from 700 €/kW for Alkaline and 1000 €/kW for PEM, to around 580 €/kW and 760 €/kW respectively by 2030 [27]. In this scenario solid oxides cells and particularly metal-supported ones, could become very competitive. It is not easy to give a meaningful cost projection because of the early development of such technology; however, it can be speculated that the 500 €/kW target could be achieved in the incoming years [28]. R&D, aimed to overcome the issues and to enhance performances related to this technology, could unlock the potentiality of solid oxide cells, which would give an important contribution for the green energy transition toward a more sustainable future.

List of Appendices

Appendix A - Theoretical OCV calculation

In this appendix is presented the procedure to find the formula for computing the theoretical open circuit voltage from the known parameters (temperature and volume flow rates).

The theoretical OCV is the reversible voltage the cell would reach in ideal conditions. Using Nernst equation (1.2) and considering that in a solid oxide cell the electrochemical reactions at the electrodes are

- $2\,H_2O + 4\,e^- \rightarrow 2\,H_2 + 2\,O^{2-}$ to the negative electrode
- $2\,O^{2-} \rightarrow O_2 + 4\,e^-$ to the positive electrode

the theoretical OCV can be computed as:

$$OCV_{theory} = \Delta E_{Nernst} = E^{+}_{Nernst} - E^{-}_{Nernst} = E_0 + \frac{\mathcal{R}\,T}{2\,F}\,ln\frac{{a_{O_2}}^{0,5}\,a_{H_2}}{a_{H_2O}} \tag{A.1}$$

Approximating the fuel mixture and air/oxygen as ideal gases, the activities can be simply expressed as ratio between partial pressure of the considered component and reference pressure, that as convention is 1 atm:

$$a_i = \frac{p_i}{p_{ref}} = x_i\frac{p_{tot}}{p_{ref}} = x_i\,p_{tot} \tag{A.2}$$

where x_i is the molar fraction.

The theoretical OCV's expression becomes:

$$OCV_{theory} = E_0 + \frac{\mathcal{R}\,T}{2\,F}\,ln\frac{\left(x_{O_2}\,p_+\right)^{0,5}\left(x_{H_2}\,p_-\right)}{\left(x_{H_2O}\,p_-\right)} \tag{A.3}$$

where the signs + and – refer respectively to positive and negative electrodes.

Mathematically simplifying:

$$OCV_{theory} = E_0 + \frac{\mathcal{R}\,T}{2\,F}\,ln\frac{\left(x_{O_2}\,p_+\right)^{0,5}\,x_{H_2}}{x_{H_2O}} \tag{A.4}$$

In the test rig the cells are tested at atmospheric pressure, so substituting to p_+ the value of 1 atm:

$$OCV_{theory} = E_0 + \frac{\mathcal{R}\,T}{2\,F}\,ln\left[{x_{O_2}}^{0,5}\,\frac{x_{H_2}}{x_{H_2O}}\right] \tag{A.5}$$

Again considering the gases as ideal, the following relation holds:

$$\frac{x_{H_2}}{x_{H_2O}} = \frac{\dot{V}_{H_2}}{\dot{V}_{H_2O}} \tag{A.6}$$

where $\dot{V}$ is the volume flow rate.

The theoretical OCV can be then expressed as:

$$OCV_{theory} = E_0 + \frac{\mathcal{R}\,T}{2\,F}\,ln\left[{x_{O_2}}^{0,5}\,\frac{\dot{V}_{H_2}}{\dot{V}_{H_2O}}\right] \tag{A.7}$$

Not all the hydrogen fed must be considered in the equation, because part of it is burnt with oxygen fed to the negative electrode and it is converted into water.

The amount of hydrogen that actually participate to the electrochemical reaction is:

$$\dot{V}_{H_2} = \dot{V}_{H_2,feed} - \dot{V}_{H_2,burnt} \tag{A.8}$$

The equation becomes:

$$OCV_{theory} = E_0 + \frac{\mathcal{R}\,T}{2\,F}\,ln\left[{x_{O_2}}^{0,5}\,\frac{\dot{V}_{H_2,feed} - \dot{V}_{H_2,burnt}}{\dot{V}_{H_2O}}\right] \tag{A.9}$$

To understand how much hydrogen is burnt and how much water is produced, the combustion reaction must be taken into account: $H_2 + \frac{1}{2}\,O_2 \rightarrow\ H_2O$.

From the stoichiometric coefficients it is possible to find the wanted amounts:

$$\dot{V}_{H_2,burnt} = 2\,\dot{V}_{O_2,fuel\ electrode} \qquad \dot{V}_{H_2O} = 2\,\dot{V}_{O_2,fuel\ electrode} \tag{A.10}$$

where $\dot{V}_{O_2,fuel\ electrode}$ is the volume flow rate of oxygen fed to the negative electrode in order to burn part of the hydrogen and get steam.

So the final formula for computing the theoretical open circuit voltage is:

$$OCV_{theory} = E_0 + \frac{\mathcal{R}\,T}{2\,F}\,ln\left[{x_{O_2}}^{0,5}\,\frac{\dot{V}_{H_2,feed} - 2\,\dot{V}_{O_2,fuel\ electrode}}{2\,\dot{V}_{O_2,fuel\ electrode}}\right] \tag{A.11}$$

The oxygen molar fraction x_{O_2} depends on the gas fed to the oxygen electrode: in case of pure oxygen, $x_{O_2} = 1$; in case of air, considering it as a mixture of just N_2 (79 %) and O_2 (21 %), the oxygen molar fraction is $x_{O_2} = 0.21$.

The only unknown parameter left is the hydrogen oxidation reaction's standard potential E_0, that depends on temperature. The values of E_0 used in this project for the different considered temperatures (650, 700, 750, 800, 850 °C) have been extrapolated from the ones reported in reference [114], that are showed in Figure A..

T (°C)	E_0 (V)
200	1.142
300	1.116
400	1.090
500	1.062
600	1.034
700	1.006
800	0.977
900	0.949
1,000	0.919

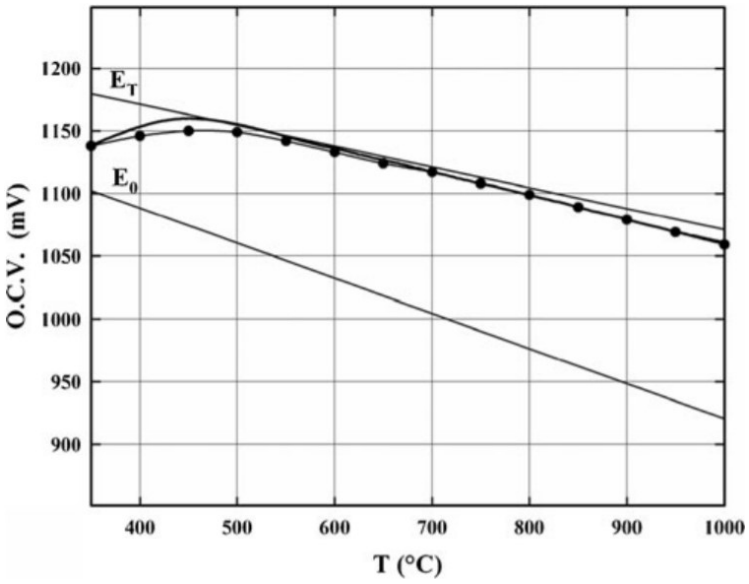

Figure A.1 - Temperature dependance of hydrogen oxidation reaction's standard potential.

Table A.1 reports the precise values of E_0 used to compute the theoretical OCV in this project.

Table A.1 - E_0 values used for theoretical OCV calculation.

T [°C]	650	700	750	800	850
E_0 [mV]	1020	1006	991,5	977	963

The values of the thermodynamics OCVs, computed using equation (A.12) at all temperatures and feed compositions adopted during this work, are written in Table A.2.

Table A.2 – Theoretical OCV values measured in mV.

Steam content	650 °C		700 °C		750 °C		800 °C		850 °C	
20%	1042	1073	1029	1062	1016	1050	1003	1039	990	1028
50%	989	1020	973	1006	957	992	941	977	925	963
90%	904	935	883	916	862	897	842	878	821	859
	Air	O_2	Air	O_2	Air	O_2	Air	O_2	Air	O_2

List of acronyms used in this work

AEM	Anion Exchange Membrane
AC	Alternating Current
ASR	Area Specific Resistance
CCUS	Carbon Capture, Utilisation and Storage
CGO	Cerium Gadolinum Oxide
CHP	Combined Heat and Power
CSP	Concentrated Solar Power
DC	Direct Current
DFT	Density Functional Theory
DTU	Danmarks Tekniske Universitet
EDS	Energy Dispersive x-ray Spectroscopy
EIS	Electrochemical Impedance Spectroscopy
GDC	Gadolinum Doped Ceria
GDL	Gas Diffusion Layer
GDP	Gross Domestic Product
GHG	GreenHouse Gas
HER	Hydrogen Evolution Reaction
ILUC	Indirect Land Use Change
INDC	Intended Nationally Determined Contribution
IPCC	Intergovernmental Panel on Climate Change
LHV	Lower Heating Value
LSM	Lanthanum Strontium Manganite
LSC	Lanthanum Strontium Cobaltite
LSCF	Lanthanum Strontium Cobalt Ferrite
LSF	Lanthanum Strontium Ferrite
LSFNT	Lanthanum Strontium Fe-Ni Titanate
MIEC	Mixed Ionic Electronic Conductors
MSC	Metal Supported Cell

OCV	Open Circuit Voltage
PEM	Polymer Electrolyte Membrane
RED	Renewable Energy Directive
RES	Renewable Energy Source
R&D	Research and Development
ScSZ	Scandia Stabilized Zirconia
SEM	Scanning Electron Microscope
SOC	Solid Oxide Cell
SOEC	Solid Oxide Electrolysis Cell
SOFC	Solid Oxide Fuel Cell
TC	Through Coupler
TPB	Triple Phase Boundary
WWI	World War I
WWII	World War II
YSZ	Yttria Stabilized Zirconia

Bibliography

[1] British Petroleum, «Statistical Review of World Energy 2020», 2020.

[2] The Intergovernmental Panel on Climate Change, «The Carbon Cycle and Atmospheric Carbon Dioxide».

[3] D. Barriopedro, E.M. Fischer, J. Luterbacher, R.M. Trigo, R. García-Herrera, «The Hot Summer of 2010: Redrawing the Temperature Record Map of Europe», *Science,* vol. 332 (6026), pp. 220-224, 2011.

[4] «EU SCIENCE HUB» [Online]. Available: https://ec.europa.eu/jrc/en/jec/renewable-energy-recast-2030-red-ii.

[5] P. Alotto, M. Guarnieri, F. Moro, «Redox flow batteries for the storage of renewable energy: A review», *Renewable and Sustainable Energy Reviews,* vol. 29, pp. 325-335, 2014.

[6] D. Connolly, H. Lund, B.V. Mathiesen, «Smart Energy Europe: The technical and economic impact of one potential 100% renewable energy scenario for the European Union», *Renewable & sustainable energy reviews,* vol. 60, p. 1634–1653, 2016.

[7] G. Sdanghi, G. Maranzana, A. Celzard, V. Fierro, «Towards Non-Mechanical Hybrid Hydrogen Compression for Decentralized Hydrogen Facilities», *Energies 2020,* vol. 13 (12), p. 3145, 2020.

[8] «IEA,» [Online]. Available: https://www.iea.org/fuels-and-technologies/hydrogen.

[9] «Office of ENERGY EFFICIENCY & RENEWABLE ENERGY» [Online]. Available: https://www.energy.gov/eere/fuelcells/hydrogen-production-thermochemical-water-splitting.

[10] M. Penconi, F. Rossi, F. Ortica, F. Elisei, P.L. Gentili, «Hydrogen Production from Water by Photolysis, Sonolysis and Sonophotolysis with Solid Solutions of Rare Earth, Gallium and Indium Oxides as Heterogeneous Catalysis», *Sustainability,* vol. 7 (7), pp. 9310-9325, 2015.

[11] W. Dönitz, E. Erdle, «High-temperature electrolysis of water vapor—status of development and perspectives for application», *International Journal of Hydrogen Energy,* vol. 10 (5), pp. 291-295, 1985.

[12] S.H. Jensen, P.H. Larsen, M.B. Mogensen, «Hydrogen and synthetic fuel production from renewable energy sources», *International Journal of Hydrogen Energy,* vol. 32, n. 15, pp. 3253-3257, 2007.

[13] R. Phillips, C.W. Dunnill, «Zero gap alkaline electrolysis cell design for renewable energy storage as hydrogen gas», *Royal Society of Chemistry,* vol. 6, p. 100643–100651, 2016.

[14] A. Pashaei, «Hydrogen production with water electrolysis method to use in fuel cell for electricity generation», *4th Conference on Emerging Trends in Energy Conservation,* 2014.

[15] C. Kongfa, D. Dehua, S.P. Jiang, «Hydrogen Production from Water and Air Through Solid Oxide Electrolysis», *Production of Hydrogen from Renewable Resources,* pp. 223-248, 2015.

[16] M. Andersson, J. Froitzheim, «Energiforsk,» 2019. [Online]. Available: https://energiforsk.se/media/26740/technology-review-solid-oxide-cells-2019-energiforskrapport-2019-601.pdf.

[17] L. Mastropasqua, S. Campanari, J. Brouwer, «Electrochemical Carbon Separation in a SOFC–MCFC Polygeneration Plant With Near-Zero Emissions», *Journal of Engineering for Gas Turbines and Power,* vol. 140 (1), p. 013001, 2018.

[18] X. Sun, P. V. Hendriksen, M.B. Mogensen, M. Chen, «Degradation in Solid Oxide Electrolysis Cells During Long Term Testing», *Fuel Cells,* vol. 19 (6), pp. 740-747, 2019.

[19] A. Hauch, R. Küngas, P. Blennow, A. B. Hansen, J. B. Hansen, B.V. Mathiesen, M. B. Mogensen, «Recent advances in solid oxide cell technology for electrolysis», *Science,* vol. 370 (6513), 2020.

[20] M. B. Mogensen, «Thermodynamics of high-temperature H2O and CO2 electrolysis», 2020.

[21] K. Zeng, D. Zhang, «Recent progress in alkaline water electrolysis for hydrogen production and applications», *Progress in Energy and Combustion Science,* vol. 36 (3), pp. 307-326, 2010.

[22] W. Dönitz, E. Erdle, R. Streicher, «Electrochemical hydrogen technologies: Electrochemical production and combustion of hydrogen», Amsterdam: Elsevier, 1990, pp. 213-259.

[23] M. Tucker, «Progress in metal-supported solid oxide electrolysis cells: A review», *International journal of hydrogen energy,* n. 45, pp. 24203-24218, 2020.

[24] A. Hagen, X. Sun, B.R. Sudireddy, Å.H. Persson, «Metal Supported SOFCs for Mobile Applications using Hydrocarbon», *Journal of The Electrochemical Society,* vol. 167, n. 10, 2020.

[25] R. Küngas, P. Blennow, T. Heiredal-Clausen, T. Holt Nørby, J. Rass-Hansen, P.G. Moses, «Lifetime Capacity – An Important Performance Metric for SOEC Stacks», *The Electrochemical Society,* vol. 91, n. 1, 2019.

[26] E4tech, «The Fuel Cell Industry Review», 2020.

[27] L. Bertuccioli, A. Chan, D. Hart, F. Lehner, B. Madden, E. Standen, «Study on development of water electrolysis in the EU», 2014.

[28] «Fuel cell technology elcogen,» [Online]. Available: https://elcogen.com/.

[29] «FIRST COMMERCIAL PLANT FOR THE PRODUCTION OF BLUE CRUDE PLANNED IN NORWAY», Sunfire, 2017. [Online]. Available: https://www.sunfire.de/en/news/detail/first-commercial-plant-for-the-production-of-blue-crude-planned-in-norway.

[30] E. Baur, H. Preis, «Über Brennstoff-Ketten mit Festleitern», *Zeitschrift für Elektrochemie und angewandte physikalische Chemie,* vol. 43 (9), pp. 727-732, 1937.

[31] L. Malavasi, C.A.J. Fisher, M.S. Islam, «Oxide-ion and proton conducting electrolyte materials for clean energy applications: structural and mechanistic features», *Chemical Society Reviews,* vol. 11, pp. 4370-4387, 2010.

[32] M. Yashima, M. Kakihana, M. Yoshimura, «Metastable-stable phase diagrams in the zirconia-containing systems utilized in solid-oxide fuel cell application», *Solid State Ionics,* vol. 86, pp. 1131-1149, 1996.

[33] J. Kilner, «Fast oxygen transport in acceptor doped oxides», *Solid State Ionics,* vol. 129 , pp. 13-23, 2000.

[34] Y. Arachi, H. Sakai, O. Yamamoto, Y. Takeda, N. Imanishai, «Electrical conductivity of the ZrO2-Ln2O3 (Ln¼lanthanides) system», *Solid State Ionics,* vol. 121, pp. 133-139, 1999.

[35] D. Kim, «Lattice Parameters, Ionic Conductivities, and Solubility Limits in Fluorite-Structure MO2 Oxide [M = Hf4+, Zr4+, Ce4+, Th4+, U4+] Solid Solutions», *Journal of the American Ceramic Society,* vol. 72 (8), pp. 1415-1421, 1989.

[36] J. Kilner, «Fast anion transport in solids», *Solid State Ionics,* vol. 8 (3), pp. 201-207, 1983.

[37] P.S. Manning, J.D. Sirman, R.A. De Souza, J.A. Kilner, «The kinetics of oxygen transport in 9.5 mol % single crystal yttria stabilised zirconia», *Solid State Ionics,* vol. 100 (1), pp. 1-10, 1997.

[38] F. Ye, T. Mori, D.R. Ou, A.N. Cormack, R.J. Lewis, J. Drennan, «Simulation of ordering in large defect clusters in gadolinium-doped ceria», *Solid State Ionics,* vol. 179 (35), pp. 1962-1967, 2008.

[39] L. Minervini, M.O. Zacate, R.W. Grimes, «Defect cluster formation in M2O3-doped CeO2», *Solid State Ionics,* vol. 116 (3), pp. 339-349, 1999.

[40] S. S. N. S. I. A. A. B. J. D.A. Andersson, «Optimization of ionic conductivity in doped ceria», *Proceedings of the National Academy of Sciences of the United States of America,* vol. 103 (10), p. 3518–3521, 2006.

[41] R.M. Kasse, J.C. Nino, «Ionic conductivity of SmxNdyCe0.9O2-δ co-doped ceria electrolytes», *Journal of Alloys and Compounds,* vol. 575, pp. 399-402, 2013.

[42] K. Park, H.K. Hwang, «Electrical conductivity of Ce0.8Gd0.2-xDyxO2-δ (0<¼x<¼0.2) co-doped with Gd3+ and Dy3+ for intermediate-temperature solid oxide fue cells», *Journal of Power Sources,* vol. 196 (11), pp. 4996-4999, 2011.

[43] P.P. Dholabhai, J.B. Adams, P.A. Crozier, R. Sharma, «In search of enhanced electrolyte materials: a case study of doubly doped ceria», *Journal of Materials Chemistry,* vol. 21 (47), pp. 18991-18997, 2011.

[44] W. Zajac, J. Molenda, «Electrical conductivity of doubly doped ceria», *Solid State Ionics,* vol. 179, pp. 154-158, 2008.

[45] M.O. Zacate, L. Minervini, D.J. Bradfield, R.W. Grimes, K.E. Sickafus , «Defect cluster formation in M2O3-doped cubic ZrO2», *Solid State Ionics,* vol. 128 (1), p. 243–254, 2000.

[46] C. Haering, A. Roosen, H. Schichl, M. Schnoller, «Degradation of the electrical conductivity in stabilised zirconia system Part II: scandia-stabilised zirconia», *Solid State Ionics ,* vol. 176 (3), p. 261–268, 2005.

[47] D.S. Lee, W.S. Kim, S.H. Choi, J. Kim, H.W. Lee, J.H. Lee , «Characterization of ZrO2 co-doped with Sc2O3 and CeO2 electrolyte for the application of intermediate temperature SOFCs», *Solid State Ionics,* vol. 176 (1), pp. 33-39, 2005.

[48] A. Spirina, V. Ivanov, A. Nikonov, A. Lipilin, S. Paranin, V. Khrustov, A. Spirina, «Scandia-stabilized zirconia doped with yttria: Synthesis, properties, and ageing behavior», *Solid State Ionics,* vol. 225, pp. 448-452, 2012.

[49] V.V. Osipov, Yu.A. Kotov, M.G. Ivanov, O.M. Samatov, V.V. Lisenkov, V.V. Platonov, A.M. Murzakaev, A.I. Medvedev, E.I. Azarkevich , «Laser synthesis of nanopowders», *Laser Physics,* vol. 16, pp. 116-125, 2006.

[50] M. Godickemeier, L.J. Gauckler , «Engineering of solid oxide fuel cells with ceria-based electrolytes», *Journal of the Electrochemical Society,* vol. 145 (2), pp. 414-421, 1998.

[51] M. Godickemeier, K. Sasaki, L.J. Gauckler, I. Riess, «Electrochemical characteristics of cathodes in solid oxide fuel cells based on ceria electrolytes», *Journal of Electrochemical Society,* vol. 144 (5), p. 1635–1646, 1997.

[52] B.C.H. Steele, «Materials for high-temperature fuel cells», *Philosophical Transactions of the Royal Society,* vol. 354, pp. 1695-1710, 1996.

[53] A. Atkinson, S. Barnett, R. J. Gorte, J. T.S. Irvine, A. J. McEvoy, M. Mogensen, S.C. Singhal, J. Vohs, «Advanced anodes for high-temperature fuel cells», *Nature materials,* vol. 3 (1), pp. 17-27, 2004.

[54] H.H. MoÈbius, «On the history of solid electrolyte fuel cells», *Journal of Solid State Electrochemistry,* vol. 1, pp. 2-16, 1997.

[55] H. Spacil.USA Brevetto 3,558,360, March 1970.

[56] M. Brown, S. Primdahl, M. Mogensen, «Structure/Performance Relations for Ni/Yttria-Stabilized Zirconia Anodes for Solid Oxide Fuel Cells», *Journal of The Electrochemical Society,* vol. 147, n. 2, pp. 475-485, 2000.

[57] M. Lang, T. Franco, G. Schiller, N. Wagner , «Electrochemical characterization of vacuum plasma sprayed thin-film solid oxide fuel cells (SOFC) for reduced operating temperatures», *Journal of Applied Electrochemistry,* vol. 32, pp. 871-874, 2002.

[58] W.Z Zhu, S. Deevi, «A Review on the Status of Anode Materials for Solid Oxide Fuel Cells», *Materials Science and Engineering A,* vol. 362 (1), pp. 228-239, 2003.

[59] T. Klemensø, C. Chung, P. H. Larsen, M. Mogensen, «The Mechanism Behind Redox Instability of Anodes in High-Temperature SOFCs», *Journal of The Electrochemical Society,* vol. 152, p. A2186, 2005.

[60] M.Cassidy, G. Lindsay, K. Kendall, «The reduction of nickel-zirconia cermet anodes and the effects on supported thin electrolytes», *Journal of Power Sources,* vol. 61 (1), pp. 189-192, 1996.

[61] B.S. Prakash, S.S. Kumar, S.T. Aruna, «Properties and development of Ni/YSZ as an anode material in solid oxide fuel cell: A review», *Renewable and Sustainable Energy Reviews,* vol. 36, pp. 149-179, 2014.

[62] A. Faes, A. Hessler-Wyser, A. Zryd, J. Van herle, «A Review of RedOx Cycling of Solid Oxide Fuel Cells Anode», *Membranes,* vol. 2 (3), pp. 585-664, 2012.

[63] F. Tietz, H.P. Buchkremer, D. Stover, «Components manufacturing for solid oxide fuel cells», *Solid State Ionics,* Vol. %1 di %2152-153, pp. 373-381, 2002.

[64] M. Tucker, «Progress in metal-supported solid oxide fuel cells: A review», *Journal of Power Sources,* vol. 195 (15), pp. 4570-4582, 2010.

[65] J. Nielsena, Å.H. Perssona, B.R. Sudireddya, J.T.S. Irvineb, K. Thydéna, «Infiltrated La0.4Sr0.4Fe0.03Ni0.03Ti0.94O3 based anodes for all ceramic and», *Journal of Power Sources,* vol. 372, p. 99–106, 2017.

[66] E.S. Hecht, G.K. Gupta, H. Zhu, A.M. Dean, R.J. Kee, L. Maier, O. Deutschmann, «Methane reforming kinetics within a Ni-YSZ SOFC anode support», *Applied Catalysis A: General,* vol. 295, pp. 40-51, 2005.

[67] P. Holtappels, L.G.J. De Haart, U. Stimming, I. C. Vinke, M. Mogensen , «Reaction of CO/CO2 gas mixtures on Ni–YSZ cermet electrodes», *Journal of Applied Electrochemistry,* vol. 29, pp. 561-568, 1999.

[68] T. Takeguchi, Y. Kania, T. Yano, R. Kikuchi, K. Eguchi, K. Tsujimoto, Y. Uchida, A. Ueno, K. Omoshiki, M. Aizawa, «Study on steam reforming of CH4 and C2 hydrocarbons and carbon deposition on Ni-YSZ cermets», *Journal of Power Sources,* vol. 112 (2), pp. 588-595, 2002.

[69] M. Boder, R. Dittmeyer, «Catalytic modification of conventional SOFC anodes with a view to reducing their activity for direct internal reforming of natural gas», *Journal of Power Sources,* vol. 155 (1), pp. 13-22, 2006.

[70] M.L. Toebes, J.H. Bitter, A.J. van Dillen, K.P. de Jong, «Impact of the structure and reactivity of nickel particles on the catalytic growth of carbon nanofibers», *Catalysis Today,* vol. 76 (1), pp. 33-42, 2002.

[71] A. Lanzini, P. Leone, C. Guerra, F. Smeacetto, N.P. Brandon, M. Santarelli, «Durability of anode supported Solid Oxides Fuel Cells (SOFC) under direct dry-reforming of methane», *Chemical Engineering Journal,* vol. 220, pp. 254-263, 2013.

[72] K. Sasaki, Y. Teraoka, «Equilibria in Fuel Cell Gases I. Equilibrium Compositions and Reforming Conditions», *Journal of The Electrochemical Society ,* vol. 150 (7), pp. A878-A884, 2003.

[73] H.S. Bengaard, J.K. Nørskov, J. Sehested, B.S. Clausen, L.P. Nielsen, A.M. Molenbroek, J.R. Rostrup-Nielsen, «Steam Reforming and Graphite Formation on Ni Catalysts», *Journal of Catalysis,* vol. 209 (2), pp. 365-384, 2002.

[74] E.P. Murray, T. Tsai, S.A. Barnett, «A direct-methane fuel cell with a ceria-based anode», *Nature,* vol. 400, pp. 649-651, 1999.

[75] H. Kim, S. Park, J.M. Vohs, R.J. Gorte, «Direct Oxidation of Liquid Fuels in a Solid Oxide Fuel Cell», *Journal of The Electrochemical Society,* vol. 148 (7), pp. A693-A695, 2001.

[76] J. Sehested, «Four challenges for nickel steam-reforming catalysts», *Catalysis Today,* vol. 111 (1), pp. 103-110, 2006.

[77] S. Zha, Z. Cheng, M. Lui, «Sulfur Poisoning and Regeneration of Ni-Based Anodes in Solid Oxide Fuel Cells», *Journal of The Electrochemical Society,* vol. 154, n. 2, pp. B201-B206, 2006.

[78] Z. Cheng, M. Lui, «Characterization of sulfur poisoning of Ni–YSZ anodes for solid oxide fuel cells using in situ Raman microspectroscopy», *Solid State Ionics,* vol. 178 (13), pp. 925-935, 2007.

[79] J.B. Goodenough, J.M. Longo, «Crystallographic and Magnetic Properties of Perovskite and Perovskite Related Compounds», vol. 4, pp. 126-314, 1970.

[80] Z. Yi, N.H. Ladi, X. Shai, H. Li, Y. Shen, M. Wang, «Will organic–inorganic hybrid halide lead perovskites be eliminated from optoelectronic applications?», *Royal Society of Chemistry,* vol. 1, pp. 1276-1289, 2019.

[81] J. Mizusaki, J. Tabuchi, T. Matsuura, S. Yamauchi, K. Fueki, «Electrical Conductivity and Seebeck Coefficient of Nonstoichiometric La1 − x Srx CoO3 − δ», *Journal of The Electrochemical Society,* vol. 136 (7), pp. 2082-2088, 1989.

[82] J. Mizusaki, T. Sasamoto, W.R. Cannon, H.K. Bowen, «Electronic Conductivity, Seebeck Coefficient, and Defect Structure of LaFeO3», *Journal of the American Ceramic Society,* vol. 65 (8), pp. 363-368, 1982.

[83] J. Mizusaki, Y. Mima, S. Yamauchi, K. Fueki, H. Tagawa, «Nonstoichiometry of the perovskite-type oxides La1−xSrxCoO3−δ», *Journal of Solid State Chemistry,* vol. 80 (1), pp. 102-111, 1989.

[84] M.H.R. Lankhorst, H.J.M. Bouwmeester, H. Verweij, «Importance of electronic band structure to nonstoichiometric behaviour of La0.8Sr0.2CoO3 − δ», *Solid State Ionics,* vol. 96 (1), pp. 21-27, 1997.

[85] B.A. van Hassel, T. Kawada, N. Sakai, H. Yokokawa, M. Dokiya, «Oxygen permeation modelling of perovskites», *Solid State Ionics,* vol. 66 (3), pp. 295-305, 1993.

[86] J.A.M. Van Roosmalen, E.H.P. Cordfunke, R.B. Helmholdt, H.W. Zandbergen, «The Defect Chemistry of LaMnO3±δ: 2. Structural Aspects of LaMnO3+δ», *Journal of Solid State Chemistry,* vol. 110 (1), pp. 100-105, 1994.

[87] H. Yokokawa, T. Horita, N. Sakai, M. Dokiya, T. Kawada, «Thermodynamic representation of nonstoichiometric lanthanum manganite», *Solid State Ionics,* vol. 86, pp. 1161-1165, 1996.

[88] J. Mizusaki, N. Mori, H. Takai, Y. Yonemura, H. Minamiue, H. Tagawa, M. Dokiya, H. Inaba, K. Naraya, T. Sasamoto, T. Hashimoto, «Oxygen nonstoichiometry and defect equilibrium in the perovskite-type oxides La1−xSrxMnO3+d», *Solid State Ionics,* vol. 129 (1), pp. 163-177, 2000.

[89]] S. Miyoshi, J.-O. Hong, K. Yashiro, A. Kaimai, Y. Nigara, K. Kawamura, T. Kawada, J. Mizusaki, «Lattice creation and annihilation of LaMnO3+δ caused by nonstoichiometry change», *Solid State Ionics,* vol. 154, pp. 257-263, 2002.

[90] K. Iwasaki, T. Ito, T. Nagasaki, Y. Arita, M. Yoshino, T. Matsui, «Thermoelectric properties of polycrystalline La1−xSrxCoO3», *Journal of Solid State Chemistry,* vol. 181 (11), pp. 3145-3150, 2008.

[91] J.A. Kilner, B.C.H. Steele, L. Ilkov, «Oxygen self-diffusion studies using negative-ion secondary ion mass spectrometry (SIMS)», *Solid State Ionics,* vol. 12, pp. 89-97, 1984.

[92] L. Wang, R. Merkle, Y.A. Mastrikov, E.A. Kotomin, J. Maier, «Oxygen exchange kinetics on solid oxide fuel cell cathode materials - general trends and their mechanistic interpretation», *Journal of Materials Research,* vol. 27 (15), pp. 2000-2008, 2012.

[93] H. Kudo, K. Yashiro, S. Hashimoto, K. Amezawa, T. Kawada, «Simulation of oxygen diffusion process on electrical conductivity relaxation», *Solid State Ionics,* vol. 262, pp. 696-700, 2014.

[94] I. Yasuda, K. Ogasawara, M. Hishinuma, T. Kawada, M. Dokiya, «Oxygen tracer diffusion coefficient of (La, Sr)MnO3 ± δ», *Solid State Ionics,* vol. 86, pp. 1197-1201, 1996.

[95] K. Kendall, M. Kendall, «High-temperature solid oxide fuel cells for the 21st century: fundamentals, design and applications», 2015.

[96] A. J. Samson, M. Søgaard, P. Hjalmarsson, J. Hjelm, N. Bonanos, S.P.V. Foghmoes, T. Ramos, «Durability and Performance of High Performance Infiltration Cathodes», *Fuel Cells - From Fundamentals to Systems,* vol. 13 (4), pp. 511-519, 2013.

[97] S. Taniguchi, M. Kadowaki, H. Kawamura, T. Yasuo, Y. Akiyama, Y. Miyake, T. Saitoh, «Degradation phenomena in the cathode of a solid oxide fuel cell with an alloy separator», *Journal of Power Sources,* vol. 55 (1), pp. 73-79, 1995.

[98] K.W. Harrison, R. Remick, G.D. Martin, A. Hoskin, «Hydrogen Production: Fundamentals and Case Study Summaries», Essen, 2010.

[99] [Online]. Available: https://h2tools.org/hyarc/calculator-tools/lower-and-higher-heating-values-fuels.

[100] M. Lang, T. Franco, G. Schiller, N. Wagner , «Electrochemical characterization of vacuum plasma sprayed thin-film solid oxide fuel cells (SOFC) for reduced operating temperatures», *Journal of Applied Electrochemistry,* vol. 32, pp. 871-874, 2002.

[101] [Online]. Available: https://en.wikipedia.org/wiki/Lamination.

[102] [Online]. Available: https://en.wikipedia.org/wiki/Sintering#Ceramic_sintering.

[103] [Online]. Available: https://en.cosel.co.jp/product/powersupply/PBA/PBA600F/PBA600F-3R3/.

[104] [Online]. Available: https://www.horiba-fuelcon.com/en/truedata-load.

[105] M.B. Mogensen, P.V. Hendriksen, «Testing of electrodes, cells and short stacks», in *High temperature solid oxide fuel cells: Fundamentals, design and applications*, Oxford, Elsevier, 2004, pp. 261-290.

[106] R. Mosbæk, «Solid Oxide Fuel Cell Stack Diagnostics», Department of Energy Conversion and Storage, Technical University of Denmark, 2014.

[107] [Online]. Available: https://www.ameteksi.com/products/frequency-response-analyzers/1255b-frequency-response-analyzer.

[108] T. Lochner, H. Henriksen, J.V.T. Høgh, «Impedance measurement correction with Solartron 1260», Risø Institute: Department of Energy Conversion, Technical University of Denmark, 2015.

[109] [Online]. Available: https://www.hitachi-hightech.com/global/about/news/2010/nr20100129.html.

[110] R.A. Budiman, T. Ishiyama, K.D. Bagarinao, H. Kishimoto, K. Yamaji, T. Horita, «Dependence of hydrogen oxidation reaction on water vapor in anode-supported solid oxide fuel cells», *Solid State Ionics,* vol. 362, p. 115565, 2021.

[111] A. Hauch, S. D. Ebbesen, S. H. Jensen, M. Mogensen, «Solid Oxide Electrolysis Cells: Microstructure and Degradation of the Ni/Yttria-Stabilized Zirconia Electrode», *Journal of The Electrochemical Society,* vol. 155 (11), p. B1184, 2008.

[112] H. Yokokawa, H. Tu, B. Iwanschitz, A. Mai, «Fundamental mechanisms limiting solid oxide fuel cell durability», *Journal of Power Sources,* vol. 182 (2), pp. 400-412, 2008.

[113] A. Hagen, R. Barfod, P. V. Hendriksen, Y.-L. Liu, S. Ramousse, «Degradation of Anode Supported SOFCs as a Function of Temperature and Current Load», *Journal of The Electrochemical Society,* vol. 153 (6), p. A1165, 2006.

[114] G. Chiodelli, L. Malavasi, «Electrochemical open circuit voltage (OCV) characterization of SOFC materials», *Ionics,* vol. 19, pp. 1135-1144, 2013.

[115] M.A. Green, A. Ho-Baillie, H.J. Snaith , «The emergence of perovskite solar cells», *Nature Photonics,* vol. 8, pp. 506-514, 2014.

[116] C. Haering, A. Roosen, H. Schichl, M. Schnoller , «Degradation of the electrical conductivity in stabilised zirconia system Part II: scandia-stabilised zirconia», *Solid State Ionics ,* vol. 176 (3), p. 261–268, 2005.

[117] M.A. Green, A. Ho-Baillie, H.J. Snaith, «The emergence of perovskite solar cells», *Nature Photonics,* vol. 8, p. 506–514, 2014.

[118] S.D. Ebbesen, R. Knibbe, M. Mogensen, «Co-Electrolysis of Steam and Carbon Dioxide in Solid Oxide Cells», *Journal of The Electrochemical Society,* vol. 159 (8), pp. F482-F489, 2012.

[119] X. Sun, M. Chen, Y. Liu, P. Hjalmarsson, S.D. Ebbesen, S.H. Jensen, M.B. Mogensen, P. Vang Hendriksen, «Durability of Solid Oxide Electrolysis Cells for Syngas Production», *Journal of The Electrochemical Society,* vol. 160 (9), pp. F1074-F1080, 2013.

[120] V. Menon, V.M. Janardhanan, O. Deutschmann, «A mathematical model to analyze solid oxide electrolyzer cells (SOECs) for hydrogen production», *Chemical EngineeringScience,* vol. 110, pp. 83-93, 2014.